Important Notice

UNIVERSITY OF CALGARY

Full waveform inversion combining rock physics for seismic reservoir characterization and monitoring

by

Qi Hu

A THESIS
SUBMITTED TO THE FACULTY OF GRADUATE STUDIES
IN PARTIAL FULFILMENT OF THE REQUIREMENTS FOR THE
DEGREE OF DOCTOR OF PHILOSOPHY

GRADUATE PROGRAM IN GEOLOGY AND GEOPHYSICS

CALGARY, ALBERTA
OCTOBER, 2023

Abstract

Quantitative estimation of rock physics properties, such as porosity, lithology, and fluid saturation, is an important part of reservoir characterization. Most current seismic workflows in this field are based on amplitude variation with offset (AVO). Full waveform inversion (FWI) methods, although computationally more complex than AVO approaches, can produce more accurate elastic models by extracting the full information content in the seismogram. Progress has been reported in using elastic FWI results as intermediate quantities to derive rock properties from seismic data. However, the question of whether FWI can be geared towards the direct determination of rock physics properties remains open. In this thesis, I formulate FWI with rock physics model parameterizations to directly estimate parameters of immediate interest in reservoir characterization. This approach allows examination of any rock physics property that has a well-defined relationship with elastic parameters. It also shares the same numerical structure as the conventional elastic FWI, allowing various existing inversion strategies to be used. The reliability of the approach is systematically examined using different synthetic examples and is quantified by comparing it to conventional two-step inversions.

Building on this approach, I formulate a time-lapse FWI framework for quantitative seismic monitoring of CO_2 storage. The method is tested on synthetic data generated for the Johansen formation model. The results demonstrate this approach's robustness for retrieving static properties, such as porosity and mineral volumes, and dynamic reservoir properties, such as CO_2 saturation. Moreover, with a joint rock physics model combining Gassmann's equation with empirical pressure relations, I illustrate the potential of this approach for the simultaneous prediction of CO_2 saturation and pore pressure.

Finally, I apply a sequential inversion scheme combining elastic FWI and Bayesian rock physics inversion to a vertical seismic profile (VSP) dataset acquired with accelerometers and a collocated distributed acoustic sensing (DAS) fiber at the Carbon Management Canada's Newell County Facility. The inverted porosity and lithology models are reasonably accurate

at the well location and are geologically meaningful in spatial distribution. This baseline (before injection) study can be used to support later monitoring of CO_2 storage.

Preface

This thesis is written in a manuscript-style format, based on two published peer-reviewed journal papers and one submitted paper, alternatively, based on five published SEG expanded abstracts. These papers have been included in this thesis with permission from the co-authors.

A version of Chapter 4 has been published as: Hu, Q., Keating, S.D., Innanen, K. A., and Chen, H., 2021. Direct updating of rock-physics properties using elastic full-waveform inversion, Geophysics, 86(3), MR117–MR132.

A version of Chapter 5 has been published as: Hu, Q., Grana, D., and Innanen, K. A., 2023. Feasibility of seismic time-lapse monitoring of CO2 with rock physics parametrized full waveform inversion, Geophysical Journal International, 233(1), 402–419.

A version of Chapter 6 has been submitted as: Hu, Q., Eaid, M.V., Keating, S.D., Innanen, K.A., and Cai, X.H., 2023, Estimation of rock physics properties via FWI of VSP data recorded by accelerometer and fiber-optic sensors, Geophysical Journal International.

Acknowledgements

First, I would like to thank my supervisor, Dr. Kris Innanen, for giving me the opportunity to work on this project. Without his guidance, patience, and support over the last five years, this thesis would not have been possible.

I would like to thank the faculty and staff of CREWES. I want to say thank you to Daniel Trad for his suggestions and encouraging words throughout the years, to Kevin Hall for his technical support and sarcastic sense of humor, and to Kevin Bertram for organizing posters and slide shows for conventions.

I would like to thank Dario Grana from the University of Wyoming, for giving me many insightful suggestions in rock physics and seismic inversion. His papers and books have greatly inspired my research.

I would like to thank Marie Macquet and Don Lawton for sharing their data collected at the CMC Newell County Facility.

Thanks to all my fellow CREWES students. Scott Keating in particular has my gratitude for providing me with FWI codes which were key for starting my project. Thanks to Matt Eaid for sharing his FWI work at field data. I must also extend my deepest thanks to my friends at CREWES, many of whom started this adventure with me in September 2018: Fu Xin, Luping Qu, Tianze Zhang, Ziguang Su, and Shang Huang, thanks for your support.

Finally, and most importantly, my heartfelt thanks go to my wife and the rest of my family. They have supported me unconditionally in all of my endeavors over the years. Words cannot express how grateful I am to have them in my life.

Contents

Abstract **ii**

Preface **iv**

Acknowledgements **v**

List of Symbols, Abbreviations, and Nomenclature **xxii**

1 Introduction **1**

1.1 Full waveform inversion 1

1.2 Rock physics 4

1.3 Seismic reservoir characterization 6

1.4 Seismic monitoring of carbon dioxide 9

1.5 Thesis overview 11

2 Implementations of elastic full waveform inversion **14**

2.1 Theory 15

2.1.1 Forward modeling 15

2.1.2 Objective function and its derivatives 15

2.1.3 Optimization methods 18

2.1.4 Model parameterization 20

2.1.5 Regularization 24

2.2 Numerical Examples 25
2.2.1 Importance of Hessian and wide-aperture data 25
2.2.2 Regularized full waveform inversion 28
2.3 Conclusions 34

3 Rock physics modeling and inversion **35**
3.1 Rock physics models 36
3.1.1 Elastic bounds 36
3.1.2 Fluid mixing laws 37
3.1.3 Granular media models 40
3.1.4 Inclusion models 42
3.1.5 Gassmann's equation 45
3.2 Global optimization for rock physics inversion 47
3.2.1 Simulated Annealing 48
3.2.2 Genetic Algorithm 49
3.2.3 Neighborhood Algorithm 50
3.2.4 Numerical Examples 51
3.2.5 Conclusions 59
3.3 Bayesian rock physics inversion 60
3.3.1 Gaussian linear inversion 61
3.3.2 Gaussian mixture approach 62
3.3.3 Kernel density estimation 63
3.3.4 Examples 64
3.3.5 Conclusions 70

4 Direct FWI prediction of rock physics properties **72**
4.1 Summary 72
4.2 Introduction 73

4.3 Theory . . . 77
4.3.1 Isotropic-elastic full-waveform inversion . . . 77
4.3.2 Rock physics parameterizations . . . 78
4.4 Numerical Analysis . . . 83
4.4.1 Direct versus indirect EFWI of Han model parameters . . . 84
4.4.2 Structure and parameter values from EFWI: Han model . . . 94
4.4.3 Structure and parameter values from EFWI: VRH and KT . . . 96
4.5 Discussion . . . 102
4.6 Conclusions . . . 104

5 Seismic time-lapse monitoring of CO_2 with rock physics parameterized FWI 106

5.1 Summary . . . 106
5.2 Introduction . . . 107
5.3 Theory . . . 110
5.3.1 Rock physics parameterized FWI . . . 110
5.3.2 Time-lapse FWI strategy . . . 112
5.4 Numerical Examples . . . 113
5.4.1 Model description . . . 113
5.4.2 Direct FWI results . . . 119
5.4.3 Two-step inversion results . . . 124
5.4.4 Direct FWI with noisy data and imperfect rock physics model . . . 127
5.5 Discussion . . . 130
5.6 Conclusion . . . 132

6 Quantitative FWI characterization of reservoir properties at the CMC Newell County Facility 133

6.1 Summary . . . 133

6.2 Introduction . . . 134
6.3 Theory . . . 137
6.3.1 FWI as a constrained optimization problem . . . 137
6.3.2 Effective source approach . . . 139
6.3.3 FWI incorporating DAS data . . . 140
6.3.4 Bayesian rock physics inversion . . . 142
6.4 Applications . . . 144
6.4.1 VSP experiment at CMC Newell County Facility . . . 144
6.4.2 Seismic data processing . . . 146
6.4.3 Rock physics analysis of well-log data . . . 147
6.4.4 Elastic FWI results . . . 149
6.4.5 Rock physics inversion results . . . 154
6.5 Discussion . . . 156
6.6 Conclusion . . . 158

7 Conclusions **159**
7.1 Summary . . . 159
7.2 Future work . . . 162

A The VRH model partial derivatives **184**

B The KT model partial derivatives **186**

C Rock physics parameterized FWI with regularization **189**

D Towards simultaneous prediction of CO_2 saturation and pore pressure **191**
D.1 Considerations for the rock physics model . . . 193
D.2 Time-lapse FWI strategy . . . 195
D.3 Numerical example . . . 197
D.4 Conclusions . . . 201

List of Figures

1.1 Seismic inversion for rock-physics properties: (a) workflow; (b) current research status 8

2.1 Radiation patterns of different physical parameters in the $\lambda - \mu - \rho$ parameterization 22

2.2 Radiation patterns of different physical parameters in the $V_{\mathrm{P}} - V_{\mathrm{s}} - \rho$ parameterization 23

2.3 (a,b) True P-wave velocity and density models. (c,d) Initial models. (e,f) Inverted models by steepest-decent FWI of surface-recorded seismic data. (g,h) Inverted models by L-BFGS FWI of surface-recorded seismic data. (i,j) Inverted models by L-BFGS FWI of surface- and subsurface-recorded data. . 27

2.4 Convergence histories of (a) P-wave velocity and (b) density for the inversion tests in Figure 2.3. 28

2.5 (a–c) True models and (d–f) initial models of V_{P}, V_{S}, and ρ, respectively. . . 29

2.6 Inverted V_{P}, V_{S}, and ρ models: (a-c) without regularization and (d–f) with regularization. 29

2.7 V_{P}-ρ crossplots of the (a) initial model, (b) inverted model without regularization, and (c) inverted model with regularization. The gray line denotes the V_{P}-ρ relationship used as a model constraint. 30

2.8 Marmousi case. True models of (a) P-wave velocity, (b) S-wave velocity, and (c) density 31

2.9 Facies classification. (a) Model points are classified into three groups, and each group is described by a quadratic function: $\rho = aV_{\mathrm{P}}^2 + bV_{\mathrm{P}} + c$. (b) The corresponding spatial distribution of facies. 31

2.10 Comparison between (a,b) unconstrained and (c,d) constrained inversion results. (e) Model profiles of density at x=0.58km. 32

2.11 Comparison between (a) unconstrained and (b) constrained inversion results. 33

3.1 Voigt, Reuss, and Voigt–Reuss–Hill averages for the (a) bulk modulus and (b) shear modulus of a mixture of quartz and clay. In this example, the quartz properties are $K_q = 37$ GPa and $\mu_q = 44$ GPa, and the clay properties are $K_c = 21$ GPa and $\mu_c = 7$ GPa. 38

3.2 (a) Voigt, Reuss, and Brie's mixing laws for a mixture of water and gas. (b) Impact of Brie's empirical constant. In this example, the water bulk modulus is 2.25 GPa and the gas bulk modulus is 0.1 GPa. 39

3.3 Illustration of the soft-sand and stiff-sand models (modified lower and upper Hashin–Shtrikman bounds) for the estimation of dry-rock modulus. The grains are pure quartz, the effective pressure is 20 MPa, the critical porosity is 0.4, and the coordination number is 9. 41

3.4 Comparison of the KT, SCA, and DEM predictions of the dry-rock (a) bulk modulus and (b) shear modulus. The grains are pure quartz. Two pore shapes, with aspect ratios $\alpha = 1$ and $\alpha = 0.1$, are examined. 44

3.5 Bulk modulus of water-saturated rock and gas-saturated rock computed by Gassmann's equation, based on the dry-rock modulus predicted by the soft-sand model in Figure 3.3. 46

3.6 Simulation results using simulated annealing. Variations of (a) data misfit and (b) inverted models as a function of temperature. 52

3.7 Simulation results using a genetic algorithm. Evolution of (a) data misfit and (b) the best-fit model. 52

3.8 Simulation results using a neighborhood algorithm. The dots represent the models produced by NA and are color-coded by data misfit. The red cross marks the true model. 53
3.9 Sensitivity study. Variations of (a) velocity and density and (b) data misfit as a function of porosity and water saturation. 54
3.10 Convergence properties for three runs of (a) simulated annealing, (b) genetic algorithm, and (c) neighborhood algorithm. 55
3.11 Test with noise-free data. The back lines denote the true models and the blue lines denote the inverted models. The true elastic models are used as input data for the rock physics inversion. 56
3.12 Test with noisy data. Mild Gaussian noises are added to the elastic models, as denoted by the black dashed lines. The blue lines represent the inverted models. 57
3.13 Test with noisy data. Only porosity and clay content are inverted, with water saturation fixed with erroneous values. 57
3.14 True, initial, and inverted models of P-wave velocity, S-wave velocity, and density. 58
3.15 True and inverted rock property models. 59
3.16 Well-log data of the Countess 10-22 well at the CMC Newell County Facility. From left to right: P-wave velocity, S-wave velocity, density, porosity, and the volume fractions of quartz and clay. The blue, red, and yellow curves denote the real data, the data predicted by the nonlinear rock physics model, and the data predicted by the linearized rock physics model. The rightmost column shows the result of facies classification based on the measured data, assuming two facies. 65

3.17 Prior distribution of rock physics variables: Gaussian case. The curves represent the 2D joint distribution of porosity and clay content with associated 1D marginal distribution, obtained by fitting the well-log data (black dots). . . . 66
3.18 Prior distribution of rock physics variables: Gaussian mixture case. The parameters of the Gaussian mixture model are obtained via facies classification of well data 67
3.19 Prior distribution of rock physics variables: non-parametric case. The Epanechnikov kernel is used. 67
3.20 Filtered velocity and density logs used as input data for the rock physics inversion. 68
3.21 Results of the Bayesian linearized rock physics inversion. The background color represents the posterior distribution, the solid red curves represent the maximum a posteriori predictions, and the solid black curves represent the actual well logs. 69
3.22 Results of the Bayesian Gaussian mixture approach. 70
3.23 Results of the Bayesian non-parametric approach. 70

4.1 (a-c) True V_{P}, V_{S}, and ρ models; (d-f) corresponding true ϕ, C, and S_{w} models within the Han model with $a_1 = 5.5$, $a_2 = 6.9$, $a_3 = 2.2$, $b_1 = 3.4$, $b_2 = 4.7$, and $b_3 = 1.8$. Note that S_{w} has no impact on V_{P} in this case. 85
4.2 Results of the indirect/sequential rock physics EFWI approach. (a-c) Inverted V_{P}, V_{S}, and ρ models respectively within the DV parameterization; (d-f) corresponding indirectly estimated ϕ, C, and S_{w} models. 85
4.3 Results of the direct rock physics EFWI approach. (a-c) Inverted ϕ, C, and S_{w} models respectively, within the PCS parameterization; (d-f) corresponding indirectly-estimated V_{P}, V_{S}, and ρ models. 86

4.4 (a-f) Model profiles for V_{P}, V_{S}, ρ, ϕ, C, and S_{w} at diagonal position x=z. The black, blue, and red lines denote the true model, the inverted model within the DV parameterization, and the inverted model within the PCS parameterization, respectively. 87

4.5 Convergence histories. (a-c) Model error reductions of V_{P}, V_{S}, and ρ and (d-f) ϕ, C, and S_{w} in the DV parameterization. (g-i) Model error reductions of ϕ, C, and S_{w} in the PCS parameterization. 88

4.6 Inversion test to eliminate over-fitting. (a-c) Inverted V_{P}, V_{S}, and ρ models respectively; (d-f) ϕ, C, and S_{w} models derived indirectly via the DV parameterization. (g-i) Inverted ϕ, C, and S_{w} derived directly within the PCS parameterization. 90

4.7 (a-c) Model error reductions of V_{P}, V_{S}, and ρ and (d-f) ϕ, C, and S_{w} in the DV parameterization. (g-i) Model error reductions of ϕ, C, and S_{w} in the PCS parameterization. 91

4.8 Layered model tests. (a-c) True models; (d-f) standard EFWI-recovered V_{P}, V_{S}, and ρ models in the DV parameterization. 92

4.9 Direct versus indirect inversion tests on layered model. (a-c) True models; (d-f) the initial ϕ, C, and S_{w} models respectively. (g-i) Indirectly inverted models via the DV parameterization. (j-l) Directly inverted models within the PCS parameterization. 93

4.10 (a-f) Model profiles for V_{P}, V_{S}, ρ, ϕ, C, and S_{w} at $x = 0.25$ km. The solid, dotted, and dash-dotted lines denote the true model, the inverted model within the DV parameterization, and the inverted model within the PCS parameterization. 94

4.11 (a-c) True models of V_{P}, V_{S}, and ρ. (d-f) True models, (g-i) initial models, and (j-l) the corresponding inversion results of ϕ, C, and S_{w}. 95

4.12 Vertical profiles extracted from the true, initial, and inverted (a) ϕ, (b) C, and (c) S_{w} models at lateral position 0.4 km. 95

4.13 Nonlinear rock physics model parameters, circular anomaly case. Inverted ϕ, C, and S_{w} models are plotted for (a-c) the VRH model and (d-f) the KT model. (g-i) Profiles extracted from the true and inverted models at diagonal position x=z. 97

4.14 Nonlinear rock physics model parameters, layered geology case. Inverted ϕ, C, and S_{w} models are plotted for (a-c) the VRH model and (d-f) the KT model. (g-i) Vertical profiles extracted from the true, initial, and inverted models at lateral position 0.25 km. 98

4.15 Nonlinear rock physics model parameters, modified Marmousi case. Inverted models of ϕ, C, and S_{w} with (a-c) VRH and (d-f) KT. (g-i) Vertical profiles extracted from the true, initial, and inverted models at lateral position 0.4 km. 99

4.16 Indirect/sequential inversion test with KT. (a-c) True V_{P}, V_{S}, and ρ models; (d-f) Inverted V_{P}, V_{S}, and ρ models via the DV parameterized EFWI. (g-i) MAP solution of ϕ, C, and S_{w} derived from (d-f) via a Bayesian rock physics inversion. The black dotted lines denote two QC logs at x=0.4 km and x=0.7 km. 100

4.17 Vertical profiles of ϕ, C, and S_{w} at (a-c) x=0.7 km and (d-f) x=0.4 km. The black, blue, and red lines denote the true model, the inverted model within the DV parameterization, and the inverted model within the PCS parameterization, respectively. 101

4.18 Scattering radiation patterns for point ϕ, C, and S_{w} perturbations in the PCS parameterization, formulated for the three rock physics models. 103

5.1 Johansen data set. (a-c) Full-field model and (d-e) corresponding model that uses a simplified geometry. The letter J indicates the location of the Johansen formation; the dashed line indicates the location of the injection well. 114

5.2 Theoretical curves of the stiff-sand model: P-wave velocity, S-wave velocity, and density versus (a-c) porosity and (d-f) CO_2 saturation. 115
5.3 True (a-c) baseline, (d-f) monitor, and (g-i) time-lapse models of P- and S-wave velocities plus density. 116
5.4 (a, d) Baseline, (b, e) monitor, and (c, f) differential seismograms computed for the true model. (a-c) Horizontal displacement. (d-f) Vertical displacement. The shot is located at position 1 km. Ricker wavelet source with a central frequency of 15 Hz is used. 117
5.5 (a) $V_P - \phi$ and (b) $V_P - C$ relationships for constructing initial ϕ and C models. The data are from the true model (Figures 5.1d, 5.1e, and 5.3a) at lateral position 0.5 km. 118
5.6 Initial models: (a) P-wave velocity, (b) porosity, and (c) clay content. 118
5.7 Inverted models: (a) Porosity and (b) clay content. (c,d) Vertical profiles extracted from the true, initial, and inverted models at lateral positions x=0.5 km and x=1.5 km. 120
5.8 Convergence properties. (a-c) Frequencies, objective functions, and model errors (after updating) within a frequency band, respectively. 120
5.9 Baseline data residuals corresponding to the (a and b) initial model and (c and d) inverted model. (e and f) Vertical profiles of the data residuals at lateral position 0.3 km. 121
5.10 (a-c) True, initial, and inverted CO_2 saturation models, respectively. (d) Errors in the inverted model. 122
5.11 Monitor data residuals corresponding to the (a and b) initial model and (c and d) inverted model. (e and f) Vertical profiles of the data residuals at lateral position 0.3 km. 123
5.12 Reconstructed velocity and density models via the rock physics parameterized FWI: (a-c) Baseline, (d-f) monitor, and (g-i) time-lapse change. 123

5.13 Vertical profiles extracted from the true and inverted models (Figures 5.3 and 5.12) at lateral position 0.5 km. 124
5.14 Reconstructed velocity and density models via velocity-density parameterized FWI: (a-c) Baseline, (d-f) monitor, and (g-i) time-lapse change. 125
5.15 Vertical profiles extracted from the true and inverted models (Figures 5.3 and 5.14) at lateral position 0.5 km. 125
5.16 Inverted porosity, clay content, and CO_2 saturation models within the (a-c) Bayesian and (d-f) NA approaches. 126
5.17 Synthetic noisy data with signal-to-noise ratio equal to 10. 128
5.18 Direct inversion results with noisy data: (a) Porosity, (b) clay content, and (c) CO_2 saturation. 129
5.19 (a) P-wave velocity versus CO_2 saturation for different mixing behaviors of fluid phases. (b) Recovered CO_2 saturation models with erroneous assumptions on fluid. 130

6.1 Schematic depiction of the effective source approach for VSP FWI. 140
6.2 (a) Shot geometry of the multi-azimuth walk-away VSP experiment at the Newell County Facility. The gray circles represent the locations of vibe points, the green square marks the location of the injection well, and the two red squares mark the locations of the geophysics and geochemistry wells, offset from the injection well by 20 m to south-west and 30 m to north-east, respectively. (b) Section view of the VSP acquisition with respect to source line 1. The horizontal dashed lines delineate the top and bottom of the Basal Belly River Sandstone target reservoir. 145

6.3 Processed accelerometer and DAS data for 5 shots on source line 1. Top row: vertical component of acceleration. Middle row: horizontal component of acceleration. Bottom row: DAS-recorded strain. Each column represents the data of a single shot. Shots 1 to 5 correspond to offsets 370 m, 170 m, -20 m, -200 m, and -430 m, respectively. 146
6.4 Well logs (upscaled) of the injection well: (a) P-wave velocity, (b) S-wave velocity, (c) density, (d) total porosity, and (e) the volume fractions of quartz, clay, and coal. Well-log data are in blue and rock physics model predictions in orange. 148
6.5 Bivariate Gaussian mixture probability density function (PDF) estimated from well-log data, in the domain of (a) P-wave velocity and quartz volume, and (b) porosity and clay volume. 149
6.6 (a)-(c) Initial models of P-wave velocity, S-wave velocity, and density. (d-f) Inverted models from accelerometer data. (g-i) Inverted models from DAS data. (j-l) Inverted models from the combined accelerometer and DAS data. 150
6.7 Comparison of the well logs and the vertical profiles extracted from the initial and inverted models (Figure 6.6) at offset 20 m. 151
6.8 Real part of frequency domain data for shot at 70 m offset. Top row: vertical component of acceleration. Middle row: horizontal component of acceleration. Bottom row: DAS-recorded strain. Columns from left to right: Field data, modeled data simulated from the initial model, modeled data simulated from the inverted model, and comparison of the 21 Hz field data (solid black line), initial modeled data (dotted gray line), and inverted data (solid gray line). . 152

6.9 Time domain data for shot at 70 m offset. Top row: vertical component of acceleration. Middle row: horizontal component of acceleration. Bottom row: DAS-recorded strain. Columns from left to right: Field data, modeled data simulated from the inverted model, and a mixture of field and modeled data. In the panels of field data I marked the different types of waves. DP: downgoing P-waves. DS: downgoing S-waves. UP: upgoing P-waves. CDS: converted downgoing S-waves. CUS: converted upgoing S-waves. 153

6.10 Posterior distributions of (a) porosity, (b) quartz volume, and (c) clay volume, truncated within the 0.95 confidence interval. The black lines represent the actual well logs and the red lines represent the maximum a posteriori. 155

6.11 Inverted models of (a) porosity, (b) quartz volume, (c) clay volume, and (d) coal volume (superimposed the actual log curve). 156

C.1 (a,e) True models and (b,f) initial models of porosity and clay content. (c,g) Inverted models without constraint. (d,h) Inverted models with constraint. . 190

C.2 ϕ-C crossplots of the (a) initial model, (b) inverted model without constraint, and (c) inverted model with constraint. The gray line denotes the ϕ-C relationship used as model constraint. 190

D.1 Example of different pressures with depth. 192

D.2 Calibration of rock physics model using Han's dataset (subset of 3 samples). Hertz-Mindlin model is combined with Gassmann's equations to predict saturated-rock velocity as a function of effective pressure including porosity and mineralogy effects. The model is calibrated at pressure 10 MPa, then automatically predicts the data at 5,20,30,40 MPa. 196

D.3 Macbeth's relation combined with Gassmann's equations to predict saturated-rock velocity as a function of effective pressure including porosity and mineralogy effects. Hertz-Mindlin predictions at pressure 10 MPa are used as input in Macbeth's model. 196
D.4 True baseline, monitor, and time-lapse models of CO_2 saturation and pore pressure. The black line indicates the location of the injection well. 197
D.5 Theoretical curves of the proposed rock physics model: P-wave velocity, S-wave velocity, and density versus (a) CO_2 saturation and (b) pore pressure. . 198
D.6 Baseline, monitor, and time-lapse models of P- and S-wave velocity plus density. 199
D.7 Baseline, monitor, and differential seismograms (horizontal and vertical displacements) computed for the true model. 199
D.8 Recovered monitor model of CO_2 saturation and pore pressure. 200
D.9 Convergence properties. (a-c) Frequencies, objective functions, and model errors (after updating) within a frequency band, respectively. 201

List of Tables

4.1 Elastic properties of minerals and fluids. 84

5.1 Rock physics parameters used in this study 111

5.2 Root mean squared error of the inverted models within different approaches. 127

List of Symbols, Abbreviations, and Nomenclature

Symbol or abbreviation	Definition
AVO	Amplitude versus offset
$\mathbf{A}$	Impedance matrix
BBRS	Basal Belly River sandstone
BFGS	Broyden-Fletcher-Goldfarb-Shanno algorithm
CG	Conjugate gradient
CCUS	Carbon capture, utilization, and storage
CaMI	Containment and monitoring institute
CO_2	Carbon dioxide
C_d	Data covariance matrix
CMC	Carbon Management Canada
DAS	Distributed acoustic sensing
DEM	Differential effective medium
DV	Density and velocity
$\mathbf{d}_{obs}$, $\mathbf{d}_{syn}$, $\delta\mathbf{d}$	Observed, synthetic, and differential data
$D_{\mathrm{x}}, D_{\mathrm{z}}$	Horizontal and vertical displacements
E	Objective function
E_d, E_m	Data misfit and model penalty

e	Brie's exponent
$\mathbf{e}$	Strain tensor
e_{tt}	Tangential strain
e_{zz}	Vertical normal strain
$\nabla_{\mathbf{m}} E$	Gradient
EFWI	Elastic full waveform inversion
FWI	Full waveform inversion
f_v	Virtual source
f_{RPM}	Rock physics model
GA	Genetic algorithm
h	Kernel bandwidth
$\mathbf{H}$	Hessian
$\mathbf{I}$	Identity matrix
$\mathbf{J}$	Jacobian matrix
K	Bulk modulus
K_m, K_f	Mineral and fluid bulk moduli
$K_{\mathrm{dry}}, K_{\mathrm{sat}}$	Dry rock and saturated rock bulk moduli
K_c, K_q	Clay and quartz bulk moduli
K_w, K_o, K_g	Bulk modulus of water, oil, and gas
$K_{\mathrm{HM}}, \mu_{\mathrm{HM}}$	Hertz-Mindlin predictions of elastic moduli
K^*, μ^*	Effective bulk and shear moduli
KT	Kuster and Toksoz model
L-BFGS	Limited-memory BFGS algorithm
L	Lagrangian
$M_{\mathrm{V}}, M_{\mathrm{R}}, M_{\mathrm{VRH}}$	Voigt bound, Reuss bound, and Hill's average
$\mathbf{m}$	Model vector
$\delta\mathbf{m}$	Search direction

NA	Neighborhood algorithm
$\mathcal{N}$	Gaussian distribution
N_a, N_d	Numbers of accelerometer and DAS sensors
N_f	Number of facies classes
$ns, n\omega$	Numbers of sources and frequencies
PCS	Porosity-Clay content-Water saturation
PDF	Probability density function
$P(\mathbf{m}), P(\mathbf{m}, \mathbf{d}), P(\mathbf{m}\|\mathbf{d})$	Prior, joint, and posterior distributions
P_c, P_p, P_e	Overburden, pore, and effective pressures
QC	Quality control
$\mathbf{R}$	Receiver sampling matrix
$\Re$	Real part
SD	Steepest descent
SA	Simulated annealing
SNR	Signal-to-noise ratio
SCA	Self-consistent approximation
S_w, S_o, S_g	Water, oil, and gas saturations
S_c	CO_2 saturation
TGN	Truncated Gauss-Newton
T, †	Transpose and conjugate transpose
$\mathbf{u}$, $\mathbf{f}$	Displacement vector and source vector
μ_m, μ_f	Shear moduli of mineral and fluid
$\mu_{\text{dry}}, \mu_{\text{sat}}$	Shear moduli of dry rock and saturated rock
μ_c, μ_q	Shear moduli of clay and quartz
V_{qu}, V_{cl}, V_{co}	Volume fractions of quartz, clay, coal
V_{P}, V_{S}	P-wave velocity and S-wave velocity
VSP	Vertical seismic profile

VRH	Voigt-Reuss-Hill average
$\mathbf{W}_{\lambda,\mu,\rho}, \mathbf{W}_{V_\mathrm{P},V_\mathrm{s},\rho}$	Radiation patterns
$\mathbf{x}_s$	Source position
$\{\hat{\mathbf{x}}, \hat{\mathbf{y}}, \hat{\mathbf{z}}\}$	Cartesian coordinate
$\{\hat{\mathbf{t}}, \hat{\mathbf{n}}, \hat{\mathbf{b}}\}$	Tangent-normal-binormal fiber coordinate
ω	Angular frequency
ρ	Density
ρ_m, ρ_f	Mineral density and fluid density
λ, μ	Lamé parameters
u, v	Horizontal and vertical displacements
α	Step length
υ	Adjoint variable
θ	Opening angle
γ	Regularization trade-off parameter
ϕ	Porosity
κ	Kernel function
$\|\|...\|\|^2$	Squared norm
$<,>$	Dot product
$\sum$	Summation
$\prod$	Multiplication
3C	Three-component
2D, 3D	Two dimensional and three dimensional

Chapter 1

Introduction

1.1 Full waveform inversion

The retrieval of physical properties of the earth using seismic data is critical for subsurface explorations. As such it has been subject to intensive research for the last decades (Russell, 1988; Sheriff and Geldart, 1995; Yilmaz, 2001; Aki and Richards, 2002; Sen, 2006; Menke, 2018). In parallel, because of the increase in computational power, complex forward modeling has become more affordable. One of the methods that potentially allows to extract more information from seismic data is Full Waveform Inversion (FWI) (Pratt et al., 1998; Tarantola, 2005; Virieux and Operto, 2009; Warner et al., 2013). In FWI an attempt is made to construct elastic models of the subsurface matching the full amplitude and phase information of the measured waveform data. Theoretically, it can provide models of physical parameters with a higher spatial resolution than other methods such as travel-time tomography (Schuster, 2017).

FWI is commonly formulated as an iterative process that seeks to improve the model by minimizing the discrepancy between measured data and the synthetic data obtained using a reference model (which can be poor in high wavenumber content), through minimizing an objective function. The synthetic data are modeled using wave equations, to exploit the

full information content in the seismogram. However, given the computational cost of one simulation of the data, stochastic methods such as Monte-Carlo are not feasible for practical FWI. Therefore FWI is generally formulated as a local optimization problem, in which the model is only allowed to update in a direction that decreases the objective function (Virieux and Operto, 2009). In this sense, the centerpiece of FWI is the adjoint-state method (Lions, 1971), which allows us to obtain the gradient of the objective function for the current model by cross-correlating the incident and back-propagated wavefields (Lailly, 1983; Tarantola, 1984). A detailed review of the adjoint-state method with illustrations from several seismic problems is given in Plessix (2006).

Several simplifications in the physical description of the subsurface are generally considered for the modeling of wave propagation. The most basic of these considers the subsurface to be an acoustic medium that can be parameterized by the P-wave velocity only (Ravaut et al., 2004; Mulder and Plessix, 2008; Barnes and Charara, 2009; Shin and Ho Cha, 2009). One advantage of acoustic FWI is dealing with less computationally expensive forward modeling than in the elastic case. Also, mono-parameter acoustic FWI is better conditioned than multiparameter FWI because only one physical parameter is involved in the inversion (Virieux and Operto, 2009). However, the full wavefield has more than just P waves, so it is natural to include more realistic physics in the forward modeling to better match the observed data, which have viscosity, elasticity, and anisotropic effects (Operto et al., 2013; Alkhalifah and Plessix, 2014). Acoustic FWI cannot invert for such information effectively. Although high-resolution P-wave velocity models can provide useful inferences for geological interpretation, a more realistic description of the subsurface physical properties, and in particular the elastic properties, is required for lithology and fluid characterizations (Prieux et al., 2013a).

The very first attempt to achieve realistic seismic inversion would be to use the isotropic elastic wave equation (Tarantola, 1986). We are now able to estimate multiple elastic properties, such as P-wave velocity, S-wave velocity, and density, using the elastic FWI (EFWI).

Despite the increasing implementation of EFWI in properly imaging and interpreting the subsurface, several key challenges remain. The first one is known as cycle skipping, which occurs when the synthetic data corresponding to a candidate FWI model matches peaks and troughs of the measured data at a different cycle from the correct match. This type of model represents a local minimum in the optimization. Second, the fact that more degrees of freedom are considered in the parameterization and that the sensitivity of the inversion can change significantly from one parameter class to another increases the ill-posedness of the inverse problem. Moreover, EFWI suffers from the trade-off/crosstalk between different parameter classes, which arises from the complex manner in which multiple subsurface elastic properties co-determine seismic waveforms, and occurs when errors in one property are mapped into the updates of other parameters (Pan et al., 2018a; Keating and Innanen, 2019b). This unwanted "interparameter contamination" increases the uncertainty of inversion outcomes. Various approaches have been proposed to address these fundamental issues of EFWI. For example, the multiscale approach of Bunks et al. (1995), in which the data are inverted from low to high frequencies, is widely used to avoid cycle-skipping. When low frequencies are unavailable, it is suggested to consider objective functions with improved convexity than the conventional L2-norm of data residuals (Bozdağ et al., 2011; Métivier et al., 2018). The uniqueness and stability of the solution can be improved using techniques such as preconditioning and regularization (Guitton et al., 2010; Asnaashari et al., 2013). Radiation pattern analysis has proven effective in predicting crosstalk (Tarantola, 1986; Operto et al., 2013; Pan et al., 2019; Yang et al., 2019). Guided by analysis of the patterns to select inversion parameters with minimal overlap between their radiation patterns, the extent of crosstalk can be reduced (Operto et al., 2013; Pan et al., 2019; Yang et al., 2019). The Hessian operator in Newton-based optimization methods also plays an important role in decoupling the elastic parameters (Métivier et al., 2017; Pan et al., 2017). These studies to improve the accuracy of EFWI could facilitate its use in reservoir characterization.

1.2 Rock physics

Rock physics provides the relationship between intrinsic rock properties such as porosity, mineralogy, and pore fluids to elastic properties that drive the seismic response such as P- and S-wave velocities and density (Mavko et al., 2020). Rock physics analysis therefore enables rock properties that were previously only available from drilling to be estimated from remotely sensed data. During the early years of the exploration of seismology, seismic data were interpreted primarily for structures that might trap hydrocarbons (Yilmaz, 2001). With the advancement of computing power and seismic processing techniques, seismic data are now commonly analyzed for determining rock physics properties (Doyen, 2007; Avseth et al., 2010; Dvorkin et al., 2014; Grana et al., 2021).

To characterize rock properties based on the behavior of seismic waves propagating through them, it is essential to have an understanding of how the composition of rock dictates its overall elastic properties. This process is often referred to as "rock physics modeling" (Dvorkin et al., 1999; Bachrach and Avseth, 2008; Grana, 2014). In theory, we make the simplifying assumption that the inherently heterogeneous rocks have some effective, i.e. averaged homogeneous properties over the scale of the measurements. Seismic studies therefore require effective elastic moduli to be defined. This depends on the elastic properties of the rock constituents and their geometric relationships. Because it is essentially impossible to obtain sufficient information to uniquely define the effective moduli, the theoretical maximum and minimum moduli, known as the Voigt and Reuss bounds are often used (Mavko et al., 2020). More refined effective moduli can be defined by accounting for the arrangement of the components. There are two general methods of doing so, depending on the relative volume fraction of the component being considered. For large relative volumes, a granular approach is usually taken, where the effective moduli are determined by considering how the contact forces on grains change the overall moduli (Dvorkin and Nur, 1996). Such methods are used for high porosity, more unconsolidated to conventional sands. For low relative volumes, the components are considered as isolated deviations from a background medium (Kuster and

Toksöz, 1974; Berryman, 1995), suitable for low porosity, unconventional isotropic rocks.

A complete rock physics modeling process can be broken down into four different parts: 1) minerals, 2) fluids, 3) the dry-rock frame, and 4) how the parts are assembled. Assembling the different parts of the model accounts for the stiffening of the rock frame due to the presence of fluids. The most common approach to include the fluid effect and compute the saturated-rock elastic properties is based on Gassmann's equation (Biot, 1956; Gassmann, 1951). Gassmann's equation assumes a homogeneous mineral modulus and statistical isotropy of the pore space. Most importantly, it is valid only at sufficiently low frequencies such that the induced pore pressures are equilibrated throughout the pore space (Mavko et al., 2020). This limitation to low frequencies makes it especially suitable for seismic data. While many effective medium theories allow direct prediction of saturated-rock moduli, they assume that the pores are isolated concerning fluid flow, thus simulating very high-frequency behavior appropriate to ultrasonic laboratory conditions. When applied to seismic or well-log data, these models are generally used to simulate the dry rock, the results of which are then used as input in Gassmann's equation.

In addition to theoretical models, the study of rock physics has also produced a large number of empirical relations/models. These relations are derived from experiments: physical properties of a suite of rock samples are measured, analyzed, and a mathematical function is fit to the data points. Some commonly used empirical models include the time-average equation of Wyllie et al. (1962), the velocity-density relations of Gardner et al. (1974) and Castagna et al. (1993), the velocity-porosity relations of Raymer et al. (1980), and the velocity-porosity-clay model of Han (1987). These models do not explicitly account for the mechanisms of elastic parameter variations due to various rock constituents and their overall architecture in the manner that theoretical rock physics models do. They often work very well for the data they were derived from but can be difficult to compare from one research project to the next. With empirical relations, one must be careful about ascribing physical meaning to what are essentially generic mathematical formulae (Wang, 2001).

1.3 Seismic reservoir characterization

Seismic reservoir characterization plays an important role in comprehensive reservoir studies from prospect identification to detailed reservoir delineation. Reservoir simulations that are based on accurately developed static reservoir models are of significant value in developing, monitoring, and managing a reservoir (Lie, 2019). Some key reservoir parameters to which geophysical measurements can contribute include (Van Riel, 2000):

- rock type and porosity
- fluid content and properties
- flow conduits and flow barriers
- pressures
- fracture orientation
- associated uncertainties
- changes over time for all of the above

To improve the accuracy of reservoir property prediction and minimize the uncertainties, considerable attention needs to be placed on generating good quality seismic data, selecting the most suitable seismic inversion method, and integrating multiple domain data, such as well data, seismic attributes, and rock physics measurements, for the calibration and interpretation phases.

From a geophysical perspective, reservoir characterization has traditionally used seismic amplitude data. This dates back to when seismic amplitudes were used for "bright spot" detection. Shortly afterward, the first attempts were made to invert amplitude data for acoustic impedance (Dubrule et al., 1998; Pendrel, 2001). There are two main benefits of using the inverted impedance compared to using amplitudes or amplitude attributes. First, inversion partially removes wavelet effects, increases the resolution, and provides impedance values that can be directly correlated with the absolute values of rock properties. This

is not the case for amplitude attributes which are related to relative changes in reservoir properties across elastic interfaces (Doyen, 2007). Second, the inverted impedance can be directly calibrated at well locations with log-derived impedance values (i.e., seismic-well tie). This calibration step is often crucial in the construction of a seismic-constrained rock property model. Nevertheless, the use of acoustic impedance for reservoir characterization has certain limitations because it is difficult to separate the effects of porosity, lithology, and fluid saturation using a single inversion parameter.

The emergence of pre-stack seismic inversion technology, primarily the amplitude-variation-with-offset (AVO) inversion, has greatly expanded the application potential of seismic data in reservoir characterization. This amplitude variation is typically associated with changes in lithology and fluid content in rocks above and below the reflector. The AVO inversion is based on the Zoeppritz equations, a set of equations that describe the partitioning of seismic wave energy at an interface, typically a boundary between two different layers of rock. Various authors have derived slightly different versions of linear approximations of the Zoeppritz equations (Shuey, 1985; Aki and Richards, 2002). These approximations express the P-wave reflection amplitude as a function of the incidence angle and the reflectivities of three elastic parameters, such as P-wave velocity, S-wave velocity, and density. Today, AVO inversion is widely used to obtain the elastic properties of the reservoir, which also leads to a sequential workflow for seismic prediction of reservoir properties: AVO inversion is performed first to estimate elastic properties from seismic data, followed by rock physics analysis/inversion to transform these elastic properties to reservoir properties (Bachrach, 2006; Bosch et al., 2010; Grana, 2016a). Another widely used approach is the joint or simultaneous inversion approach, in which the combination of seismic inversion and rock physics models is not stepwise but unified in a single formulation (Spikes et al., 2007; Buland et al., 2008; Grana et al., 2020). It is debatable whether a sequential or joint approach is better. As illustrated by Doyen (2007), the sequential workflow is less demanding and gives the user more control over parameter calibration for the different steps. On the other hand, the more ambitious

joint approach guarantees better consistency between inverted elastic and rock properties. However, the joint approach is becoming more and more popular in the industry.

(a)

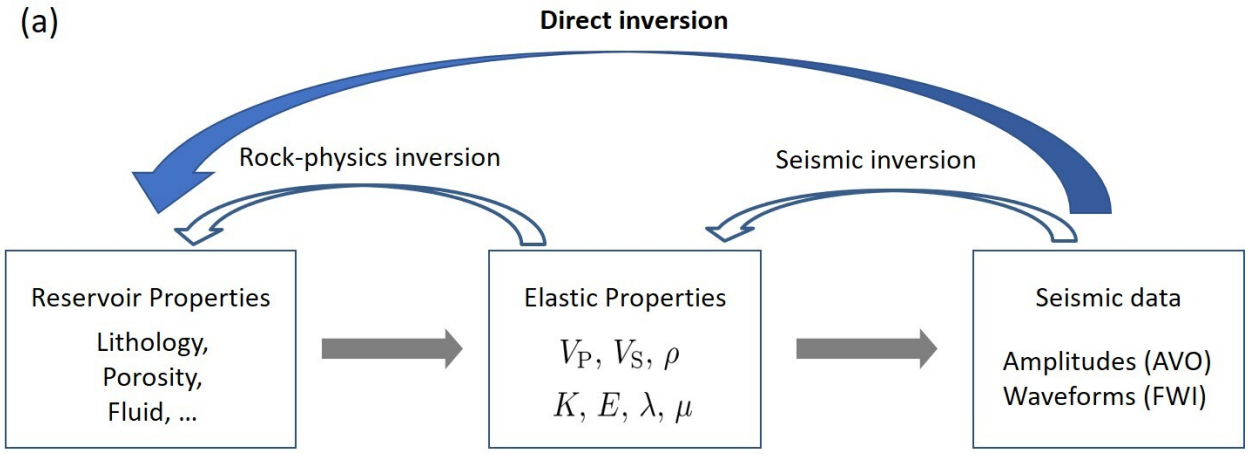

(b)

	Two-step inversion	One-step inversion
AVO-based	✓	✓
FWI-based	✓	?

Figure 1.1: Seismic inversion for rock-physics properties: (a) workflow; (b) current research status

In light of these remarks, a natural research direction arises. Currently, rock physics or reservoir properties are determined using reflection amplitude information rather than full waveform information. Can we formulate FWI algorithms that do something similar? The application of FWI in the construction of high-resolution rock property models is still at an early stage. Although some studies revealed the potential of multiparameter elastic FWI in reservoir characterization (Pan et al., 2018a; Singh et al., 2018; Zhang et al., 2018), they were performed in the elastic domain of velocity and density and did not go into the rock physics domain. In other words, these analyses are qualitative in terms of reservoir parameters. There are few reports on quantitative reservoir parameter prediction based on FWI (Queißer and Singh, 2013a; Dupuy et al., 2021a), and these studies all use the

conventional two-step inversion scheme. As elastic FWI technology is gradually becoming practical, we need to fully explore the way of combining FWI and rock physics, to maximize the role of FWI in reservoir characterization. The previous work in the field of AVO provides us with a reference, prompting us to think about whether the direct update and sensitivity analysis of rock physics parameters can be realized under the framework of FWI. Also, what are the advantages and limitations of this direct inversion compared to the conventional two-step inversion? These are important points that I hope to explore in the thesis. In Figure 1.1, I briefly summarized the seismic inversion-based reservoir characterization framework and research status.

1.4 Seismic monitoring of carbon dioxide

Carbon capture and storage (CCS) in geological formations is becoming a key technology for the permanent reduction of carbon dioxide (CO_2) concentrations in the atmosphere (Davis et al., 2019; Ringrose, 2020). Several large-scale CO_2 storage experiments have already been conducted around the globe, for example at Sleipner in Norway (Arts et al., 2008), Quest in Canada (Duong et al., 2019), and Ketzin in Germany (Ivandic et al., 2015). In 2020, 26 large-scale facilities were operating, the majority of which are CO_2 enhanced oil recovery (EOR) projects, and six are dedicated geological storage projects. The last decade has seen the emergence of most of the projects (19). Worldwide, the facilities capture and store 40 Mt of CO_2 per year (Macquet et al., 2022).

The Containment and Monitoring Institute (CaMI) of Carbon Management Canada (CMC), in collaboration with the University of Calgary, has developed, and now operates, a comprehensive field research station in Newell County, Alberta, Canada (Lawton et al., 2019; Macquet et al., 2022). The injection at this pilot site (at approximately 300 m depth) is designed to simulate an unplanned CO_2 leakage from a deeper and larger scale CO_2 storage project. CREWES has been closely involved in seismic surveys that have already been acquired to characterize the subsurface baseline for the monitoring of CO_2 injection (Isaac

and Lawton, 2016; Eaid et al., 2022; Pan et al., 2023). CaMI and CREWES are now developing new seismic technologies to monitor the CO_2 injection program, with an emphasis on time-lapse analysis. Changes in rock properties through fluid substitution impact seismic velocity and density of the target formation which can be detected as a change in the reflection amplitudes relating to the baseline survey (Lumley, 2001). Numerous papers demonstrate the potential of using time-lapse seismic to monitor the evolution of the CO_2 plume in a large-scale CO_2 reservoir (Johnston, 2013; Furre et al., 2015; Ivandic et al., 2015). The CaMI site has already been instrumented with optical fibre for Distributed Acoustic Sensing (DAS) in wells and a 1.1 km long trench. CREWES has participated in several VSP DAS surveys, yielding promising baseline images of the target reservoir around the CO_2 injection well (Hall et al., 2019). This facility available to CREWES through collaboration with CaMI will enable testing and real data applications of methods described in this thesis.

The overall objective of a CO_2 storage site monitoring program is to verify storage and minimize the risk of leakage. In addressing the technical objectives of monitoring, there are two main goals which are generally defined as 1) Containment: activities to ensure and verify that the injected CO_2 is contained within the storage unit, and 2) Conformance: the process of verifying that storage performance in the subsurface proceeds as expected (Ringrose, 2020). The conformance monitoring should prove that the operator understands the behavior of the CO_2 in the reservoir, i.e. that there is consistency between the model predicted behavior and the CO_2 accumulation estimated from monitoring data. For reliable conformance verification, the monitoring (from well log measurements or seismic data) should, in addition to locating the plume, provide quantitative information, ideally on both CO_2 saturation and pore pressure, to be compared to reservoir modeling predictions (Dupuy et al., 2021a). Given these needs, basic consideration of how to optimally extract rock and fluid properties from seismic data becomes increasingly important. In CO_2 storage applications, rock properties are typically extracted sequentially, with the seismic inversion process geared towards the determination of elastic properties, from which the actual properties of interest

are subsequently determined, often qualitatively. Reports of quantitative, waveform-based saturation and pressure predictions are uncommon.

1.5 Thesis overview

Combining full waveform inversion with rock physics can extend the role of FWI from seismic imaging to quantitative prediction and monitoring of reservoir parameters. I first introduce the forward and inverse problems in FWI and rock physics, then provide novel approaches to FWI integrating rock physics, and finally apply FWI methods to the field data acquired at the CMC Newell County Facility. The focus of each chapter is as follows:

In Chapter 2, I detail the frequency-domain elastic FWI implementation and some wave propagation and optimization strategies used extensively in this thesis. Optimization methods such as gradient and Newton-based methods are explained, key concepts such as virtual sources and radiation patterns in model parameterization studies are illustrated, and a regularized FWI framework incorporating prior model information is described. I then perform a numerical comparison of the ability of different optimization methods and acquisition geometries to reduce parameter crosstalk and illustrate how regularization techniques could help constrain the inversion results.

In Chapter 3, I introduce the forward and inverse problems in rock physics. The forward problem is to construct a rock physics model that converts rock and fluid properties into elastic properties. A complete rock physics modeling process generally includes multiple theoretical models to gradually simulate the effects of minerals, pores, and fluids on the elastic properties of saturated rocks. The inverse problem is the process of estimating rock properties from elastic parameters based on a constructed rock physics model. Solving this problem requires some deterministic or stochastic inversion algorithm. This chapter introduces several commonly used isotropic rock physics models in detail, most of which will be used in conjunction with FWI in later chapters. I then investigated two classes of algorithms for solving rock physics inverse problems: global optimization and Bayesian

methods. Understanding the principles and limitations of these algorithms would facilitate a step-wise seismic reservoir characterization workflow: first, the elastic parameters are obtained by FWI, and then the reservoir parameters are obtained by rock physics inversion. This approach will be applied to the field data in Chapter 6.

In Chapter 4, I propose a new FWI algorithm: direct inversion of rock physics parameters by FWI. My approach to this is to modify the model parameterization of FWI through a rock physics model. I verify the feasibility of this algorithm through different types of rock physics models and different numerical experiments. I perform an analysis of the inversion sensitivity for three key rock physics properties including porosity, clay content, and fluid saturation. In addition, I focus on comparing the new method with the traditional indirect inversion method of rock physics parameters, and analyze the advantages and limitations of the new algorithm. What I want to emphasize is that this algorithm has the same numerical structure and similar computational cost as the conventional FWI method, so it is easy to integrate various strategies proposed to improve the accuracy of FWI and enhance its practicability. For instance, in Appendix C I give an example of FWI regularization in the rock physics domain.

In Chapter 5, I formulate a time-lapse FWI framework based on the rock physics parameterized FWI approach proposed in Chapter 4, to predict the time evolution of CO_2 saturation from seismic data. To set out the results of these tests, I first describe the time-lapse FWI strategy. I then systematically examine the response of the inversion to a synthetic time-lapse dataset. Specifically, I recover porosity and lithology parameters from the baseline seismic data, and then use these results as input in the monitor seismic survey, producing estimates of CO_2 saturation. The reliability of the approach is quantified by comparing it to conventional approaches. I end this chapter by discussing how uncertainties related to data and rock physics model affect CO_2 saturation reconstructions. In Appendix D, I discuss the FWI prediction of pore pressure, another key dynamic reservoir parameter in CO_2 monitoring. This discussion is for the case where the time-lapse seismic response is affected by both

fluid substitution and pressure build-up.

In Chapter 6, I apply a sequential inversion scheme combining elastic FWI (Chapter 2) and Bayesian rock physics inversion (Chapter 3) to a VSP dataset acquired with accelerometers and DAS fiber at the CMC's Newell County Facility. The goal is to build a baseline model of porosity and lithology parameters to support later monitoring of CO_2 storage. The key strategies include an effective source approach to cope with near-surface complications, a modeling strategy to simulate DAS data directly comparable to the field data, and a Gaussian mixture approach to capture the bimodality of rock properties. I perform FWI tests on the accelerometer, DAS, and combined accelerometer-DAS data, and compare and analyze the results. I note that the direct rock physics FWI method in Chapter 4 could also be applied to this set of data, but in the hope of doing more analysis in the elastic domain, and to compare with previous FWI results for the field site, I ended up implementing the sequential inversion approach.

In Chapter 7, I provide a summary of the novel contributions of this thesis. I go on to explain some of the challenges with combing FWI and rock physics, and suggest possible avenues for future research in FWI-based reservoir characterization and monitoring.

Chapter 2

Implementations of elastic full waveform inversion

In this chapter, I introduce the forward and inversion problems in the frequency-domain EFWI. Optimization methods such as gradient and Newton-based methods are explained, key concepts such as virtual sources and radiation patterns in model parameterization studies are illustrated, and a regularized FWI framework incorporating prior model information is described. I then numerically compare the ability of different optimization methods and acquisition geometries for reducing parameter crosstalk, and show how regularization techniques constrain the inversion results.

2.1 Theory

2.1.1 Forward modeling

In this analysis, I consider isotropic elasticity and a 2D medium. In the frequency domain, the 2D elastic wave equations can be written as

$$\begin{aligned}\omega^2\rho u + \frac{\partial}{\partial x}\left[(\lambda+2\mu)\frac{\partial u}{\partial x} + \lambda\frac{\partial v}{\partial z}\right] + \frac{\partial}{\partial z}\left[\mu\left(\frac{\partial u}{\partial z} + \frac{\partial v}{\partial x}\right)\right] + f = 0,\\ \omega^2\rho v + \frac{\partial}{\partial z}\left[(\lambda+2\mu)\frac{\partial v}{\partial z} + \lambda\frac{\partial u}{\partial x}\right] + \frac{\partial}{\partial x}\left[\mu\left(\frac{\partial u}{\partial z} + \frac{\partial v}{\partial x}\right)\right] + g = 0,\end{aligned} \tag{2.1}$$

where ω is the angular frequency, $\rho = \rho(x, z)$ is the density, $\lambda = \lambda(x, z)$ and $\mu = \mu(x, z)$ are the Lamé parameters, $u = u(x, z, w)$ and $v = v(x, z, w)$ are Fourier components of the horizontal and vertical displacements, $f = f(x, z, w)$ and $g = g(x, z, w)$ are Fourier components of the horizontal and vertical body forces (Pratt, 1990). Equation 2.1 can be discretized and solved using finite difference approaches, which take the form

$$\mathbf{A}(\mathbf{m}, \omega)\mathbf{u}(\mathbf{m}, \mathbf{x}_s, \omega) = \mathbf{f}(\mathbf{x}_s, \omega), \tag{2.2}$$

where $\mathbf{m} = (\rho, \lambda, \mu)$ is the model vector, $\mathbf{u} = (u, v)$ is the displacement vector, $\mathbf{f} = (f, g)$ is the source vector, $\mathbf{x}_s$ is the source location, and $\mathbf{A}$ is the impedance matrix, which is a sparse matrix with the number of non-zero diagonals related to the finite-difference scheme (Marfurt, 1984). The wavefield $\mathbf{u}$ can be obtained by the inverse of the impedance matrix, which is usually replaced by direct matrix factorization methods, such as lower and upper (LU) triangular decomposition (Virieux and Operto, 2009).

2.1.2 Objective function and its derivatives

As a nonlinear optimization problem, FWI seeks to estimate subsurface parameters through an iterative process by minimizing the difference between the synthetic data $\mathbf{d}_{syn}$ and observed data $\mathbf{d}_{obs}$ (Tarantola, 1986). The objective function is formulated in a least-squares

form:

$$E(\mathbf{m}) = \frac{1}{2} \sum_{ns} \sum_{n\omega} \|\mathbf{d}_{obs}(\mathbf{x}_s, \omega) - \mathbf{d}_{syn}(\mathbf{m}, \mathbf{x}_s, \omega)\|_2^2, \tag{2.3}$$

where $\mathbf{d}_{syn}(\mathbf{m}, \mathbf{x}_s, \omega) = \mathbf{R}\mathbf{u}(\mathbf{m}, \mathbf{x}_s, \omega)$ is the synthetic data generated using the current model $\mathbf{m}$, and $\mathbf{R}$ is the sampling operator that extracts the wavefields at receivers' locations. ns and $n\omega$ are the number of sources and the number of frequencies, respectively.

The Newton optimization approach is based on the second-order Taylor expansion of the objective function:

$$E(\mathbf{m} + \delta\mathbf{m}) \approx E(\mathbf{m}) + \delta\mathbf{m}^T \nabla_{\mathbf{m}} E + \frac{1}{2} \delta\mathbf{m}^T \mathbf{H} \delta\mathbf{m}, \tag{2.4}$$

where the superscript T denotes the transpose, $\delta\mathbf{m}$ is the search direction, $\nabla_{\mathbf{m}} E$ is the gradient, and $\mathbf{H}$ is the Hessian. To minimize equation 2.4, the search direction $\delta\mathbf{m}$ is the solution of

$$\mathbf{H}\ \delta\mathbf{m} = -\nabla_{\mathbf{m}} E, \tag{2.5}$$

and the updated model $\mathbf{m}'$ can be written as

$$\mathbf{m}' = \mathbf{m} + \alpha\ \delta\mathbf{m}, \tag{2.6}$$

where α is the step length, a scalar constant calculated by a line-search method (Nocedal and Wright, 2006).

The gradient is the first-order partial derivative of the objective function with respect to model parameters:

$$\nabla_{\mathbf{m}} E = \frac{\partial E(\mathbf{m})}{\partial \mathbf{m}} = -\Re \left\{ \sum_{ns} \sum_{n\omega} \left[\left(\frac{\partial (\mathbf{R}\mathbf{u}(\mathbf{m}, \mathbf{x}_s, \omega))}{\partial \mathbf{m}} \right)^{\dagger} \delta\mathbf{d} \right] \right\}, \tag{2.7}$$

where $\dagger$ is the adjoint operator (conjugate transpose), $\delta\mathbf{d} = \mathbf{d}_{obs}(\mathbf{x}_s, \omega) - \mathbf{d}_{syn}(\mathbf{m}, \mathbf{x}_s, \omega)$, and $\Re$ denotes the real-part operator. The sensitivity matrix $\mathbf{J} = \partial(\mathbf{R}\mathbf{u}(\mathbf{m}, \mathbf{x}_s, \omega))/\partial\mathbf{m}$

is composed by the Fréchet derivatives of the synthetic data with respect to the model parameters (Virieux and Operto, 2009). To calculate the Fréchet derivatives, I take the partial derivative of equation 2.2 with respect to $\mathbf{m}$:

$$\mathbf{A}(\mathbf{m},\omega)\frac{\partial \mathbf{u}(\mathbf{m},\mathbf{x}_s,\omega)}{\partial \mathbf{m}} = -\frac{\partial \mathbf{A}(\mathbf{m},\omega)}{\partial \mathbf{m}}\mathbf{u}(\mathbf{m},\mathbf{x}_s,\omega). \tag{2.8}$$

This illustrates that the first-order partial derivative of the wavefield, $\partial \mathbf{u}(\mathbf{m},\mathbf{x}_s,\omega)/\partial \mathbf{m}$, can be obtained by solving the wave equation with a virtual source (Pratt et al., 1998) :

$$f_v = -\frac{\partial \mathbf{A}(\mathbf{m},\omega)}{\partial \mathbf{m}}\mathbf{u}(\mathbf{m},\mathbf{x}_s,\omega). \tag{2.9}$$

The radiation pattern of each parameter class $\partial \mathbf{A}/\partial \mathbf{m}$ is included in the virtual source, and the calculation for it depends on the details of the finite approximation method.

Substituting the virtual source back to the gradient, the gradient becomes

$$\begin{aligned}\nabla_{\mathbf{m}} E &= \Re\left\{\sum_{ns}\sum_{n\omega}\left(\mathbf{R}\mathbf{A}^{-1}(\mathbf{m},\omega)\frac{\partial \mathbf{A}(\mathbf{m},\omega)}{\partial \mathbf{m}}\mathbf{u}(\mathbf{m},\mathbf{x}_s,\omega)\right)^{\dagger}\delta\mathbf{d}\right\},\\ &= \Re\left\{\sum_{ns}\sum_{n\omega}\left(\frac{\partial \mathbf{A}(\mathbf{m},\omega)}{\partial \mathbf{m}}\mathbf{u}(\mathbf{m},\mathbf{x}_s,\omega)\right)^{\dagger}\upsilon(\mathbf{m},\mathbf{x}_s,\omega)\right\},\end{aligned} \tag{2.10}$$

where $\upsilon(\mathbf{m},\mathbf{x}_s,\omega)$ is the adjoint variable/state that is the solution of

$$\mathbf{A}^{\dagger}(\mathbf{m},\omega)\upsilon(\mathbf{m},\mathbf{x}_s,\omega) = \mathbf{R}^{\dagger}\delta\mathbf{d}. \tag{2.11}$$

Equation 2.7 illustrates that the gradient with respect to a single parameter is based on the product of data residuals and the wavefield scattered by a perturbation of this parameter recorded by the receivers. As a result, the model perturbation $\delta\mathbf{m}$ given by the gradient is built through the extraction of the specific contribution of each parameter from the residuals, assuming the residuals contain only single scattered events (Métivier et al., 2017). Therefore, relying only on the gradient direction is dangerous, because any residuals coming from

multi-scattered events are wrongly accounted for as single-scattered events. In addition, for two parameter classes p and q with similar radiation patterns, $\frac{\partial \mathbf{A}}{\partial \mathbf{m}_p(\mathbf{x})} = \frac{\partial \mathbf{A}}{\partial \mathbf{m}_q(\mathbf{x})}$, their model perturbations provided by the gradient will also be similar, while in reality their true perturbations might be completely different. This is usually referred to as parameter crosstalk. The Hessian operator is important in model updating because it helps to mitigate these issues.

For multiparameter FWI, the Hessian is a large block matrix. If the number of parameter classes is N, then the Hessian has $N \times N$ blocks, with each element in the blocks representing the second-order derivative of the misfit function with respect to model parameters:

$$\begin{aligned}\mathbf{H}_{\mathbf{m}_p\mathbf{m}_q}(\mathbf{x},\mathbf{x}') = \Re\Bigg\{\sum_{ns}\sum_{n\omega}\Bigg[\left(\frac{\partial \mathbf{u}(\mathbf{m},\mathbf{x}_s,\omega)}{\partial \mathbf{m}_p(\mathbf{x})}\right)^{\dagger}\mathbf{R}^{\dagger}\mathbf{R}\frac{\partial \mathbf{u}(\mathbf{m},\mathbf{x}_s,\omega)}{\partial \mathbf{m}_q(\mathbf{x}')} \\ - \left(\frac{\partial^2 \mathbf{u}(\mathbf{m},\mathbf{x}_s,\omega)}{\partial \mathbf{m}_p(\mathbf{x})\partial \mathbf{m}_q(\mathbf{x}')}\right)^{\dagger}\mathbf{R}^{\dagger}\delta\mathbf{d}\Bigg]\Bigg\}.\end{aligned} \tag{2.12}$$

When $p = q$, equation 2.12 indicates the elements in diagonal blocks, and when $p \neq q$, it indicates off-diagonal blocks. When the spatial position $\mathbf{x} = \mathbf{x}'$, it indicates diagonal elements within a single block, and when $\mathbf{x} \neq \mathbf{x}'$, it indicates off-diagonal elements. The first-order term in 2.12 measures the correlations of two Fréchet derivatives and is essential in overcoming crosstalk in multiparameter FWI. The second term contains the second-order partial derivative of the wavefield and accounts for the second-order scattering (Métivier et al., 2017).

2.1.3 Optimization methods

FWI is classically formulated as a local optimization problem, where model updates are designed based on the derivatives of the objective function at the current model location and only steps decreasing the objective function are allowed.

The full Newton method uses the quadratic search direction from equation 2.5: $\triangle \mathbf{m}_k = -\mathbf{H}_k^{-1}\mathbf{g}_k$. The Gauss-Newton method approximates the full Hessian by only accounting for

the first term in equation 2.12. Although the Newton methods benefit from a fast convergence rate, the computation, storage, and inversion of Hessian at each iteration are prohibitively expensive, this limits their applications for large-scale inverse problems (Pan et al., 2018a).

Gradient-based methods, such as steepest-descent (SD) and nonlinear conjugate-gradient (CG) are computationally more attractive when inverting a large number of unknown model parameters. SD simply determines the search direction to be the negative of the gradient:

$$\delta \mathbf{m}_k = -\nabla_{\mathbf{m}_k} E, \tag{2.13}$$

and CG uses a linear combination of the current gradient and the previous search direction:

$$\delta \mathbf{m}_k = -\nabla_{\mathbf{m}_k} E + \beta_k \delta \mathbf{m}_{k-1}, \tag{2.14}$$

where β_k is a scalar selected such that $\delta \mathbf{m}_k$ and $\delta \mathbf{m}_{k-1}$ are conjugate. The gradient-based methods are known to converge to the global minimum, but possibly very slowly. In most cases, preconditioning is necessary to ensure the fast convergence of CG methods (Pan et al., 2017).

As a low-rank approximation of the Hessian, the L-BFGS method is an attractive alternative to Newton-based and gradient-based methods, by approximating the inverse Hessian iteratively instead of constructing the Hessian explicitly (Nocedal and Wright, 2006). Using a pair of vectors $\mathbf{s}_k = \mathbf{m}_{k+1} - \mathbf{m}_k$ and $\mathbf{y}_k = \nabla_{\mathbf{m}_{k+1}} E - \nabla_{\mathbf{m}_k} E$ that indicate the model and gradient changes that satisfy the condition $\mathbf{s}_k^\dagger \mathbf{y}_k > 0$, the inverse Hessian approximation $\mathbf{H}_{k+1}^{-1}$ is given by

$$\mathbf{H}_{k+1}^{-1} = \mathbf{v}_k^\dagger \mathbf{H}_k^{-1} \mathbf{v}_k^\dagger + \mathbf{w}_k \mathbf{s}_k \mathbf{s}_k^\dagger, \tag{2.15}$$

where $\mathbf{w}_k = 1/\mathbf{y}_k^\dagger \mathbf{s}_k, \mathbf{v}_k = \mathbf{I} - \mathbf{w}_k \mathbf{y}_k \mathbf{s}_k^\dagger$, and $\mathbf{I}$ is the identity matrix. The initial inverse Hessian approximation is usually set as an identity matrix to make sure that the updated matrix maintains positive definiteness (Pan et al., 2017). The model and gradient are stored

for a limited number (typically <10) of previous iterations. For multiparameter FWI, the L-BFGS algorithm provides a suitable scaling of the gradient computed for each parameter class and can help reduce crosstalk.

Instead of constructing inverse Hessian approximations, the truncated-Newton (TN) optimization (Métivier et al., 2017) finds the search direction by numerically solving the Newton linear system (equation 2.5). This optimization problem is given by

$$\delta \mathbf{m}_k = \min \left[\delta \mathbf{m}^T \nabla_{\mathbf{m}_k} E + \frac{1}{2} \delta \mathbf{m}^T \mathbf{H}_k \delta \mathbf{m} \right]. \tag{2.16}$$

The CG method is often used as the optimization strategy for the inner-loop problem because it only requires computing the Hessian-vector products instead of forming the Hessian matrix explicitly. The Hessian-vector products can be calculated via the finite-difference method or the adjoint-state method (Plessix, 2006). Compared to the L-BFGS approach, the TN approach can work with an effective level of second-derivative information even at the first step of the optimization.

2.1.4 Model parameterization

The term "model parameterization" is understood as a set of independent parameter classes that fully describe the subsurface properties (Operto et al., 2013). For example, we need three elastic parameters to define isotropic-elastic media, such as the two Lamé parameters and density, or P-wave velocity, S-wave velocity, and density. Although, in theory, these are equivalent, the reconstruction of these constants from seismic will not yield the same results. The main reason behind this is the trade-off between different physical parameters and the resolution with which they can be reconstructed.

The choice of model parameterization is often based on the analysis of scattering/radiation patterns, which represent the amplitude variation of Fréchet derivative wavefield with varying scattering angles, and can be used to evaluate the sensitivity of a seismic wavefield to

small perturbations of the material properties. A good choice of parameterizations should give radiation patterns that are as different as possible, to allow easy identification of parameters. Tarantola (1986) examined the resolving abilities of various model parameterizations for isotropic-elastic FWI based on radiation patterns. His analysis suggested that the velocity-density parameterization is more appropriate for inversion with large-offset data, while impedance-density parameterization is more suitable for near-offset data. Virieux and Operto (2009) showed the radiation pattern of different parameter classes in acoustic FWI and also pointed out that velocity and density are difficult to reconstruct from short-offset data because of the same radiation pattern at short apertures. Pan et al. (2018a) analyzed the resolving abilities of various model parameterizations in a vertical seismic profile (VSP) environment. His study showed that all model parameterizations can reconstruct the P-wave velocity and S-wave velocity models reasonably, but only the velocity-density parameterization is able to provide relatively reliable density estimations.

There are two ways to calculate the radiation pattern. One is to compute the scattered wavefield numerically by perturbing one parameter and keeping other parameters fixed at its background value (Operto et al., 2013). The amplitude variations of the scattered wavefield are representative of the radiation pattern of the virtual source. The other is to extract the analytical expressions for the radiation patterns based on the Born approximation (Wu and Aki, 1985; Stolt and Weglein, 2012). A summary of the analytic scattering coefficients of isotropic-elastic parameters can be found in Pan et al. (2018a) and Chen (2018).

For example, the analytical expressions for the radiation patterns of Lamé parameters plus density $[\delta\lambda/\lambda, \delta\mu/\mu, \delta\rho/\rho]$ are given by:

$$\mathbf{W}_{\lambda,\mu,\rho} = \begin{bmatrix} W_\lambda^{P-P} & W_\mu^{P-P} & W_\rho^{P-P} \\ W_\lambda^{P-SV} & W_\mu^{P-SV} & W_\rho^{P-SV} \\ W_\lambda^{SV-P} & W_\mu^{SV-P} & W_\rho^{SV-P} \\ W_\lambda^{SV-SV} & W_\mu^{SV-SV} & W_\rho^{SV-SV} \end{bmatrix} = \begin{bmatrix} 1-2\sigma^2 & 2\sigma^2\cos^2\theta & \cos\theta \\ 0 & \sigma\sin 2\theta & \sin\theta \\ 0 & -\sigma\sin 2\theta & -\sin\theta \\ 0 & \cos 2\theta & \cos\theta \end{bmatrix}, \tag{2.17}$$

where W_{λ}^{P-P} represents the P- to P-wave scattering coefficient due to the perturbation $\delta\lambda/\lambda$, and W_{μ}^{P-SV} represents the P- to SV-wave scattering coefficient due to the perturbation $\delta\mu/\mu$, and so on. θ represents the opening angle between the incident wave and scattered wave, and σ is the $V_{\mathrm{S}}/V_{\mathrm{P}}$ ratio of the unperturbed medium.

Similarly, the radiation patterns of P- and S-wave velocities plus density are given by:

$$\mathbf{W}_{V_{\mathrm{P}},V_{\mathrm{S}},\rho} = \begin{bmatrix} W_{V_{\mathrm{P}}}^{P-P} & W_{V_{\mathrm{S}}}^{P-P} & W_{\rho}^{P-P} \\ W_{V_{\mathrm{P}}}^{P-SV} & W_{V_{\mathrm{S}}}^{P-SV} & W_{\rho}^{P-SV} \\ W_{V_{\mathrm{P}}}^{SV-P} & W_{V_{\mathrm{S}}}^{SV-P} & W_{\rho}^{SV-P} \\ W_{V_{\mathrm{P}}}^{SV-SV} & W_{V_{\mathrm{S}}}^{SV-SV} & W_{\rho}^{SV-SV} \end{bmatrix} = \begin{bmatrix} 2 & -4\sigma^2\sin^2\theta & 2(1-\sigma^2\sin^2\theta-\sin^2(\theta/2)) \\ 0 & 2\sigma\sin 2\theta & \sigma\sin 2\theta+\sin\theta \\ 0 & -2\sigma\sin 2\theta & -\sigma\sin 2\theta-\sin\theta \\ 0 & 2\cos 2\theta & \cos 2\theta+\cos\theta \end{bmatrix}. \tag{2.18}$$

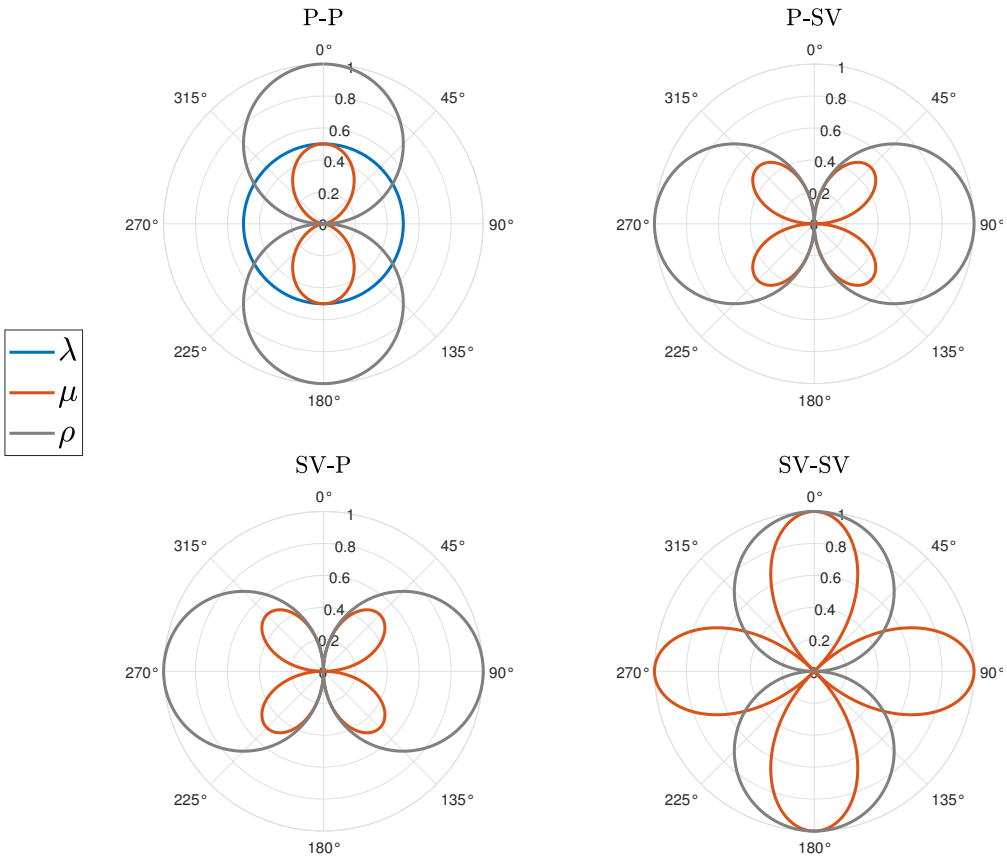

Figure 2.1: Radiation patterns of different physical parameters in the $\lambda-\mu-\rho$ parameterization

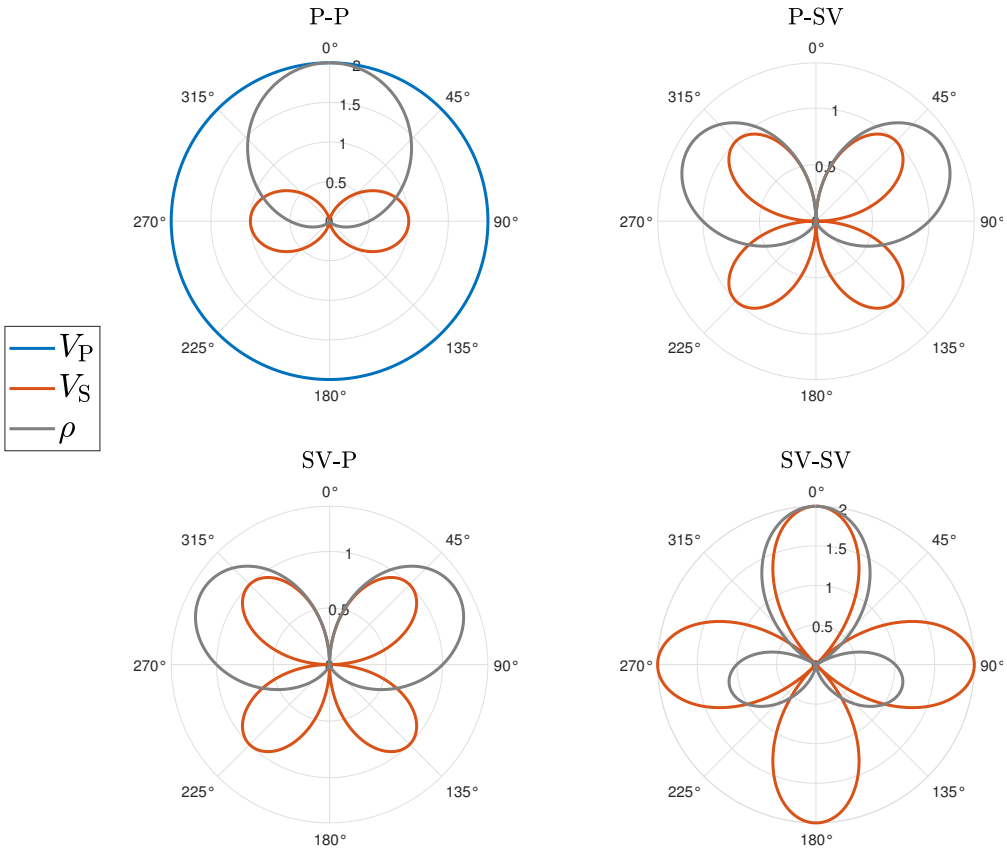

Figure 2.2: Radiation patterns of different physical parameters in the $V_P - V_s - \rho$ parameterization

In Figures 2.1 and 2.2, I plot the radiation patterns for the two parameterizations, $\lambda-\mu-\rho$ and $V_P - V_s - \rho$, respectively. These provide information for us to understand the potential parameter crosstalk in the inversion. In general, the higher the degree of overlapping of radiation patterns with different parameters, the lower the ability of inversion algorithms to differentiate responses caused by them. According to this criterion, the radiation patterns in the $\lambda - \mu - \rho$ parameterization overlap more significantly than they are in the $V_P - V_s - \rho$ parameterization, indicating a lower parameter resolution. In the $V_P - V_s - \rho$ parameterization, the three variables will be more distinguished in a transmission survey than they would be in a reflection survey because a change in density mostly alters the back-scattered wavefield. For each parameterization, introducing a more powerful survey of wide apertures will help to mitigate the crosstalk.

2.1.5 Regularization

EFWI methods hold strong potential to provide high-resolution estimates of subsurface properties. However, the nonlinearity of EFWI and parameter crosstalk can prevent convergence toward the global minimum, delivering results not consistent with existing data, such as those contained in wells.

Regularization techniques allow stabilizing ill-posed inverse problems by incorporating prior information about the model in the inversion (Sen and Roy, 2003). This essentially involves modification of the objective function by adding a model penalty term:

$$E(\mathbf{m}) = E_d(\mathbf{m}) + \gamma E_m(\mathbf{m}), \tag{2.19}$$

where the data misfit term $E_d(\mathbf{m})$ is based on a norm of the residuals between observed data and synthetic data, and the model term $E_m(\mathbf{m})$ is based on a norm of a model penalty function. γ is the trade-off parameter that controls the relative importance of the data and model terms.

The model term can take different forms, depending on the type of prior information. The prior information can consist of the estimates of model parameters (Asnaashari et al., 2013) and desired structure of the model, e.g., smoothness (Tikhonov and Arsenin, 1977) or blockiness (Guitton, 2012). In recent years, some authors propose using the physical relationships between elastic parameters to constrain the inversion. Because this type of model constraint is often derived from well data and is related to the distribution of facies in the subsurface, it is often called petrophysical constraint (Rocha and Sava, 2018; Aragao and Sava, 2020) or facies-based rock-physics constraint (Kamali et al., 2017; Zhang et al., 2018; Singh et al., 2020). Their methods distinguish from each other by the form of the penalty function included in the objective function. For example, Rocha and Sava (2018) use a logarithmic function to confine the inverted models to a feasible region. Aragao and Sava (2020) use probability density functions to impose complex petrophysical relations. Zhang

et al. (2018) use a facies-based prior estimate and update it iteratively during the inversion. These approaches have been demonstrated to guide the inversion toward high-resolution and geologically plausible models.

I have developed a method for EFWI that enforces explicit physical relationships between the model parameters (Hu and Innanen, 2021). The underlying assumption is that a strong correlation between the desired physical parameters can be observed from existing data. In this approach, the model term is defined as

$$E_m = \frac{1}{2}\sum_{\mathbf{x}}(m_1 - f(m_2))^2, \tag{2.20}$$

where $\mathbf{x}$ denotes model space coordinates, $m_1 = m_1(\mathbf{x})$ and $m_2 = m_2(\mathbf{x})$ are different physical parameters, and $f = f(\mathbf{x})$ is a predefined function mapping m_2 to m_1. For example, let m_1 represent density and m_2 represent P-wave velocity, this term forces the inverted velocity and density models to satisfy the relation $\rho = f(V_{\mathrm{P}})$. I make this function position-dependent so that each model cell, based on its associated lithology or geologic facies, is subject to a specific velocity-density trend (Gardner et al., 1974; Castagna et al., 1993; Martin et al., 2006). This method is easy to implement when the lithology is relatively simple and the regression relationship can be derived from existing data, such as well logs. For complex lithology, prior information for the spatial distribution of lithofacies is required for imposing this constraint.

2.2 Numerical Examples

2.2.1 Importance of Hessian and wide-aperture data

The importance of acquisition geometry to the reduction of parameter crosstalk in FWI can be inferred from the radiation patterns. In the velocity-density parameterization, we observe that the perturbation of velocity scatters the same energy for different angles, and density

has the same radiation pattern as velocity at short apertures but does not scatter energy at wide apertures. This implies that the two parameters are difficult to reconstruct using only short-offset data. In the theory section, I also pointed out that for multi-parameter FWI, the Newton-based algorithms have more advantages than the gradient-based ones, because the information of Hessian is used, which can theoretically alleviate the coupling between different parameters. Therefore, an ideal inversion environment should include a wide observation aperture and an inversion framework based on the Newton algorithms. To verify this, I conduct the following inversion test.

I consider a Gaussian anomaly model where the velocity anomaly and density anomaly are on the left and right sides of the model respectively. The initial models are homogeneous, with a constant velocity of 3000 m/s and a constant density of 2300 kg/m^3. The model is constructed of 50 $\times$ 100 grid cells with a grid interval of 10 m. The default acquisition configuration is surface-only sources and receivers. A total of 10 sources are deployed at 20 m depth and spread from 20 to 980 m with an interval of 100 m in the horizontal direction. A total of 100 receivers are distributed on the surface from 10 to 1000 m with an interval of 10 m. I use a multiscale approach by successively iterating over 10 frequency bands, from 3 HZ to 21 HZ, with 20 iterations per band. In this environment, I examine respectively the steepest descent (SD) method and L-BFGS method for inversion. Finally, I consider a more complete acquisition geometry by adding a receiver line at the bottom of the model space and rerun the L-BFGS test.

Figure 2.3 summarizes the inversion results. The velocity estimates are reasonably accurate in all tests, but the density inversion is difficult. We can observe significant parameter crosstalk in the SD models, especially density, which also suffers from insufficient updates. The L-BFGS method alleviates the parameter crosstalk to some extent and improves the convergence by introducing Hessian information in the inversion, but it still underestimates the density anomaly. By further introducing subsurface geophones, the accuracy of density estimates is significantly improved. This is consistent with our observations of the velocity-

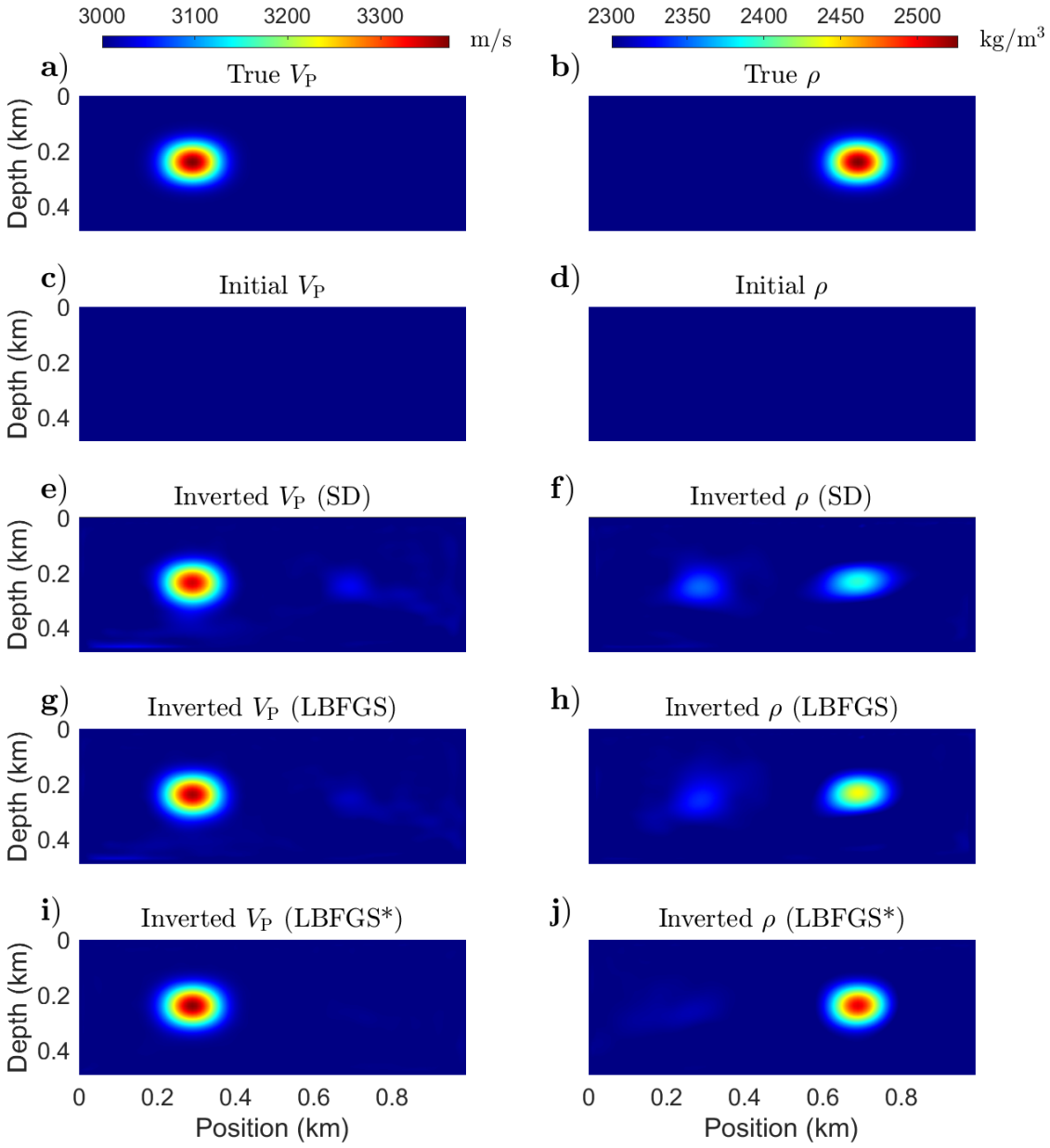

Figure 2.3: (a,b) True P-wave velocity and density models. (c,d) Initial models. (e,f) Inverted models by steepest-decent FWI of surface-recorded seismic data. (g,h) Inverted models by L-BFGS FWI of surface-recorded seismic data. (i,j) Inverted models by L-BFGS FWI of surface- and subsurface-recorded data.

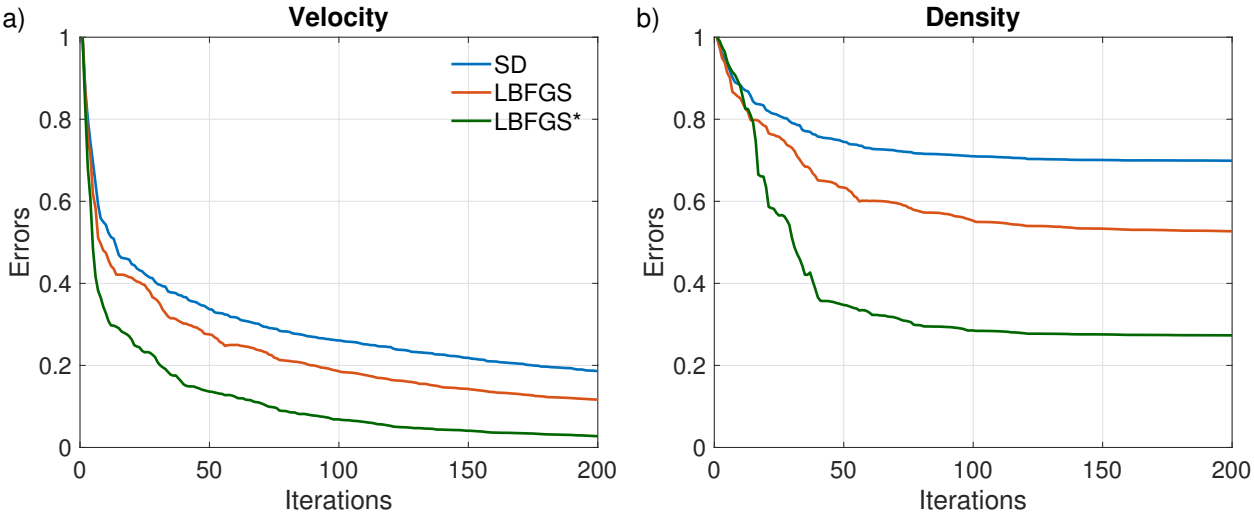

Figure 2.4: Convergence histories of (a) P-wave velocity and (b) density for the inversion tests in Figure 2.3.

density radiation pattern. However, it should be pointed out that the above-mentioned acquisition geometry considering that the geophones are arranged horizontally underground is too ideal, and it is only to illustrate the importance of the observation aperture. In reality, a good alternative is to add subsurface sources and receivers through wells, such as the vertical seismic profile (VSP) and cross-well techniques. In Figure 2.4, the convergence properties of the above inversion tests are summarized.

2.2.2 Regularized full waveform inversion

In this section, I examine the behavior of the penalty term that is based on explicit relations between model variables. I give two examples, corresponding to single lithofacies and complex lithofacies.

The first example uses a three-layer model, in which a constant P-wave velocity V_{P}, S-wave velocity V_{S}, and density ρ are assigned to each layer (Figures 2.5a-2.5c). The initial models (Figures 2.5d-2.5f) are smoothed versions of the true models. In Figure 2.6, the inversion results are summarized. Without regularization, apart from some mild oscillatory behavior, the recovered V_{P} and V_{S} models (Figures 2.6a and 2.6b) match closely with the

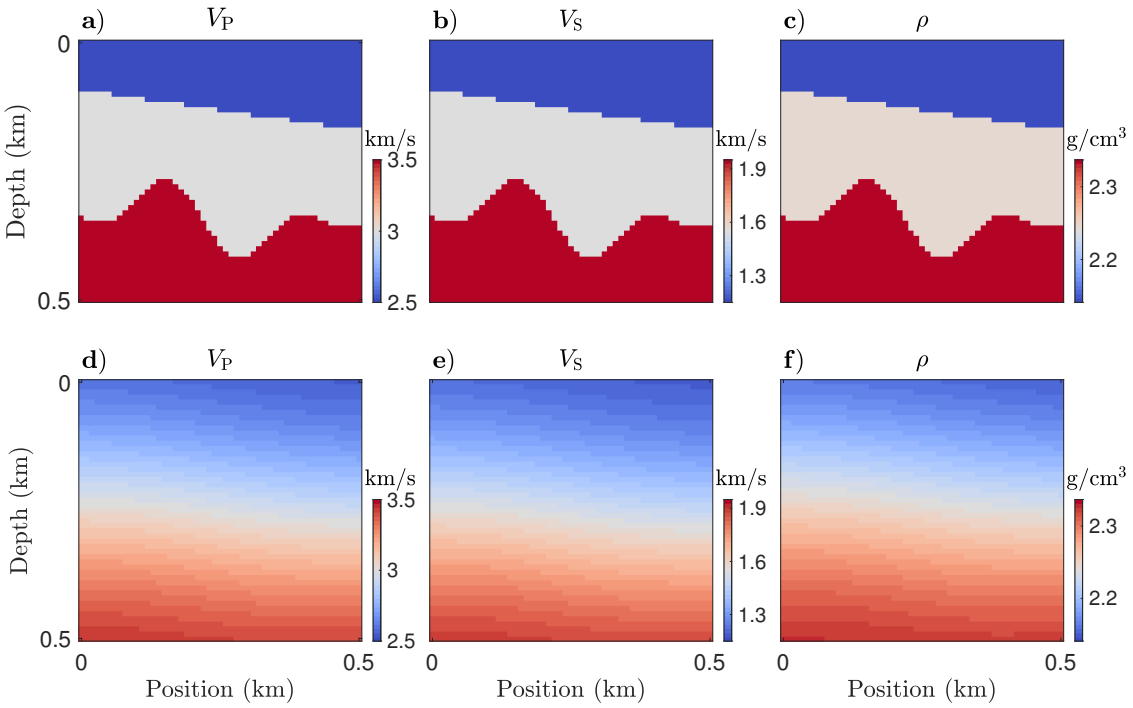

Figure 2.5: (a–c) True models and (d–f) initial models of V_P, V_S, and ρ, respectively.

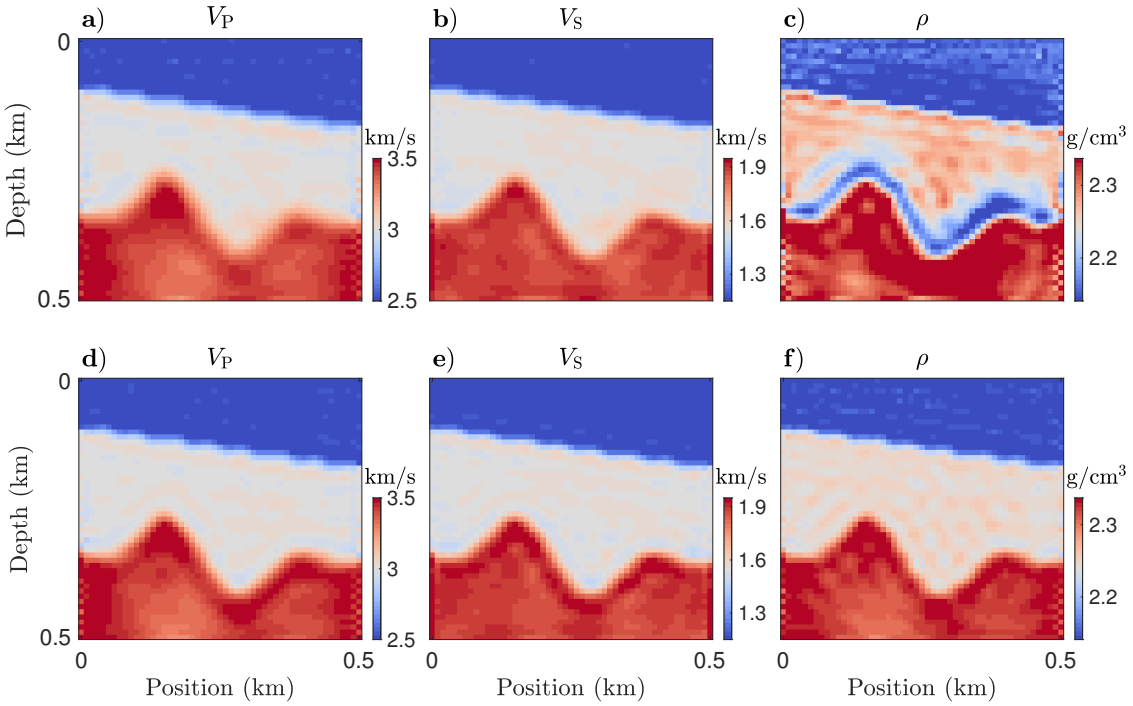

Figure 2.6: Inverted V_P, V_S, and ρ models: (a-c) without regularization and (d–f) with regularization.

true ones. However, the recovered ρ model appears particularly distorted (Figure 2.6c). In contrast, the recovered ρ model with regularization exhibits reduced artifacts and the spatial extent of each layer can be identified (Figure 2.6f). In addition, the V_{P} and V_{S} models are recovered with slightly higher resolution (Figures 2.6d and 2.6e).

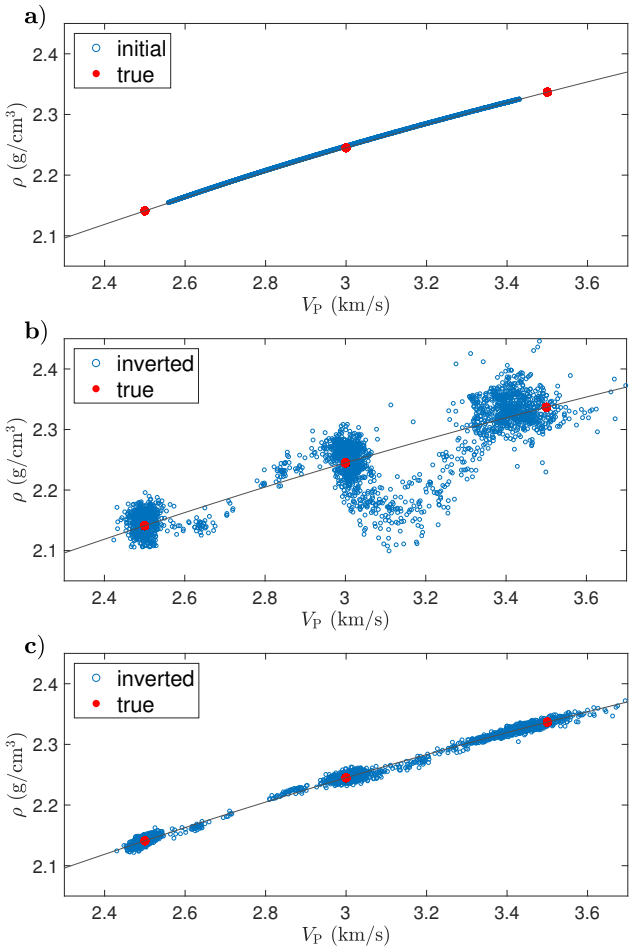

Figure 2.7: V_{P}-ρ crossplots of the (a) initial model, (b) inverted model without regularization, and (c) inverted model with regularization. The gray line denotes the V_{P}-ρ relationship used as a model constraint.

In Figure 2.7 I display the true, initial, and inverted models in the V_{P}-ρ crossplot; As the iteration proceeds, I expect the blue dots in Figure 2.7a, which denote the initial models, to move toward the red dots that denote the true models. However, we observe a poor convergence of the unconstrained inversion, with the updated ρ values deviating significantly from the true ones (Figure 2.7b). In Figure 2.7c, by enforcing an explicit relationship between

V_P and ρ, which takes the form of $\rho = -0.02V_P^2 + 0.3V_P + 1.4$, I obtain a reliable model update for ρ. My explanation is that imposing the constraint reduces undesired model updates, which can be caused by parameter crosstalk, the low sensitivity of seismic data to density, and the nonlinearity of the inverse problem, thereby improving the inversion convergence.

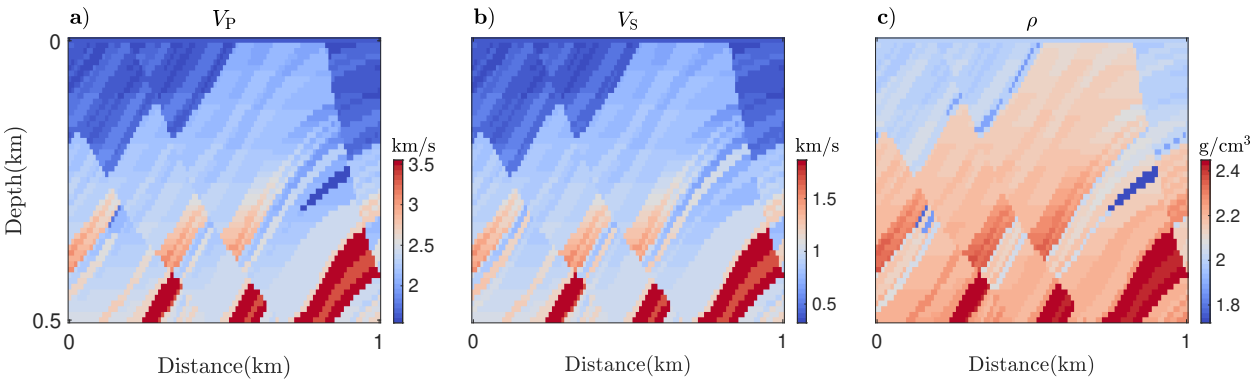

Figure 2.8: Marmousi case. True models of (a) P-wave velocity, (b) S-wave velocity, and (c) density

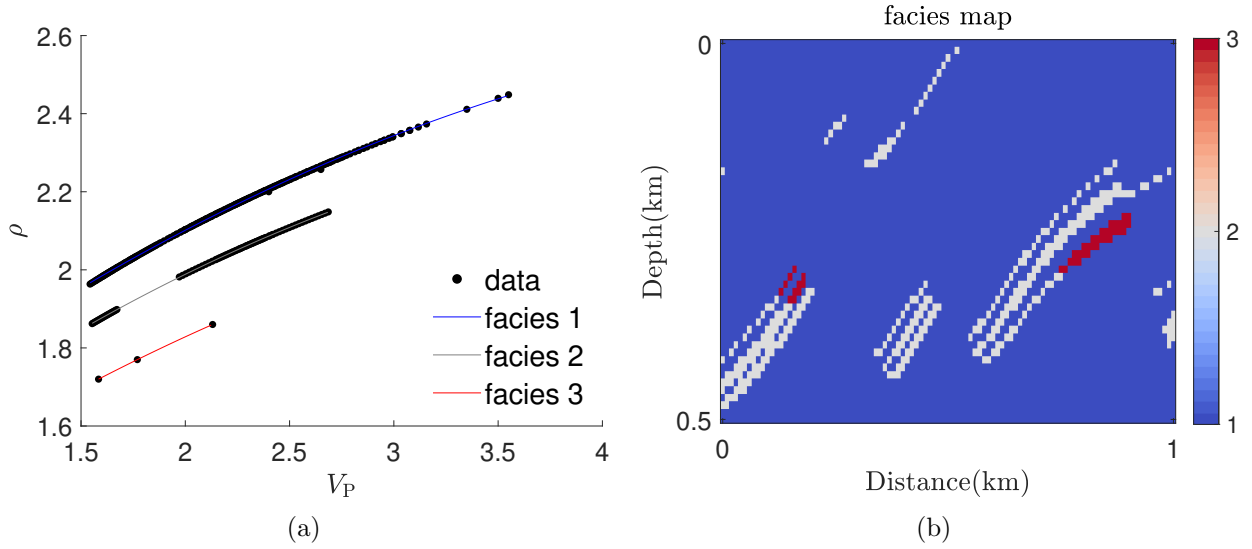

Figure 2.9: Facies classification. (a) Model points are classified into three groups, and each group is described by a quadratic function: $\rho = aV_P^2 + bV_P + c$. (b) The corresponding spatial distribution of facies.

The second example is based on a selected target of the Marmousi model (Figure 2.8). In Figure 2.9a I display the true models using a V_P-ρ crossplot. The model points (black dots)

can be classified into three categories, each corresponding to a single facies or V_P-ρ relation. Labeling every point based on the facies it falls into, a facies map can be generated (Figure 2.9b). Notably, the solution of the facies map is not unique. It depends on how I separate those points. More groups and different fitting equations are allowed. Even the terminology "facies" I use is not strict, it is rather a tool for us to assign the correct V_P-ρ relation to each grid.

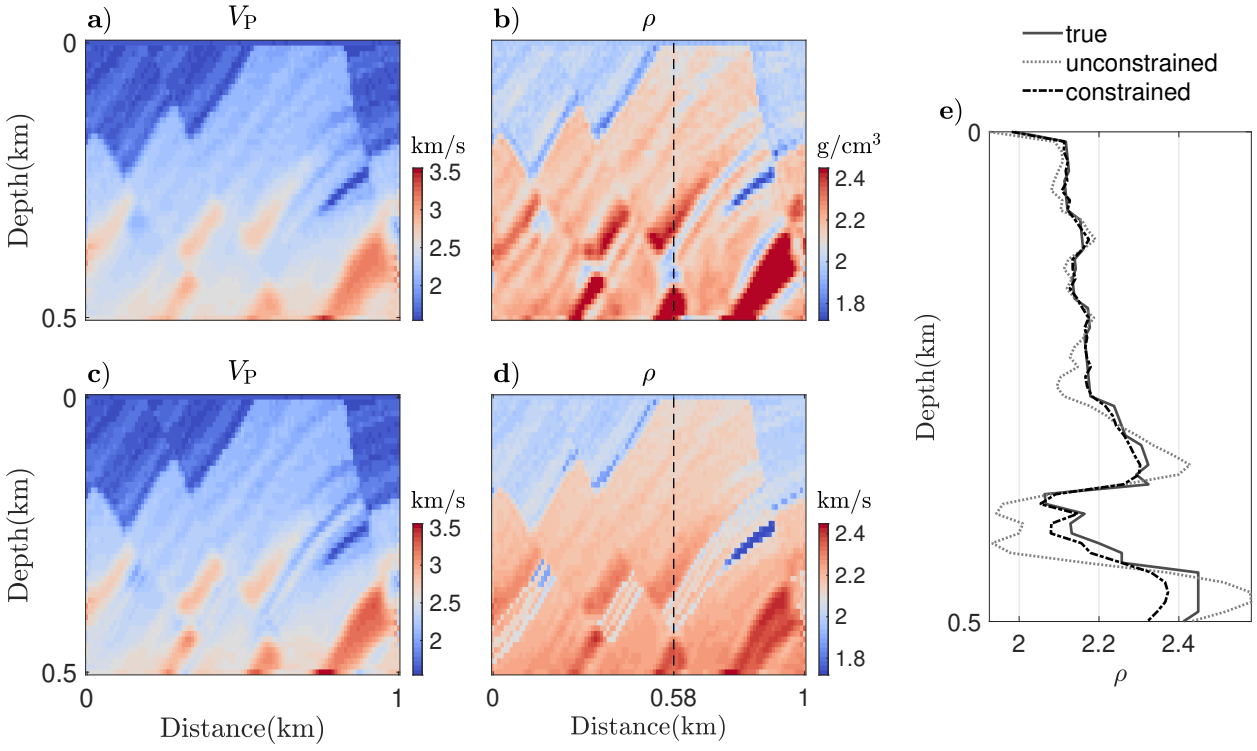

Figure 2.10: Comparison between (a,b) unconstrained and (c,d) constrained inversion results. (e) Model profiles of density at x=0.58km.

However, it is unrealistic to obtain the facies map from the true model. A facies classification technique is required. Some authors have proposed using an iterative approach to impose facies-based constraints (e.g., Singh et al., 2018; Zhang et al., 2018), which consists of estimating the facies distribution based on the current inverted model and then using this facies distribution to constrain the inversion at the next iteration. By doing so the facies map is updated interactively with the model during the inversion. They ended up achieving

a good estimation of both subsurface models and facies maps. Unfortunately, I have not yet found this approach effective for imposing the kind of constraint I propose. My study indicates that the iterative approach will inevitably assign the wrong facies to part of the model at each iteration, and hinder the model from updating towards reducing data misfit. As a result, it can be less efficient than the unconstrained inversion.

While my research into facies classification is ongoing, I examine the proposed method using the exact facies distribution (Figure 2.9). In Figure 2.10 I compare the inversion results between the unconstrained and constrained approaches. The recovered density model using the constrained approach has a higher resolution (Figure 2.10d) and matches the true model more closely (Figure 2.10e). Figure 2.11 illustrates that the inverted model points are confined to different lines honoring their corresponding facies, thus being more likely to recover the true model points.

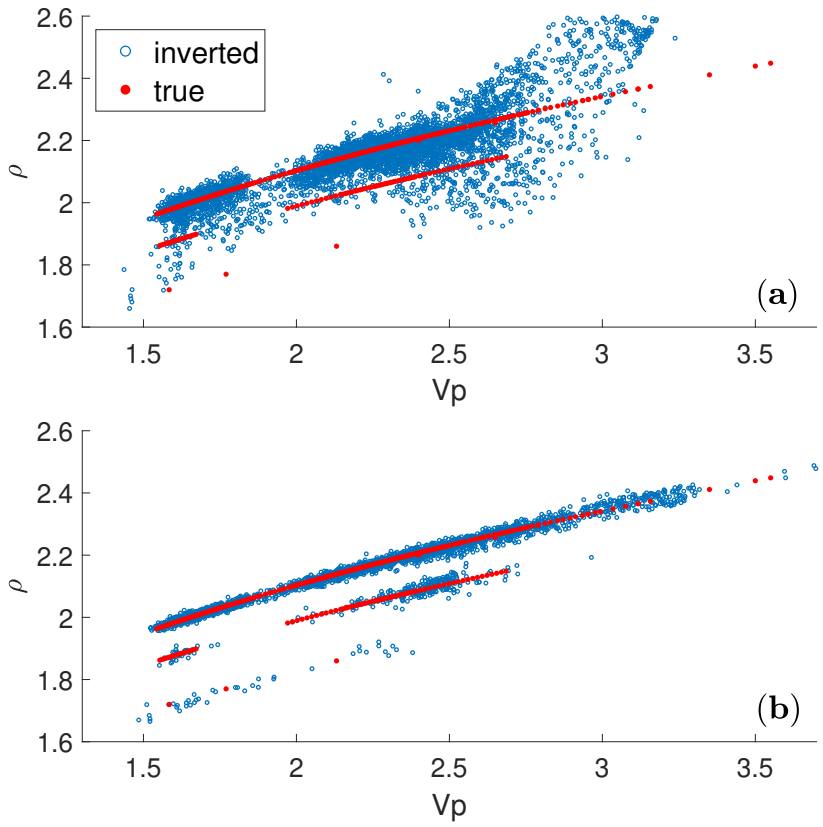

Figure 2.11: Comparison between (a) unconstrained and (b) constrained inversion results.

2.3 Conclusions

In this chapter, I presented a general form of EFWI and the challenges associated with EFWI, such as nonlinearity, ill-posedness, and parameter crosstalk. I introduced three important factors that affect the performance of EFWI: optimization method, acquisition geometry, and model parameterization. I demonstrated that the Newton-based optimization algorithms outperform the gradient-based ones in mitigating crosstalk and ensuring convergence. Based on the analysis of radiation patterns, I illustrated the importance of wide aperture data for improved parameter resolution. I also proposed a regularized EFWI scheme that encourages the interdependence of different physical parameters. Although my research is based on 2D, frequency-domain, isotropic-elastic FWI, the considerations in this chapter should apply to most multiparameter FWI frameworks, such as time domain, viscoelastic, or anisotropic inversions. Also under this framework, I combined FWI with rock physics in various ways, which will be discussed in detail in subsequent chapters.

Chapter 3

Rock physics modeling and inversion

In this chapter, I will introduce the forward and inverse problems in rock physics. The forward problem is to construct a rock physics model that converts rock and fluid properties (such as porosity, lithology, and saturation) into elastic properties (such as velocity, density, and modulus). A complete rock physics modeling process generally includes multiple theoretical models to gradually simulate the effects of minerals, pores, and fluids on the elastic properties of saturated rocks. The inverse problem is the process of estimating rock physics variables from elastic parameters based on a constructed rock physics model. Solving this problem requires some deterministic or stochastic inversion algorithm. This chapter introduces several commonly used isotropic rock physics models in detail, most of which will be used in combination with FWI in later chapters. I then investigated two classes of algorithms for solving the rock physics inverse problem: global optimization and Bayesian methods. Understanding the principles and limitations of these algorithms would facilitate a step-wise seismic reservoir characterization workflow: first, the elastic parameters are obtained by FWI, and then the reservoir parameters are obtained by rock physics inversion. This approach will be applied to the field data in Chapter 6.

3.1 Rock physics models

According to the Hooke's law, only two elastic moduli are needed to specify the stress–strain relation of an isotropic elastic medium. The majority of theoretical rock physics models have been developed in the domain of bulk modulus K and shear modulus μ (Mavko et al., 2020). The former is defined as the ratio of hydrostatic stress to volumetric strain, while the latter is defined as the ratio of shear stress to shear strain. The P- and S-wave velocities of the saturated rock can be computed from K and μ as:

$$V_{\mathrm{P}} = \sqrt{\frac{K + \frac{4}{3}\mu}{\rho}}, \quad V_{\mathrm{S}} = \sqrt{\frac{\mu}{\rho}}. \tag{3.1}$$

where the density ρ is generally computed as a linear average of the densities of mineral and fluid phases, ρ_m and ρ_f, weighted by porosity ϕ:

$$\rho = (1 - \phi)\rho_m + \phi\rho_f. \tag{3.2}$$

A complete rock physics modeling process includes several steps (Grana et al., 2021): if there are multiple minerals and fluids, the elastic moduli of an effective solid matrix and an effective fluid are calculated using mixing laws; then, based on the assumption for the geometric details of how pores are arranged relative to mineral grains, the elastic moduli of the dry rock are calculated; finally, the fluid effect is included to obtain the elastic moduli of the saturated rock.

3.1.1 Elastic bounds

The solid matrix is a composite of several pure minerals. Based on the elastic moduli of each component and their volume fractions, it is possible to define the upper and lower bounds of the elastic moduli of the effective mineral.

The Voigt upper bound is defined as:

$$M_{\mathrm{V}} = \sum_{i=1}^{N} v_i M_i, \tag{3.3}$$

where N is the number of mineral components, M_i is the elastic modulus of the ith component, and v_i is the volume fraction of the ith component, assuming $\sum_{i=1}^{N} v_i = 1$. M can represent any modulus, such as the bulk modulus K and the shear modulus μ. The Voigt bound represents the isostrain average because it gives the ratio of the average stress to the average strain when all components are assumed to have the same strain.

The Reuss lower bound M_{R} is

$$\frac{1}{M_{\mathrm{R}}} = \sum_{i=1}^{N} \frac{v_i}{M_i}. \tag{3.4}$$

This bound represents the isostress average because it gives the ratio of the average stress to the average strain when all constituents are assumed to have the same stress.

The effective moduli of the solid phase are often computed as the arithmetic average (also referred to as Hill's average) of the Voigt and Reuss bounds (Hill, 1952):

$$M_{\mathrm{VRH}} = \frac{M_{\mathrm{V}} + M_{\mathrm{R}}}{2}. \tag{3.5}$$

In Figure 3.1, I provide an example of the Voigt–Reuss–Hill average for a mixture of quartz and clay. A very similar approach can be used with more rigorous elastic bounds, such as the Hashin-Shtrikman upper and lower bounds.

3.1.2 Fluid mixing laws

Similar to the solid matrix case, the mixing laws based on volumetric averages are generally used to compute the bulk modulus of the fluid mixture, the components of which may include water, oil, and gas. Since most fluids do not resist shear deformation, the shear modulus is zero. Contrasting to mineral properties, the bulk modulus and density of individual

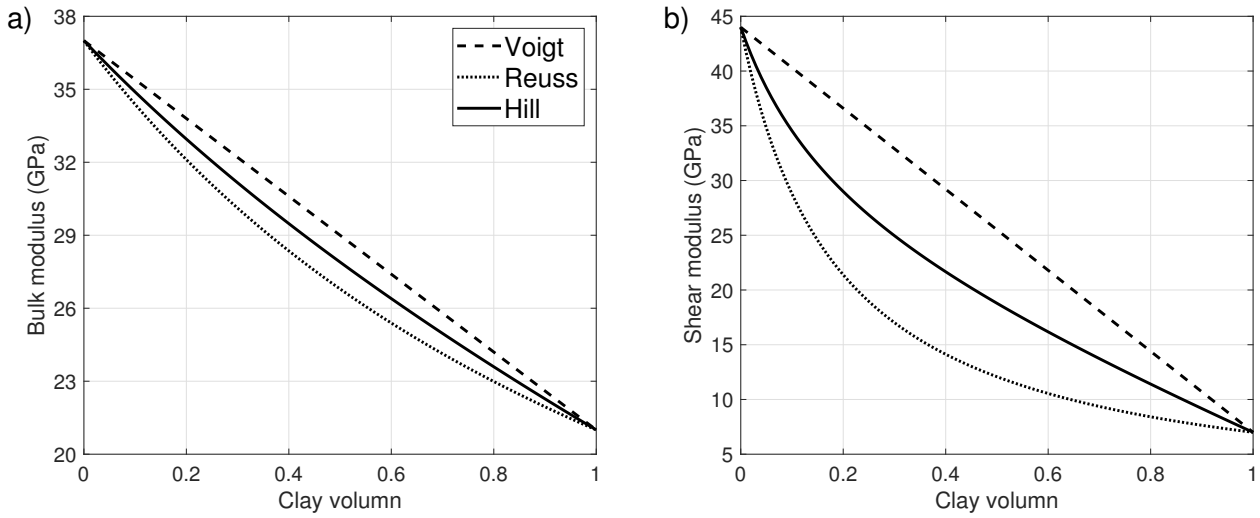

Figure 3.1: Voigt, Reuss, and Voigt–Reuss–Hill averages for the (a) bulk modulus and (b) shear modulus of a mixture of quartz and clay. In this example, the quartz properties are $K_q = 37$ GPa and $\mu_q = 44$ GPa, and the clay properties are $K_c = 21$ GPa and $\mu_c = 7$ GPa.

fluid components are more variable, depending on reservoir properties (e.g., temperature and pressure) as well as fluid composition (e.g., water salinity, oil gravity, and gas gravity). The formulas for calculating fluid properties are mostly based on the empirical equations summarized by Batzle and Wang (1992).

The Reuss average (weighted harmonic mean) is used to compute the effective bulk modulus K_f when the fluid components are mixed at the finest scales:

$$\frac{1}{K_f} = \frac{S_w}{K_w} + \frac{S_o}{K_o} + \frac{S_g}{K_g}. \tag{3.6}$$

where K_w, K_o, and K_g are the bulk modulus of water, oil, and gas, and S_w, S_o, and S_g are the corresponding saturations, assuming $S_w + S_o + S_g = 1$.

The Voigt average (weighted arithmetic mean) is used when each fluid component is grouped in relatively large patches and the hydraulic communication between these patches is restricted (Dvorkin, 2004):

$$K_f = S_w K_w + S_o K_o + S_g K_g. \tag{3.7}$$

Brie et al. (1995) suggest an empirical fluid mixing law:

$$K_f = \left[\left(\frac{S_w}{K_w} + \frac{S_o}{K_o} \right)^{-1} - K_g \right] (1 - S_g)^e + K_g. \tag{3.8}$$

where e is an empirical constant, equal to 3 in the original experiments.

The effective fluids modeled by Reuss average, Voigt average, and Brie's equation are often referred to as 'uniform', 'patchy', and 'semi-patchy' mixtures, respectively (Mavko et al., 2020; Dupuy et al., 2021b). In Figure 3.2, the three mixing laws and the impact of Brie's exponent e are examined. We see that by changing the e value, Brie's model alone can determine the range for the effective fluid modulus. In fact, this exponent is often used to describe the degree of patchiness for the fluid mixture, with low values (down to 1) corresponding to patchy mixing and high values (up to 40) corresponding to uniform mixing (Dupuy et al., 2021b).

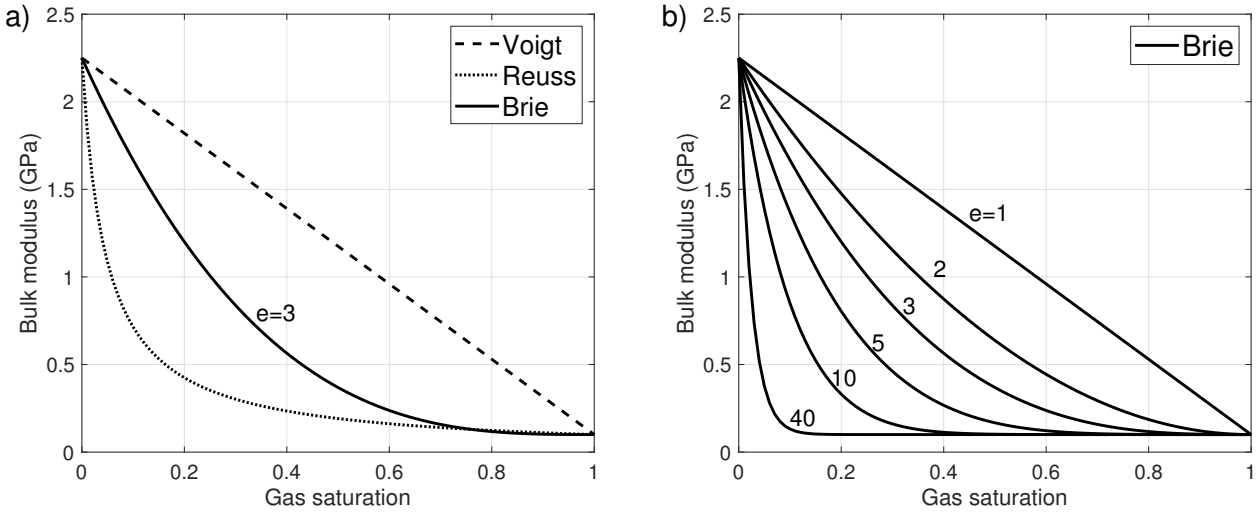

Figure 3.2: (a) Voigt, Reuss, and Brie's mixing laws for a mixture of water and gas. (b) Impact of Brie's empirical constant. In this example, the water bulk modulus is 2.25 GPa and the gas bulk modulus is 0.1 GPa.

3.1.3 Granular media models

A dry rock is a porous rock with no fluid. Alternatively, it can be modeled by setting the fluid moduli and density to zero. The prediction of dry-rock elastic moduli is a relatively complex step in rock physics modeling because it needs to specify the geometric details of how rock constituents are arranged relative to each other. Popular approaches include the approximation of the rock by a random pack of spherical grains, whose elastic properties are determined by the stiffness of grain contacts, and the description of the rock as an elastic solid containing cavities (inclusions) representing the pore space. These two classes of models are referred to as granular media models and inclusion models (Dvorkin, 2004; Grana et al., 2021).

The widely used granular media models include the Hertz–Mindlin model, soft-sand model, and stiff-sand model. The Hertz-Mindlin model (Mindlin, 1949) provides an estimation of the bulk and shear moduli of a dry rock, K_{HM} and μ_{HM}, under the assumption that the rock frame is a random pack of spherical grains, subject to an effective pressure P_{e}, with a given porosity ϕ, and an average number of contacts per grain n (coordination number):

$$K_{\mathrm{HM}} = \left[\frac{n^2(1-\phi)^2\mu_m^2}{18\pi^2(1-\upsilon_m)^2}P_{\mathrm{e}}\right]^{1/3}, \tag{3.9}$$

$$\mu_{\mathrm{HM}} = \frac{2+3f-\upsilon_m(1+3f)}{5(2-\upsilon_m)}\left[\frac{3n^2(1-\phi)^2\mu_m^2}{2\pi^2(1-\upsilon_m)^2}P_{\mathrm{e}}\right]^{1/3}, \tag{3.10}$$

where μ_m and υ_m are the shear modulus and Poisson's ratio of the solid matrix, and f is the degree of adhesion between the grains.

The soft-sand and stiff-sand models (Dvorkin and Nur, 1996) both act as a connector between two endpoints in the porosity–elastic-modulus domain: the zero-porosity endpoint is simply the elastic moduli of the solid matrix, while the high-porosity endpoint is the dry-rock moduli at the critical porosity ϕ_c (about 0.4), estimated by the Hertz-Mindlin model. The soft-sand model connects these two endpoints with a modified Hashin–Shtrikman lower

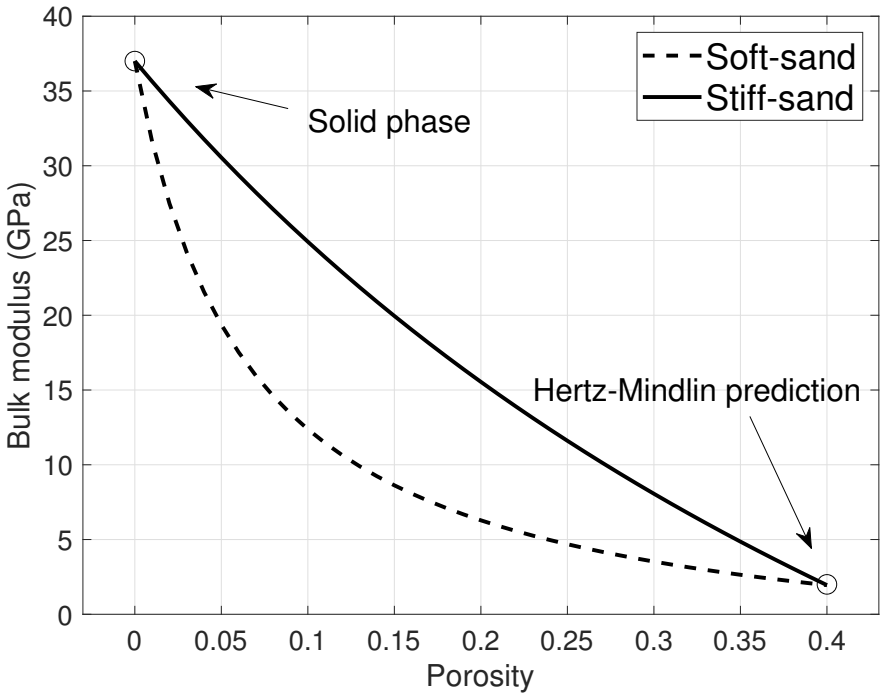

Figure 3.3: Illustration of the soft-sand and stiff-sand models (modified lower and upper Hashin–Shtrikman bounds) for the estimation of dry-rock modulus. The grains are pure quartz, the effective pressure is 20 MPa, the critical porosity is 0.4, and the coordination number is 9.

bound as an interpolator:

$$K_{\rm dry} = \left(\frac{\phi/\phi_c}{K_{\rm HM} + 4/3\mu_{\rm HM}} + \frac{1-\phi/\phi_c}{K_m + 4/3\mu_{\rm HM}} \right)^{-1} - 4/3\mu_{\rm HM}, \tag{3.11}$$

$$\mu_{\rm dry} = \left(\frac{\phi/\phi_c}{\mu_{\rm HM} + \xi} + \frac{1-\phi/\phi_c}{\mu_m + \xi} \right)^{-1} - \xi, \tag{3.12}$$

where

$$\xi = \frac{\mu_{\rm HM}}{6} \frac{9K_{\rm HM} + 8\mu_{\rm HM}}{K_{\rm HM} + 2\mu_{\rm HM}}, \tag{3.13}$$

while the stiff-sand model connects them with a modified Hashin–Shtrikman upper bound as an interpolator:

$$K_{\rm dry} = \left(\frac{\phi/\phi_c}{K_{\rm HM} + 4/3\mu_m} + \frac{1-\phi/\phi_c}{K_m + 4/3\mu_m} \right)^{-1} - 4/3\mu_m, \tag{3.14}$$

$$\mu_{\text{dry}} = \left(\frac{\phi/\phi_c}{\mu_{\text{HM}} + \xi} + \frac{1 - \phi/\phi_c}{\mu_m + \xi} \right)^{-1} - \xi, \tag{3.15}$$

where

$$\xi = \frac{\mu_m}{6} \frac{9K_m + 8\mu_m}{K_m + 2\mu_m}. \tag{3.16}$$

In Figure 3.3, I provide an example for the prediction of dry-rock modulus using the soft-sand and stiff-sand models.

3.1.4 Inclusion models

Most of the granular media models assume that the rock is initially formed by an unconsolidated grain pack at the critical porosity, and then the porosity decreases as a result of either diagenesis or grain sorting. Rather than from the critical porosity, the inclusion models build a rock from the zero-porosity endpoint by placing cavities (inclusions) into the solid matrix (Dvorkin, 2004). While these models are perhaps more relevant to carbonate rocks where the pores appear as inclusions in a calcite or dolomite matrix, they can also be applied to clastic rocks (Grana et al., 2021). Several commonly used inclusion models include the Kuster and Toksöz (KT) model, the self-consistent approximation (SCA) model, and the differential effective medium (DEM) model.

The KT model for predicting the effective elastic moduli, K^* and μ^*, for a variety of inclusion shapes can be written as

$$\begin{aligned} (K^* - K_m) \frac{K_m + \frac{4}{3}\mu_m}{K^* + \frac{4}{3}\mu_m} &= \sum_{i=1}^{N} v_i (K_i - K_m) P_i, \\ (\mu^* - \mu_m) \frac{\mu_m + \xi}{\mu^* + \xi} &= \sum_{i=1}^{N} v_i (\mu_i - \mu_m) Q_i, \end{aligned} \tag{3.17}$$

where

$$\xi = \frac{\mu_m}{6} \frac{9K_m + 8\mu_m}{K_m + 2\mu_m}. \tag{3.18}$$

where subscripts m and f indicate solid and fluid phases, respectively. The summation is over

the different inclusion types with volume fraction v_i and geometric factors P_i and Q_i. Typical inclusion shapes include spheres, needles, disks, and penny cracks. However, arbitrary shapes can be defined by the parameter called "aspect ratio α", and the corresponding P and Q values can be analytically obtained (Berryman, 1995).

Dry rock can be modeled by setting the inclusion moduli to zero. Assuming a single, spherical inclusion type ($\alpha = 1$), the dry-rock elastic moduli are

$$\begin{aligned} K_{\text{dry}} &= \frac{4K_m\mu_m(1-\phi)}{3K_m\phi + 4\mu_m}, \\ \mu_{\text{dry}} &= \frac{\mu_m(9K_m + 8\mu_m)(1-\phi)}{9K_m + 8\mu_m + 6(K_m + 2\mu_m)\phi}. \end{aligned} \tag{3.19}$$

The KT model regards a certain phase in the multiphase medium as a matrix and other phases as inclusions embedded in this infinite background matrix, therefore it is formally limited to the case where inclusions are very sparsely distributed, i.e., low porosity. An alternative model that may apply to slightly higher concentrations of inclusions is the SCA model (Berryman, 1995), which replaces the background matrix with the as-yet-unknown effective medium:

$$\begin{aligned} \sum_{i=1}^{N} v_i(K_i - K^*)P_i = 0, \\ \sum_{i=1}^{N} v_i(\mu_i - \mu^*)Q_i = 0, \end{aligned} \tag{3.20}$$

where the summation is over all phases, including minerals and pores. The equations are coupled and must be solved iteratively.

The DEM model (Zimmerman, 1990) is a coupled system of ordinary differential equations, which is used to simulate two-phase composites by incrementally adding inclusions

(phase 2) to the host material (phase 1)):

$$
\begin{aligned}
(1-y)\frac{d}{dy}[K^*(y)] &= (K_2 - K^*)P_2(y) \\
(1-y)\frac{d}{dy}[\mu^*(y)] &= (\mu_2 - \mu^*)Q_2(y),
\end{aligned}
\tag{3.21}
$$

with initial conditions $K^*(0) = K_1$ and $\mu^*(0) = \mu_1$. The DEM model is different from the SCA model in that it specifies one rock constituent as the host material and the others as inclusions. In Figure 3.4, I compare the dry-rock moduli computed by KT, SCA, and DEM models for two types of pores: a stiff, spherical pore with an aspect ratio of 1 and a more compliant one with an aspect ratio of 0.1. It reveals that the pore shape has a large impact on the elastic properties of the rock. For spherical pores, the inclusion model predictions are generally higher than those of the granular media models. The prediction results of the three inclusion models are very similar when the porosity is less than 0.1, as the porosity increases, they deviate from each other more significantly. For a fixed inclusion shape and porosity, the SCA effective moduli are smaller than the KT and DEM predictions.

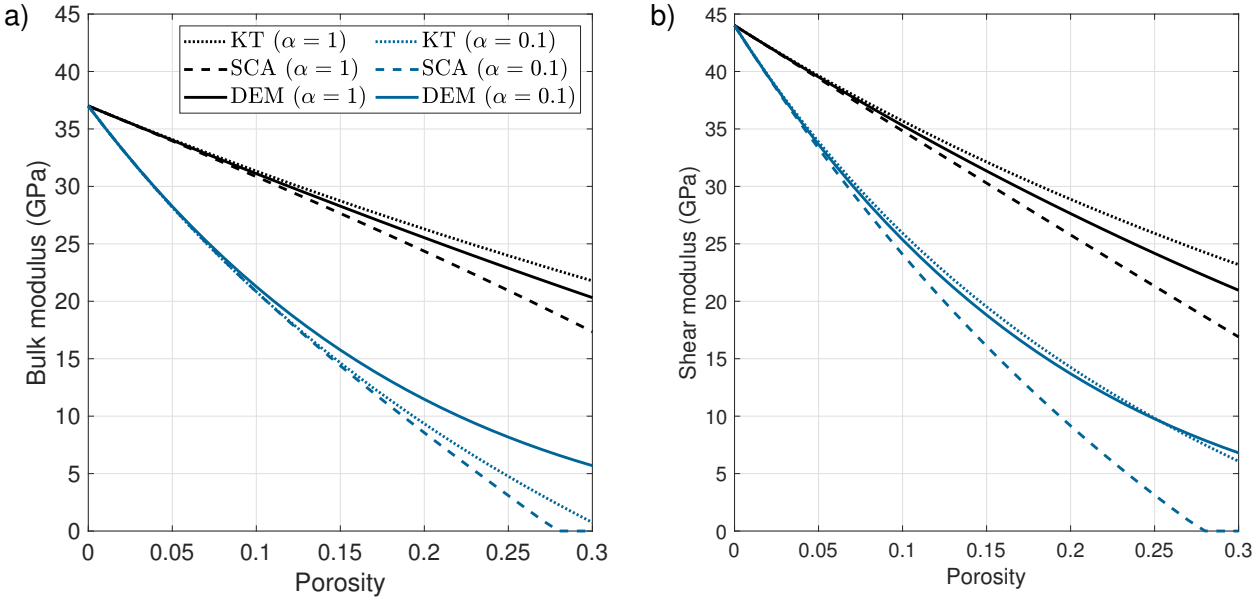

Figure 3.4: Comparison of the KT, SCA, and DEM predictions of the dry-rock (a) bulk modulus and (b) shear modulus. The grains are pure quartz. Two pore shapes, with aspect ratios $\alpha = 1$ and $\alpha = 0.1$, are examined.

Unlike the granular medium model, which is established in the elastic domain of dry rocks, the inclusion models can directly simulate fluid-saturated rocks, only needing to regard the inclusions as fluids. However, an important assumption of the inclusion theory is that the cavities are isolated with respect to flow, resulting in unequilibrated pore pressures (Mavko et al., 2020). Therefore this approach simulates very high-frequency behavior appropriate to ultrasonic laboratory conditions. For low-frequency seismic data applications, it is better to use the inclusion models to compute the dry-rock elastic moduli, and then use Gassmann's equation to include the fluid effect.

3.1.5 Gassmann's equation

Gassmann's equation (Gassmann, 1951; Biot, 1956) is the most common approach to compute the saturated-rock elastic properties. Two of its major applications include predicting the elastic changes when one fluid is replaced with another, a problem called fluid substitution, and predicting saturated-rock moduli from dry-rock moduli. Gassmann's equation assumes that the solid phase is homogeneous, the pore space distribution is statistically isotropic, and that there is sufficient time for the pore fluid to flow and eliminate wave-induced pore-pressure gradients (Mavko et al., 2020). This limitation to low frequencies explains why Gassmann's equation works best for seismic data (<100 Hz) and may perform less well for well-log data ($\approx 10^4$ Hz) and laboratory ultrasonic measurements ($\approx 10^6$ Hz).

According to Gassmann's equation, the shear modulus of the saturated rock $\mu_{\text{sat}} = \mu_{\text{dry}}$, and the bulk modulus of the saturated rock K_{sat} is given by

$$K_{\text{sat}} = K_{\text{dry}} + \frac{(1 - K_{\text{dry}}/K_m)^2}{\phi/K_f + (1-\phi)/K_m - K_{\text{dry}}/K_m^2}, \tag{3.22}$$

where K_m is the solid-matrix bulk modulus, K_f is the fluid bulk modulus, and ϕ is porosity. In Figure 3.5, I provide an example of computing the saturated-rock modulus from the dry-rock modulus using Gassmann's equation. If the water-saturated rock is taken as a reference,

it can be seen from the figure the gas-induced decrease in the elastic modulus of the rock. This reduction in the fluid-saturated rock modulus (and also density) caused by the presence of gas is the basis for our prediction of gas using seismic properties.

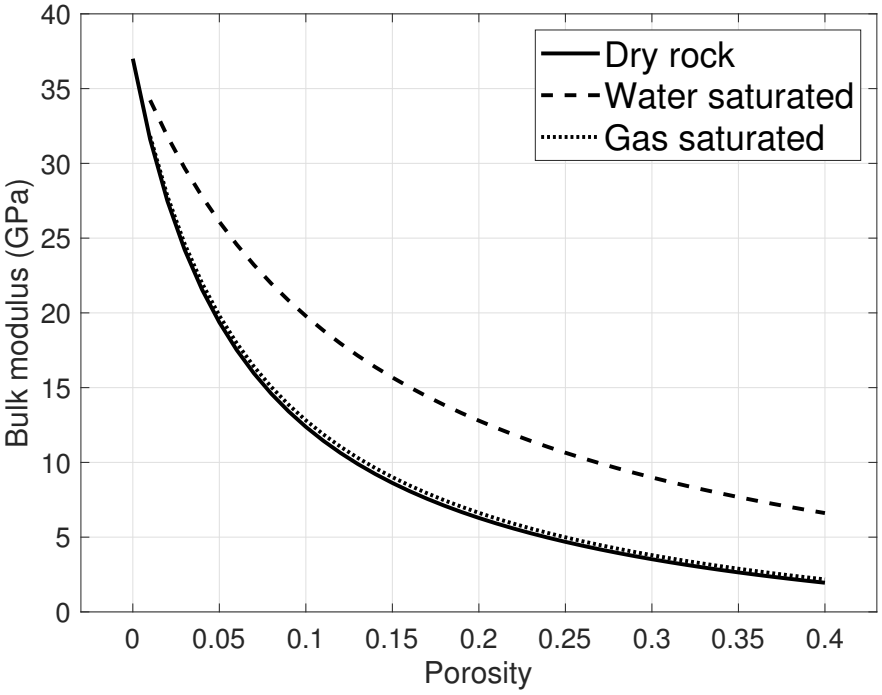

Figure 3.5: Bulk modulus of water-saturated rock and gas-saturated rock computed by Gassmann's equation, based on the dry-rock modulus predicted by the soft-sand model in Figure 3.3.

Eventually, combining those theoretical models to calculate K_{sat} and μ_{sat}, through equations 3.1 and 3.2, we build a rock physics model, f_{RPM}, that links rock physics properties to seismic attributes:

$$(V_{\text{P}}, V_{\text{S}}, \rho) = f_{\text{RPM}}(\text{porosity}, \text{lithology}, \text{saturation}, ...). \tag{3.23}$$

3.2 Global optimization for rock physics inversion

In rock physics inversion, we invert the elastic attributes obtained from seismic inversion to estimate a model of rock properties, such as porosity, lithology, and fluid saturations. Because rock physics models are generally nonlinear, the inverse problem requires nonlinear optimization algorithms, such as gradient-based methods, or global optimization methods, such as simulated annealing and genetic algorithms (Sen and Stoffa, 2013). Unlike gradient-based methods that attempt to find a local minimum in the neighborhood of the starting model, global optimization methods are stochastic in nature, making use of randomness as part of the search procedure. This may increase the probability of locating the global minimum of the objective function. Due to the high cost and large model dimension of forward modeling, global optimization methods are usually not suitable for FWI but can be used for rock physics inversion. One reason is that most rock physics models are analytic, so the forward process is very fast. Another reason is that the inversion is performed in a point-by-point manner, allowing a parallel computation for multiple low-dimensional inverse problems. In this section, I introduce three well-developed global optimization algorithms, including simulated annealing (SA), genetic algorithm (GA), and neighborhood algorithm (NA), for solving the rock physics inverse problem.

The general form of the inverse problem can be written as

$$\mathbf{d} = f_{\mathrm{RPM}}(\mathbf{m}) + \mathbf{e}, \tag{3.24}$$

where the model vector $\mathbf{m}$ contains the rock physics properties to be estimated, the data vector $\mathbf{d}$ contains elastic attributes such as velocity and density, $\mathbf{e}$ is the data error, and f_{RPM} is a nonlinear rock physics model. The optimization aims to minimize the least squared difference between the observed data $\mathbf{d}$ and calculated data $f_{\mathrm{RPM}}(\mathbf{m})$:

$$E(\mathbf{m}) = \frac{1}{2}[(\mathbf{d} - f_{\mathrm{RPM}}(\mathbf{m}))^T C_d^{-1}(\mathbf{d} - f_{\mathrm{RPM}}(\mathbf{m}))], \tag{3.25}$$

where C_d^{-1} is the data covariance matrix, which contains information on data uncertainties.

3.2.1 Simulated Annealing

SA is based on an analogy with the physical process of annealing, which occurs when a solid in a heat bath is initially heated by increasing the temperature such that all the particles are distributed randomly in a liquid phase. This is followed by slow cooling such that all the particles arrange themselves in the low-energy ground state where crystallization occurs. In geophysical inverse problems, the energy function is identified with the objective function. We are interested in finding the state (or model) to minimize this function.

SA is implemented using an algorithm that simulates the physical annealing process. SA based on the Metropolis algorithm can be described as follows (adopted from course materials of Dr. Jan Dettmer):

1) Pick starting model $\mathbf{m}$ with upper and lower bounds for all parameters, and starting temperature T.

2) Perturb $\mathbf{m}$ to $\mathbf{m}'$, therefore, the difference in the energy between the two states $\Delta E = E(\mathbf{m}') - E(\mathbf{m})$.

3) Accept or reject $\mathbf{m}'$ as a new state according to:

   a. if $\Delta E \leq 0$, accept, $\mathbf{m} = \mathbf{m}'$.

   b. if $\Delta E > 0$, draw random number $\xi \sim U(0,1)$.

      i. If $\xi \leq \exp(-\Delta E/T)$, accept, $\mathbf{m} = \mathbf{m}'$.

      ii. if $\xi > \exp(-\Delta E/T)$, reject $\mathbf{m}'$ and return to $\mathbf{m}$.

4) Repeat steps 1 and 2 many times and periodically reduce T by a small amount.

Therefore, SA provides a random walk that always accepts a downhill step (in E) and sometimes accepts an uphill step (allows escape from local minima). As T reduces, the probability of accepting uphill steps decreases, and our search spends more time in regions

of minima, but can climb out. As T approaches zero, the probability of accepting uphill steps also approaches zero, and eventually, no more downhill steps are available, leading SA to converge.

3.2.2 Genetic Algorithm

GA is based on an analogy with the processes of biologic evolution. Unlike SA, an initial population of models is selected at random, and the GA seeks to improve the fitness of the population generation after generation. This is principally accomplished by the genetic processes of selection, crossover, and mutation (Sen and Stoffa, 2013). Also, because GA works with models that are coded in some suitable form, we need to design a coding scheme that represents the model parameters. The basic steps of GA are:

1) Coding. In the simple binary coding scheme, each bit corresponds to a gene that can take a value of 0 or 1, and each individual in the population is completely described by its bit string or chromosome.

2) Selection. Once the fitness (data fit) of each individual model in the population is determined, the selection pairs individual models for reproduction. Models with higher fitness values are more likely to get selected.

3) Crossover. Once the models are selected and paired, crossover allows genetic information between the paired models to be shared. New models will be generated via the exchange of some information between the paired models.

4) Mutation. The mutation is the random alteration of a bit, which represents a random walk in model space.

After mutation, a new population of models is generated, and it often contains new models and some of which are identical to previous models. We then repeat the genetic processes, i.e., from step 2) to step 4), many times to update the population.

3.2.3 Neighborhood Algorithm

NA is proposed by Sambridge (1999), which was motivated by a fundamental question: How can a search for new models be best guided by all previous models for which the forward problem has been solved (and hence the data misfit evaluated)? To address this, NA makes use of the geometrical constructs known as Voronoi cells to derive the search in model space. Each cell is simply the nearest neighbor region of one of the previous samples. For example, the Voronoi cell about point $\mathbf{m}_i$ is given by

$$V(\mathbf{m}_i) = \{\mathbf{x} | \|\mathbf{x} - \mathbf{m}_i\|_2 \leq \|\mathbf{x} - \mathbf{m}_j\|_2 \; for \; j \neq i\}. \tag{3.26}$$

The algorithm uses the spatial properties of Voronoi cells to directly guide the sampling of parameter space. It can be summarized in four steps:

1) Generate an initial set of n_s models uniformly (or otherwise) in parameter space;

2) Calculate the misfit function for the most recently generated a set of n_s models and determine the n_r models with the lowest misfit of all models generated so far;

3) Generate n_s new models by performing a uniform random walk in the Voronoi cell of each of the n_r chosen models (i.e. n_s/n_r samples in each cell);

4) Go to step 2.

The philosophy behind the algorithm is that the misfit of each of the previous models is representative of the region of space in its neighborhood (defined by its Voronoi cell). Therefore at each iteration, new samples are concentrated in the neighborhoods surrounding the better data-fitting models. In this way, the algorithm exploits the information contained in the previous models to adapt the sampling.

3.2.4 Numerical Examples

For all of the numerical tests carried out in this section, I assume a rock frame consisting of quartz and clay saturated with water and gas, therefore I define three model unknowns: porosity, clay content, and water saturation $(\phi, C, S_{\mathrm{w}})$. The input data are P-wave velocity, S-wave velocity, and density $(V_{\mathrm{P}}, V_{\mathrm{S}}, \rho)$. The rock physics relation used to connect the model and data vectors is the KT model, namely $(V_{\mathrm{P}}, V_{\mathrm{S}}, \rho) = f_{\mathrm{KT}}(\phi, C, S_{\mathrm{w}})$. First, I conduct a single-point test to compare the convergence of SA, GA, and NA. Next, I test the algorithm on synthetic well logs to check how errors in the input data would affect the inversion. Finally, I combine EFWI for elastic attributes and the global optimization scheme to predict the spatial distribution of rock physics properties.

Convergence properties

I consider a sample with porosity, clay content, and water saturation of 0.1, 0.2, and 0.3, respectively. The corresponding elastic parameters, P-wave velocity, S-wave velocity, and density, are computed by rock physics modeling and used as input data. The ranges of possible values in model space are $0 \leq \phi \leq 0.4$, $0 \leq C \leq 1$, and $0 \leq S_{\mathrm{w}} \leq 1$. I try to avoid exhaustive testing and do not expect the values to be perfect. If an extremely large number of random walks is allowed, each algorithm can resemble a grid-search method, which involves searching through every point in the model space, but this is not usually a practical approach.

Figure 3.6 shows the evolution of data misfit and the inverted model using Metropolis SA. I employ a cooling schedule $T_k = T_0(0.9)^k$, where T_0 is the starting temperature and k is the temperature step (or iteration number). The starting temperature $T_0 = 200$ is picked so that most random walks are accepted at the beginning of the simulation. As the temperature reduces, the probability of accepting uphill steps decreases. Eventually, the algorithm converges to near the global optimal solution within 250 iterations. The porosity and clay contents are correctly estimated, whereas the inverted water saturation deviates

from its true value.

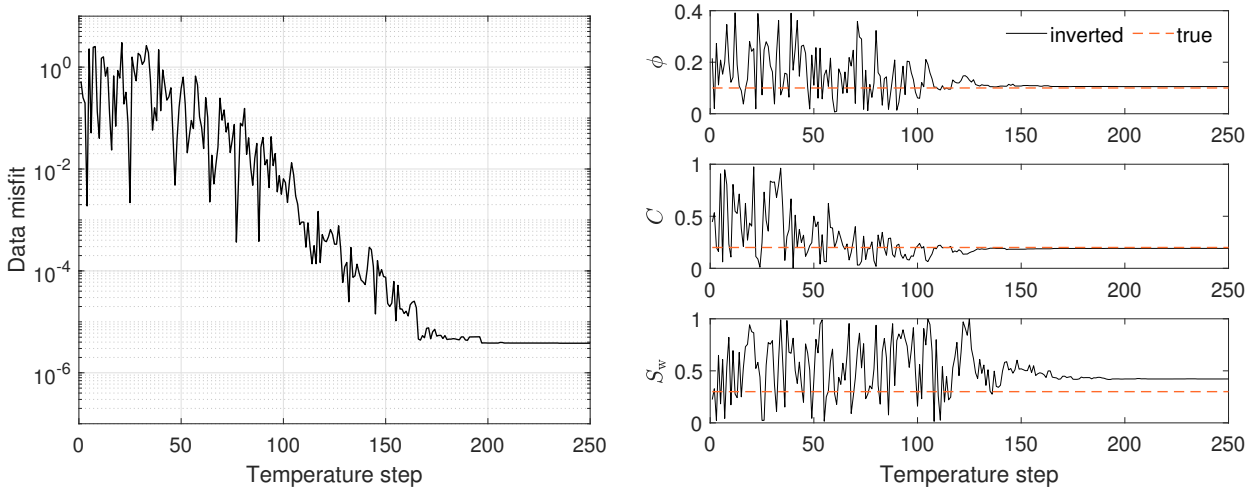

(a) (b)

Figure 3.6: Simulation results using simulated annealing. Variations of (a) data misfit and (b) inverted models as a function of temperature.

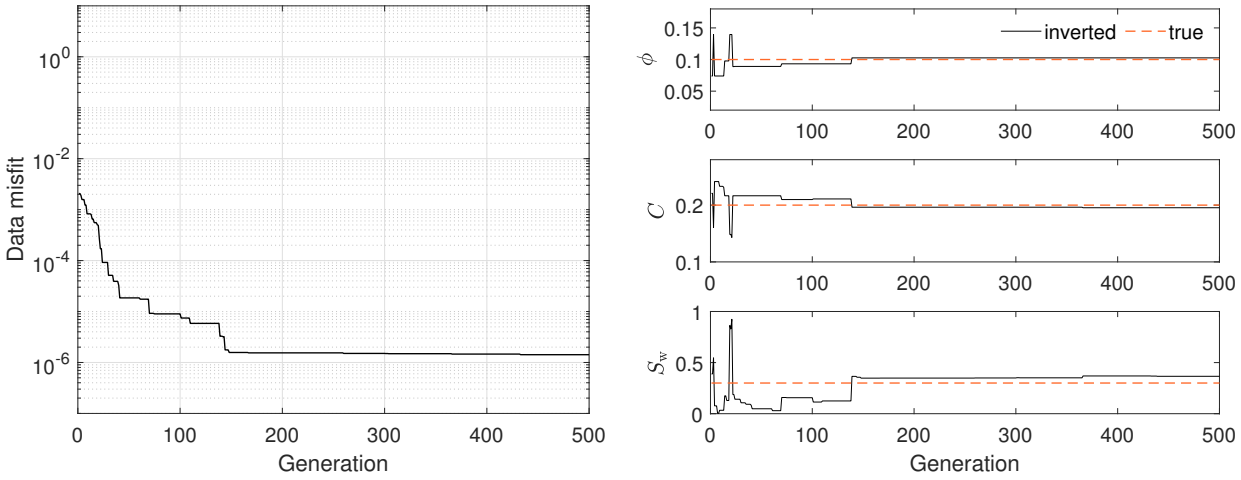

(a) (b)

Figure 3.7: Simulation results using a genetic algorithm. Evolution of (a) data misfit and (b) the best-fit model.

Figure 3.7 shows the simulation process using GA. I use a population size of 100 models, a crossover probability of 0.5, and a mutation probability of 0.5. Unlike the SA curve where an uphill step is allowed, in GA the best-fit model of the current generation is saved for the next generation, making GA always converge toward models with lower data misfits. The

best-fit model is reasonably accurate after 200 iterations.

Figure 3.8 illustrates the process of searching the model space using NA. At each iteration, the NA generates 200 samples of a uniform random walk inside each of the Voronoi cells of the current five best models (i.e. $ns = 200$, $nr = 5$). The initial 200 samples are generated randomly. As the algorithm proceeds, the information in the misfit surface is exploited to concentrate sampling in the regions where the misfit is low. Consequently, the porosity and clay content are well estimated, with only one main minimum located close to the true value in the $\phi - C$ space. However, the water saturation is not well estimated, displaying several local minima.

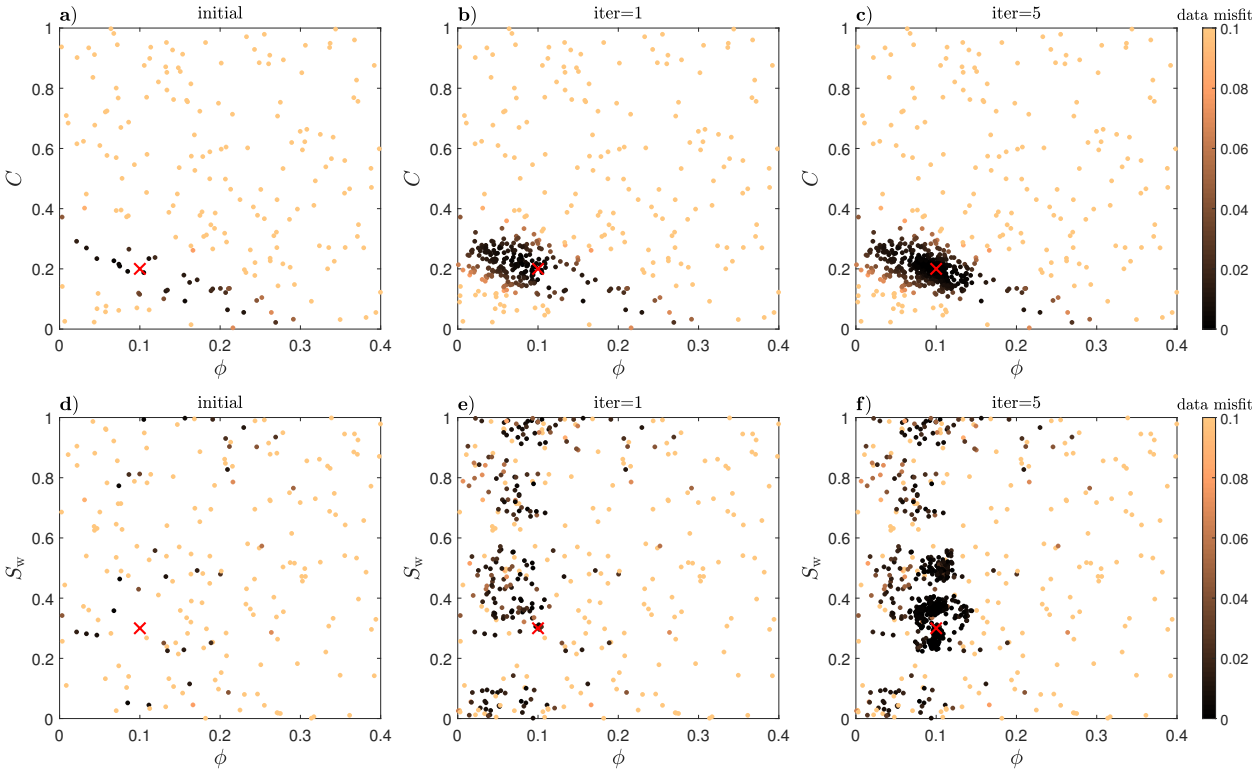

Figure 3.8: Simulation results using a neighborhood algorithm. The dots represent the models produced by NA and are color-coded by data misfit. The red cross marks the true model.

We observe in the preceding example that water saturation is more difficult to estimate than porosity and clay content. This is explained in Figure 3.9. The rock physics template is generated by fixing C and calculating the velocity and density for each combination of ϕ and S_{w}. It illustrates that V_{P} and ρ are far more sensitive to ϕ than to S_{w} (note that the S_{w} is given a wider range). The contour plot reveals that the misfit function has a flat trough with respect to S_{w}.

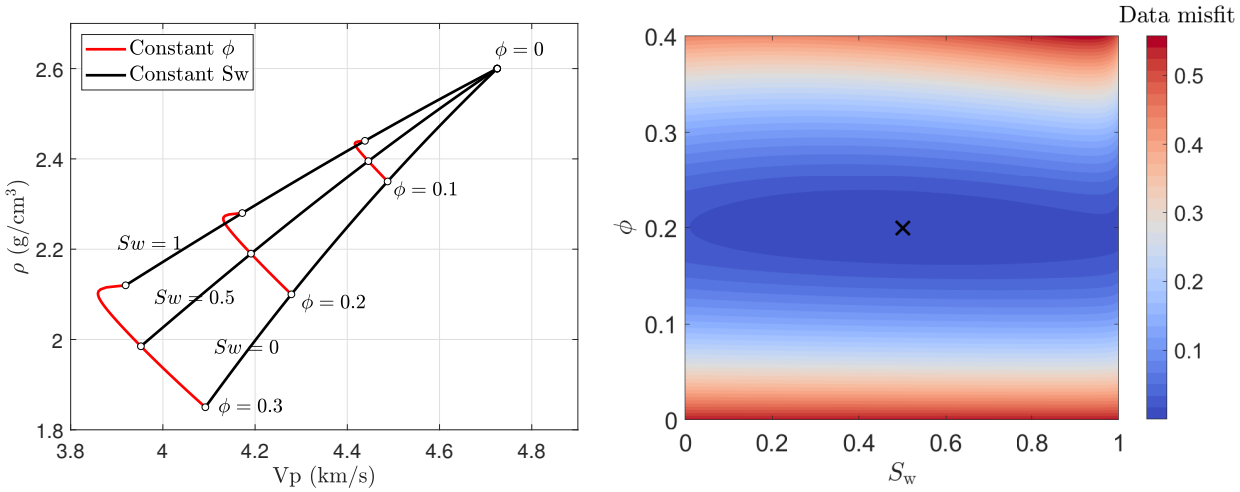

(a) (b)

Figure 3.9: Sensitivity study. Variations of (a) velocity and density and (b) data misfit as a function of porosity and water saturation.

I compare the three algorithms in Figure 3.10, where the misfit function is plotted against the number of models for which the forward problem has been solved. There are three runs in each case. I note that the misfit reduction of NA has a more favorable character, exhibiting more large steps in the early stage. As a result, two of the three NA curves have lower data misfits than the best SA and GA curves. Therefore, with the specific details I design for the three algorithms, NA is the most efficient and is therefore selected for my further study on larger models.

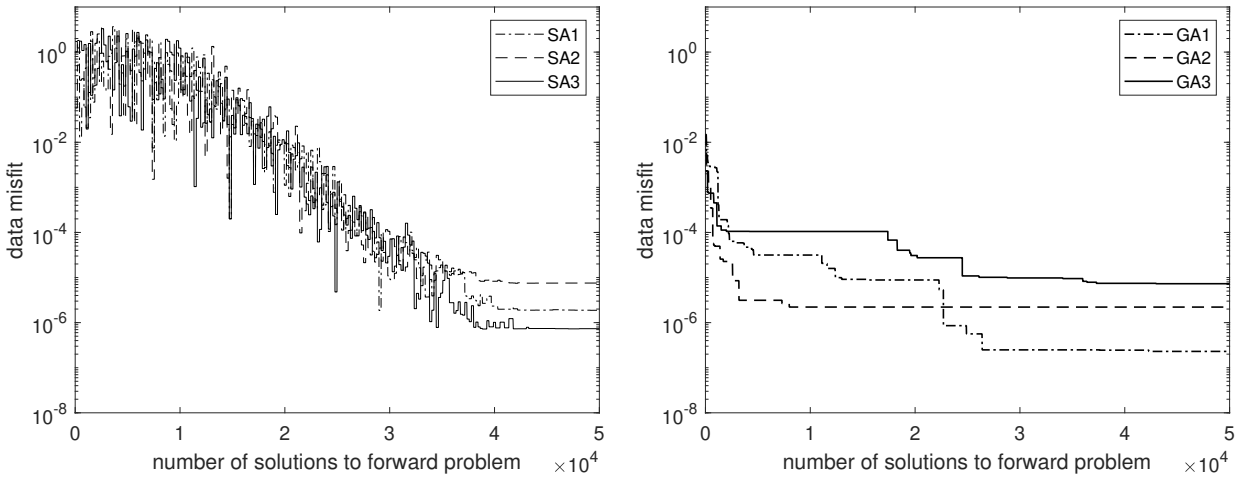

(a)

(b)

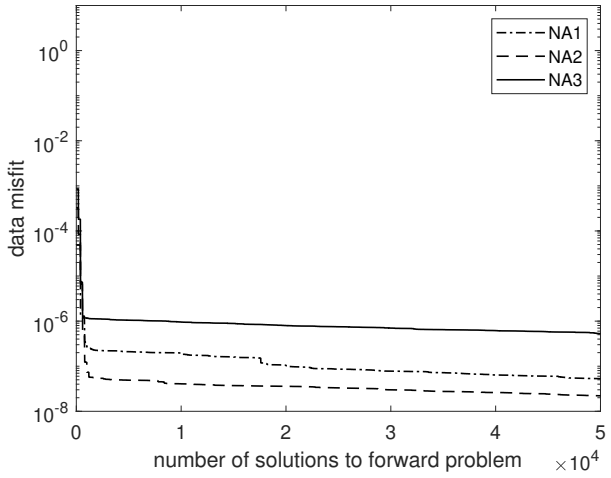

(c)

Figure 3.10: Convergence properties for three runs of (a) simulated annealing, (b) genetic algorithm, and (c) neighborhood algorithm.

Inversion stability

To test the inversion stability, I generate synthetic well-logs of ϕ, C, and S_{w}, and use them to compute the velocity and density logs based on the KT model. These logs are denoted by the black solid lines in Figure 3.11. If the exact velocity and density logs are used as input data for rock physics inversion, the ϕ and C logs can be accurately reconstructed, whereas the S_{w} estimate exhibits visible oscillation around the true model. Still, this is due to the very low sensitivity of velocity and density to S_{w}. Nonetheless, the S_{w} estimate is acceptable since it captures the major structures.

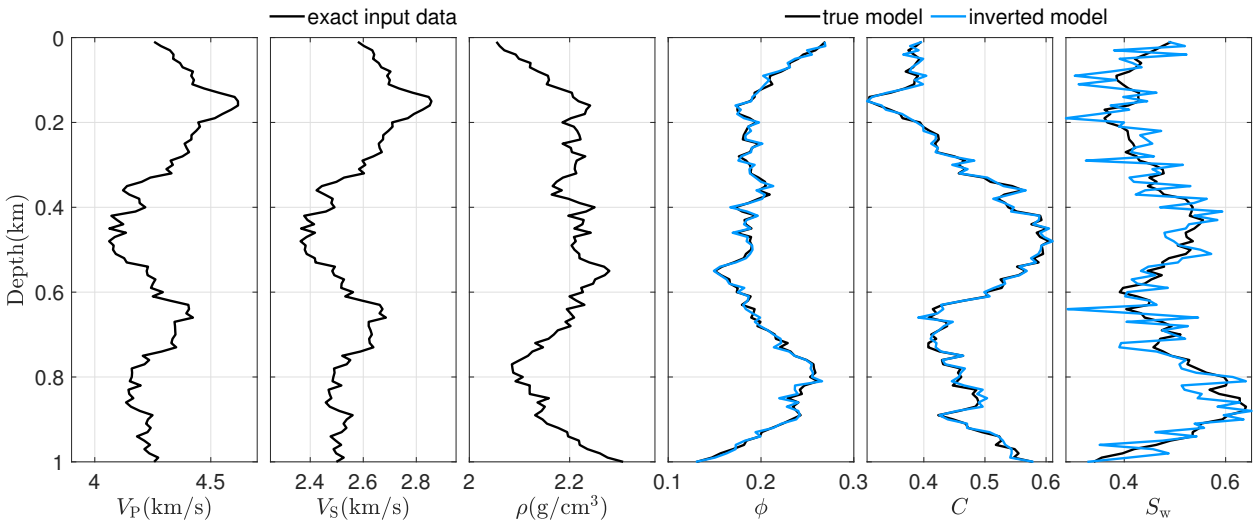

Figure 3.11: Test with noise-free data. The back lines denote the true models and the blue lines denote the inverted models. The true elastic models are used as input data for the rock physics inversion.

However, after we add some mild Gaussian noise to the input data, as denoted by the black dashed line in Figure 3.12, the inverted rock physics properties become far from satisfactory. The relatively small errors as they appear in the elastic model are magnified significantly in the ϕ, C, and S_{w} recoveries. The S_{w} estimate appears to fair the worst, covering the entire search space. I conclude that the simultaneous inversion of the three rock physics parameters is ill-conditioned (i.e., lack of stability and robustness), as the model is very sensitive to errors in the data.

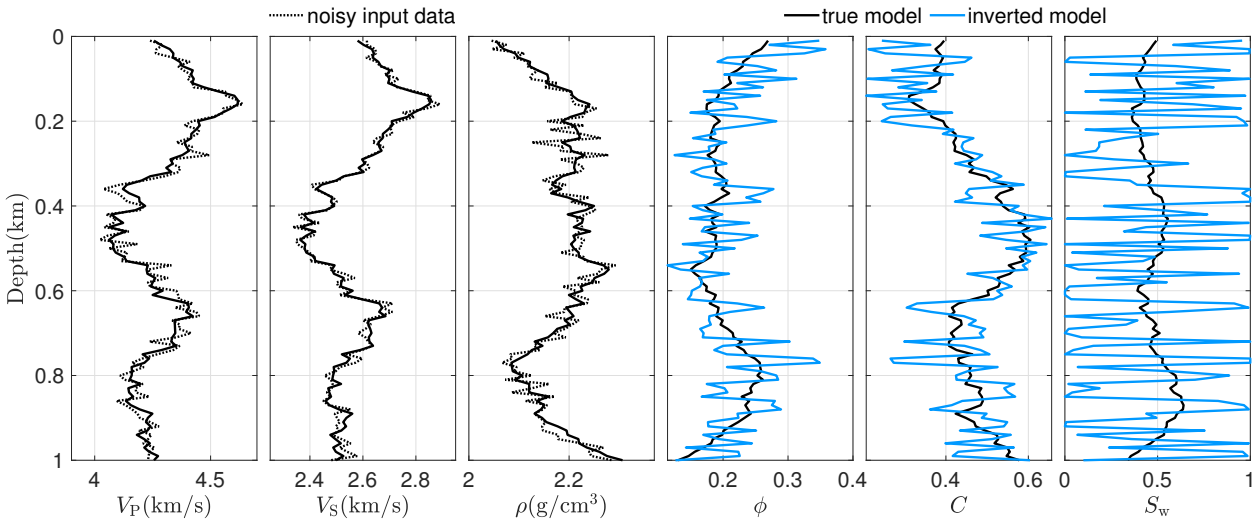

Figure 3.12: Test with noisy data. Mild Gaussian noises are added to the elastic models, as denoted by the black dashed lines. The blue lines represent the inverted models.

Given that it is difficult to retrieve the whole set of (ϕ, C, S_w) from noisy data, I treat S_w as an a priori parameter rather than an unknown variable, and only update ϕ and C. The result is shown in Figure 3.13. Although the prior S_w has a large error, we observe a significant improvement in the ϕ and C recoveries, which exhibit mild oscillation around the true model.

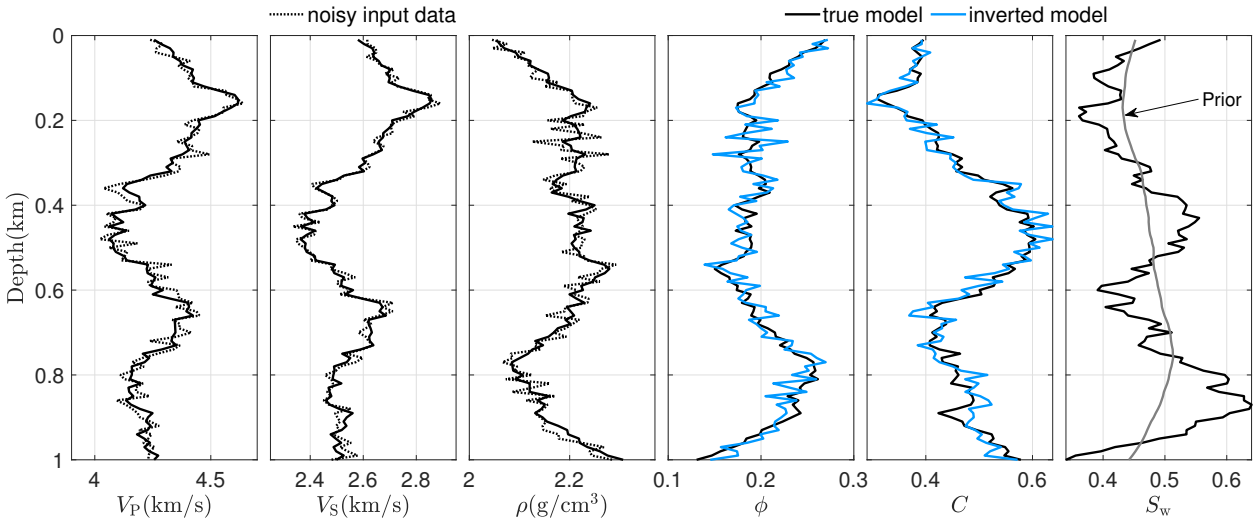

Figure 3.13: Test with noisy data. Only porosity and clay content are inverted, with water saturation fixed with erroneous values.

FWI models as input

Finally, I present a synthetic example to combine EFWI with rock physics using global optimization methods. For the EFWI algorithm, a 2D, frequency-domain, three-parameter elastic inversion is set up. I select a 1 km $\times$ 1 km part of the elastic Marmousi2 model and assign rock property values to each cell. Figure 3.14 shows the true elastic model, the initial model which is a smoothed version of the true model, and the EFWI result. The recovered model slightly underestimates the deep part of the model, but overall has a good agreement with the true one. These recovered models are next used as input data for rock physics inversion.

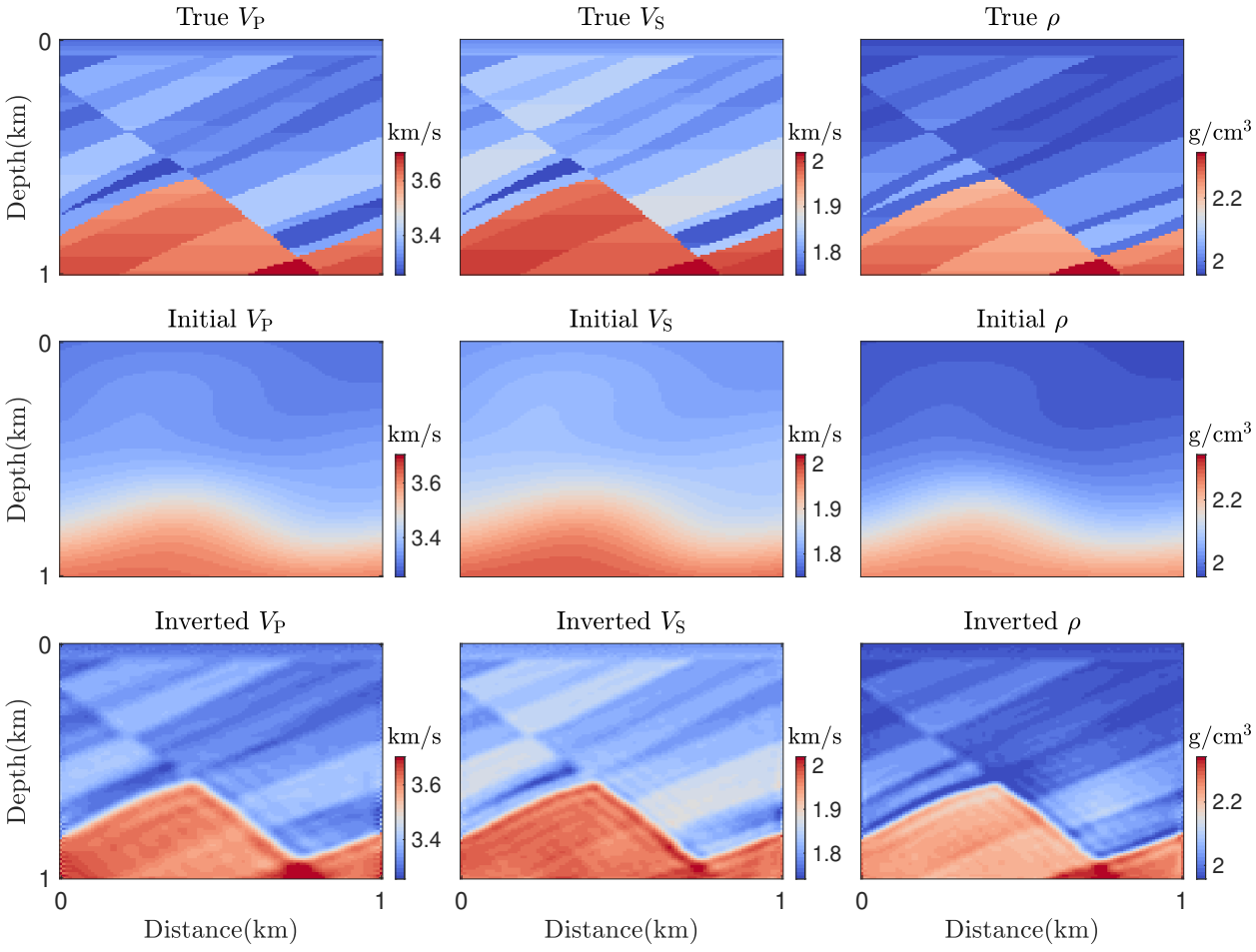

Figure 3.14: True, initial, and inverted models of P-wave velocity, S-wave velocity, and density.

Figure 3.15 plots the true and inverted rock property models. Also, I treat a coarse S_{w} model as prior information, which will not be updated in the inversion. The structure and values of the porosity model are well recovered, whereas the clay content model is more contaminated by artifacts.

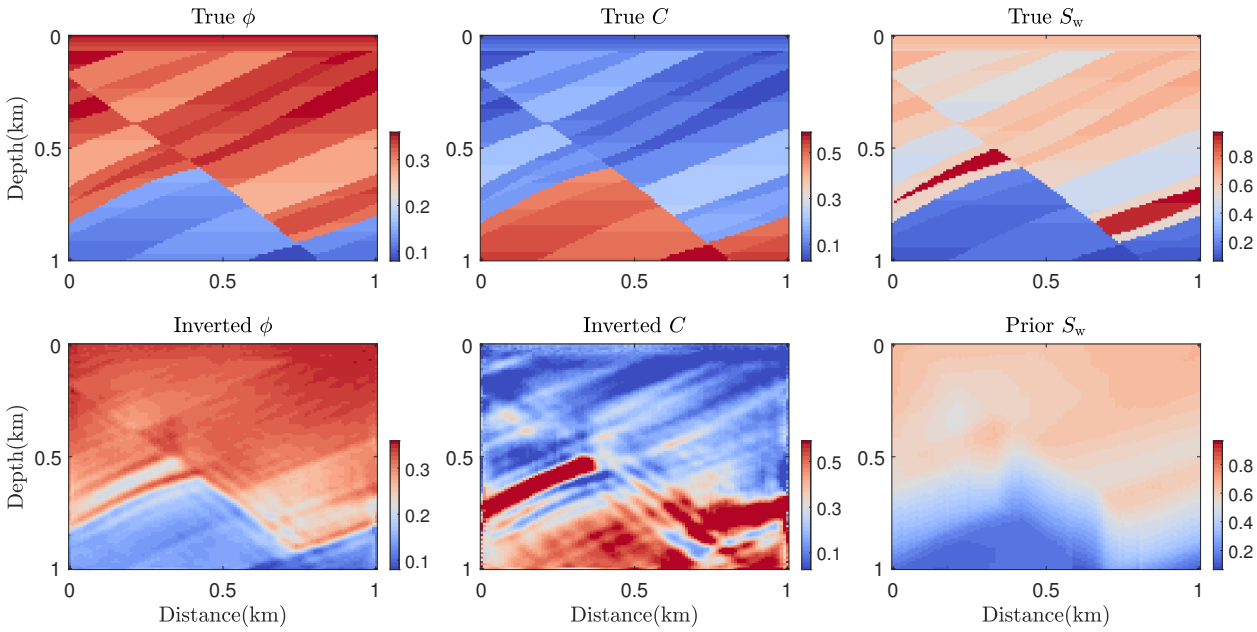

Figure 3.15: True and inverted rock property models.

3.2.5 Conclusions

In this work, I studied three global optimization methods: simulated annealing, genetic algorithm, and neighborhood algorithm for a rock physics inversion problem: estimating porosity, clay content, and water saturation from velocities and density. It is illustrated that the neighborhood algorithm is more efficient in reducing data misfits for the experiment I set up, however, this conclusion may vary with user-defined parameters of the algorithms. I also illustrate that the simultaneous inversion of porosity, clay content, and water saturation is ill-conditioned, because the results are very sensitive to data errors. Removing less sensitive parameters like fluid saturation from the inversion stabilizes the inversion, but also makes us lose access to fluid information. My conclusion is that the inversion of multiple rock

physics parameters cannot only rely on data residuals, and needs to be combined with certain prior information of the model. This prior information can be added through regularization techniques or Bayesian methods.

3.3 Bayesian rock physics inversion

Bayesian rock physics inversion refers to a set of probabilistic methods for the prediction of rock physics properties from elastic attributes, based on different statistical assumptions for the model variables (Grana et al., 2021). The solution is represented by the posterior distribution of rock physics properties $\mathbf{m}$ conditioned on the elastic data $\mathbf{d}$:

$$P(\mathbf{m}|\mathbf{d}) = \frac{P(\mathbf{m},\mathbf{d})}{\int P(\mathbf{m},\mathbf{d})d\mathbf{m}} = \frac{P(\mathbf{d}|\mathbf{m})P(\mathbf{m})}{\int P(\mathbf{d}|\mathbf{m})P(\mathbf{m})d\mathbf{m}}, \tag{3.27}$$

where $P(\mathbf{m},\mathbf{d})$ is the joint distribution of the rock and elastic properties, $P(\mathbf{m})$ is the prior distribution, and $P(\mathbf{d}|\mathbf{m})$ is the likelihood function of the data.

Under some restrictive assumptions, we can derive a closed-form solution of equation 3.27 and significantly reduce the computational cost. These assumptions generally include that the forward model is linear, the prior distribution is Gaussian, and the data error term is Gaussian (Buland and Omre, 2003; Tarantola, 2005; Grana, 2016a). However, the Gaussian assumption is not valid in many applications, where the lithofacies are complex and the rock properties are multimodal. Also, the linearization of the rock physics model might fail for highly nonlinear models. Grana and Rossa (2010) extend the Bayesian approach to Gaussian mixture models (GMM), which allow modeling each lithofacies as a single Gaussian component of the mixture. Moreover, the analytical results valid for Gaussian distributions can be extended to Gaussian mixtures, provided the rock physics model is not too far from linearity. If these assumptions with respect to the forward model and prior distribution are not in agreement with well-log data, the posterior distribution must be evaluated numerically.

In this case, Bayesian approaches based on kernel density estimation have been proposed in Mukerji et al. (2001), Doyen (2007), and Grana and Rossa (2010), where the joint distribution of model and data is described by a non-parametric probability density function (PDF). Compared to the GMM approach, the non-parametric approach is more computationally demanding and it requires tuning of the kernel widths.

This study examines the three Bayesian approaches (Gaussian, Gaussian mixture, and non-parametric) using an actual set of well-log data. I first describe the methods and then present their applications.

3.3.1 Gaussian linear inversion

Grana (2016a) proposes a mathematical approach for the linearization of slightly nonlinear rock physics models, using first-order Taylor series approximations:

$$\mathbf{d} \approx f_{\text{RPM}}(\mathbf{m_0}) + \mathbf{J_{m_0}}(\mathbf{m} - \mathbf{m_0}) + \mathbf{e} \tag{3.28}$$

where $\mathbf{J_{m_0}}$ is the Jacobian of the function f_{RPM} evaluated at the value $\mathbf{m_0}$, which can be the mean of the prior distribution. Equation 3.28 can be rewritten as

$$\mathbf{d} \approx \mathbf{J_{m_0}}\mathbf{m} + f_{\text{RPM}}(\mathbf{m_0}) - \mathbf{J_{m_0}}\mathbf{m_0} + \mathbf{e} = \mathbf{G}\mathbf{m} + \mathbf{c} + \mathbf{e}, \tag{3.29}$$

where $\mathbf{G} = \mathbf{J_{m_0}}$ is the linearized rock physics model and $\mathbf{c} = f_{\text{RPM}}(\mathbf{m_0}) - \mathbf{J_{m_0}}\mathbf{m_0}$ is a constant.

If we assume that the model $\mathbf{m}$ is Gaussian distributed $\mathcal{N}(\boldsymbol{\mu}_m, \boldsymbol{\Sigma}_m)$ and the data error ϵ is Gaussian $\mathcal{N}(\mathbf{0}, \boldsymbol{\Sigma}_e)$, then the posterior distribution $P(\mathbf{m}|\mathbf{d})$ is also Gaussian $\mathcal{N}(\boldsymbol{\mu}_{m|d}, \boldsymbol{\Sigma}_{m|d})$, and it can be analytically estimated through the following expressions for the conditional

mean and covariance:

$$\begin{aligned}\boldsymbol{\mu}_{m|d} &= \boldsymbol{\mu}_m + \boldsymbol{\Sigma}_m \mathbf{G}^T (\mathbf{G}\boldsymbol{\Sigma}_m \mathbf{G}^T + \boldsymbol{\Sigma}_e)^{-1} (\mathbf{d} - \mathbf{G}\boldsymbol{\mu}_m) \\ \boldsymbol{\Sigma}_{m|d} &= \boldsymbol{\Sigma}_m - \boldsymbol{\Sigma}_m \mathbf{G} (\mathbf{G}^T \boldsymbol{\Sigma}_m \mathbf{G}^T + \boldsymbol{\Sigma}_e)^{-1} - \mathbf{G}\boldsymbol{\Sigma}_m.\end{aligned} \tag{3.30}$$

The mathematical derivation of these expressions can be found in Tarantola (2005). The main limitation of this approach is the Gaussian (unimodal) assumption of the model properties. Many rock properties in the subsurface, for example, porosity and fluid saturation, are multimodal. In addition, owing to the linearization of the rock physics operator, this approach may fail for highly nonlinear models.

3.3.2 Gaussian mixture approach

In many applications, the multimodal behavior of rock properties can be approximated by Gaussian mixture distributions, i.e. linear combinations of Gaussian distributions:

$$P(\mathbf{m}) = \sum_{k=1}^{N_f} \lambda_k \mathcal{N}(\mathbf{m}; \boldsymbol{\mu}_m^k, \boldsymbol{\Sigma}_m^k), \tag{3.31}$$

where the distributions $\mathcal{N}(\mathbf{m}; \boldsymbol{\mu}_m^k, \boldsymbol{\Sigma}_m^k)$ represent the k^{th} Gaussian component and the coefficients λ_k represent the weights of the linear combination. One of the advantages of Gaussian mixture models in geophysical applications is the possibility to identify the components of the mixtures with facies classifications.

For nonlinear rock physics models, Grana and Rossa (2010) propose a semi-analytical approach based on Monte Carlo simulations. According to this approach, we randomly sample the prior distribution (equation 3.31) and apply the rock physics model to obtain the corresponding set of elastic properties $\mathbf{d}$. We then use these samples as a training dataset to estimate the joint distribution of rock and elastic properties assuming a Gaussian mixture

distribution:

$$P(\mathbf{m},\mathbf{d}) = \sum_{k=1}^{N_f} \lambda_k \mathcal{N}(\mathbf{y}; \boldsymbol{\mu}_y^k, \boldsymbol{\Sigma}_y^k), \tag{3.32}$$

where $\mathbf{y} = (\mathbf{m}, \mathbf{d})$. The joint mean and covariance of each component are given by

$$\boldsymbol{\mu}_y^k = \begin{bmatrix} \boldsymbol{\mu}_m^k \\ \boldsymbol{\mu}_d^k \end{bmatrix}, \quad \boldsymbol{\Sigma}_y^k = \begin{bmatrix} \boldsymbol{\Sigma}_{m,m}^k & \boldsymbol{\Sigma}_{m,d}^k \\ \boldsymbol{\Sigma}_{d,m}^k & \boldsymbol{\Sigma}_{d,d}^k \end{bmatrix}, \tag{3.33}$$

These quantities of the joint distribution can be inferred from the training dataset using maximum likelihood estimation methods such as the expectation-maximization algorithm. Then the conditional distribution $P(\mathbf{m}|\mathbf{d})$ is again a Gaussian mixture:

$$P(\mathbf{m}|\mathbf{d}) = \sum_{k=1}^{N_f} \lambda_k^{'} \mathcal{N}(\mathbf{m}; \boldsymbol{\mu}_{m|d}^k, \boldsymbol{\Sigma}_{m|d}^k), \tag{3.34}$$

with conditional mean and covariance are given by

$$\begin{aligned} \boldsymbol{\mu}_{m|d}^k &= \boldsymbol{\mu}_m^k + \boldsymbol{\Sigma}_{m,d}^k (\boldsymbol{\Sigma}_{d,d}^k)^{-1} (\mathbf{d} - \boldsymbol{\mu}_d^k) \\ \boldsymbol{\Sigma}_{m|d}^k &= \boldsymbol{\Sigma}_{m,m}^k - \boldsymbol{\Sigma}_{m,d}^k (\boldsymbol{\Sigma}_{d,d}^k)^{-1} \boldsymbol{\Sigma}_{d,m}^k. \end{aligned} \tag{3.35}$$

This approach is robust when the rock physics model is not highly nonlinear.

3.3.3 Kernel density estimation

If the assumptions for the aforementioned approaches are not in agreement with well-log data, a non-parametric approach for the conditional probability estimation $P(\mathbf{m}|\mathbf{d})$ should be adopted. Kernel density estimation is a non-parametric technique that allows us to estimate the probability distribution by fitting a base function at each data point including only those observations close to it.

Let $\mathbf{m} = (m_1, ..., m_M)$ represent a model vector with M variables, for instance, $M = 3$ when the model consists of porosity, clay content, and water saturation at a single point,

$\mathbf{d} = (d_1, ..., d_D)$ represent a data vector with D parameters, for instance, $D = 3$ when using the P- and S-wave velocities plus density at the same point as input data, and $\{\mathbf{m}_i, \mathbf{d}_i\}_{i=1,...,N_s}$ represent the set of N_s Monte Carlo samples, then the joint distribution $P(\mathbf{m}, \mathbf{d})$ can be estimated as

$$P(\mathbf{m}, \mathbf{d}) = \frac{1}{N_s \prod_{u=1}^{M} h_{m_u} \prod_{v=1}^{D} h_{d_v}} \sum_{i=1}^{N_s} \prod_{u=1}^{M} \kappa\left(\frac{m_u - m_{u_i}}{h_{m_u}}\right) \prod_{v=1}^{D} \kappa\left(\frac{d_v - d_{v_i}}{h_{d_v}}\right), \tag{3.36}$$

where κ is the kernel function, such as the Gaussian kernel and the Epanechnikov kernel, and $\mathbf{h}_m$ and $\mathbf{h}_d$ are the vectors of kernel bandwidths of each variable (Grana et al., 2021). Then, the conditional distribution $P(\mathbf{m}|\mathbf{d})$ can be numerically evaluated using equation 3.27. Because the joint and conditional distributions are numerically evaluated in a discretized domain for all the possible combinations of $(\mathbf{m}, \mathbf{d})$, one of the limitations of the proposed approach is the memory requirement for the fine discretization of the model and data domains.

3.3.4 Examples

I present the application of the method to well-log data analysis. The well logs in this example were measured in the Countess 10-22 well at the Carbon Management Canada (CMC) Newell County Facility, located in Southwest Brooks, Alberta. The well was drilled to a depth of 550 m, with the shallow stratigraphy composed of interbedded mudstone, fine-grained sandstone, and uncleated coals (Lawton et al., 2019). A comprehensive log suite including a dipole sonic log was acquired at the well. The wireline logs were further studied using Schlumberger's elemental log analysis (ELAN) which provided depth profiles of porosity and lithology parameters.

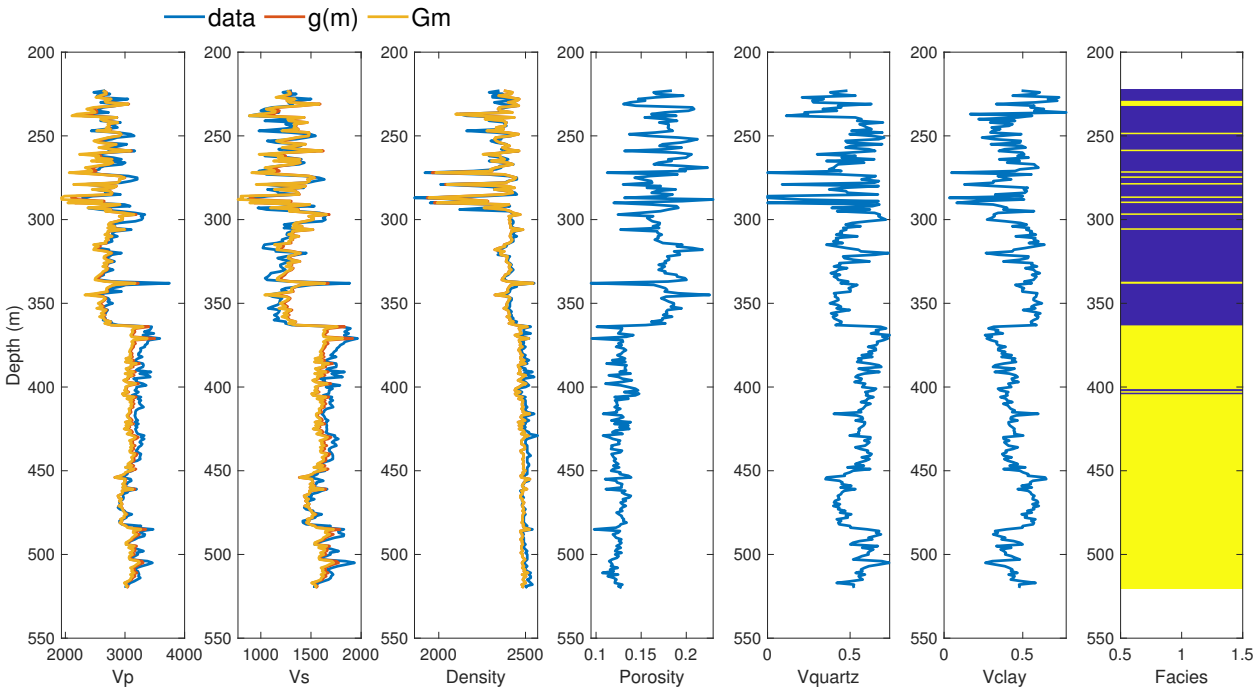

Figure 3.16: Well-log data of the Countess 10-22 well at the CMC Newell County Facility. From left to right: P-wave velocity, S-wave velocity, density, porosity, and the volume fractions of quartz and clay. The blue, red, and yellow curves denote the real data, the data predicted by the nonlinear rock physics model, and the data predicted by the linearized rock physics model. The rightmost column shows the result of facies classification based on the measured data, assuming two facies.

Figure 3.16 plots the well logs of velocities, density, porosity (ϕ), and the volume fractions of quartz (V_{qu}) and clay (V_{cl}) within the depth interval 220m-530m. I construct a rock physics model combining the soft-sand model and Gassmann's equation to link the elastic and rock property logs. The rock physics model f_{RPM} can be written as

$$(V_{\mathrm{P}}, V_{\mathrm{S}}, \rho) = f_{\mathrm{RPM}}(\phi, V_{\mathrm{qu}}, V_{\mathrm{cl}}, V_{\mathrm{co}}, P_e), \tag{3.37}$$

where V_{co} is the coal volume and $V_{\mathrm{qu}} + V_{\mathrm{cl}} + V_{\mathrm{co}} = 1$. The brine saturation was assumed to be 100%, according to Macquet et al. (2019). The effective pressure P_e initially used in

rock physics modeling increases linearly with depth. However, using an average pressure value of 5 MPa, we can still obtain a good match between the predicted and measured logs. Therefore, I simplify the rock physics model by reducing the number of unknown variables:

$$(V_{\mathrm{P}}, V_{\mathrm{S}}, \rho) = f_{\mathrm{RPM}}(\phi, V_{\mathrm{qu}}, V_{\mathrm{cl}}), \tag{3.38}$$

The implementation of the linear Bayesian approach requires the linearization of the rock physics model. In Figure 3.16, we notice that the linearized model approximates the exact rock physics model very well.

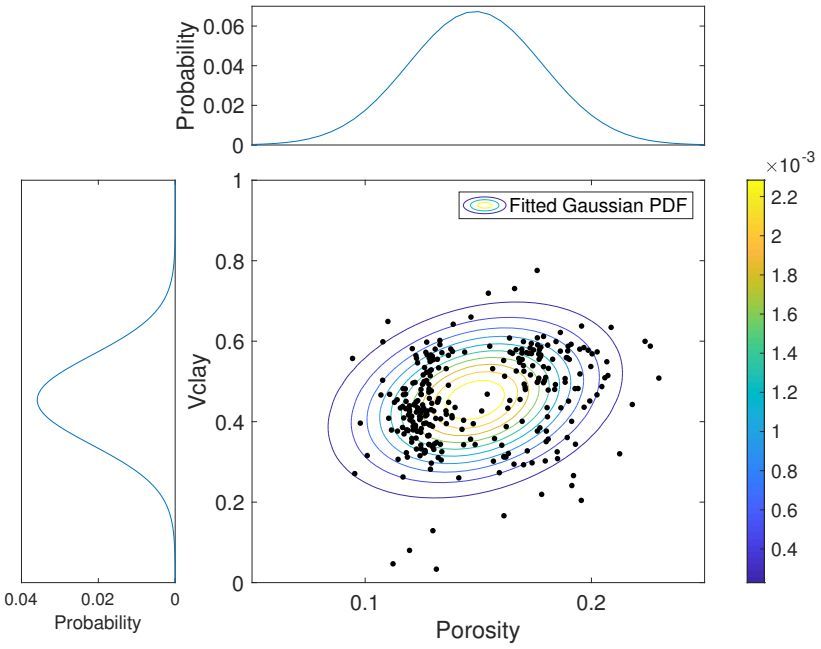

Figure 3.17: Prior distribution of rock physics variables: Gaussian case. The curves represent the 2D joint distribution of porosity and clay content with associated 1D marginal distribution, obtained by fitting the well-log data (black dots).

Figures 3.17-3.19 show the parametric and non-parametric distributions fitted to the well-log data of the rock physics properties. For illustration purposes, I only display the bivariate projections in the domain of porosity and clay content. I assume a Gaussian mixture distribution of two components, corresponding to high-porosity sand and low-porosity shale, based on the result of facies classification at the well (Figure 3.16); Compared to the Gaus-

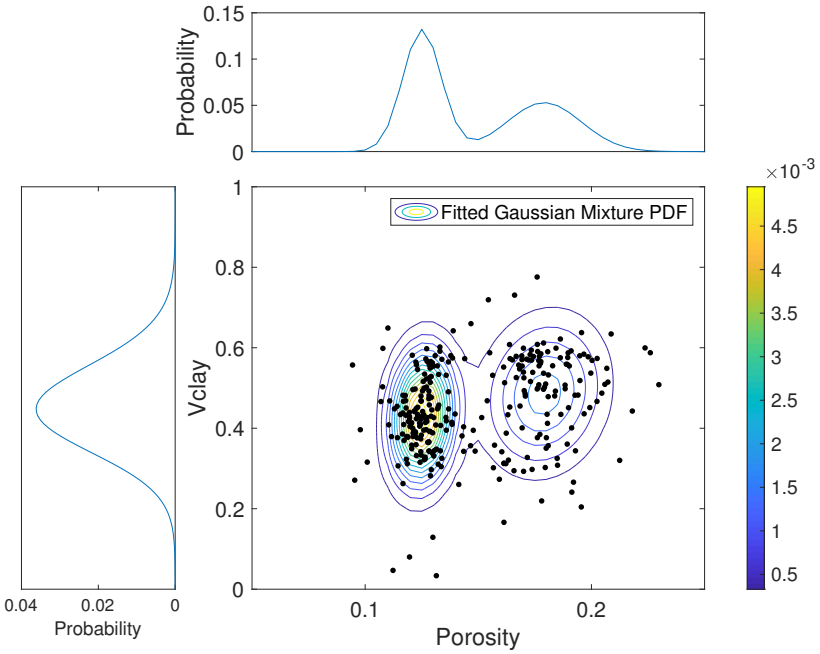

Figure 3.18: Prior distribution of rock physics variables: Gaussian mixture case. The parameters of the Gaussian mixture model are obtained via facies classification of well data

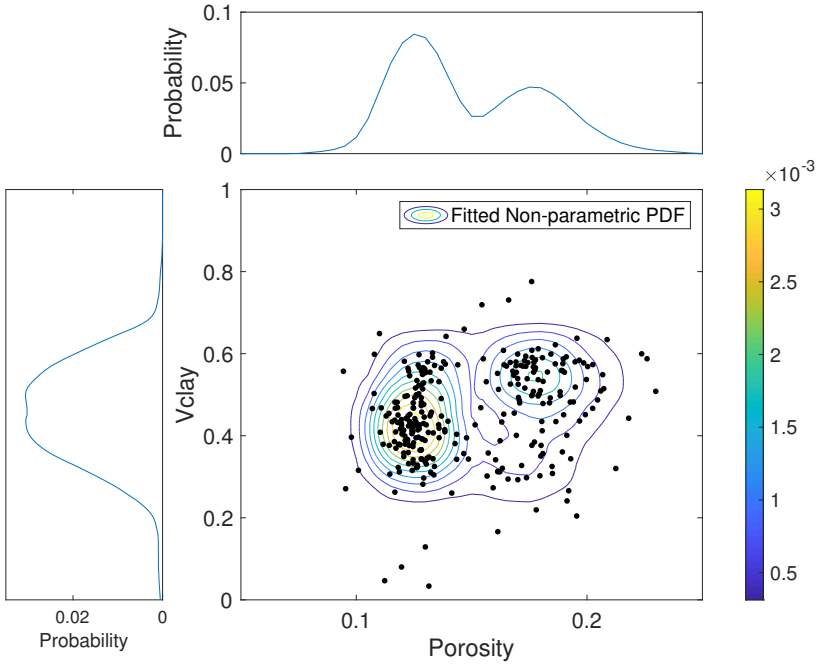

Figure 3.19: Prior distribution of rock physics variables: non-parametric case. The Epanechnikov kernel is used.

sian assumption (Figure 3.17), the Gaussian mixture PDF might be more appropriate for this application, given the bimodality of the data (Figure 3.18). The non-parametric PDF is calculated using the Epanechnikov kernel (Figure 3.19), and it provides an even more accurate description of the joint distribution, compared to the Gaussian mixture model.

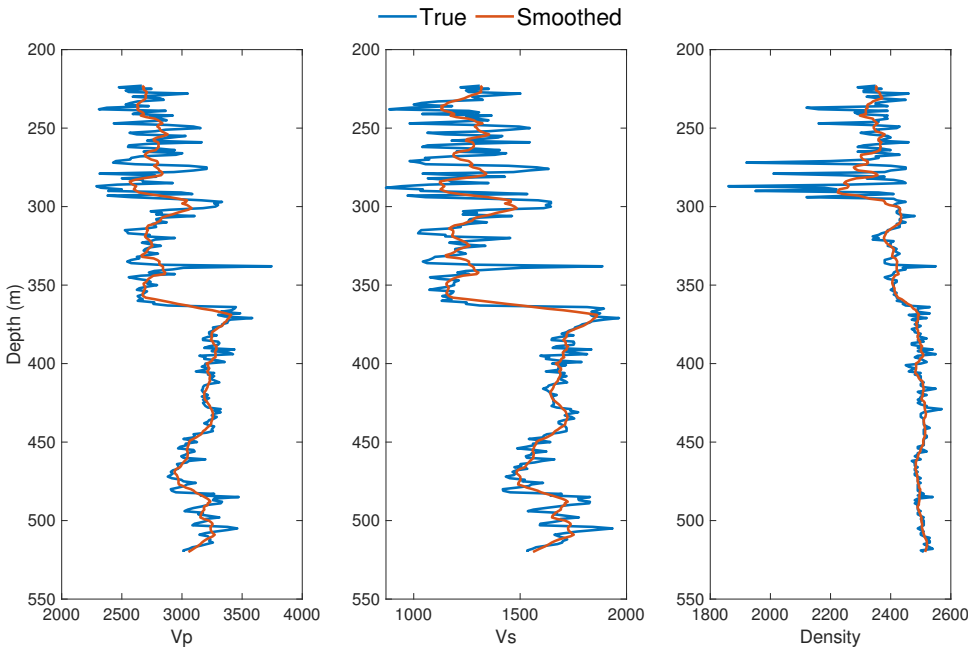

Figure 3.20: Filtered velocity and density logs used as input data for the rock physics inversion.

To mimic seismic resolution, I filter the velocity and density logs using a step size of 5 m (Figure 3.20) and then use the smooth logs as input data for the rock physics inversion. The Bayesian linearized inversion provides the posterior mean, the posterior covariance matrix, and the full posterior distribution evaluated on the multidimensional grid for each measured data. The marginal distributions are obtained by numerically integrating the posterior distribution. Overall, the probability distributions capture the trend of the actual logs (Figure 3.21). Given the good match between the actual rock-physics model and the linearized approximation, I point out that the prediction errors are mainly caused by the errors in the original rock-physics model and those in the input data (smooth elastic logs).

I then repeat the inversion using the Gaussian mixture approach. To compensate for the

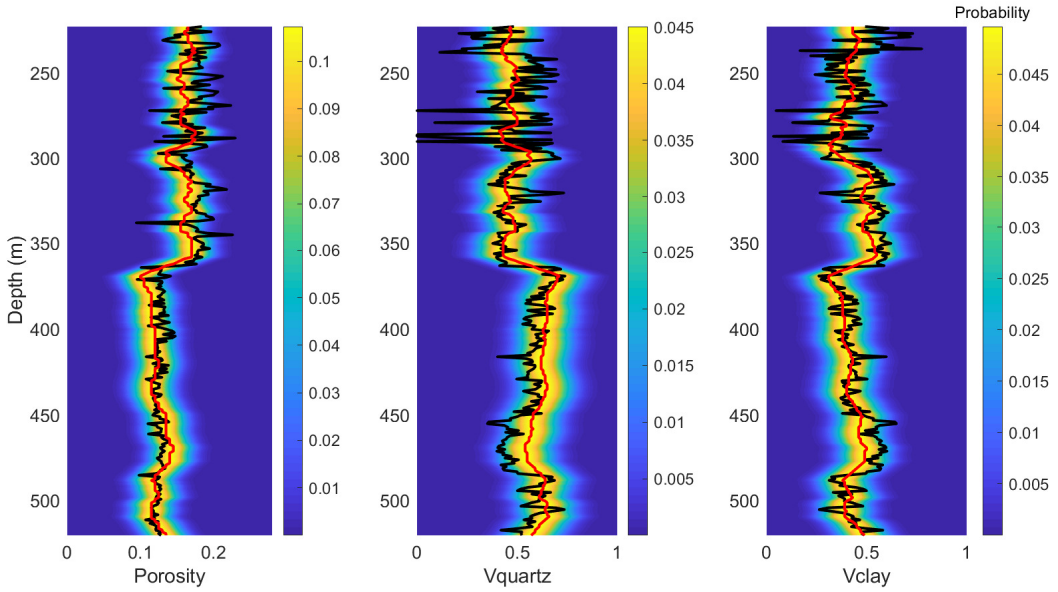

Figure 3.21: Results of the Bayesian linearized rock physics inversion. The background color represents the posterior distribution, the solid red curves represent the maximum a posteriori predictions, and the solid black curves represent the actual well logs.

parameter values not sampled at the well, I explore the prior model space using Monte Carlo simulations and then apply the rock physics model to obtain the corresponding set of elastic samples. A training dataset of 1000 samples is then used to evaluate the joint distribution of the model and data variables. The Gaussian mixture approach (Figure 3.22) provides a slightly more accurate and precise result than the Gaussian-linear inversion, however, these two results are similar. My interpretation is that for the depth range of the data, the nonlinearity of the rock physics model is weak and the Gaussian assumption is acceptable.

For the non-parametric approach, I numerically estimate the joint PDF of the model and data variables from the training dataset using kernel density estimation. The computation is performed on a discretized six-dimensional grid. The kernel widths are assumed to be equal to 1/10 of the length of the domain of each property. Also, this approach provides a good estimation of the posterior probability (Figure 3.23). However, the uncertainty of the porosity estimate is larger than the Gaussian and Gaussian mixture cases, and I might need a finer discretization for this property, which is more computationally demanding.

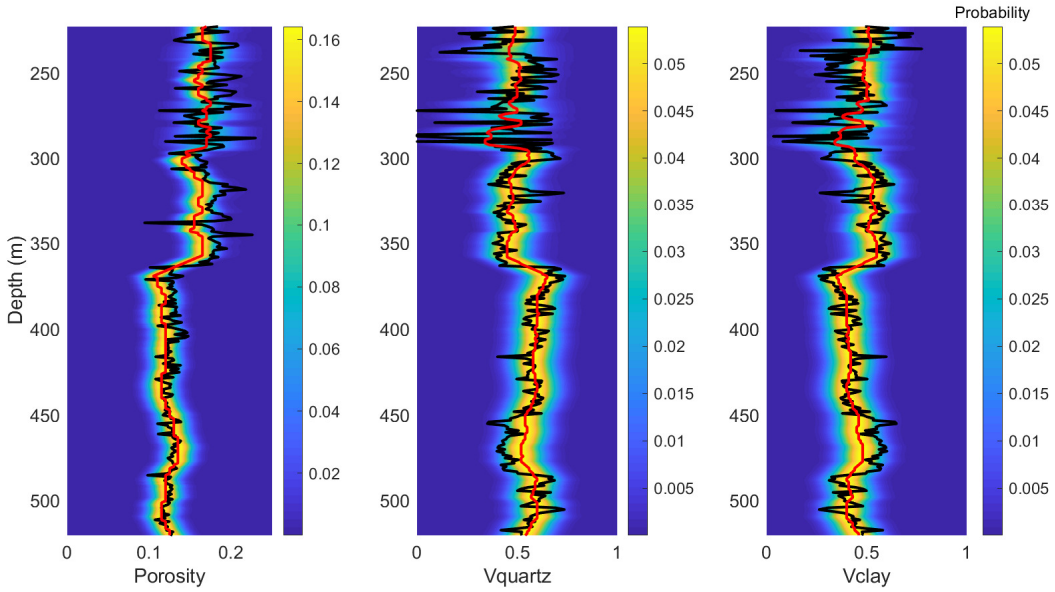

Figure 3.22: Results of the Bayesian Gaussian mixture approach.

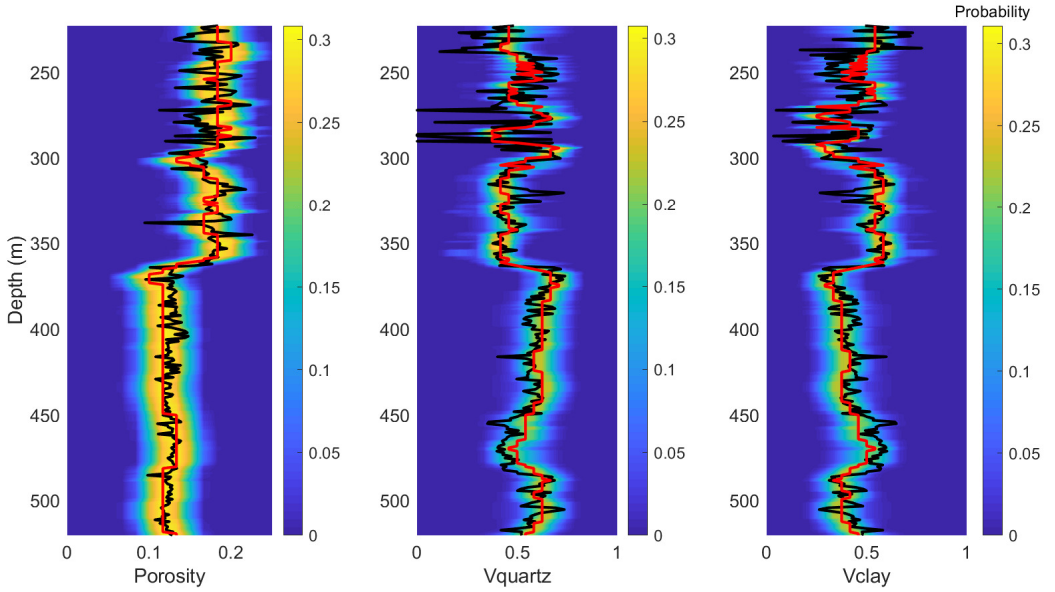

Figure 3.23: Results of the Bayesian non-parametric approach.

3.3.5 Conclusions

I have applied different parametric and non-parametric Bayesian rock physics inversion approaches to the well-log data acquired at the CMC Newell County Facility. The solution is

represented by the posterior distribution of porosity and lithology parameters conditioned on elastic data. All these approaches provide reasonably accurate results. In particular, the Gaussian mixture model is a suitable solution because of its analytical convenience and its ability to capture the features of different litho-fluid classes. The non-parametric approach based on kernel density estimation does not exhibit a clear advantage in this application because the model variables are approximately Gaussian distributed and because it suffers from computational issues.

Chapter 4

Direct FWI prediction of rock physics properties

4.1 Summary

Quantitative estimation of rock physics properties is an important part of reservoir characterization. Most current seismic workflows in this field are based on amplitude variation with offset. Building on recent work on high-resolution multi-parameter inversion for reservoir characterization, I construct a rock-physics parameterized elastic full-waveform inversion (EFWI) scheme. Within a suitably-formed multi-parameter EFWI, in this case, a 2D frequency-domain isotropic-elastic FWI with a truncated Gauss-Newton optimization, any rock physics model with a well-defined mapping between its parameters and seismic velocity/density can be examined. I select a three-parameter porosity, clay content, and water saturation (PCS) parameterization, and link them to elastic properties using three representative rock physics models: the Han empirical model, the Voigt-Reuss-Hill boundary model, and the Kuster and Toksöz inclusion model. Numerical examples suggest that conditioning issues, which make a sequential inversion (in which velocities and density are first determined through EFWI, followed by PCS parameters) unstable, are avoided in this direct approach.

Significant variability in inversion fidelity is visible from one rock physics model to another. However, the response of the inversion to the range of possible numerical optimization and frequency selections, as well as acquisition geometries, varies widely. Water saturation tends to be the most difficult property to recover in all situations examined. This can be explained with radiation pattern analysis, where very low relative scattering amplitudes from saturation perturbations are observed. An investigation performed with a Bayesian approach illustrates that the introduction of prior information may increase the inversion sensitivity to water saturation.

4.2 Introduction

Application of multi-parameter elastic seismic full waveform (EFWI) inversion to high-resolution reservoir-scale rock property model construction is at a relatively early stage of research and development (e.g., Dupuy et al., 2016a; Naeini et al., 2016; Connolly, 2017). However, progress has been reported in managing many of the challenges of practical EFWI (Brossier et al., 2009; Virieux and Operto, 2009; Métivier et al., 2017; Singh et al., 2018; Brittan and Jones, 2019; Pan et al., 2019; Aragao and Sava, 2020). As this occurs, consideration of how to formulate and parameterize full-wave extraction of rock properties becomes more relevant. In this chapter, I assume that the end goal of high-frequency EFWI is the estimation of the parameters of some suitable rock physics model. That is, I assume a desired outcome that goes beyond determination of elastic attributes (e.g., velocity, density, and modulus) within the seismic volume, and aims at determination of sets of petrophysical properties, such as lithology, porosity, and fluid information (Doyen, 2007; Bosch et al., 2010).

Rock physics inversion can occur either in a sequential (two-step) workflow, where an estimation of elastic attributes is followed by rock physics inversion, which transforms those elastic attributes to rock physics properties (Saltzer et al., 2005; Bachrach, 2006; Grana and Rossa, 2010; Johansen et al., 2013; Dupuy et al., 2016b,c; Grana, 2016a), or in a joint

workflow, where seismic data are directly inverted for rock physics properties, often in a Bayesian formulation, with the likelihood combining rock physics and seismic forward modelings (Bosch et al., 2007; Spikes et al., 2007; Buland et al., 2008). These seismic inversion methods, and the considerations by which a sequential versus direct approach is decided upon, are centered around linearized amplitude variation with offset (AVO) and the convolutional model. This framework is computationally inexpensive and robust (e.g., Buland and Omre, 2003). However, AVO inversion makes use of a limited subset of the information contained in seismic data (i.e., amplitudes of reflected events), makes strong assumptions about the origins of those events (i.e., layered media), and has several sensitivities to uncertainties in data pre-processing, e.g., velocity model errors (Sen and Roy, 2003). EFWI, though not without challenges of its own, addresses these limitations through its treatment of each datum in terms of an elastodynamic equation. Gauss-Newton EFWI updates are furthermore understood to include a generalized AVO inversion component when pre-critical reflection amplitudes influence the residuals (Innanen, 2014). There also exists a practical compromise between AVO and EFWI that uses an analytical solution to the wave equation assuming a locally 1D structures for each location. This approach is referred to as prestack waveform inversion (PWI) (Mallick, 1999; Sen and Roy, 2003; Tetyukhina et al., 2014). The superiority of PWI over AVO inversion has been demonstrated with both synthetic seismograms (Mallick, 2007) and realistic reservoir applications (Mallick and Adhikari, 2015). However, because PWI assumes 1D subsurface structure, it is applicable only to areas with simple geology. For complex geology, development of EFWI with a modeling methodology that honors 2D or 3D structures is necessary.

FWI based on the poroelastodynamic theories (e.g., Biot, 1956; Johnson et al., 1994), i.e, poroelastic FWI, is a direct approach to retrieve rock physics parameters from seismic waveforms. The study of poroelastic FWI is still in its infancy, with most work investigating the feasibility of this approach. De Barros and Dietrich (2008) derive poroelastic Fréchet derivatives in terms of the Green's functions of a 1-D reference medium; Morency et al. (2009)

determine the finite-frequency sensitivity kernels based upon adjoint methods; and Yang et al. (2019) derive analytical radiation patterns for different parameterizations in poroelastic media. De Barros et al. (2010) and Yang and Malcolm (2019) also test poroelastic FWI on plane-layered synthetic models and achieve a good reconstruction of a single parameter assuming all other parameters are perfectly known. Despite these advances, challenges associated with poroelastic FWI have also been pointed out. With significantly more subsurface parameters and more complex physical mechanisms than EFWI, poroelastic FWI is expected to be more nonlinear (Yang et al., 2019). The strong coupling of these parameters makes inversion more difficult. As a result, whether or not poroelastic FWI can simultaneously recover multiple parameter values and their structural features remains an open question. In this chapter, I explore a less complex issue, which is the potential of EFWI to predict rock physics properties.

The literature contains a range of examples of EFWI incorporating rock physics information, most often with the rock physics information supplying constraints to narrow the gap between seismic imaging and reservoir characterization (Naeini et al., 2016; Kamath et al., 2017; Zhang et al., 2018). Constraints can be derived from facies classification using well-logs, with linear relationships between elastic parameters subsequently included in a penalty term (Kemper and Gunning, 2014; Kamath et al., 2017; Rocha and Sava, 2018). The spatial distribution of the facies has been determined in recent studies by employing a Bayesian framework (Singh et al., 2018; Zhang et al., 2018; Zhang and Alkhalifah, 2019), where the facies with the maximum posterior probability at a specific grid point determines the corresponding value in the model constraint. As opposed to analytic model constraints, Aragao and Sava (2020) apply probabilistic constraints to deal with complex relationships among elastic parameters. These rock-physics-constrained approaches have been demonstrated to guide the inversion toward high-resolution and geologically plausible solutions. However, their use of rock physics models has primarily been to improve elastic attribute estimation, after which additional workflows, for instance the application of rock physics templates cali-

brated with well data (Carcione and Avseth, 2015; Picotti et al., 2018), are employed. Rock physics inversions using FWI results as input data have also been developed (Dupuy et al., 2016b,c).

EFWI-derived attributes which, though not constructed through direct updating of rock physics model parameters, nevertheless lead to rock physics interpretations, have also been reported. Shi et al. (2006) design an adaptive controller to calculate a suitable step length for model updating. This method significantly accelerates the inversion convergence, and the inverted Lamé parameters yield a clear image of gas sands. Pan et al. (2018b) recommend that trade-offs between different parameter classes be evaluated using inter-parameter contamination kernels. These kernels explained why the velocity-density parameterization was optimal for characterizing a producing heavy oil reservoir (low Poisson's ratio) with walk-away vertical seismic profile (W-VSP) data (Pan et al., 2018a). Prieux et al. (2013a) introduce a hierarchical approach, using visco-acoustic FWI to reconstruct P-wave velocity (V_{P}), density, and attenuation, to interpret geological features such as gas traps and soft quaternary sediments. In a later study of visco-elastic FWI with the same field data (Prieux et al., 2013b), these geological features were even more pronounced. In particular, recovery of the $V_{\mathrm{P}}/V_{\mathrm{S}}$ ratio allowed gas-saturated regions to be discriminated. These studies are an expression of the potential of FWI-derived elastic attributes as lithology or fluid indicators, but the question of whether similar insights can be derived through direct EFWI prediction of rock physics properties remains open.

Nowadays, most efforts to involve EFWI in rock physics or petrophysical model construction are of the sequential type. There has been little reported work on direct updating of reservoir rock properties, i.e., the parameters of a rock physics model, within EFWI. In this chapter, I examine that possibility by formulating and numerically exploring a direct estimation of rock physics properties using isotropic-elastic FWI. This amounts to adopting a viewpoint within EFWI similar to that of, for instance, Russell et al. (2011), within an AVO environment, in which seismic amplitudes are directly interrogated to determine the

parameters of a static-poroelastic fluid term (Biot, 1956; Gassmann, 1951). I set out an EFWI formulation in which the updates occur directly in terms of the parameters of one of a large class of possible rock physics models, using descent-based optimization methods (i.e., steepest descent, nonlinear conjugate gradient, or Newton-type). For this initial testing, I select three representative sets of relations between elastic and rock physics parameters: the Han empirical model, the Voigt-Reuss-Hill boundary model, and the Kuster and Toksöz (KT) inclusion model. These are comparable models in the sense that each can be used to set up a three-parameter inversion scheme for the estimation of porosity, clay content, and water saturation.

The remainder of this chapter is organized as follows. First, I present my EFWI framework which allows for direct updates in rock physics properties. Then, I use several numerical examples to verify the effectiveness of my approach. I also demonstrate its advantages over an indirect approach, in which the rock physics properties are transformed from EFWI-derived elastic attributes. Finally, I discuss possible steps in moving this research forward.

4.3 Theory

4.3.1 Isotropic-elastic full-waveform inversion

The forward modeling approach I consider here is the frequency-domain isotropic-elastic wave equations described in Chapter 2. For our discussion here, it is only important to note that those equations can be discretized and formulated in a matrix form:

$$\mathbf{A}(\mathbf{m})\mathbf{u} = \mathbf{f}, \tag{4.1}$$

where $\mathbf{u}$ is a vector containing horizontal and vertical displacements, $\mathbf{f}$ is the source term, and $\mathbf{A}$ is the impedance matrix containing the finite-difference coefficients. A perfectly matched layers (PML) method (Berenger, 1994) is implemented to absorb reflections from

model boundaries. The objective function I consider is the L2 data-matching term, discussed in Chapter 2, with no added regularization term:

$$E(\mathbf{m}) = \frac{1}{2} \left\| \mathbf{d} - \mathbf{R}\mathbf{u}(\mathbf{m}) \right\|_2^2 , \tag{4.2}$$

where $\mathbf{d}$ is the observed data and R is a matrix representing the receiver sampling of the wavefield simulated from model $\mathbf{m}$.

The gradient of E with respect to the ith model parameter m_i can be expressed in a simple, general form as

$$\nabla_{m_i} E = \left\langle \frac{\partial \mathbf{A}}{\partial m_i} \mathbf{u}, \upsilon \right\rangle . \tag{4.3}$$

where υ is the adjoint wavefield. The quantity $\partial \mathbf{A} / \partial m_i$, expressed in terms of the incoming and outgoing wave vector directions, is the scattering radiation pattern associated with the unknown model m_i. I use a truncated Gauss-Newton (TGN) method (Métivier et al., 2017) to update the model, involving only gradient and Hessian-vector products, which can be efficiently calculated using the adjoint-state method (Plessix, 2006).

4.3.2 Rock physics parameterizations

A wide range of sets of isotropic-elastic parameter classes, for instance the Lamé parameters plus density, (λ, μ, ρ), or the P- and S-wave velocities plus density, $(V_\mathrm{P}, V_\mathrm{S}, \rho)$, can be selected for inversion (e.g., Tarantola, 1986). Although any triplet (λ, μ, ρ) can be uniquely computed from its associated triplet $(V_\mathrm{P}, V_\mathrm{S}, \rho)$, and vice versa, which suggests that the parameterization is irrelevant, in practice the class chosen for updating is very important. It is a feature of FWI that if one computes a model by updating $(V_\mathrm{P}, V_\mathrm{S}, \rho)$ directly, and compares it to the model determined by (1) updating (λ, μ, ρ), and (2) subsequently mapping to $(V_\mathrm{P}, V_\mathrm{S}, \rho)$, large differences tend to be observed (e.g., Anagaw and Sacchi, 2018; Pan et al., 2018a).

Let $\mathbf{p} = [p_1, p_2, p_3]^T$ represent a reference FWI parameterization, with p_i being the ith parameter class with $i = (1, 2, 3)$, so that, in the velocity/density parameterization above,

for instance, p_2 represents the S-wave velocity. Let $m_i^{p_j}$ represent the model parameter in class p_j at the ith spatial position. From equation 4.3 we observe that this model parameter is changed at each iteration by an update proportional to $\partial \mathbf{A}/m_i^{p_j}$. To transform to a new parameterization, say $\mathbf{q} = [q_1, q_2, q_3]^T$, we compute the chain rule

$$\frac{\partial \mathbf{A}}{\partial m_i^{q_j}} = \frac{\partial \mathbf{A}}{\partial m_i^{p_1}} \frac{\partial m_i^{p_1}}{\partial m_i^{q_j}} + \frac{\partial \mathbf{A}}{\partial m_i^{p_2}} \frac{\partial m_i^{p_2}}{\partial m_i^{q_j}} + \frac{\partial \mathbf{A}}{\partial m_i^{p_3}} \frac{\partial m_i^{p_3}}{\partial m_i^{q_j}}, \tag{4.4}$$

for each of $j = (1, 2, 3)$. Given an FWI scheme set up to update parameters $\mathbf{p}$, within which the partial derivatives of $\mathbf{A}$ are known, and given relations between these parameters and any new desired set $\mathbf{q}$, of the form $m_i^{p_j}(m_i^{q_1}, m_i^{q_2}, m_i^{q_3})$, through equation 4.4 we can move to a new scheme in which the $\mathbf{q}$ are updated. This allows us to transform between different elastic parameter sets, e.g., $(V_\mathrm{P}, V_\mathrm{S}, \rho)$, (λ, μ, ρ), (κ, μ, ρ); however, it also allows us to transform from a base elastic parameter scheme to any desired rock physics model, provided a suitable mapping exists between the parameters of this model and the three base elastic properties.

Here I consider a rock physics model, in which $\mathbf{q}$ embodies porosity parameters, compositional properties, and fluid saturation parameters. Three classic rock physics models are selected to support this early-stage, broad analysis: the Han empirical model (Han, 1987), the Voigt-Reuss-Hill (VRH) boundary model (Hill, 1952), and the Kuster and Toksöz (KT) inclusion model (Kuster and Toksöz, 1974). Within these, I focus on three rock physics properties central to reservoir characterization: porosity (ϕ), defined as the ratio of pore volume to the total volume of the rock; clay content (C), the ratio of clay volume to the total volume of mineral grains; and water saturation (S_w), the ratio of water volume to pore volume. I parameterize my inversion in terms of these variables, which I refer to as the porosity, clay content, and water saturation (PCS) parameterization; the base elastic parameterization is based on P- and S-wave velocity and density (referred to as DV). Although the rock physics models I consider arise from different theories, or even empirical considerations, each provides V_P, V_S, and ρ as explicit functions of ϕ, C, and S_w. The relations can be used as discussed above to obtain the partial derivatives of the objective function with respect to ϕ,

C, and S_{w}.

Han empirical model

Han (1987) introduces an empirical model relating ultrasonic P- and S-wave velocities in km/s with porosity and clay content. The relationships take the form

$$\begin{aligned} V_{\mathrm{P}} &= a_1 - a_2\phi - a_3 C, \\ V_{\mathrm{S}} &= b_1 - b_2\phi - b_3 C, \end{aligned} \tag{4.5}$$

where a_1, a_2, a_3, b_1, b_2, and b_3 are positive constants. Assuming a solid mixture of clay and quartz, and a fluid mixture of brine and hydrocarbon (which is assumed for each of the models I consider), the density is computed as a weighted average of the densities of mineral and fluid components:

$$\begin{aligned} \rho &= (1-\phi)\rho_m + \phi\rho_f, \\ \rho_m &= \rho_c C + \rho_q(1-C), \\ \rho_f &= \rho_w S_w + \rho_h(1-S_w), \end{aligned} \tag{4.6}$$

where the subscripts m, f, c, q, w, and h indicate solid matrix, fluid phase, clay, quartz, water, and hydrocarbon (oil or gas), respectively. The partial derivatives needed for equation 4.4 to be set out for the Han model are

$$\begin{gathered} \frac{\partial V_{\mathrm{P}}}{\partial \phi} = -a_2 \ , \quad \frac{\partial V_{\mathrm{P}}}{\partial C} = -a_3 \ , \quad \frac{\partial V_{\mathrm{P}}}{\partial S_w} = 0 \ , \\ \frac{\partial V_{\mathrm{S}}}{\partial \phi} = -b_2 \ , \quad \frac{\partial V_{\mathrm{S}}}{\partial C} = -b_3 \ , \quad \frac{\partial V_{\mathrm{S}}}{\partial S_w} = 0 \ , \\ \frac{\partial \rho}{\partial \phi} = \rho_f - \rho_m \ , \quad \frac{\partial \rho}{\partial C} = (1-\phi)(\rho_c - \rho_q) \ , \quad \frac{\partial \rho}{\partial S_w} = \phi(\rho_w - \rho_h) \ . \end{gathered} \tag{4.7}$$

The substitution of equation 4.7 into equation 4.4 re-parameterizes the three-parameter

elastic FWI scheme such that ϕ, C and S_w are explicitly updated as the residuals are reduced. I examine this possibility in contrast to an indirect approach, in which the standard FWI scheme is used to determine $V_{\rm P}$, $V_{\rm S}$ and ρ models, after which the system

$$\begin{bmatrix} a_2 & a_3 & 0 \\ b_2 & b_3 & 0 \\ 0 & 0 & 1 \end{bmatrix} \begin{bmatrix} \phi \\ C \\ S_w \end{bmatrix} = \begin{bmatrix} a_1 - V_{\rm P} \\ b_1 - V_{\rm S} \\ A \end{bmatrix}, \tag{4.8}$$

where

$$\begin{aligned} A &= \frac{\rho - (1-X)(\rho_c Y - \rho_q Y + \rho_q) - X\rho_h}{X(\rho_w - \rho_h)}, \\ X &= \frac{b_3 V_{\rm P} - a_3 V_{\rm S} + a_3 b_1 - a_1 b_3}{a_3 b_2 - a_2 b_3}, \quad \text{and} \\ Y &= \frac{-b_2 V_{\rm P} + a_2 V_{\rm S} + a_1 b_2 - a_2 b_1}{a_3 b_2 - a_2 b_3}, \end{aligned} \tag{4.9}$$

can be solved for ϕ, C and S_w.

Voigt-Reuss-Hill (VRH) boundary model

As described in Chapter 3, the Voigt and Reuss models define the upper and lower bounds for the elastic moduli of a mixture of mineral grains, and Hill's average of these bounds is used to obtain the effective mineral moduli. However, the Voigt and Reuss bounds also apply to the mixture of mineral and pore fluids, regardless of the geometric arrangement of these components, although the bounds will become quite separated and their averages will be less predictive. In this numerical study, I use the VRH model alone to predict the elastic moduli of fluid-saturated rocks, mainly because of its computational convenience. Also, this simple theoretical model allows me to illustrate the proposed FWI framework more intuitively.

Within the VRH model, the effective bulk and shear moduli of the saturated rock are given by

$$K_{\rm sat} = \frac{K_{\rm V} + K_{\rm R}}{2}, \quad \mu_{\rm sat} = \frac{\mu_{\rm V} + \mu_{\rm R}}{2}, \tag{4.10}$$

where

$$K_{\mathrm{V}} = (1-\phi)[K_c C + K_q(1-C)] + \phi[K_w S_w + K_h(1-S_w)],$$

$$K_{\mathrm{R}} = 1 \Bigg/ \left[\frac{(1-\phi)C}{K_c} + \frac{(1-\phi)(1-C)}{K_q} + \frac{\phi S_w}{K_w} + \frac{\phi(1-S_w)}{K_h}\right],$$

$$\mu_{\mathrm{V}} = (1-\phi)[\mu_c C + \mu_q(1-C)],$$

$$\mu_{\mathrm{R}} = 0. \tag{4.11}$$

The velocities as functions of the elastic moduli and density are then

$$\begin{aligned} V_{\mathrm{P}} &= \sqrt{\frac{K_{\mathrm{sat}} + \frac{4}{3}\mu_{\mathrm{sat}}}{\rho}}, \\ V_{\mathrm{S}} &= \sqrt{\frac{\mu_{\mathrm{sat}}}{\rho}}, \end{aligned} \tag{4.12}$$

where the density ρ is computed by equation 4.6. The partial derivatives needed to carry out FWI updates of the ϕ, C, and S_w emerging from this model are derived in Appendix A.

Kuster and Toksöz (KT) inclusion model

For simplicity, I use the KT model to directly calculate the saturated rock moduli, instead of combing it with Gassmann's equation, as discussed in Chapter 3. For a single, spherical inclusion shape, within the KT model the elastic moduli of the saturated rock are given by

$$\begin{aligned} K_{\mathrm{sat}} &= \frac{4K_m\mu_m + 3K_mK_f + 4\mu_mK_f\phi - 4K_m\mu_m\phi}{4\mu_m + 3K_f - 3K_f\phi + 3K_m\phi}, \\ \mu_{\mathrm{sat}} &= \frac{\mu_m(9K_m + 8\mu_m)(1-\phi)}{9K_m + 8\mu_m + 6(K_m + 2\mu_m)\phi}. \end{aligned} \tag{4.13}$$

where the subscripts sat, m, and f indicate saturated rock, solid matrix, and fluid phase, respectively. The elastic moduli of the solid matrix, K_m and μ_m, are calculated using the VRH average. The fluid bulk modulus K_f is calculated assuming a patchy fluid mixture. I then compute density and the P- and S-wave velocities with equations 4.6 and 4.12. The

partial derivatives needed to carry out FWI updates of the ϕ, C, and S_w emerging from this model are derived in Appendix B. More geometrical scenarios, with single or multiple inclusion shapes, are possible within the KT model; these lead to more complex derivative expressions.

4.4 Numerical Analysis

Several questions regarding direct iterative updating of rock physics model parameters within an EFWI scheme can be answered by setting up numerical simulations in a 2D elastic environment. In these simulations, I naturally neglect practical issues associated with field data (e.g., acquisition limitations, noise, complex near-surface environment), and I furthermore carry out FWI with data generated using the same simulation through which the inversion quantities are computed. However, the numerical tests allow us to examine parameter resolution issues, and make clear comparisons between the model solutions which are selected when rock physics parameters are directly updated, versus those which are indirectly determined (i.e., computed after the fact from the results of iterative updating of elastic properties). Each of the three rock physics models reviewed in the previous section is incorporated in a PCS parameterization of FWI, which allows us to compare direct inversion for porosity, clay content, and water saturation across the three; the Han empirical relations are selected as a convenient model to compare direct and sequential approaches.

For all numerical tests carried out in this chapter, I assume a rock frame consisting of quartz and clay saturated with water and gas. The elastic properties of each component are listed in Table 4.1. For the EFWI algorithm, a 2D frequency-domain, three parameters elastic inversion is set up, using vertical and horizontal components of particle velocity as the data set and using data frequencies within the interval 2-25 Hz; within this band, the source is considered to have a uniform amplitude spectrum (i.e., I assume a bandlimited wavelet has been estimated and deconvolved). I adopt a multiscale approach (Bunks et al., 1995) by inverting five frequency bands, each containing three evenly-spaced frequencies from 2 Hz to

a maximum frequency; the maximum frequency is 3 Hz for the first band, and increases to 25 Hz for the last band (following the strategy advocated by Keating and Innanen, 2019b). A truncated Gauss-Newton optimization method, comprising 30 inner iterations and 20 outer iterations for each frequency band. I employ an acquisition geometry with receivers mimicking a simultaneous surface seismic and vertical seismic profile (VSP) configuration: a line of sources every 50 m at the top of the model illuminates receivers every 20 m on the top and sides of the model.

Table 4.1: Elastic properties of minerals and fluids.

	Bulk modulus (GPa)	Shear modulus (GPa)	Density (g/cm^3)
Quartz	37	44	2.65
Clay	21	10	2.55
Water	2.25	0	1.0
Gas	0.04	0	0.1

4.4.1 Direct versus indirect EFWI of Han model parameters

I begin by reconstructing a simple geometric model, with a homogeneous background porosity, clay content, and water saturation of 0.2, 0.2, and 0.4 respectively. The model is 1 km in width and 1 km in depth, and discretized into 10 m$\times$10 m cells. Circular porosity, clay content, and saturation anomalies of 0.3, 0.4, and 0.8 respectively are placed in spatially separated locations within the background medium (see Figure 4.1d-4.1f). Within Han's model (equations 4.5 and 4.6), these imply P-wave velocity, S-wave velocity, and density anomalies as plotted in Figure 4.1a-4.1c, assuming fixed Han coefficients of $a_1 = 5.5$, $a_2 = 6.9$, $a_3 = 2.2$, $b_1 = 3.4$, $b_2 = 4.7$, and $b_3 = 1.8$ (Han, 1987). In all inversions to follow (including both DV and PCS parameterizations), the initial models are homogeneous and equal to the background values in Figure 4.1.

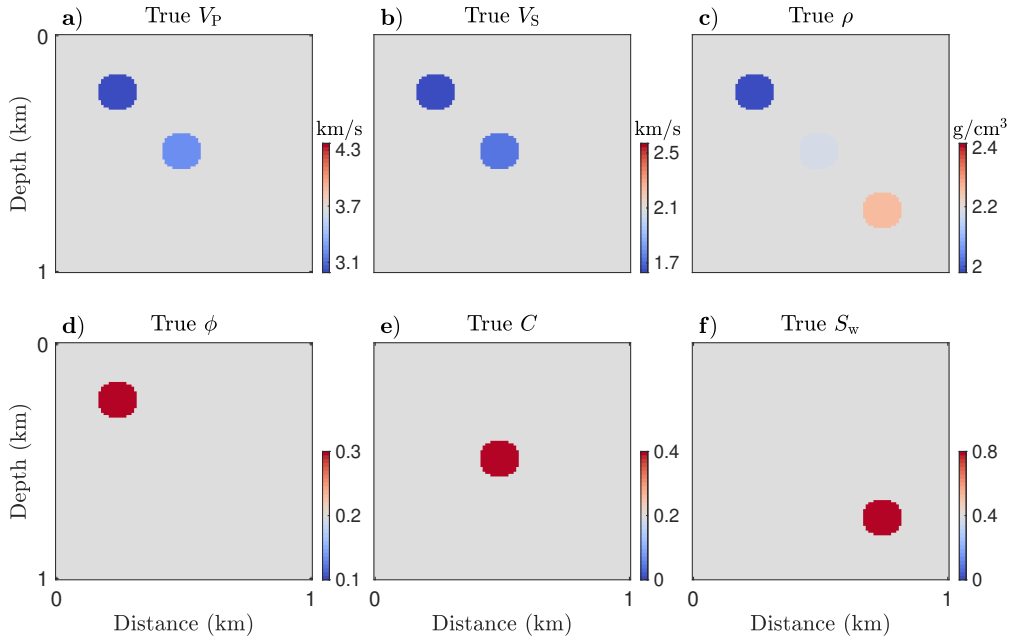

Figure 4.1: (a-c) True V_P, V_S, and ρ models; (d-f) corresponding true ϕ, C, and S_w models within the Han model with $a_1 = 5.5$, $a_2 = 6.9$, $a_3 = 2.2$, $b_1 = 3.4$, $b_2 = 4.7$, and $b_3 = 1.8$. Note that S_w has no impact on V_P in this case.

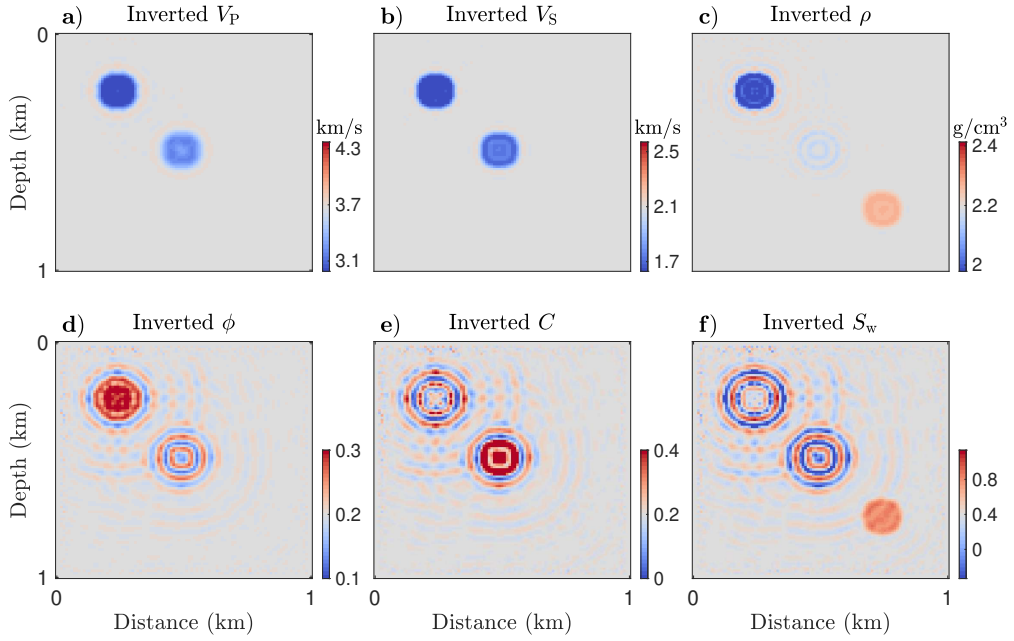

Figure 4.2: Results of the indirect/sequential rock physics EFWI approach. (a-c) Inverted V_P, V_S, and ρ models respectively within the DV parameterization; (d-f) corresponding indirectly estimated ϕ, C, and S_w models.

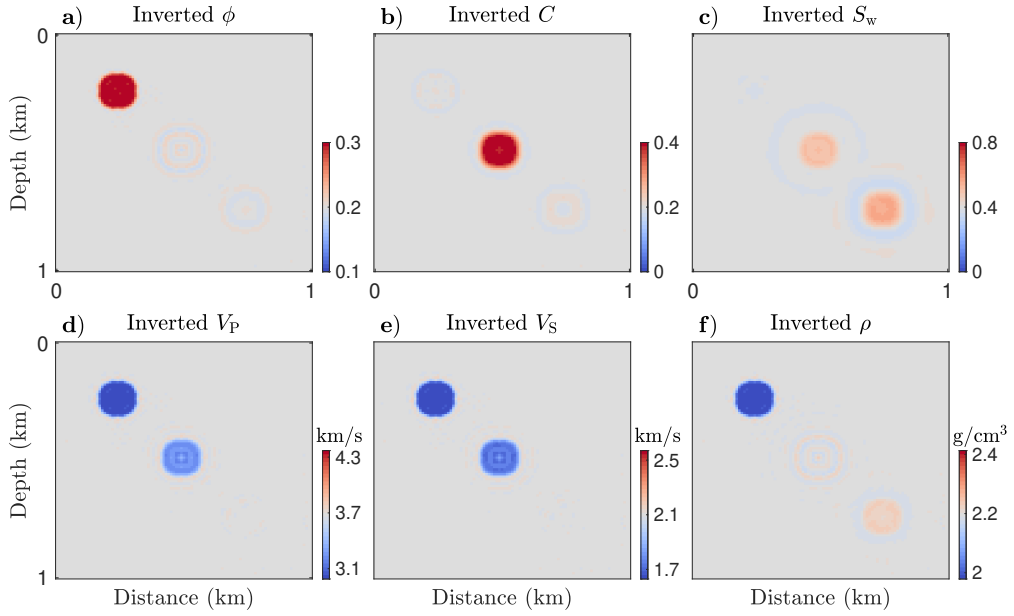

Figure 4.3: Results of the direct rock physics EFWI approach. (a-c) Inverted ϕ, C, and S_w models respectively, within the PCS parameterization; (d-f) corresponding indirectly-estimated V_P, V_S, and ρ models.

I begin with a comparison between indirect/sequential, and direct, updating of Han model parameters. In Figure 4.2 the results of the indirect approach are summarized. In the top row, Figure 4.2a-4.2c, the EFWI reconstruction of the P-wave velocity, S-wave velocity, and density models within the DV parameterization are plotted. These are next converted to porosity, clay content, and water saturation (Figure 4.2d-4.2f) based on the Han model, i.e., by solving the system in equation 4.8. In the context of the simple problem I have set up, involving simulated data from receivers with both lateral and vertical coverage, we observe the expected close match between the true and recovered density and velocity anomalies (i.e., comparing the top rows of Figures 4.1 and 4.2). However, the relatively small errors appearing in the elastic property model are magnified significantly in the ϕ, C and S_w recoveries. The estimate of water saturation appears to fair the worst, and can be observed to contain non-physical negative values. In Figure 4.3 the results of the direct approach are summarized, with the recovered ϕ, C and S_w models plotted in Figure 4.3a-4.3c

respectively. We observe a strong difference between the models derived using this direct, PCS-parameterized approach; the porosity and clay content models exhibiting particular increases in accuracy and reduced cross-talk (Figure 4.3a and 4.3b). Cross-talk remains present in the recovered water saturation (Figure 4.3c), but is suppressed as compared to the indirect DV-parameterized results. Moreover, the velocity and density models (Figure 4.3d-4.3f) derived from these directly inverted rock physics properties by equations 4.5 and 4.6 also closely match the true model (Figure 4.2a-4.2c).

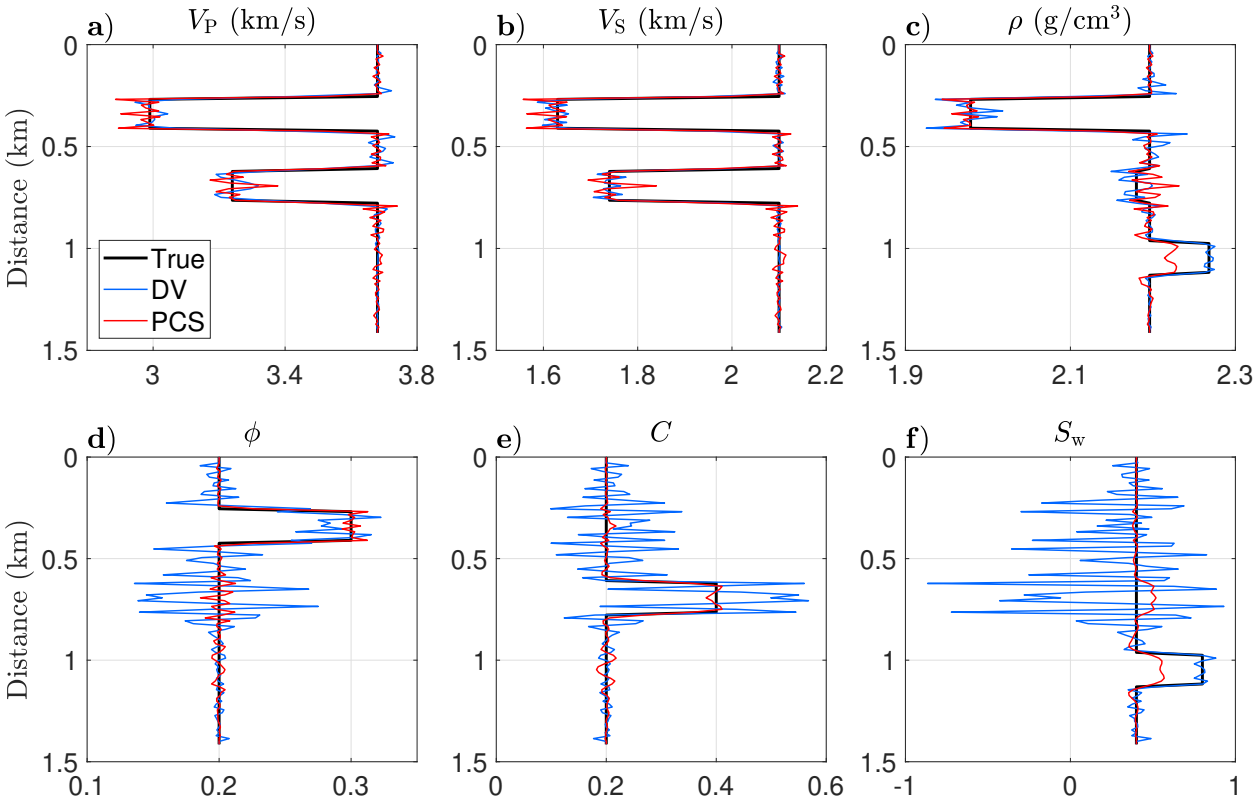

Figure 4.4: (a-f) Model profiles for V_P, V_S, ρ, ϕ, C, and S_w at diagonal position x=z. The black, blue, and red lines denote the true model, the inverted model within the DV parameterization, and the inverted model within the PCS parameterization, respectively.

In Figure 4.4 profiles of the true and inverted models at diagonal position x=z are plotted. The significant magnification of spurious variations is observed with the DV parameterization (comparing the blue lines in Figure 4.4d-4.4f with those in Figure 4.4a-4.4c). In contrast,

the directly recovered rock physics properties (red lines in Figure 4.4d-4.4f) exhibit mild oscillations around the true model, and the converted velocities (red lines in Figure 4.4a and 4.4b) overlap with the true and directly inverted velocities.

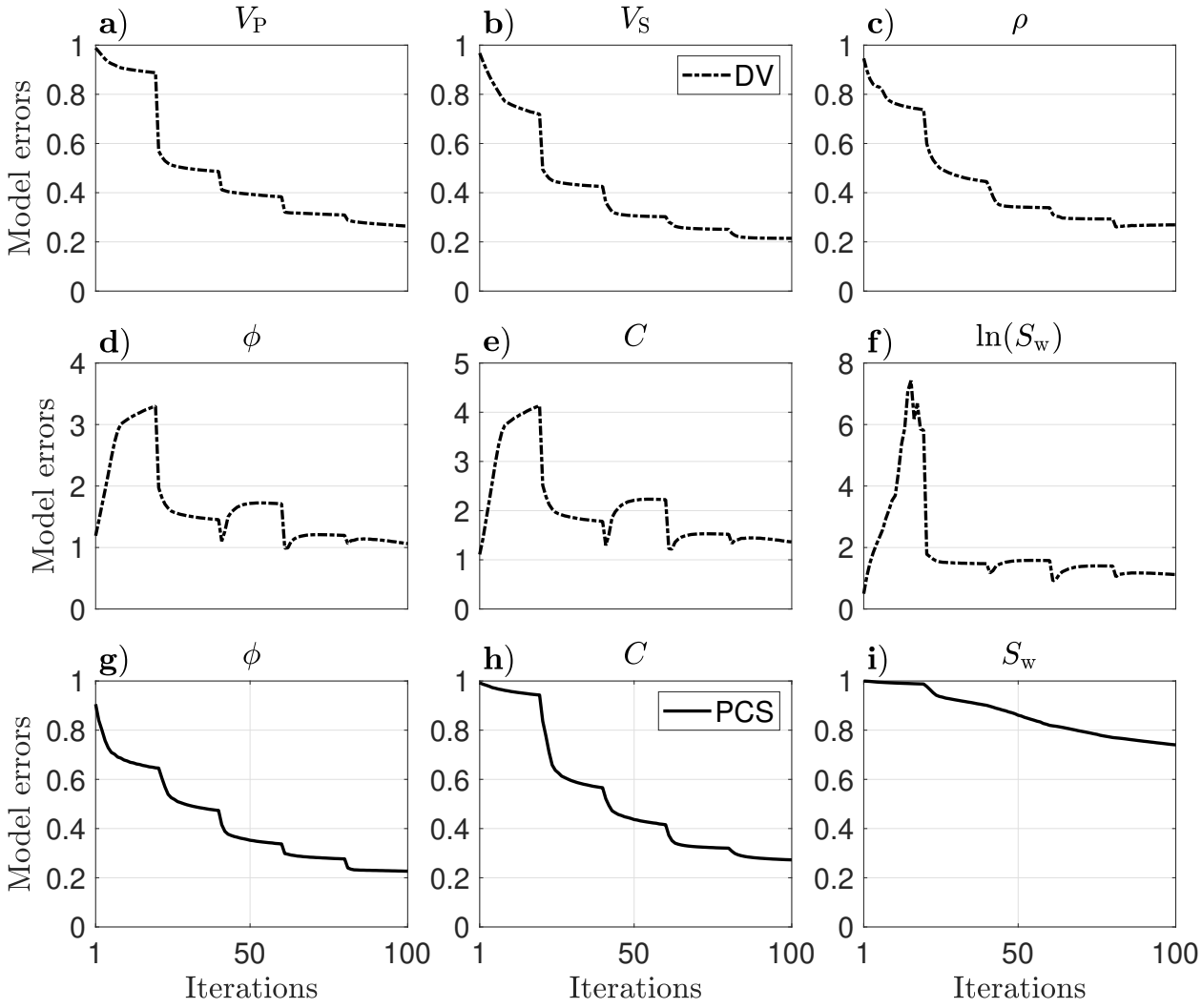

Figure 4.5: Convergence histories. (a-c) Model error reductions of V_P, V_S, and ρ and (d-f) ϕ, C, and S_w in the DV parameterization. (g-i) Model error reductions of ϕ, C, and S_w in the PCS parameterization.

The convergence properties of the solutions are examined via the relative model error $e = \|\mathbf{m} - \mathbf{m}_t\|_2 / \|\mathbf{m}_0 - \mathbf{m}_t\|_2$, where $\mathbf{m}$, $\mathbf{m}_0$, and $\mathbf{m}_t$ represent the inverted, initial and true models, respectively. The quantities are normalized such that each model starts its

iteration with a unit error. In Figure 4.5a-4.5c we observe the convergence characteristics of a reliable inversion for velocity and density with the DV parameterization. The model errors decrease monotonically, with sudden rate-changes at iterations where the frequency band varies. However, if the DV model parameters are mapped to their corresponding rock physics properties iteration by iteration, we observe a very different evolution (Figure 4.5d-4.5f), with large and sustained increases in model error, especially at early stages after the introduction of higher frequency data. Comparing this to the evolution of rock physics property error with the direct EFWI, or PCS parameterization, the steady, monotonically decreasing reduction of model error is once again observed. Although this convergence history comparison does not answer precisely *why* the direct/PCS inversion is an improvement over the indirect/DV inversion for the same set of rock physics properties, we observe that the two approaches involve very different paths through the PCS model space as the EFWI iteration proceeds.

There are two mathematical/numerical mechanisms which could be responsible for the poor estimates of rock physics properties emerging from the DV parameterization. One derives from the conditioning of the coefficient matrix in equation 4.8 (whose condition number is ≈ 52), which implies that small errors in the input (V_{P}, V_{S} and ρ values) will lead to large errors in the output (ϕ, C, and S_{w} values) both after and during iterations. The other mechanism is that our particular optimization parameters and frequency selection strategy have led to data overfitting. That is, the model may have been forced to conform too closely to the data in one frequency band, making it overly complex and impairing its use of data information at other frequencies. This would also explain the increase in model error with iterations (Figure 4.5d-4.5f), and the "ringing" in the images (Figure 4.2d-4.2f).

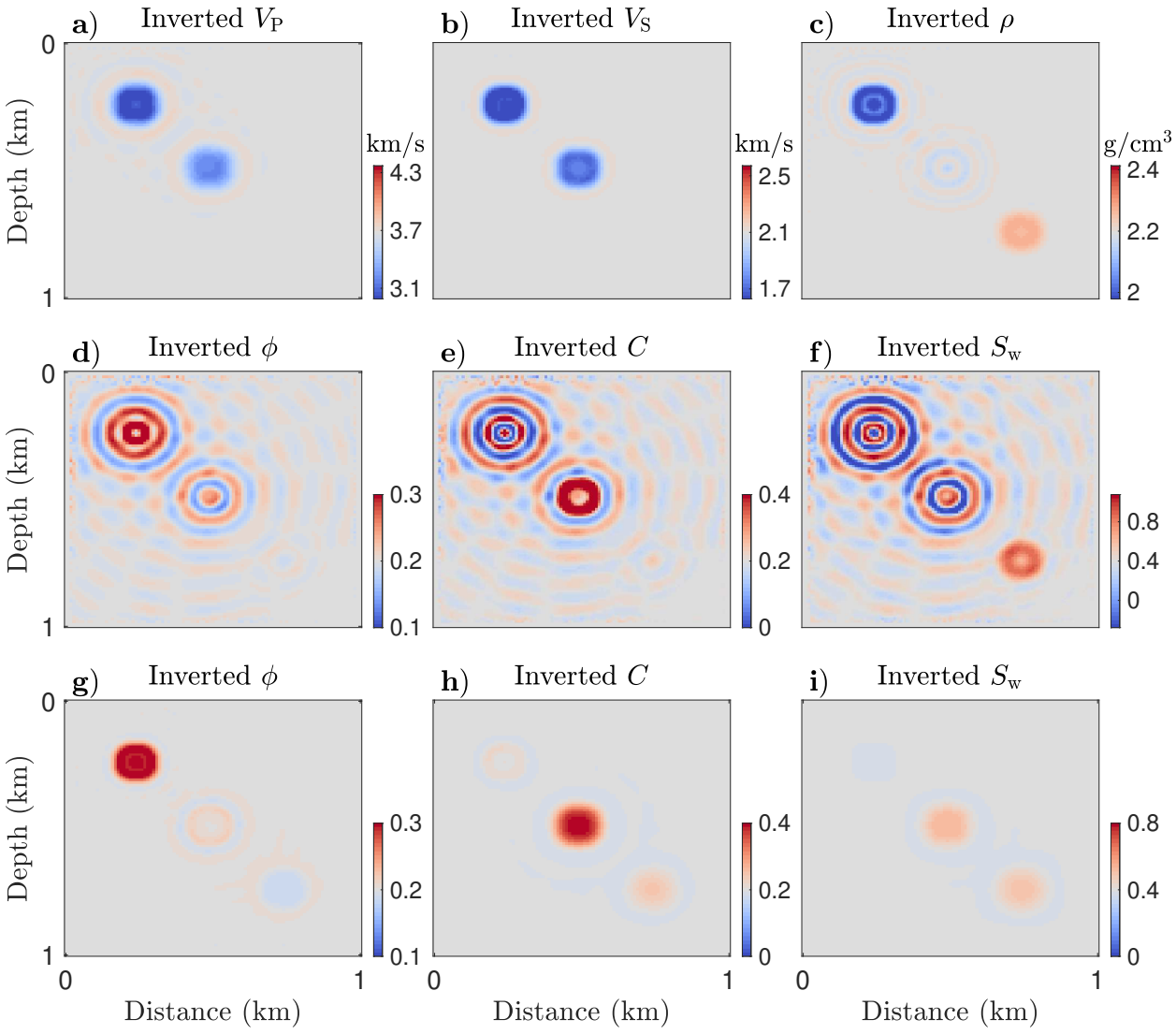

Figure 4.6: Inversion test to eliminate over-fitting. (a-c) Inverted V_P, V_S, and ρ models respectively; (d-f) ϕ, C, and S_w models derived indirectly via the DV parameterization. (g-i) Inverted ϕ, C, and S_w derived directly within the PCS parameterization.

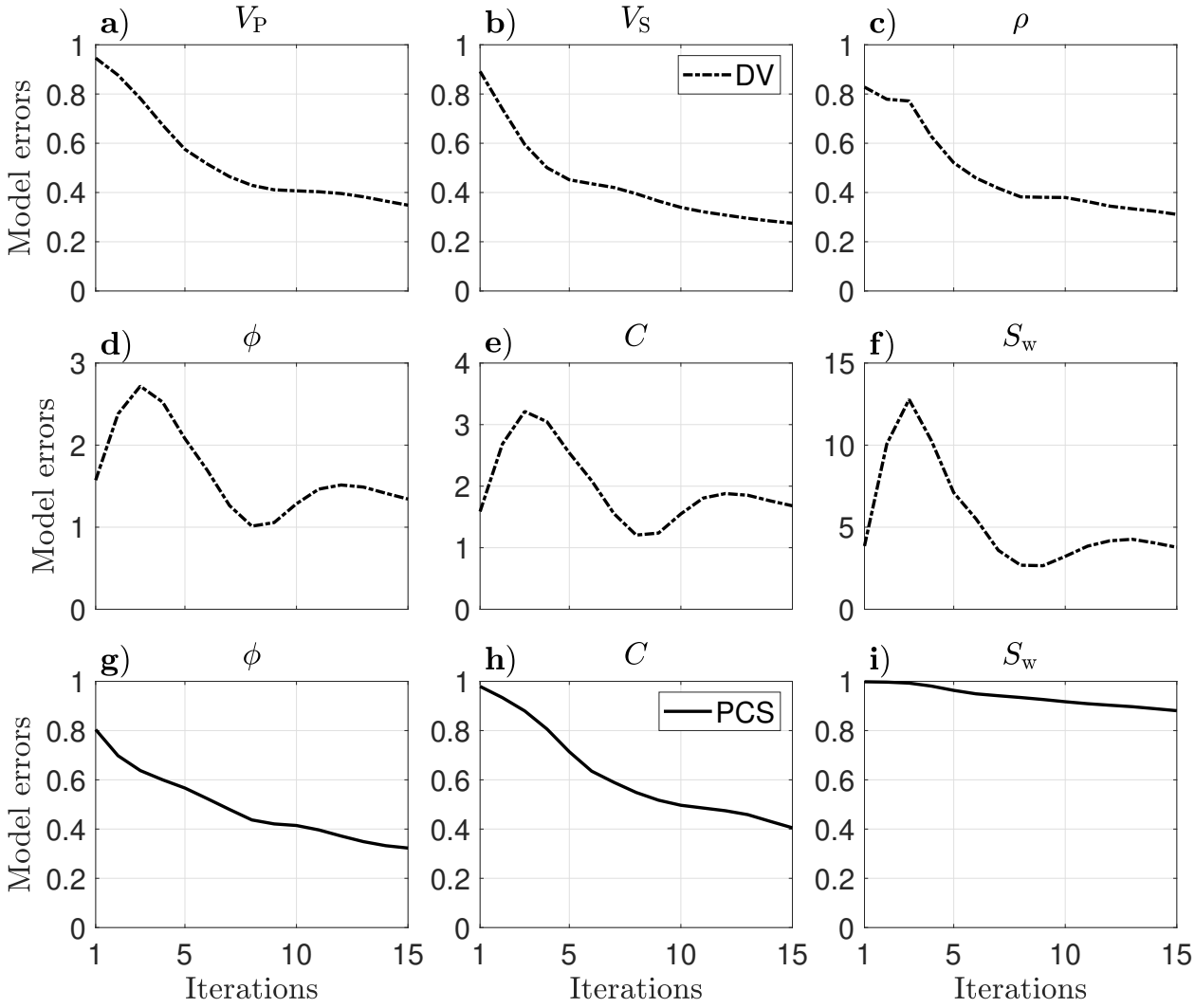

Figure 4.7: (a-c) Model error reductions of V_P, V_S, and ρ and (d-f) ϕ, C, and S_w in the DV parameterization. (g-i) Model error reductions of ϕ, C, and S_w in the PCS parameterization.

To distinguish between these two possible causes, I repeat the experiment employing a frequency strategy which, although more expensive, is much less prone to overfitting. In this attempt, only one outer FWI iteration is carried out per band, and each band contains six frequencies, distributed from 2 Hz to a maximum frequency that grows as the iteration progresses, beginning at 3 Hz, and increasing by 1 Hz per iteration to a maximum of 17 Hz. This increase in the total number of frequencies reduces the chances of overfitting to any particular frequency band. The results are plotted in Figures 4.6 and 4.7. The indirect/DV

parameterization still has difficulty recovering the rock physics properties (Figure 4.6d-4.6f); in fact similar results to those of the previous case (Figure 4.2d-4.2f) are estimated. Moreover, the error curves (Figure 4.7d-4.7f) increase in a manner very similar to those in Figure 4.5d-4.5f. Thus we see no evidence within the numerical tests that the issues with the indirect approach come from overfitting. My interpretation is that the ill-conditioned mapping from the DV parameters to the PCS parameters tends to magnify spurious variations in the DV parameters produced through the EFWI iterations. Within the direct approach this error magnification is avoided.

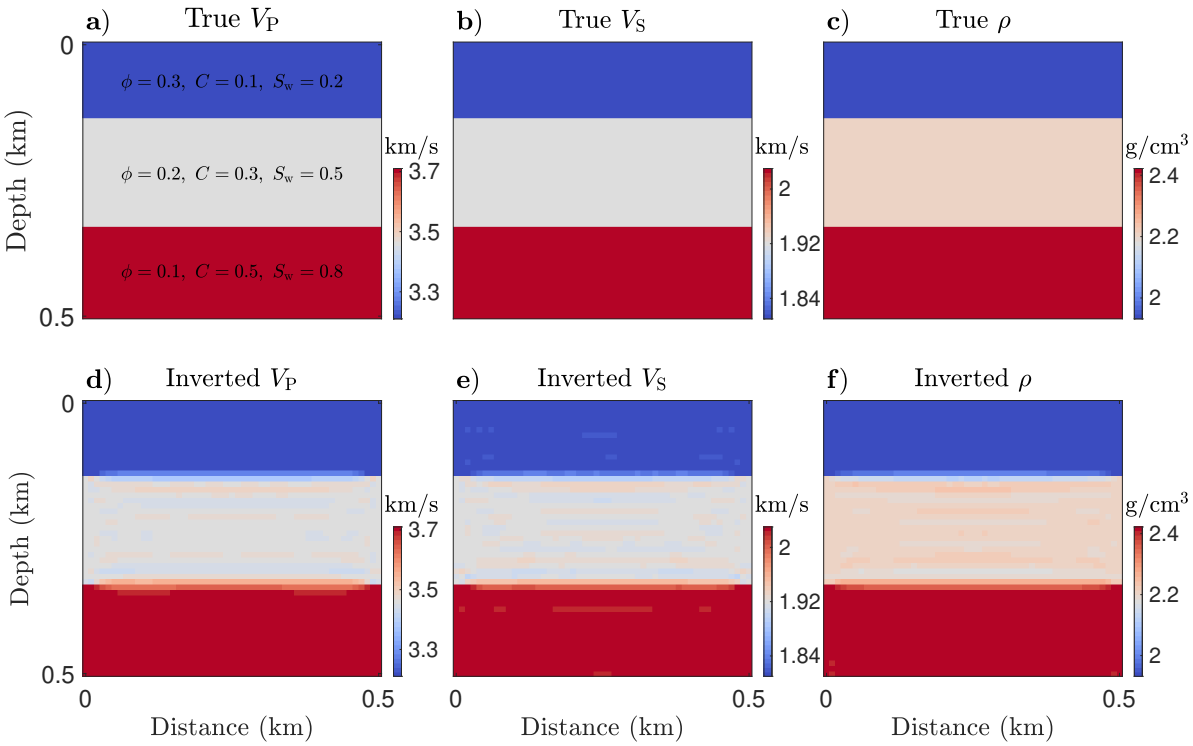

Figure 4.8: Layered model tests. (a-c) True models; (d-f) standard EFWI-recovered V_P, V_S, and ρ models in the DV parameterization.

We next move away from the circular anomaly model, to one involving a simple layered geology. A three-layer model (0.5 km $\times$ 0.5 km), where a constant porosity, clay content, and water saturation are assigned to each layer (Figure 4.8a). The initial models are generated by smoothing the true models. Within the DV parameterization, apart from some mild

oscillatory behavior, the inverted velocity and density models match closely with the true ones (Figure 4.8). After converting these recovered velocity and density model values to the rock physics properties with the Han model, the artifacts become significantly more pronounced, and in fact begin to mimic structure (Figure 4.9g-4.9i). The recovered water saturation appears particularly distorted. In contrast, the directly recovered models within the PCS parameterization exhibit reduced artifacts and the spatial extent of each layer can be clearly identified (Figure 4.9j-4.9l).

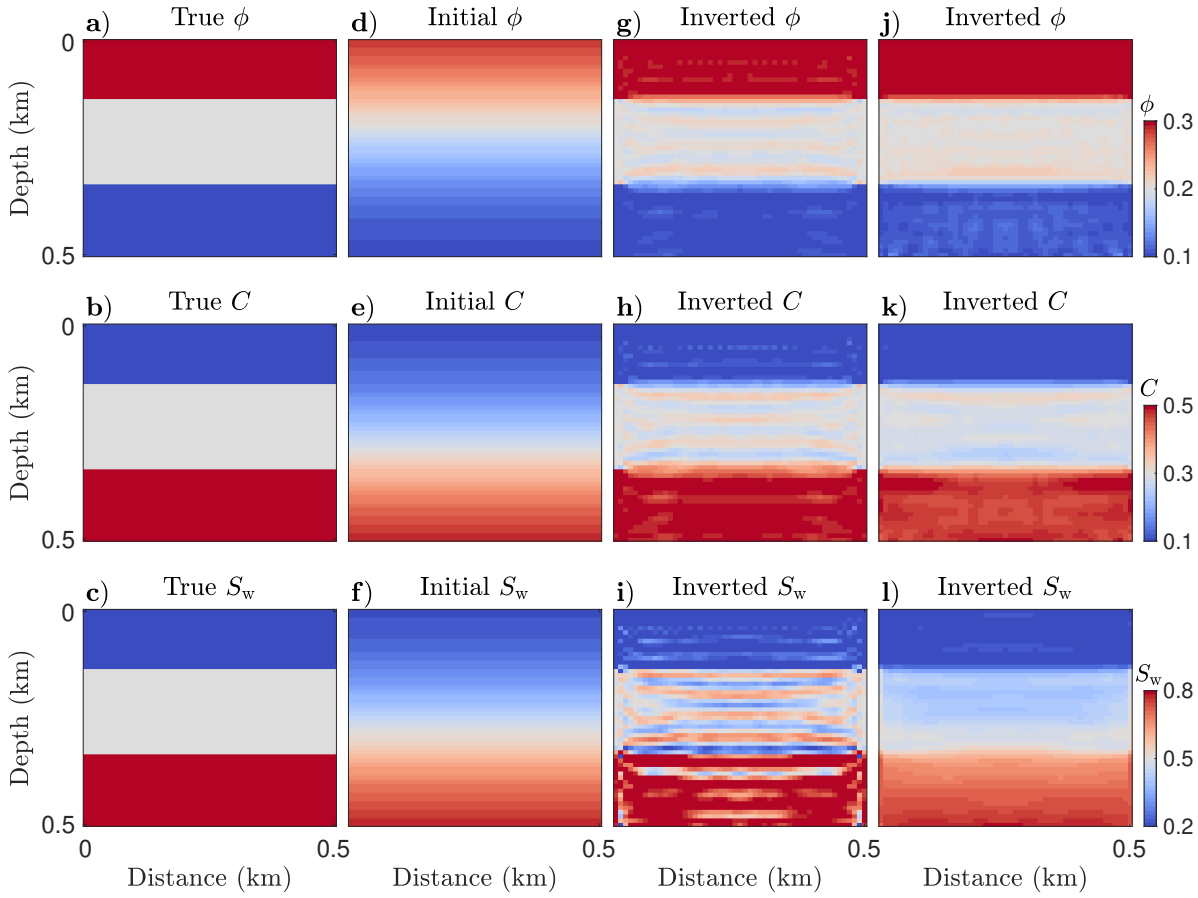

Figure 4.9: Direct versus indirect inversion tests on layered model. (a-c) True models; (d-f) the initial ϕ, C, and S_w models respectively. (g-i) Indirectly inverted models via the DV parameterization. (j-l) Directly inverted models within the PCS parameterization.

Extracted profiles at a lateral position of x =250 m are plotted in Figure 4.10: we observe more clearly the magnification of the oscillatory artifacts within the indirect/DV parameter-

ization. However, we also observe that the recovered C and S_{w} models, though oscillatory, appear to oscillate about a more accurate average within each layer. The direct/PCS inversion appears to be selecting a smoother, more stable solution.

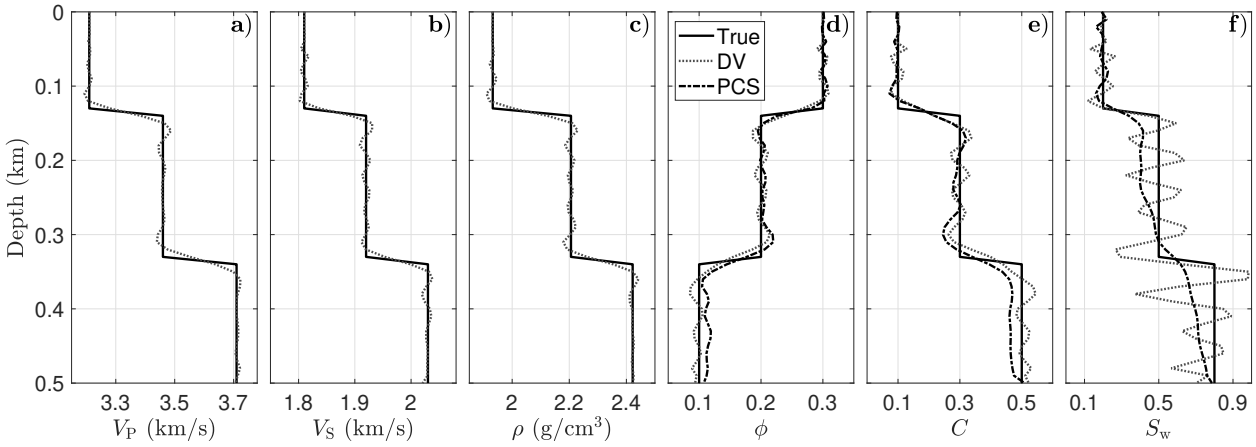

Figure 4.10: (a-f) Model profiles for V_{P}, V_{S}, ρ, ϕ, C, and S_{w} at $x = 0.25$ km. The solid, dotted, and dash-dotted lines denote the true model, the inverted model within the DV parameterization, and the inverted model within the PCS parameterization.

4.4.2 Structure and parameter values from EFWI: Han model

With this set of comparisons in place, I introduce a more geologically realistic reservoir model to examine the ability of the direct rock-physics EFWI approach to identify and characterize hydrocarbon units. I select a 1 km×1 km part of the elastic Marmousi2 model and assign rock physics properties to each cell (Figure 4.11a-4.11c). In Figure 4.11d-4.11f the "true" porosity, clay content, and water saturation models are plotted. A gas sand trap, at a depth of 0.38 km and positioned at 0.4 km laterally, is distinguished by a higher porosity of 0.31, a lower clay content of 0.13, and a lower water saturation of 0.34.

The initial rock physics property models in Figure 4.11g-4.11i are smoothed versions of the true models. With the PCS parameterization, we observe that a high-resolution inversion result, capturing the relevant reservoir structures, is recovered (Figure 4.11j-4.11l). Within the recovered models, the gas sand can be identified. In Figure 4.12 vertical profiles of the

true, initial, and inverted models at lateral position 0.4 km are plotted.

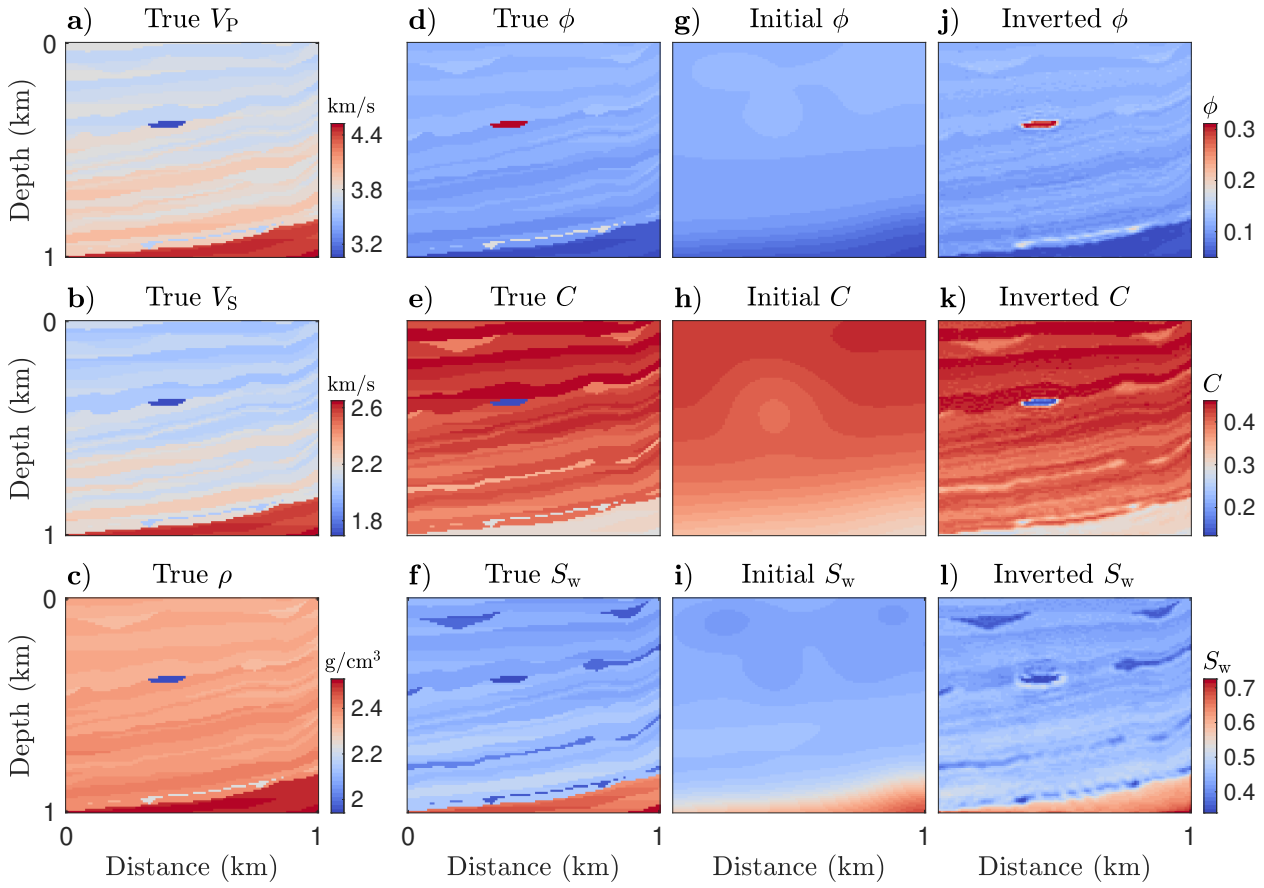

Figure 4.11: (a-c) True models of V_P, V_S, and ρ. (d-f) True models, (g-i) initial models, and (j-l) the corresponding inversion results of ϕ, C, and S_w.

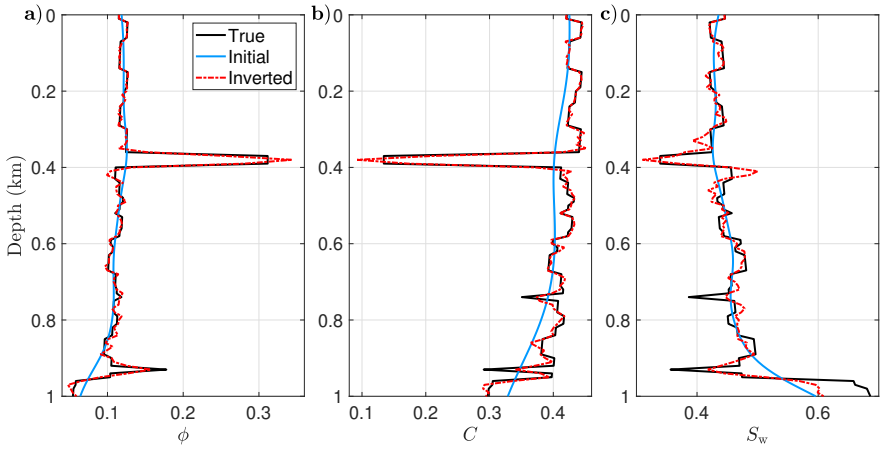

Figure 4.12: Vertical profiles extracted from the true, initial, and inverted (a) ϕ, (b) C, and (c) S_w models at lateral position 0.4 km.

4.4.3 Structure and parameter values from EFWI: VRH and KT

I next examine direct/PCS parameterized inversions within the more complex VRH and the KT rock physics models, both of which involve nonlinear relationships between the rock physics properties and the standard elastic properties (i.e., velocity and density). I apply the direct EFWI algorithm to each of the three simulated models used previously. In all of these experiments, the true and initial rock physics properties are fixed to be the same as those used for the Han model. Because the rock physics relations are different, this means that the P-wave, S-wave, and density values are different from those in the Han examples. In Figures 4.13-4.15 the inversion results for the circular anomaly model, the layered geological model, and the modified Marmousi model, respectively, are plotted for both the VRH and KT cases. We observe that in each experiment, the three rock physics properties can be resolved to some extent, indicating that the direct approach is suitable for a range of different rock physics relations, even those exhibiting relatively high degrees of nonlinearity. However, we also observe significant variations between the results for the three models, though all other features of the inversions are kept fixed. Comparing with the Han model, VRH and KT appear to be less capable of recovering the Marmousi model parameters, but more capable with the three-layer model. This implies that the complexity (or degree of non-linearity) of the rock-physics relations is not the sole governing factor in how rock physics EFWI performs. I am not in this chapter advancing any full explanation for this aspect of the results — further study is needed. The results are suggestive that parameter cross-talk is generally an issue for recovering rock physics properties (especially Figure 4.13d-4.13f).

Because most rock physics models are nonlinear, an analytical solution of the rock physics inverse problem, as in the case of the Han model (equation 4.8), is not available. To improve the comparison between the direct and indirect inversions, I examine here an indirect approach for recovering KT parameters in the Marmousi case. The method adopted to transform elastic attributes to rock physics properties is the Bayesian approach proposed by Grana (2016a), where a linearization of the KT model is derived and validated. Combining

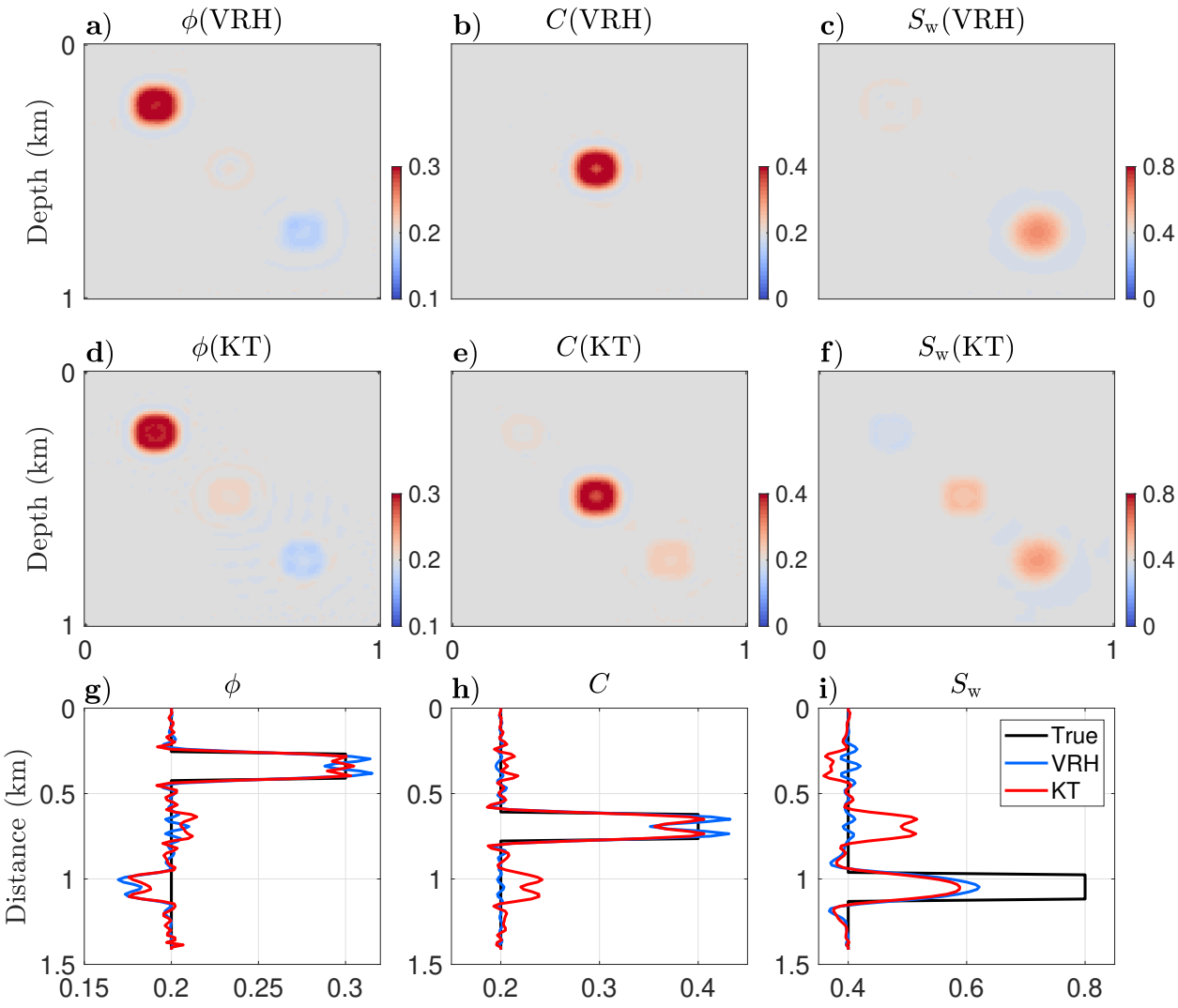

Figure 4.13: Nonlinear rock physics model parameters, circular anomaly case. Inverted ϕ, C, and S_w models are plotted for (a-c) the VRH model and (d-f) the KT model. (g-i) Profiles extracted from the true and inverted models at diagonal position x=z.

this with a Gaussian assumption for the prior model, the solution of the inverse problem is represented by a Gaussian posterior distribution with explicit expressions for the posterior mean and covariance. In this experiment, I assume only one well is available, and it is located at a lateral position x=0.7 km. I also assume the well-log data of elastic and rock physics properties are exact. The prior information of ϕ, C, and S_w is collected from this well. The data errors in V_P, V_S, and ρ are assumed to be Gaussian distributions with zero mean and with standard deviations estimated by comparing their EFWI results at the well location

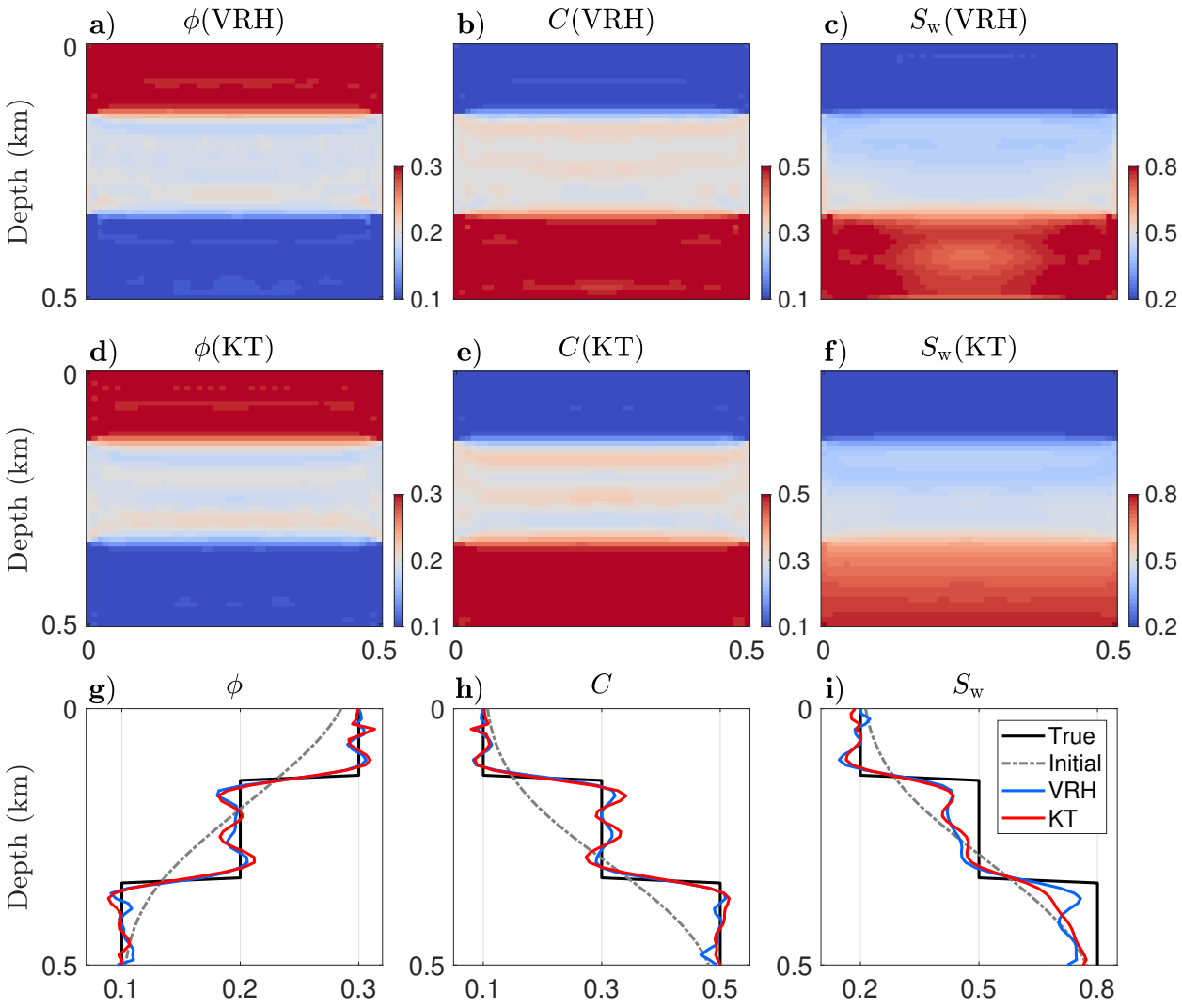

Figure 4.14: Nonlinear rock physics model parameters, layered geology case. Inverted ϕ, C, and S_w models are plotted for (a-c) the VRH model and (d-f) the KT model. (g-i) Vertical profiles extracted from the true, initial, and inverted models at lateral position 0.25 km.

with their logs. In Figure 4.16 the results of the indirect approach are summarized. The true V_P, V_S, and ρ models (Figure 4.16a-4.16c) are calculated from the true ϕ, C, and S_w models (Figure 4.11d-4.11f) based on KT. The estimated V_P, V_S, and ρ models via the DV parameterized EFWI are plotted in Figure 4.16d-4.16f. These are used next as input data in the Bayesian approach to find the MAP (maximum a posterior) solution of ϕ, C, and S_w (Figure 4.16g-4.16i).

In Figure 4.17 I plot the vertical profiles of the true model (Figure 4.11d-4.11f), the

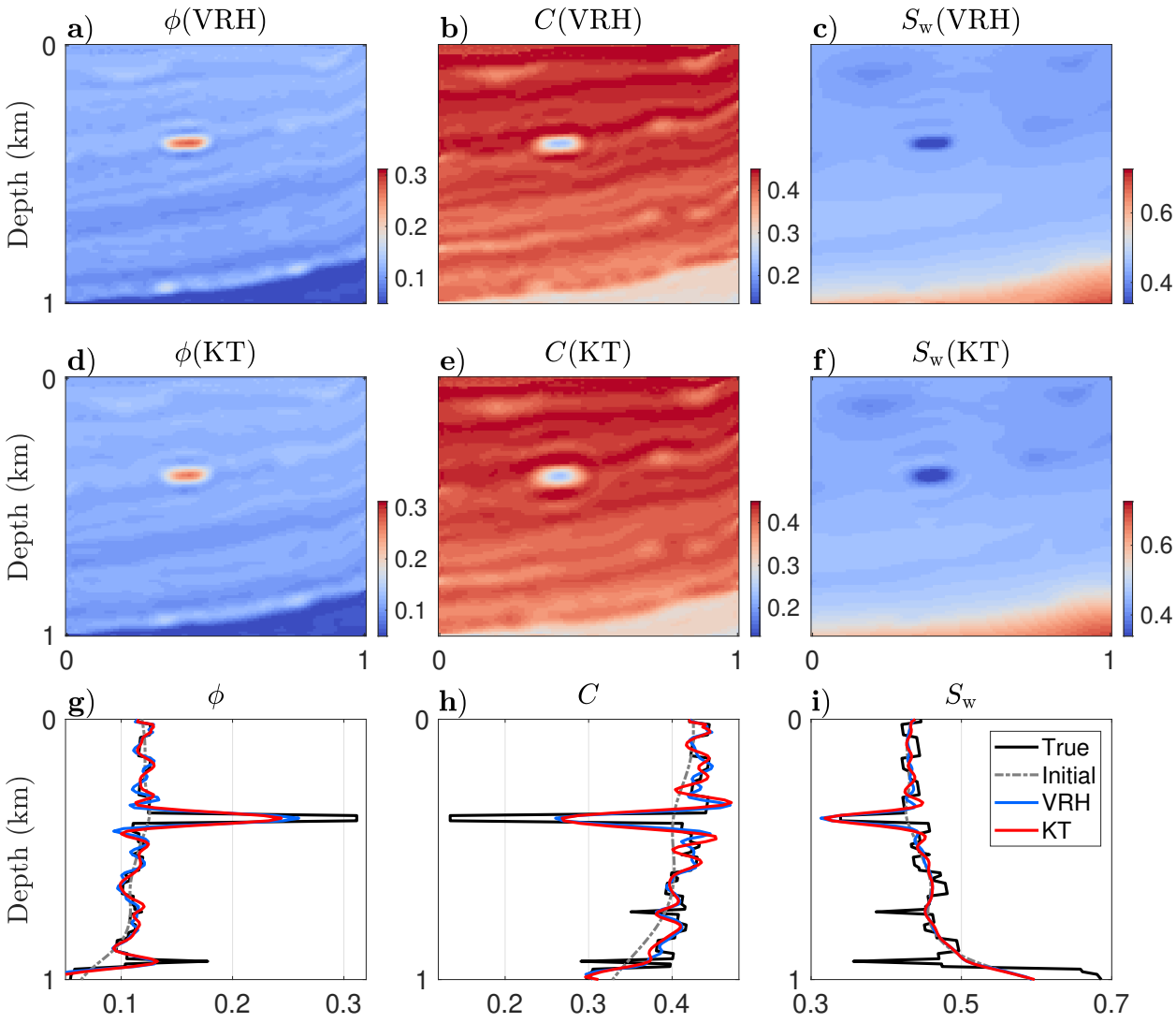

Figure 4.15: Nonlinear rock physics model parameters, modified Marmousi case. Inverted models of ϕ, C, and S_w with (a-c) VRH and (d-f) KT. (g-i) Vertical profiles extracted from the true, initial, and inverted models at lateral position 0.4 km.

inverted model within the direct/PCS parameterization (Figure 4.15d-4.15f), and the inverted model within the indirect/DV parameterization (Figure 4.16g-4.16i) at lateral positions x=0.7 km (Figure 4.17a-4.17c) and x=0.4 km (Figure 4.17d-4.17f), respectively. Within the DV parameterization, I consider the recovered rock physics properties at the well location to be reasonably accurate, however, they deviate significantly from their true models in the gas sand area at x=0.4 km. This is because the prior information derived from the

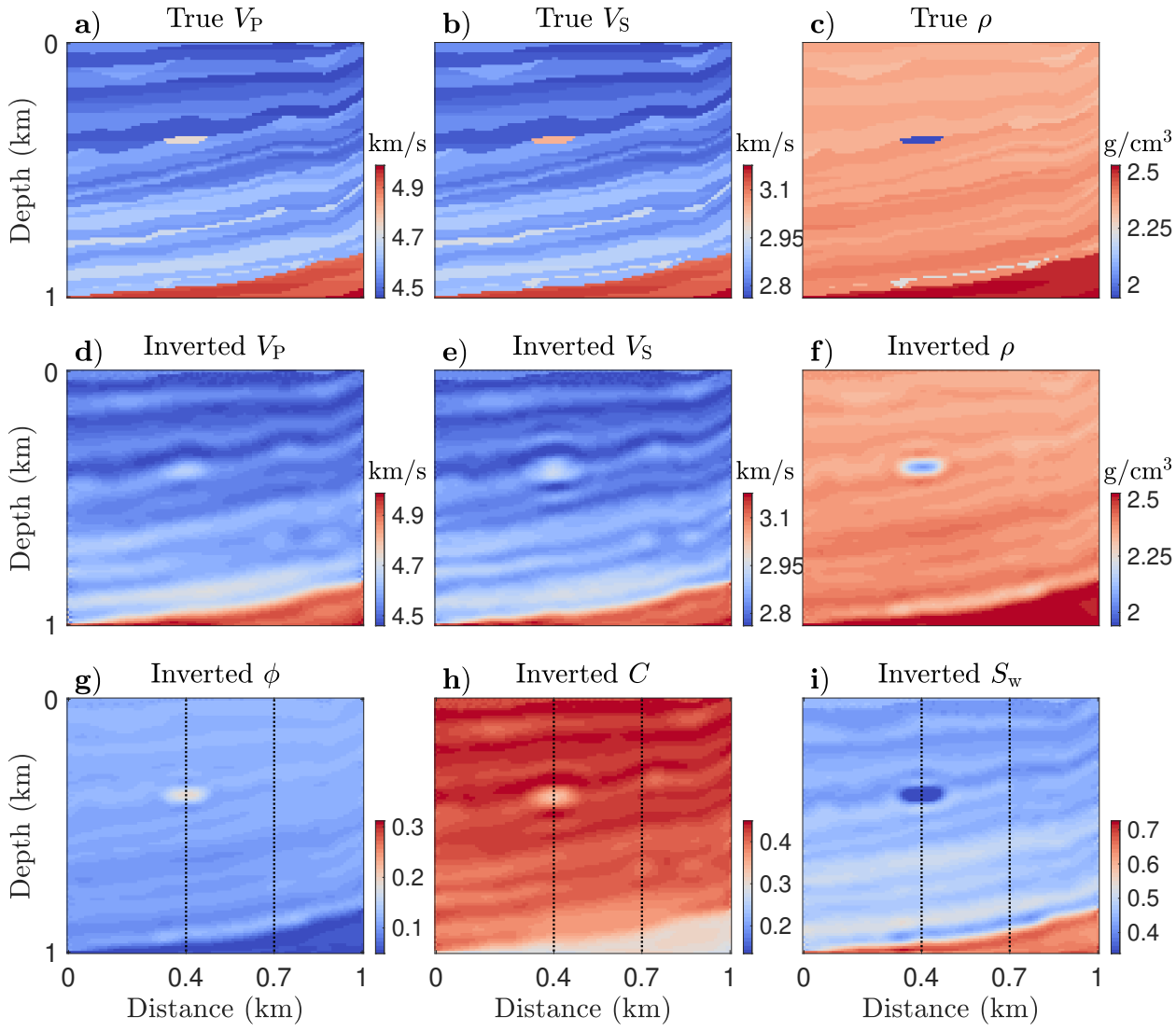

Figure 4.16: Indirect/sequential inversion test with KT. (a-c) True V_P, V_S, and ρ models; (d-f) Inverted V_P, V_S, and ρ models via the DV parameterized EFWI. (g-i) MAP solution of ϕ, C, and S_w derived from (d-f) via a Bayesian rock physics inversion. The black dotted lines denote two QC logs at x=0.4 km and x=0.7 km.

well is insufficient to include lateral heterogeneity. Within the PCS parameterization, the recovered ϕ and C match more closely the true models, especially at the gas sand; the S_w of the gas sand is also better estimated. However, we also observe a significantly improved overall reconstruction of S_w using the indirect approach, which, by contrast, leads to a poor estimate of S_w in the Han model case. I explain the improved performance of the indirect approach as a consequence of incorporating prior information into the inversion. The

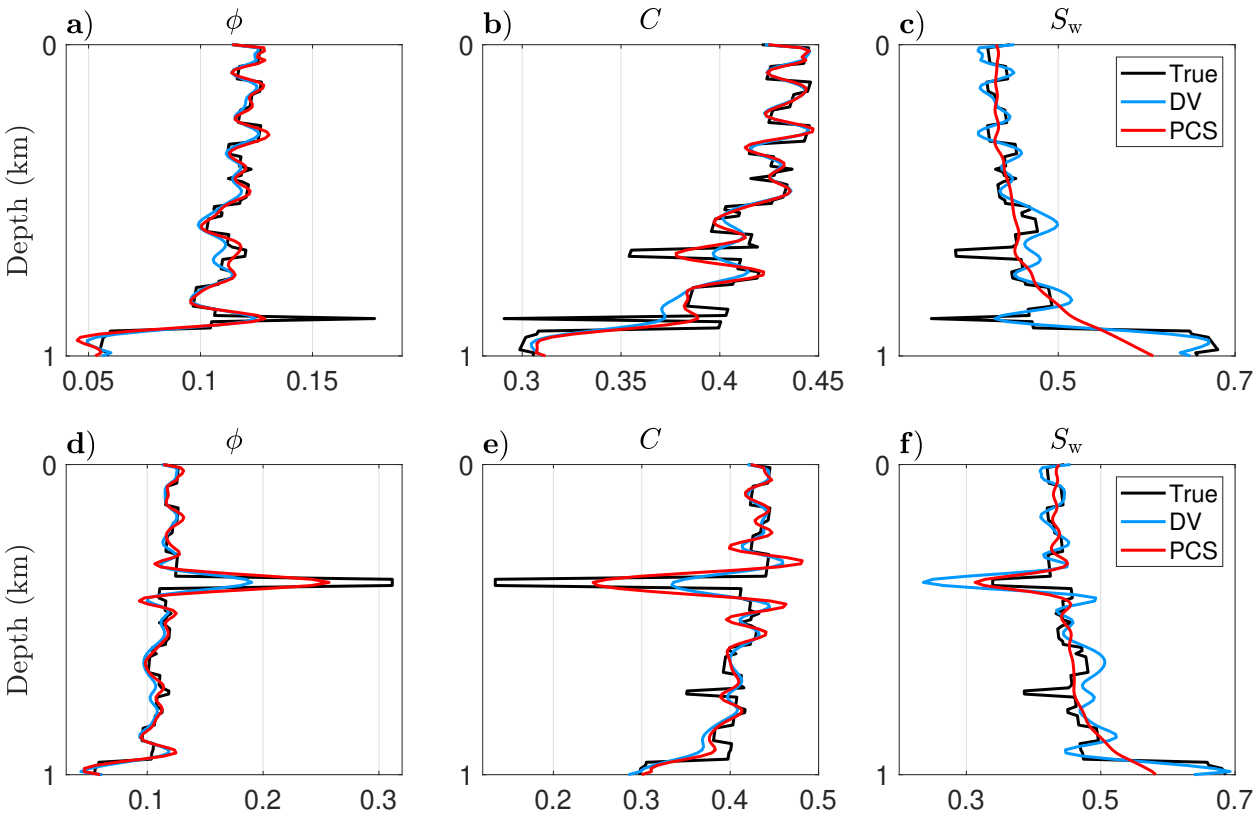

Figure 4.17: Vertical profiles of ϕ, C, and S_w at (a-c) x=0.7 km and (d-f) x=0.4 km. The black, blue, and red lines denote the true model, the inverted model within the DV parameterization, and the inverted model within the PCS parameterization, respectively.

prior information, including the prior marginal distribution of each rock physics property (although not informative enough) and the exact correlation between them, helps stabilize the inversion, and eventually brings the most benefit to S_w, which is unlikely to be resolved without any prior information.

We also note that the Bayesian rock physics inversion allows for uncertainty quantification, but this uncertainty only makes a statement about the probability of the rock physics properties, given the inverted elastic model, i.e., $P(\phi, C, S_w|V_P, V_S, \rho)$. There is no such mode of uncertainty in the direct inversion, for which the only meaningful uncertainty relates to the probability of the rock physics properties given the measured seismic data, i.e., $P(\phi, C, S_w|d_{obs})$. For an FWI problem, this probability is impractical to assess given the high cost of forward modeling and the large dimensionality of the model.

4.5 Discussion

Water saturation is evidently the most difficult property to recover with the formulations I have considered. This, as well as the cross-talk observed in many of the results, can be explained via scattering radiation pattern analysis. Given the scattering coefficients of an elastic parameter set (e.g., Pan et al., 2018a), I derive the PCS radiation patterns using the chain rule (Figure 4.18), assuming background porosity, clay content, and water saturation values of 0.2, 0.4, and 0.8, respectively. We observe that the radiation patterns of the three rock physics properties exhibit, in many cases, significant correlation, which helps explain the leakage in the circular anomaly examples. Moreover, we observe that the scattered wave amplitude per unit water saturation is much less than that of the amplitude per unit of clay content and porosity. Because my expectation is that each of these parameters could vary with similar amplitude ranges, it is apparent that the water saturation will have less impact on measured data than the other two, making it more difficult to recover. Also, within the Han model, the saturation has no impact on P-wave or S-wave velocities and may therefore be expected to experience many of the same difficulties in inversion as does density.

One possible solution to manage the difficulties of extraction of water saturation is to use a sequential strategy, in which two or more inversion stages are involved. Updating of the water saturation could be delayed in such an approach, until it could be supported by reasonable inverted porosity and clay content models. Another approach would be to move away from the water saturation parameter with a new parameter to which seismic data are more sensitive. The density and bulk modulus of the fluid mixture, ρ_f and K_f, are candidates. Historically various fluid factors used in AVO inversion (e.g., Russell et al., 2011), have produced useful results.

We also find a consistency between my sensitivity analysis and those done in poroelastic FWI. For example, De Barros and Dietrich (2008) illustrate that, for consolidated fluid-saturated poroelastic media, the seismograms are strongly influenced by perturbations of porosity and solid phase properties (e.g., ρ_s and G_s). On the other hand, changes in fluid

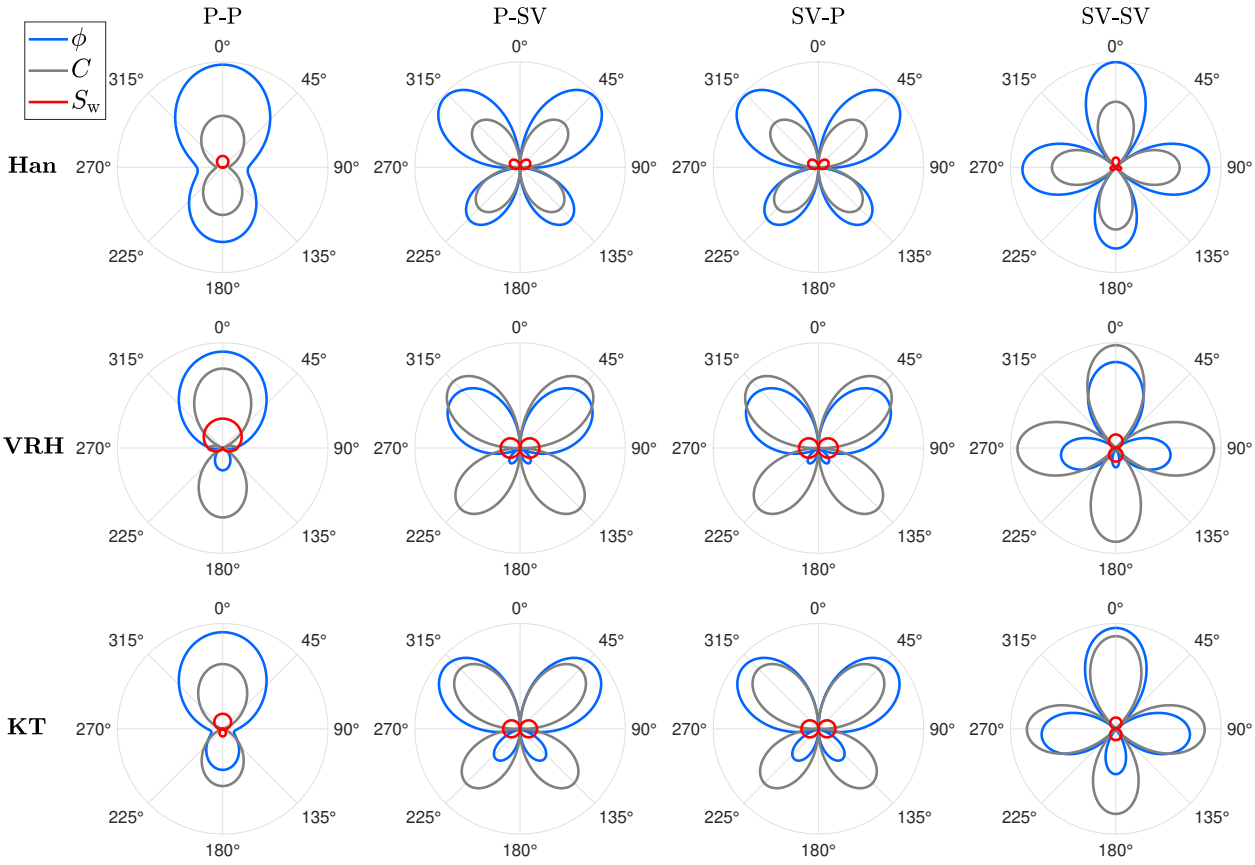

Figure 4.18: Scattering radiation patterns for point ϕ, C, and S_{w} perturbations in the PCS parameterization, formulated for the three rock physics models.

properties (e.g., ρ_f and K_f) have only a weak influence on wave amplitudes. Moreover, the radiation patterns of (ϕ, C, S_w) in my study are similar to the radiation patterns of (ϕ, G_s, ρ_f) within the (K_s, G_s) parameterization from Yang et al. (2019). As a result, I anticipate that some conclusions from the poroelastic case might be applicable as well to an EFWI-based parameter resolution study with respect to rock physics properties.

In the indirect approach, when the Bayesian framework is used, the prior information of rock physics properties is incorporated into the inversion. In contrast, the direct inversion for rock physics properties is a naive EFWI which relies on data residuals only. As a result, the two approaches are not compared in a completely fair manner, as prior information can be used as well for EFWI, e.g., through a model regularization term (Asnaashari et al., 2013; Aragao and Sava, 2020), to deliver more reliable results. The fact that direct inversion

generates improved results over the two-stage indirect approach, despite the lack of prior information, is suggestive of the merit of the approach, though naturally more analysis is required. Also, if assuming more well logs are available, in the meantime we improve the indirect results by allowing a more informative prior model, we should explore if this prior model can make the direct EFWI better posed. The difference between these two approaches remains methodological, whereas a crucial issue is to develop the direct inversion by combining prior information. In Appendix C, I provide an example of employing regularization techniques in the rock physics parameterized FWI framework.

Examination of optimization and model type are also important steps in moving this research forward. Optimization method changes are likely needed to reduce the degree of cross-talk, especially within EFWI-PCS when the rock physics model is complex/nonlinear. Other rock physics models, empirical or theoretical, based on either effective media or contact theory, are worth examining, if only because of the variations we have observed across the three test models, Han, VRH, and KT. One possible limitation in setting up a PCS inverse scheme arises for non-analytic rock physics models. Most rock physics models are analytic, i.e., provide elastic attributes as explicit functions of PCS. The computation of their partial derivatives is straightforward. However, for models such as the self-consistent approximation and the differential effective medium (Berryman, 1995) that can only be numerically solved, it might be difficult to evaluate the chain rule in equation 4.4.

4.6 Conclusions

I formulate elastic FWI with rock physics model parameterizations to achieve a direct estimation of parameters of immediate interest in reservoir characterization. Three rock physics models, Han, VRH, and KT, are chosen to formulate the inversion with a parameterization of porosity, clay content, and water saturation. Synthetic examples show that porosity and clay content can be reliably recovered, whereas water saturation is prone to insufficient updating. Analysis of the relevant radiation patterns reveals the very low sensitivity of seismic

data to this property. The proposed framework can be easily adjusted for examination of other rock physics relations and parameterizations.

It is also demonstrated that the direct approach can generate improved results over the two stage indirect approach, which suffers from the ill-conditioned mapping from elastic to rock physics properties. This conditioning issue, however, can be managed using prior model information such as those collected in wells. A further study of how similar information could be incorporated into the direct inversion is essential for better addressing the difference between the two workflows.

Chapter 5

Seismic time-lapse monitoring of CO_2 with rock physics parameterized FWI

5.1 Summary

Carbon capture and storage is an important technology for greenhouse gas mitigation. Monitoring of CO_2 storage should, in addition to locating the plume, provide quantitative information on CO_2 saturation. I propose a full waveform inversion (FWI) algorithm for the prediction of the spatial distribution of CO_2 saturation from time-lapse seismic data. The methodology is based on the application of a rock-physics parameterized FWI scheme that allows for direct updating of reservoir properties. I derive porosity and lithology parameters from baseline data and use them as input to predict CO_2 saturation from monitor data. The method is tested on synthetic time-lapse data generated for the Johansen formation model. Practical issues associated with field data applications, such as acquisition limitations, construction of the initial model, noise, and uncertainty in the rock physics model, are taken into account in the simulation. The results demonstrate the robustness of this approach for reconstructing baseline and monitor models. I also illustrate the potential of the approach as compared to conventional two-step inversion algorithms, in which an elastic FWI prediction

of velocities and density is followed by rock physics inversion.

5.2 Introduction

An important technology supporting reduction of greenhouse gas emissions is the geological storage of carbon dioxide (Davis et al., 2019; Ringrose, 2020; Pörtner et al., 2022); for instance, deep saline aquifers have been identified as promising sites for carbon dioxide (CO_2) storage. To ensure and verify the safe geological containment of CO_2 underground, monitoring of CO_2 storage site performance is mandatory (Rütters et al., 2013). Injection of CO_2 into the brine-saturated rocks of a saline aquifer changes the elastic moduli, and therefore the seismic response of these media, making seismic a primary technology for monitoring. Time-lapse seismic surveys, in which a series of seismic data sets are acquired at time intervals, provide a monitoring mode in which migration and distribution of the injected CO_2 can be tracked, and leakage problems if any can be identified (Arts et al., 2003; Chadwick et al., 2005; Romdhane and Querendez, 2014; Ghosh et al., 2015). Ideally, for reliable conformance verification, quantitative estimates/maps of CO_2 saturation would be produced by such technology, to be compared against reservoir modeling predictions (Dupuy et al., 2021a).

Qualitative interpretation of CO_2 from analysis of amplitude changes and time shifts on post-stack seismic images is generally insufficient to understand detailed reservoir conditions (Alemie, 2017). Moreover, multiple reflections, interference effects such as tuning, and attenuation introduce ambiguities into seismic images which impede estimation of CO_2 position (Queißer and Singh, 2013b; Furre et al., 2015). A promising approach to address these issues involves seismic full waveform inversion (FWI), a set of methods with the capacity to produce high-resolution subsurface models, by involving a more complete subset of the information content of seismic data (Tarantola, 1986; Brossier et al., 2009; Virieux and Operto, 2009). FWI, although computationally intensive, in principle accounts for all of these wave propagation effects, and high-resolution elastic parameter models (e.g., velocity,

density, and modulus) derived from FWI can be directly linked to reservoir (or rock physics) properties, such as porosity, fluid saturation, and pore pressure. FWI therefore appears to be a potentially powerful tool for quantitative CO_2 characterization and monitoring.

Progress has been reported in managing many of the challenges of practical FWI, which include its computational complexity, dependence on the starting model, sensitivity to incomplete data, etc. (Operto et al., 2013; Prieux et al., 2013a; Métivier et al., 2017; Pan et al., 2019). Time-lapse FWI faces several additional challenges, not least of which is the need to detect very small changes in the model, changes that are easily obscured by ambient noise, variable near-surface conditions, and acquisition non-repeatability (Kamei and Lumley, 2017). Efforts have been made to mitigate non-repeatability, through design of monitoring systems (Shulakova et al., 2015), data processing strategies (Roach et al., 2015), and inversion strategies (Asnaashari et al., 2015; Maharramov et al., 2016; Alemie, 2017; Kamei and Lumley, 2017; Fu et al., 2020). As these progress, basic consideration of how to optimally extract critical parameters, especially fluid saturation indicators, becomes increasingly important. In CO_2 storage applications, rock properties are typically extracted sequentially, with the seismic inversion process geared towards determination of elastic properties, from which the actual properties of interest are subsequently determined, often qualitatively (Johnston, 2013; Zhang et al., 2013). Queißer and Singh (2013a) applied elastic FWI to the Sleipner time-lapse seismic data, and correlated velocity changes with CO_2 saturation changes using Gassmann's equation; also at Sleipner, Dupuy et al. (2017, 2021a) combined acoustic FWI and rock physics inversion to obtain spatial distribution of CO_2 saturation with uncertainty assessment. This aspect of uncertainty quantification is critical for CO_2 storage monitoring as decisions have to be taken based on the monitoring results. However, reports of quantitative, waveform-based CO_2 saturation predictions are uncommon.

The sequential approach itself is neither a necessary, nor always optimal, strategy. The estimation of reservoir properties directly from the seismic data (as opposed to serially, after

elastic parameters are first estimated) has several distinct advantages, the main one being that it involves an integrated wave propagation and rock physics formulation, maintaining consistency between elastic and reservoir properties (Doyen, 2007; Bosch et al., 2010). Inversions of this type can be found in seismic amplitude variation with offset (AVO) settings (Bosch et al., 2007; Spikes et al., 2007; Grude et al., 2013; Liu and Grana, 2018; Grana et al., 2020), but only very recently have FWI formulations in this mode been examined. Poroelastic FWI (De Barros and Dietrich, 2008; Morency et al., 2009; Yang et al., 2019) moves in this direction, for instance, though the inverse problem is reported to be highly under-determined and ill-posed, and the computational burden very large (Dupuy et al., 2021a). Nonetheless, I identify the expansion of these efforts as a high priority, in order to take advantage of the more general models available to FWI over AVO (Mallick and Adhikari, 2015). In Chapter 4, I formulated a direct procedure for updating rock and fluid properties within elastic FWI (i.e., EFWI). This was achieved by re-parameterizing the inversion in terms of rock physics properties, adopting a viewpoint similar to that of Russell et al. (2011) within an AVO environment. The main advantages of this approach are: 1) it allows examination of any rock physics property that has a well-defined relationship with elastic parameters; 2) it leads to more stable solutions in comparison to those produced through sequential inversion; and 3) it shares the same numerical structure as the conventional EFWI. I also extended the approach to incorporate prior model information.

In this chapter, I have applied the rock physics parameterized FWI approach to the problem of CO_2 saturation prediction from time-lapse seismic data. To set out the results of these tests, I first describe the time-lapse FWI framework. I then systematically examine the response of the inversion to a synthetic time-lapse dataset. Specifically, I recover porosity and lithology parameters from the baseline seismic data, and then use these results as input in the monitor seismic survey, producing estimates of CO_2 saturation. The reliability of the approach is quantified by comparing it to conventional approaches. I end by discussing how uncertainties related to data and rock physics model affect CO_2 saturation reconstructions.

5.3 Theory

5.3.1 Rock physics parameterized FWI

The FWI algorithm I apply is an outgrowth of that set out in Chapter 4. I have illustrated that if we can express the elastic variables at each spatial position as a function of the rock physics variables at the same position: $(V_{\mathrm{P}}, V_{\mathrm{S}}, \rho) = f_{\mathrm{RPM}}(r_1, r_2, ..., r_n)$, using the chain rule we can move from the conventional FWI scheme to a new scheme in which the n different rock physics variables are directly updated. The implementation of this method requires a rock physics model f_{RPM}. In practice, the model used for inversion depends on the local geology and must be calibrated using well-log data or laboratory measurements, an example of which is given in Figure 3.16. For the numerical simulations in this chapter, I still assume that the model is known, as in Chapter 4, the difference is that I consider a more complete rock physics modeling process, and will analyze the influence of model errors on the inversion results.

For the target rock, I assume two mineral components, quartz and clay, and two fluid components, water and supercritical CO_2. Hence, I define three model unknowns: porosity (ϕ), clay content (C), and CO_2 saturation (Sc). The rock physics model f_{RPM} includes the following steps:

1) The mineral elastic moduli are computed using the VRH average (equation 3.5).

$$(K_m, \mu_m) = f_{\mathrm{VRH}}(C). \tag{5.1}$$

2) The fluid elastic moduli are computed using Brie's equation (equation 3.8), assuming semi-patchy mixing of water and CO_2.

$$(K_f, \mu_f) = f_{\mathrm{Brie}}(Sc). \tag{5.2}$$

3) The dry-rock elastic moduli are calculated using the stiff-sand model (equations 3.14-3.16).

$$(K_{\text{dry}}, \mu_{\text{dry}}) = f_{\text{Sand}}(\phi, K_m, \mu_m). \tag{5.3}$$

4) The fluid effect is included via Gassmann's equation to compute the elastic moduli of the saturated rock (equation 3.22).

$$(K_{\text{sat}}, \mu_{\text{sat}}) = f_{\text{Gassmann}}(\phi, K_m, K_f, K_{\text{dry}}, \mu_{\text{dry}}). \tag{5.4}$$

5) The density of the saturated rock is computed as a weighted average of the densities of mineral and fluid components. Consequently, we can express the velocity and density of the saturated rock as a function of the porosity, clay content, and CO_2 saturation:

$$(V_{\text{P}}, V_{\text{S}}, \rho) = f_{\text{RPM}}(\phi, C, Sc). \tag{5.5}$$

Other rock physics parameters in addition to the three variables, including the elastic moduli and density of each mineral/fluid component and the parameters of the stiff-sand model that describe grain contact, are fixed with the values in Table 5.1. The modulus and density of CO_2 at temperature 37 °C and pressure 0.01 GPa, given by Mavko et al. (2020), are used.

Table 5.1: Rock physics parameters used in this study

Parameter	Value	Parameter	Value
Quartz bulk modulus	37 GPa	CO_2 bulk modulus	0.02 GPa
Quartz shear modulus	44 GPa	CO_2 density	0.68 g/cm^3
Quartz density	2.65 g/cm^3	Effective pressure	0.01 GPa
Clay bulk modulus	25 GPa	Critical porosity	0.4
Clay shear modulus	9 GPa	Coordination number	9
Clay density	2.55 g/cm^3	Degree of adhesion	1
Water bulk modulus	2.25 GPa	Brie's exponent	5
Water density	1.03 g/cm^3		

5.3.2 Time-lapse FWI strategy

Quantitative CO_2 monitoring requires accurate and precise predictions of the CO_2 saturation model at any time at which the data are measured. Although it is possible to jointly invert the three parameters (porosity, clay content, and CO_2 saturation) from a single seismic survey, preliminary tests showed that fluid saturation is very difficult to estimate within this parameterization because of the large trade-off between rock physics parameters and its relatively small impact on the data. Here I consider a favorable case by making two assumptions: 1) before CO_2 injection, there is only one fluid component (water) in the subsurface; 2) porosity and lithology parameters are constant in time. Therefore, I propose to estimate the variables sequentially, a strategy similar to that of Grana et al. (2020) within a stochastic inversion framework and Dupuy et al. (2021a) within an FWI environment. First, I apply the rock physics FWI approach to the baseline (pre-injection) data for the estimation of porosity and clay content; then, I use the same inverse method and use the inverted porosity and clay content models as prior knowledge (fixed values) to estimate CO_2 saturation from the monitor (post-injection) data. The objective function for baseline model reconstruction is expressed as

$$E_b = \left\| \mathbf{d}_{\text{obs\_b}}(\phi^t, C^t) - \mathbf{d}_{\text{syn\_b}}(\phi, C) \right\|^2, \tag{5.6}$$

where $\mathbf{d}_{\text{obs\_b}}$ and $\mathbf{d}_{\text{syn\_b}}$ denote the observed and synthetic baseline data, respectively. ϕ^t and C^t denote the true porosity and clay content models. The baseline CO_2 saturation model is equal to 0 everywhere. The goal is to recover the ϕ and C models by iteratively minimizing the difference between $\mathbf{d}_{\text{obs\_b}}$ and $\mathbf{d}_{\text{syn\_b}}$.

The objective function for monitor model reconstruction is

$$E_m = \left\| \mathbf{d}_{\text{obs\_m}}(\phi^t, C^t, S^t_{c\_m}) - \mathbf{d}_{\text{syn\_m}}(\phi_{\text{inv}}, C_{\text{inv}}, S_{c\_m}) \right\|^2, \tag{5.7}$$

where $\mathbf{d}_{\text{obs\_m}}$ and $\mathbf{d}_{\text{syn\_m}}$ are the observed and synthetic monitor data, respectively. ϕ_{inv} and

C_{inv} are the inverted porosity and clay content models from the baseline survey. They are not updated in the monitor stage. The goal is to recover the saturation model S_{c_m} by iteratively minimizing the difference between $\mathbf{d}_{\text{obs\_m}}$ and $\mathbf{d}_{\text{syn\_m}}$.

5.4 Numerical Examples

I apply the proposed approach to a synthetic model generated from the Johansen data set. The Johansen formation is a deep saline aquifer located offshore of the southwest coast of Norway. The aquifer is a chosen site for the Northern Lights project, which plans to start operations in mid-2024, for storage of 1.5 million tonnes of CO_2 per year. The MatMoRA project of SINTEF has developed a set of geological models of Johansen based on seismic and well data (Eigestad et al., 2009; Bergmo et al., 2011). Petrophysical data including porosity and permeability are available.

5.4.1 Model description

The original full-field model is discretized by a $149 \times 189 \times 16$ grid, with 3 layers in Johansen. However, I consider 100×16 cells defined on an irregular grid in the vertical direction (Figure 5.1a). The uppermost layer situated approximately 600 m above Johansen is the Sognefjord formation, which is the main reservoir for the Troll hydrocarbon field. The low porosity layers above and below Johansen are the Dunlin shale and Amundsen shale, respectively. In particular, the Dunlin shale serves as a cap rock for the Johansen formation. To account for the lithologies of the geomodel, I introduce a clay volume (Figure 5.1b) negatively correlated with porosity, with a correlation coefficient of -0.9. Assuming the initial water saturation (before injection) is equal to 1 everywhere, the CO_2 saturation distribution within Johansen (Figure 5.1c) was calculated by simulating the fluid flow in year 110, 10 years after stopping a 100-year injection with a constant injection rate of 1.4×10^4 m^3/day (Grana et al., 2020).

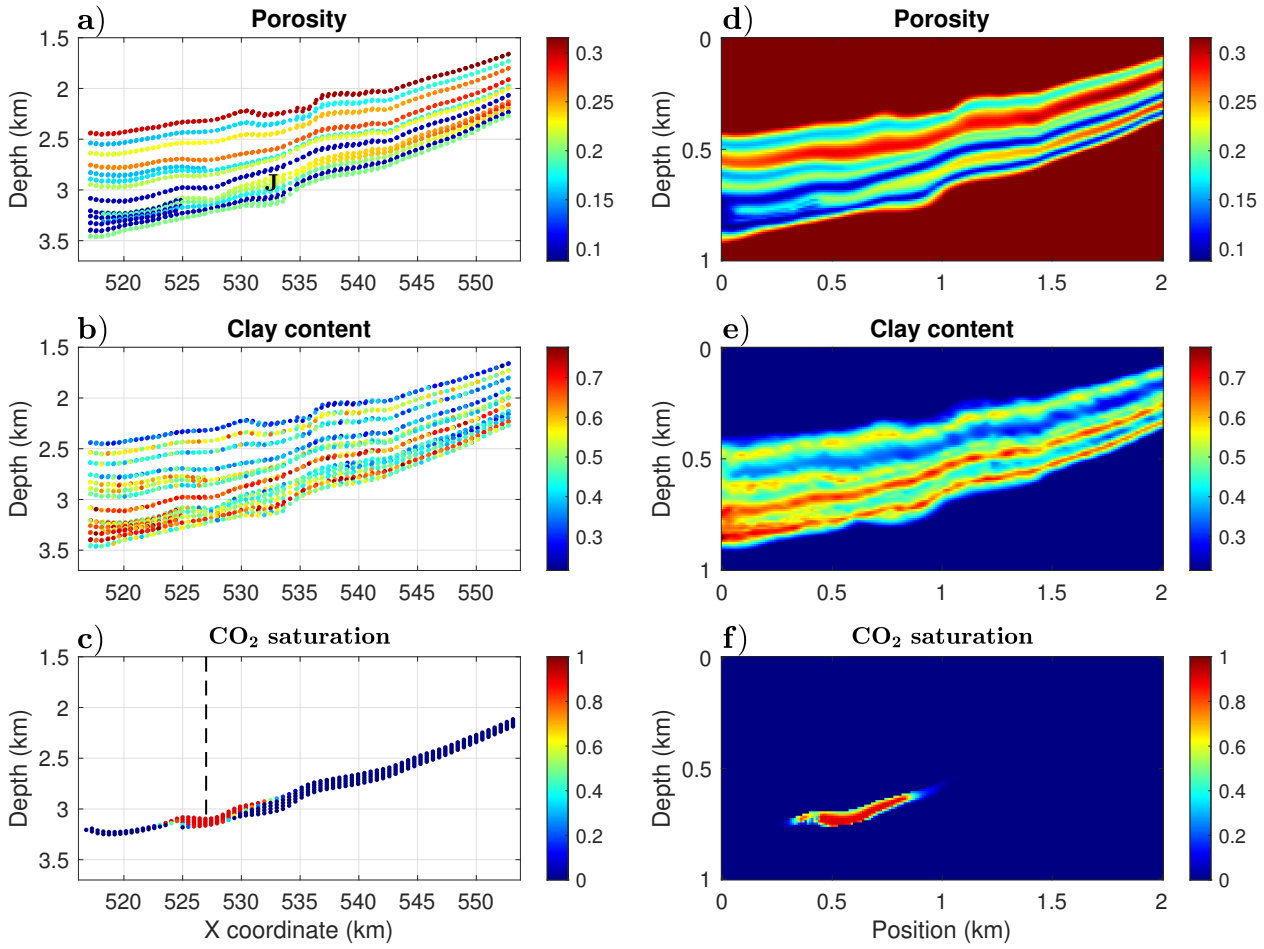

Figure 5.1: Johansen data set. (a-c) Full-field model and (d-e) corresponding model that uses a simplified geometry. The letter J indicates the location of the Johansen formation; the dashed line indicates the location of the injection well.

Because of computational limitations and lack of data, I create a synthetic model with the injection much shallower than in reality, and the top and bottom layers of the model are assumed to be homogeneous: first, I define a regular grid and interpolate the original data over the grid. The grid consists of 101×201 node points with a depth increment of 20 m and a position increment of 180 m; second, I change the spatial step to 10 m and use relative depth and position. The models in Figures 5.1(d)-(f) are then used to examine the proposed FWI method. The sandstone reservoir is distinguished by higher porosity and lower clay

content values compared to the surrounding shale. Porosity in the reservoir varies between 0.15 and 0.29, with the porosity within a zone degrading towards south as the depth of the formation increases. The initial CO_2 saturation is 0 everywhere and then changes locally due to the injection at 750 m depth. The maximum CO_2 saturation is 0.9.

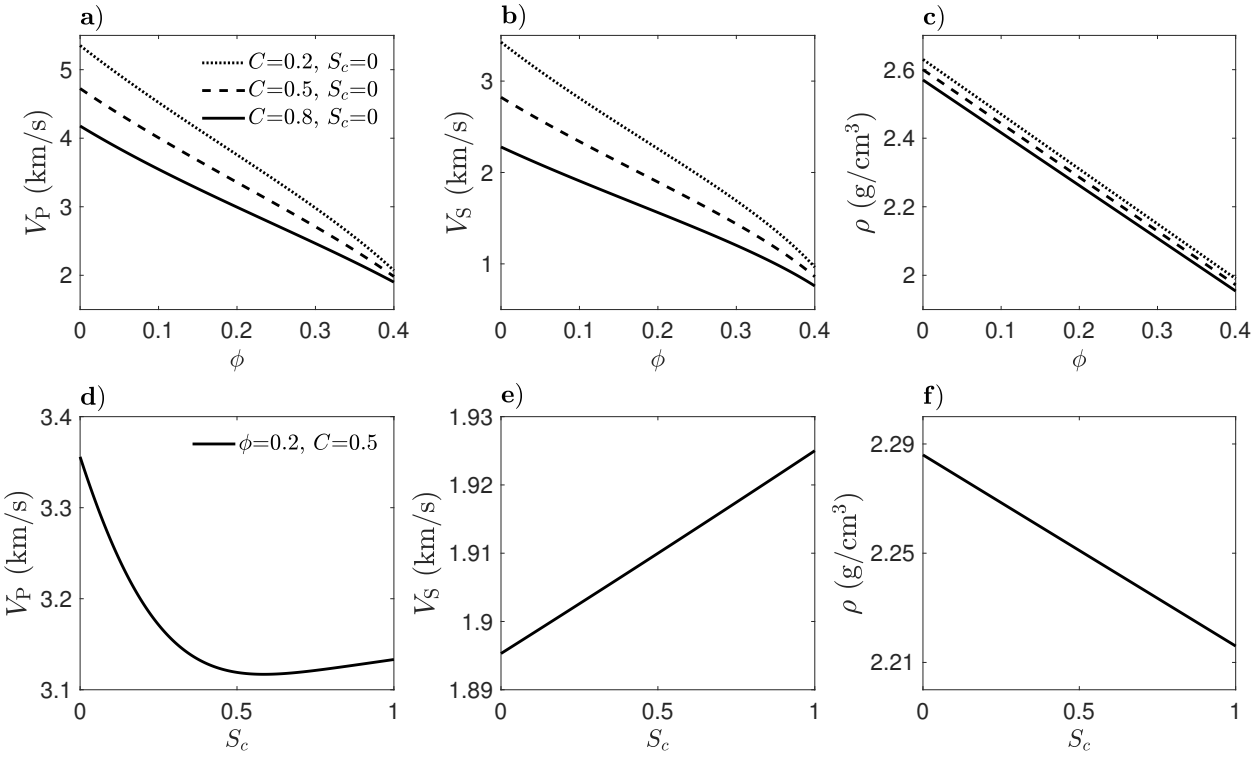

Figure 5.2: Theoretical curves of the stiff-sand model: P-wave velocity, S-wave velocity, and density versus (a-c) porosity and (d-f) CO_2 saturation.

In Figure 5.2, I compute velocities and density as a function of porosity, clay content, and CO_2 saturation based on the stiff-sand model. With CO_2 replacing water, the P-wave velocity of the saturated rock decreases due to the lower bulk modulus of CO_2, the density decreases due to the lower density of CO_2, and the S-wave velocity slightly increases since the fluid only affects the density in the S-wave velocity expression. The P-wave velocity does not decrease monotonically as CO_2 saturation increases because the relative change in bulk modulus is smaller than that in density when CO_2 saturation is larger than 0.6. It also shows that the sensitivity of the elastic attributes is dominated by porosity and to a lesser

degree by clay content and fluid saturation. In Figure 5.3, I plot the velocity and density models corresponding to the rock property model (Figures 5.1d-f). The time-lapse elastic changes are consistent with the analysis in Figure 5.2. The fluid effect is also well illustrated in the noise-free synthetic data (Figure 5.4).

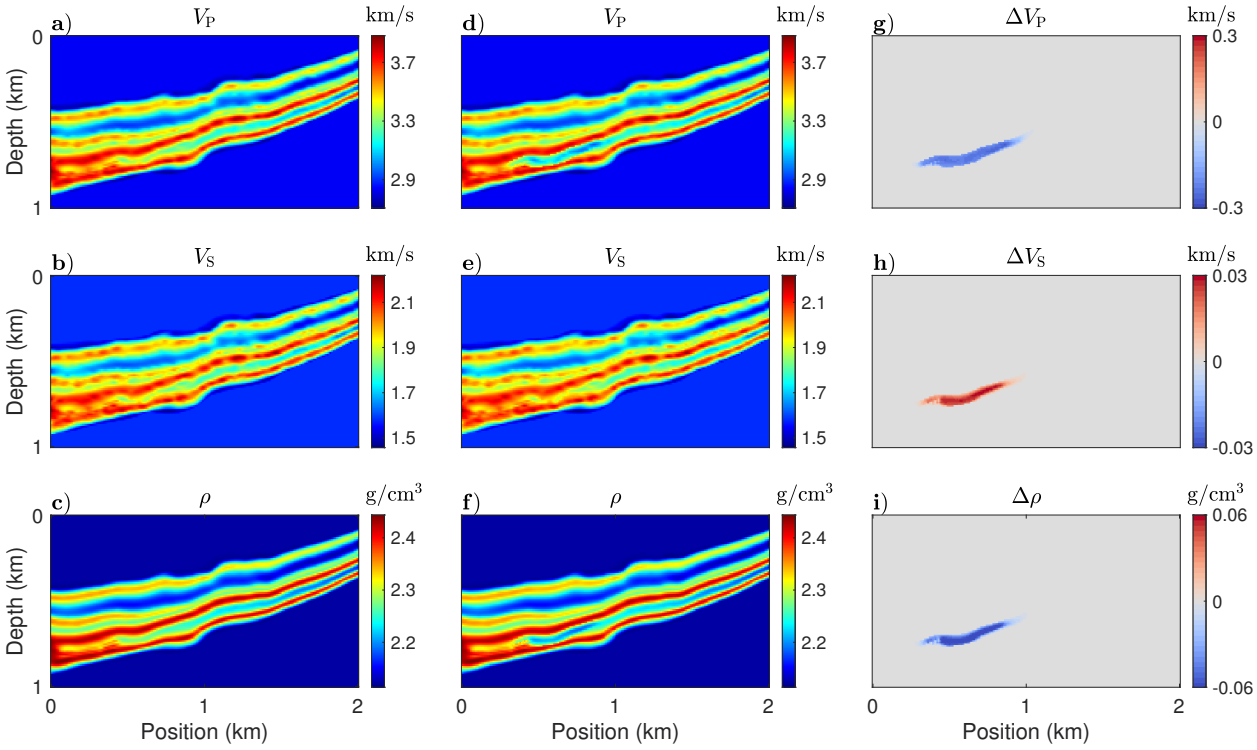

Figure 5.3: True (a-c) baseline, (d-f) monitor, and (g-i) time-lapse models of P- and S-wave velocities plus density.

The inversion experiments are presented in three parts. First, I carry out the direct, rock physics parameterized FWI approach with noise-free data (Figure 5.4), and compute the synthetic data in inversion using the same simulation through which the observed data are generated. Then, I repeat the test using conventional two-step inversions, in which velocities and density are first determined through elastic FWI, followed by rock physics properties. These simulations allow us to examine parameter resolution issues and make clear comparisons between the results of direct and two-step inversions. Finally, I take into account two different sources of uncertainty within the direct approach: uncertainty in the

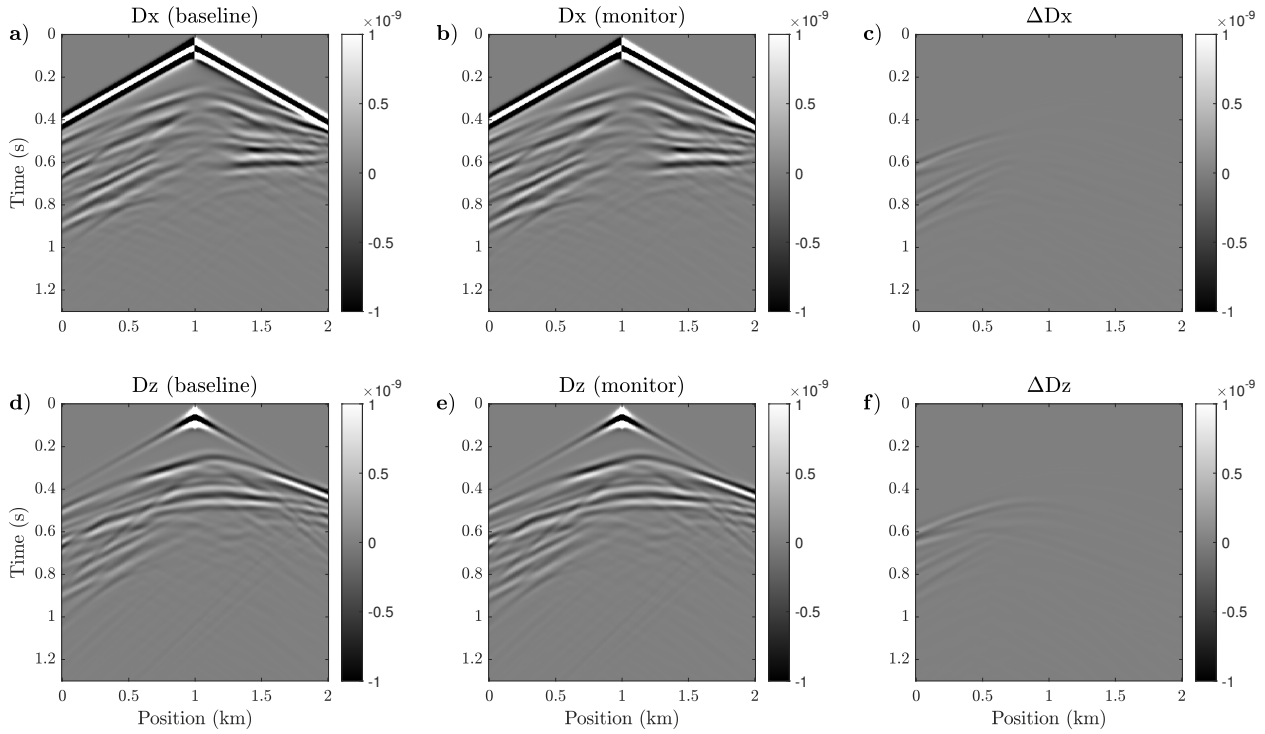

Figure 5.4: (a, d) Baseline, (b, e) monitor, and (c, f) differential seismograms computed for the true model. (a-c) Horizontal displacement. (d-f) Vertical displacement. The shot is located at position 1 km. Ricker wavelet source with a central frequency of 15 Hz is used.

data and uncertainty in the rock physics model.

In all tests, I consider a surface acquisition geometry, with 20 explosive sources every 100 m at 20 m depth and 100 receivers every 20 m at 10 m depth. The source signature is assumed to be known. The recorded data are multicomponent displacements. I adopt a multiscale approach (Bunks et al., 1995; Brossier et al., 2009) by inverting 10 frequency bands, each containing five evenly spaced frequencies from 2 Hz to a maximum frequency; the maximum frequency is 3 Hz for the first band, and it increases to 25 Hz for the last band (following the strategy advocated by Keating and Innanen, 2019b). A truncated Gauss-Newton optimization method (Métivier et al., 2017), comprising 20 inner iterations and 1 outer iteration for each frequency band, is used.

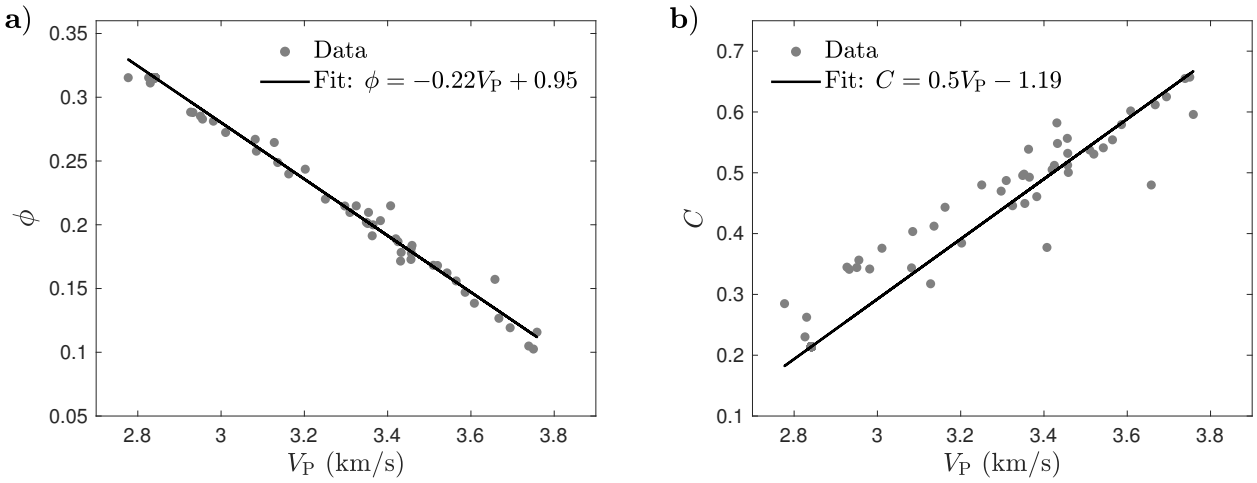

Figure 5.5: (a) $V_P - \phi$ and (b) $V_P - C$ relationships for constructing initial ϕ and C models. The data are from the true model (Figures 5.1d, 5.1e, and 5.3a) at lateral position 0.5 km.

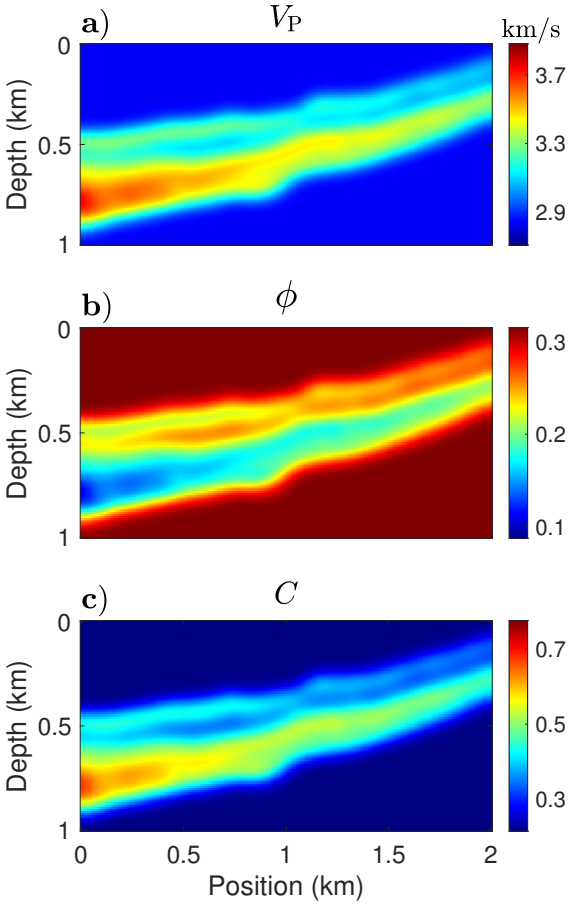

Figure 5.6: Initial models: (a) P-wave velocity, (b) porosity, and (c) clay content.

5.4.2 Direct FWI results

Baseline model reconstruction

One of the challenges of predicting rock physics properties from seismic data is the low frequency (initial) model. In a typical elastic inversion, the low-frequency model of velocity is often related to models used for seismic processing, for example stacking velocities. In the rock physics domain, a low-frequency model is more challenging to define because different lithologies might have different rock physics models (Grana et al., 2021). Here I derive the initial porosity and clay models from a filtered P-wave velocity model, using regressions of the direct measurements (well log data) of these variables, which are assumed to be available. I use linear regressions because the nonlinearity of the $V_{\mathrm{P}} - \phi$ and $V_{\mathrm{P}} - C$ relationships are not strong (Figure 5.5). As a result, the initial models in Figures 5.6 (b) and (c) are used in the inversion.

The recovered porosity and clay content models are reasonably accurate, with relatively low resolution near the left edge of the model due to limited observation aperture (Figure 5.7). The porosity seems better resolved than clay content thanks to the larger impact of porosity on seismic attributes (Figure 5.2). In Figure 5.8, the convergence properties of the inversion are summarized. I start iterations at low frequencies to prevent convergence of the objective function toward local minima, and then slowly introduce higher frequencies to image fine structures. The objective function has a sudden increase when entering into the next frequency band, but decreases to close to the original number after model updating. The solutions are examined via the relative model error $\xi = \|\mathbf{m} - \mathbf{m}_{\mathrm{t}}\|_2 / \|\mathbf{m}_0 - \mathbf{m}_{\mathrm{t}}\|_2$, where $\mathbf{m}$, $\mathbf{m}_0$, and $\mathbf{m}_{\mathrm{t}}$ represent the inverted, initial and true models, respectively, so that each model starts its iteration with a unit error. I observe the convergence characteristics of a reliable inversion. The model errors decrease monotonically, with porosity updated more efficiently than clay content. Figure 5.9 shows the comparison between the initial and inverted models in terms of the modeled data. The data residual is significantly reduced after inversion.

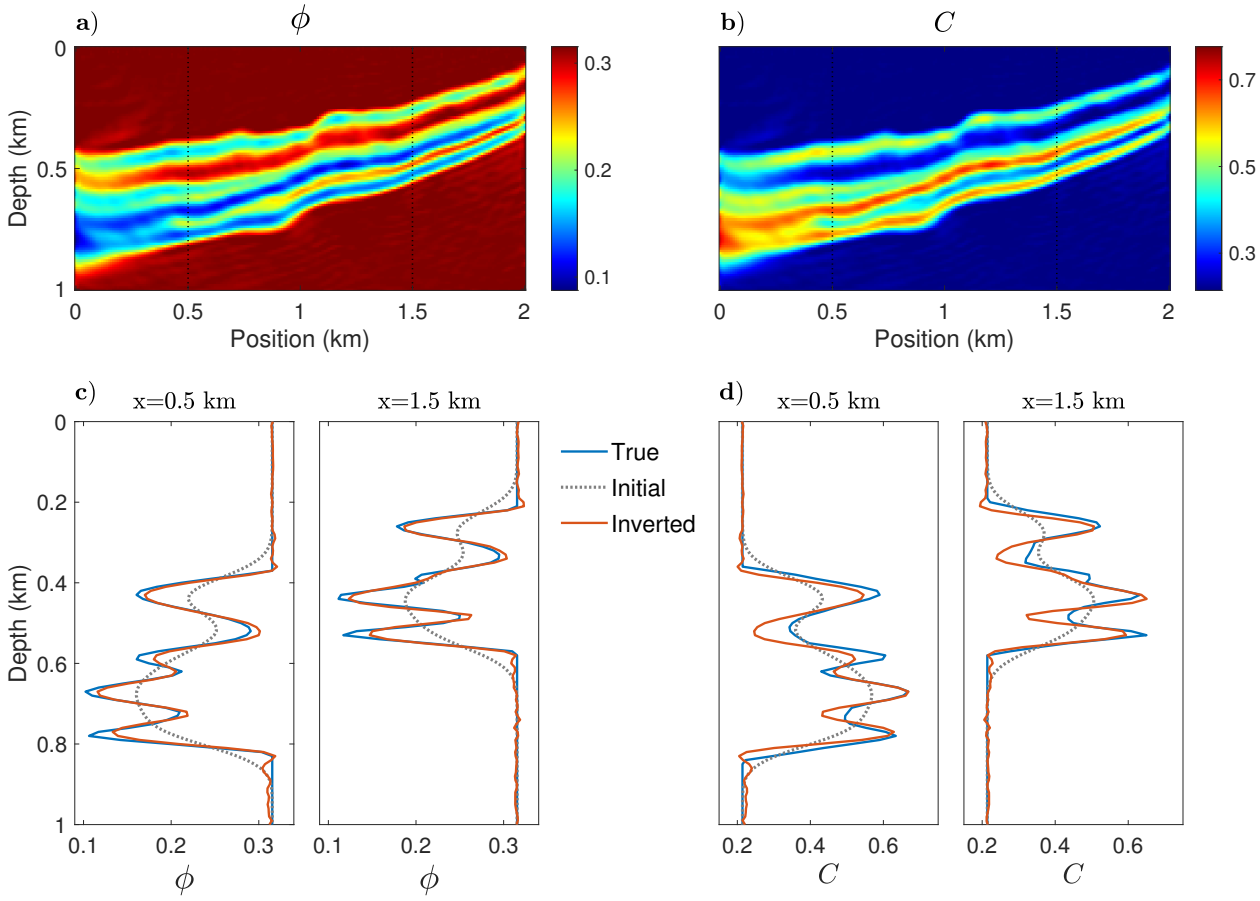

Figure 5.7: Inverted models: (a) Porosity and (b) clay content. (c,d) Vertical profiles extracted from the true, initial, and inverted models at lateral positions x=0.5 km and x=1.5 km.

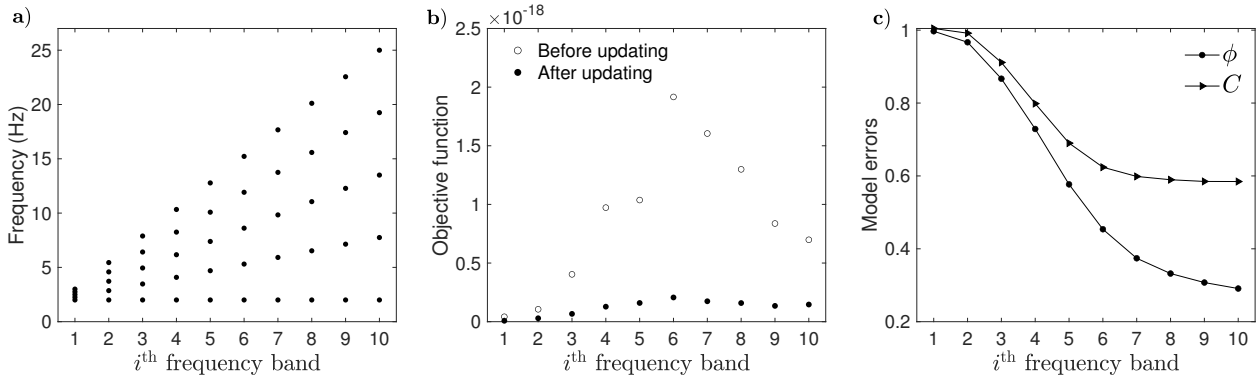

Figure 5.8: Convergence properties. (a-c) Frequencies, objective functions, and model errors (after updating) within a frequency band, respectively.

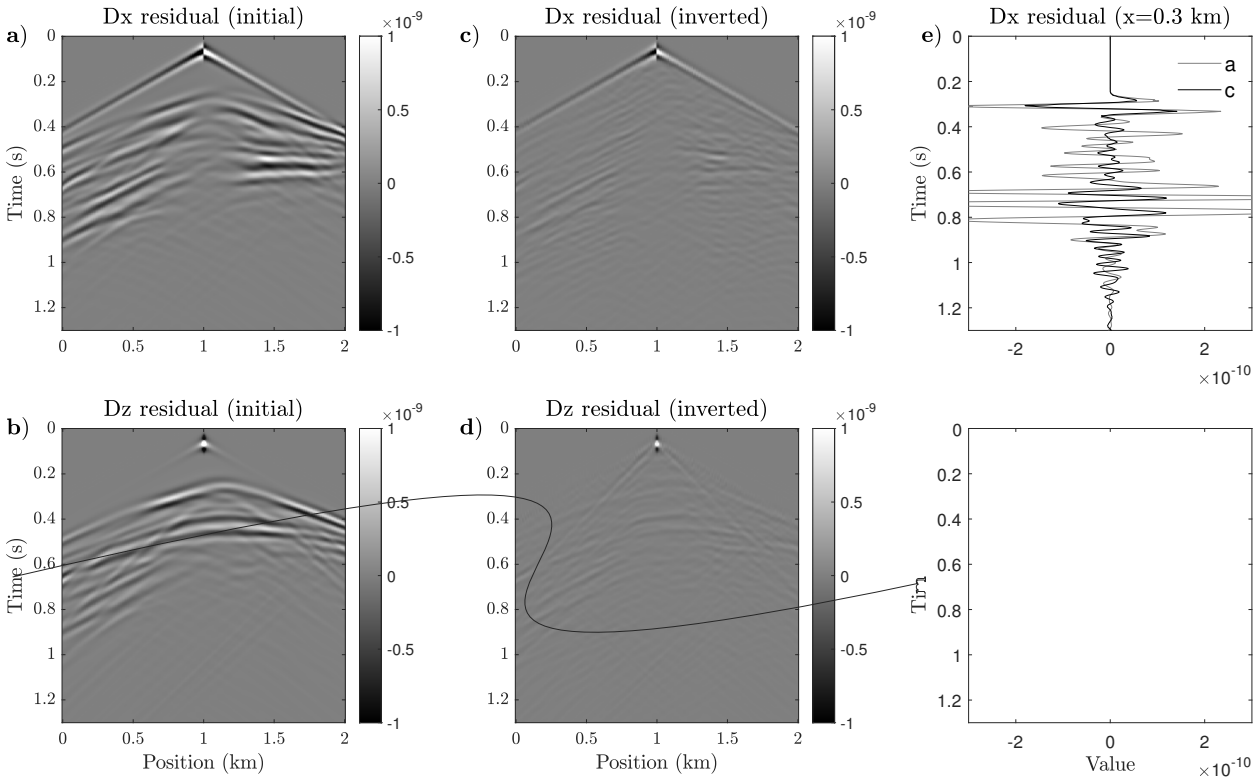

Figure 5.9: Baseline data residuals corresponding to the (a and b) initial model and (c and d) inverted model. (e and f) Vertical profiles of the data residuals at lateral position 0.3 km.

Monitor model reconstruction

In the monitor survey, the observed data is generated from the true model (Figure 5.1); the synthetic data is generated from the recovered baseline model (Figure 5.7) plus the current estimate of CO_2 saturation. For the initial guess of CO_2, I interpret the reservoir horizons from baseline estimates and restrict saturation variations within the reservoir. The interpreted horizons do not match exactly the rim of the plume (Figure 5.10a), allowing uncertainty related to horizons to be taken into account. Regarding saturation values, I use a Gaussian function varying only in the x direction with a maximum value of 0.9 at the location of the injection well (Figure 5.10b). For the inversion, I incorporate the first-order Tikhonov regularization term (Tikhonov and Arsenin, 1977; Asnaashari et al., 2013) into the objective function, to encourage a small degree of smoothness in the solution. The hyper-

parameter is chosen such that the ratio between the regularization term and data misfit is 1×10^{-4} at each iteration. The recovered model (Figure 5.10c) shows a good agreement with the true one, with both the spread of the plume and saturation values well estimated. The data residuals corresponding to the initial and inverted models are shown in Figure 5.11.

One of the advantages of the direct approach is that it allows elastic attributes to be jointly output with rock physics properties. In Figures 5.12 and 5.13, the velocity and density models corresponding to the rock physics estimates (Figures 5.7 and 5.10) are summarized. The elastic models are correctly retrieved, in particular, the predicted time-lapse elastic changes match closely the true ones, showing great consistency between the baseline and monitor reconstructions.

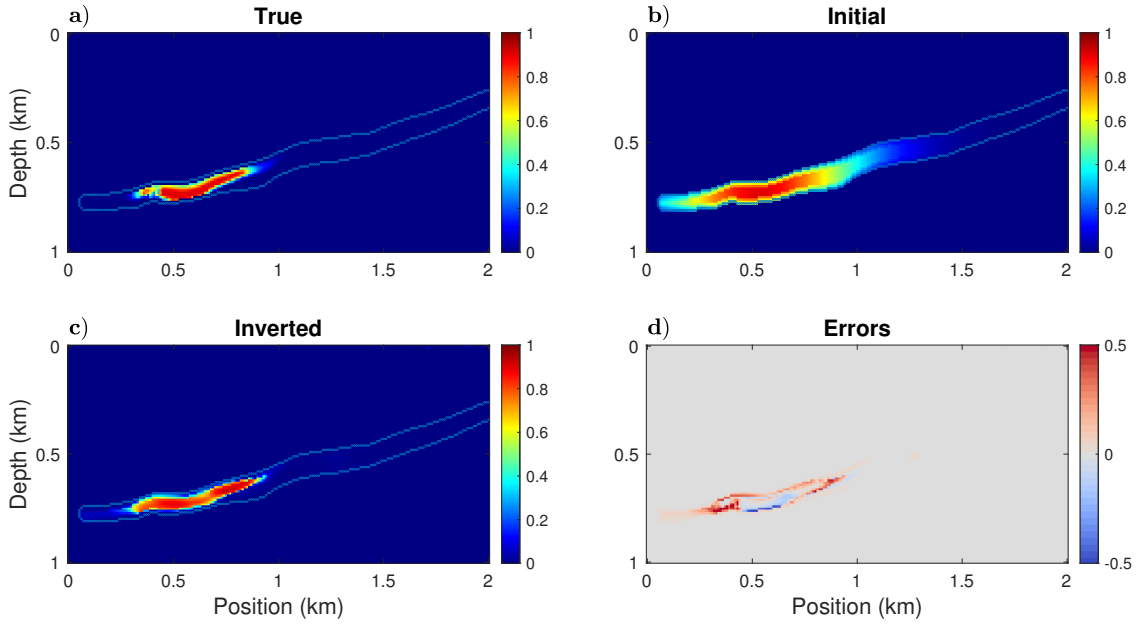

Figure 5.10: (a-c) True, initial, and inverted CO_2 saturation models, respectively. (d) Errors in the inverted model.

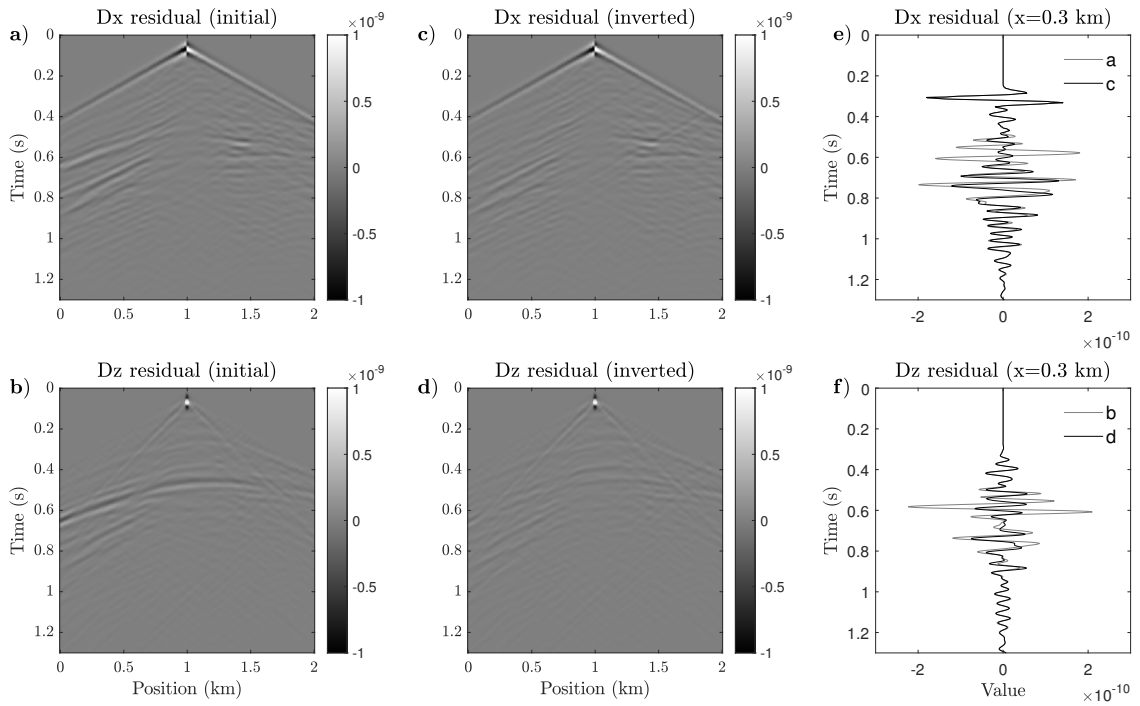

Figure 5.11: Monitor data residuals corresponding to the (a and b) initial model and (c and d) inverted model. (e and f) Vertical profiles of the data residuals at lateral position 0.3 km.

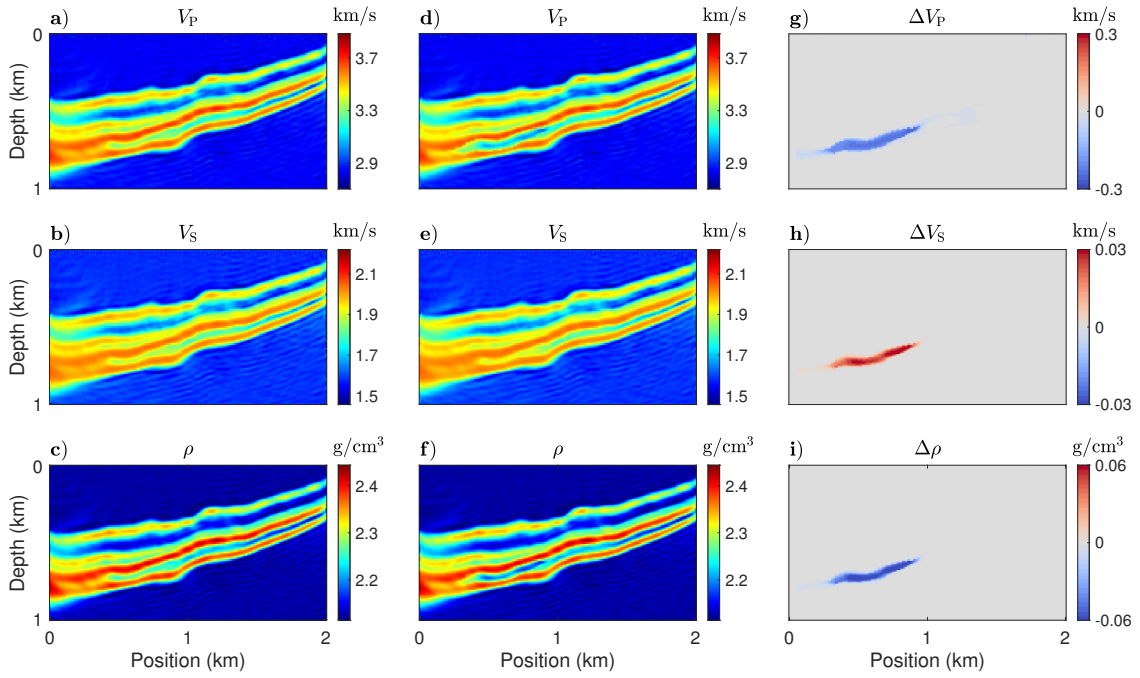

Figure 5.12: Reconstructed velocity and density models via the rock physics parameterized FWI: (a-c) Baseline, (d-f) monitor, and (g-i) time-lapse change.

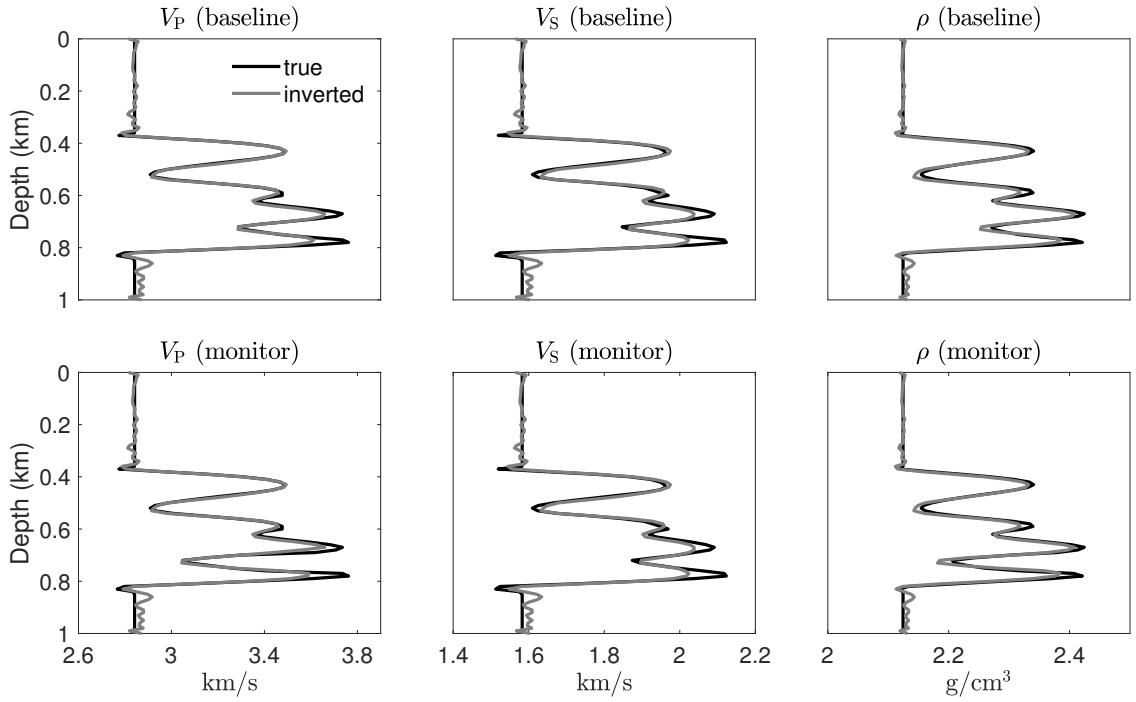

Figure 5.13: Vertical profiles extracted from the true and inverted models (Figures 5.3 and 5.12) at lateral position 0.5 km.

5.4.3 Two-step inversion results

The two-step inversion combines FWI for elastic attributes and rock physics inversion that transforms the elastic attributes into reservoir properties. For the elastic inversion, I parameterize FWI in terms of P-wave velocity, S-wave velocity, and density. I use the parallel difference strategy (Plessix et al., 2010; Asnaashari et al., 2015) which independently inverts the baseline and monitor data sets (Figure 5.4) starting from the same initial model (Figure 5.6). The time-lapse variation is simply the subtraction between the recovered monitor model and the recovered baseline model. The results are plotted in Figures 5.14 and 5.15. The velocity and density models are well recovered, but less accurately compared to the result of the rock physics FWI approach, and the predicted time-lapse variations are contaminated by artifacts more seriously. I attribute this deficit to a slower convergence of the velocity-density parameterized FWI, when compared to that of the rock physics parameterized inversion, which results from the fact that more variables are inverted simultaneously.

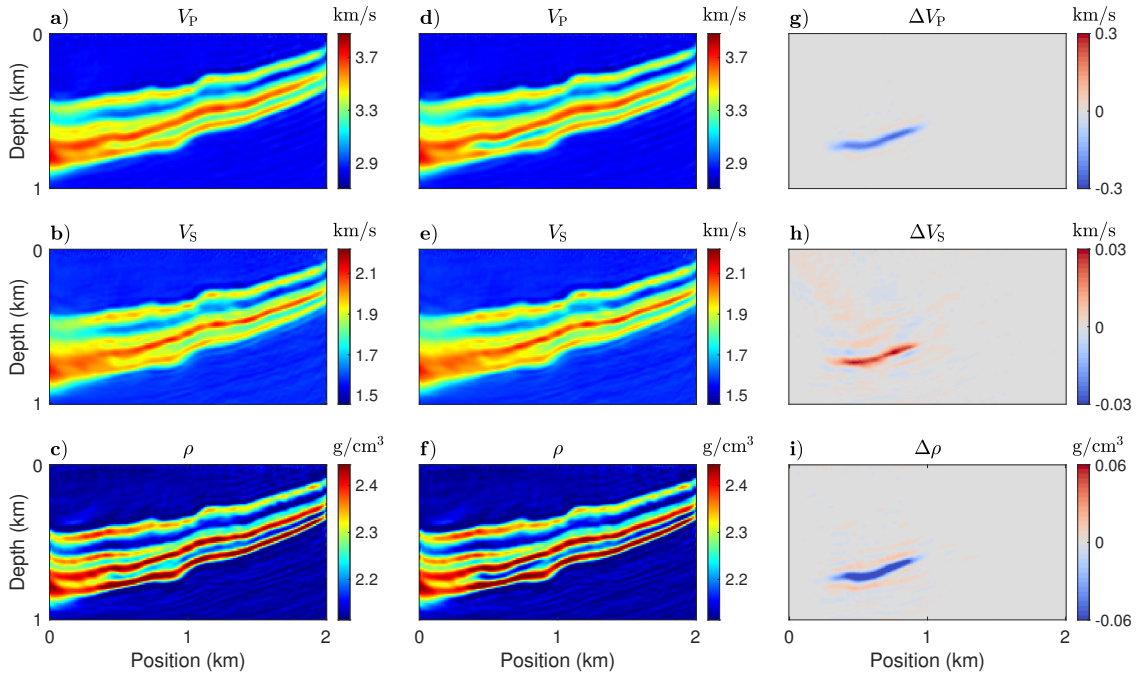

Figure 5.14: Reconstructed velocity and density models via velocity-density parameterized FWI: (a-c) Baseline, (d-f) monitor, and (g-i) time-lapse change.

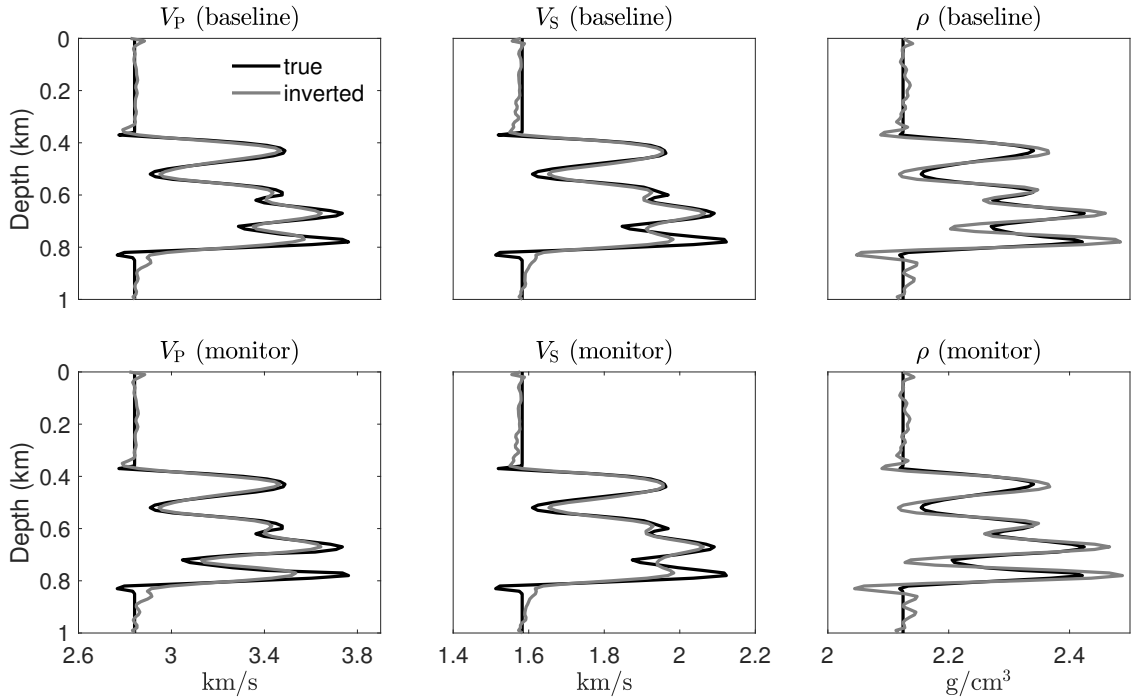

Figure 5.15: Vertical profiles extracted from the true and inverted models (Figures 5.3 and 5.14) at lateral position 0.5 km.

I examine two approaches for the prediction of rock physics properties from velocities and density. One is a Bayesian non-parametric approach, in which the joint distribution of elastic and rock physics properties is described by a non-parametric probability density function estimated using kernel density estimation (Doyen, 2007; Grana et al., 2021). I compute the joint distribution based on a training dataset collected from wells and then use it to compute the conditional probability of rock physics variables given velocities and density. The most likely model (i.e., maximum a posteriori estimate) is subsequently used for analysis. The other one is a global optimization method called the neighborhood algorithm (NA), which involves random sampling of model space but makes use of previous samples to guide the search (Sambridge, 1999; Sen and Roy, 2003; Dupuy et al., 2016c). For both approaches, I predict porosity and clay content from baseline velocity and density estimates, and CO_2 saturation from monitor estimates. Each inversion is tuned to provide robust results.

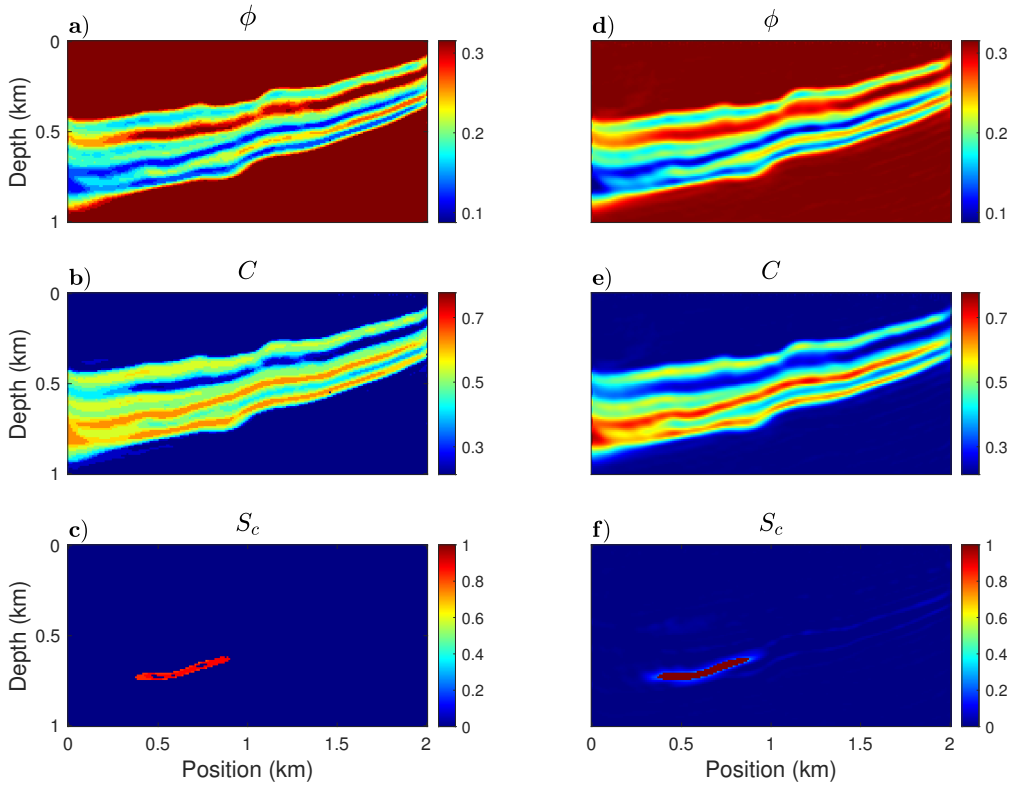

Figure 5.16: Inverted porosity, clay content, and CO_2 saturation models within the (a-c) Bayesian and (d-f) NA approaches.

Figure 5.16 shows that the two approaches yield comparable results of porosity and clay content to the direct inversion, capturing the relevant reservoir structures. The recovered CO_2 model is less than satisfactory, with the shape of the plume clearly distorted and the variation in saturation underestimated. Overall, the direct approach predicts CO_2 saturation more accurately (Figure 5.10c). In Table 5.2, the quality of the inverted models within different approaches, measured using root mean squared error, is summarized.

Table 5.2: Root mean squared error of the inverted models within different approaches.

	FWI+Bayesian	FWI+NA	Direct FWI
V_{P} (km/s, base)	0.060	–	0.048
V_{S} (km/s, base)	0.040	–	0.033
ρ (g/cm^3, base)	0.022	–	0.015
V_{P} (km/s, monitor)	0.062	–	0.050
V_{S} (km/s, monitor)	0.040	–	0.033
ρ (g/cm^3, monitor)	0.023	–	0.016
ϕ	0.011	0.012	0.011
C	0.038	0.043	0.044
Sc	0.062	0.046	0.035

5.4.4 Direct FWI with noisy data and imperfect rock physics model

To make the numerical study more realistic, I repeat the experiments in section 5.4.2 considering two sources of uncertainty: uncertainty in the measured data owing to noise, and uncertainty in the rock physics model owing to the assumption of the way fluid phases are mixed. The two uncertainties are examined separately.

First, I add white Gaussian noise to the noise-free data (Figure 5.4) using a signal-to-noise ratio of 10. As a result, the time-lapse seismic events are obscured by noise (Figure 5.17). However, the inversion results (Figure 5.18) remain consistent with the noise-free test, even though more noisy. The prediction error of porosity and clay content is larger toward the left side of the model due to the lack of illumination, and this likely causes data residuals

that have been back-projected to the CO_2 estimate. Also, the sharpness of the recovered model is a bit degraded, indicating that the noise has impeded the convergence.

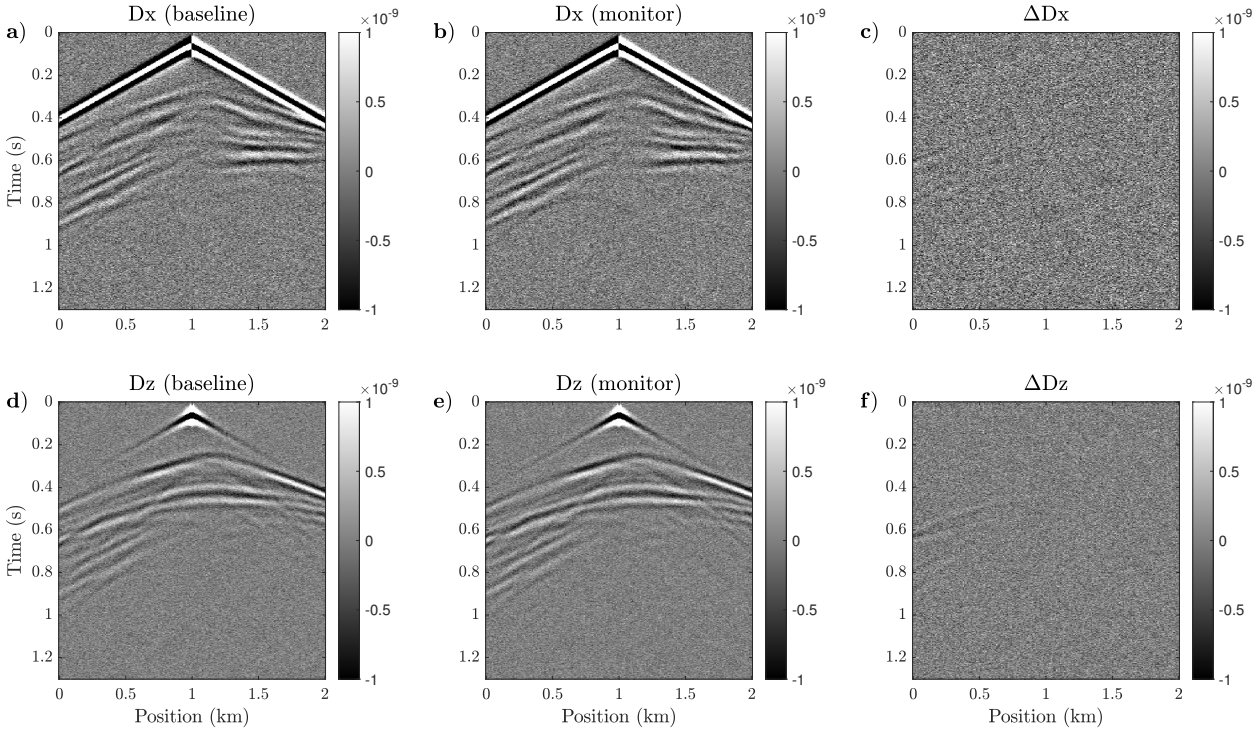

Figure 5.17: Synthetic noisy data with signal-to-noise ratio equal to 10.

I next consider an imperfect rock physics model that has errors on a priori parameter: the patchiness exponent e of Brie's equation, which describes the way CO_2 and water are mixed in the pore space. In Figure 5.19(a), I plot P-wave velocity as a function of CO_2 saturation, assuming patchy ($e = 1$), semipatchy ($e = 5$), and uniform ($e = 40$) mixing behaviors, respectively, following the analysis of Dupuy et al. (2021b). It shows that the patchiness exponent has a large impact on P-wave velocity, especially when CO_2 saturation is low (but nonzero). To account for the uncertainty in the rock physics model, I generate the observed data using a patchiness exponent ($e = 1$ and $e = 40$) different from that used to compute the data in inversion ($e = 5$). The results are shown in Figure 5.19(b). In the case of $e = 40$, we observe a similar result to the previous example, where the rock

physics model is assumed perfect (Figure 5.10c). This is attributed to the bimodality of the true model and the fact that the velocity difference between $e = 5$ and $e = 40$ at high CO_2 saturations ($Sc > 0.6$) is almost negligible. In the case of $e = 1$, the estimation error increases, but may still be considered acceptable. Since the patchiness exponent only affects P-wave velocity, my interpretation is that the use of multicomponent elastic data helps to constrain the saturation estimation.

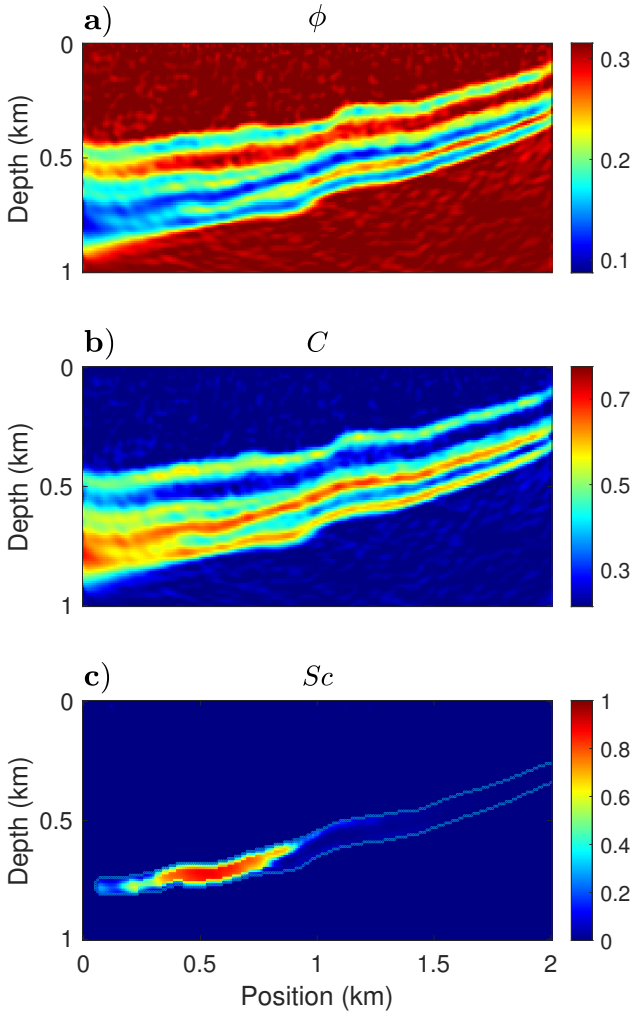

Figure 5.18: Direct inversion results with noisy data: (a) Porosity, (b) clay content, and (c) CO_2 saturation.

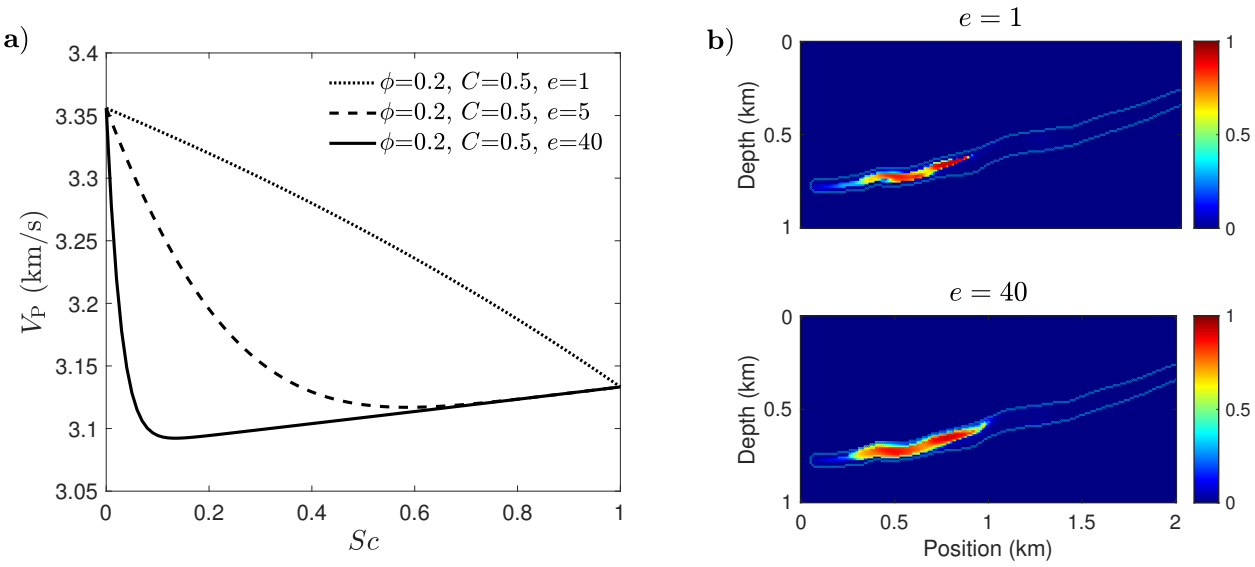

Figure 5.19: (a) P-wave velocity versus CO_2 saturation for different mixing behaviors of fluid phases. (b) Recovered CO_2 saturation models with erroneous assumptions on fluid.

5.5 Discussion

To validate the methodology some assumptions on the mineral and fluid phases were made. Indeed, I assume that the mineral phase consists of two minerals only and the fluid phase consists of water and CO_2. The methodology can be extended to more complex rocks as long as the elastic property of the minerals is known and the effective elastic properties can be modeled using rock physics elastic averages. Potentially the method can be applied in carbonate, however adequate rock physics models should be developed to account for the interaction of the fluid with fractured rocks (Vialle and Vanorio, 2011; Vanorio, 2015). Furthermore the approach could also be extended to a three-phase fluid system with water, oil, and CO_2, to model CO_2 sequestration in oil reservoirs for enhanced oil recovery, but it requires some prior knowledge or assumptions on the initial fluid distribution.

In my simulation, the pressure variations are relatively small and we can assume that the effect of pressure changes on elastic properties and density is negligible. In case of

larger variations, a joint rock physics model combining Gassmann's equation with empirical pressure relations (MacBeth, 2004; Grana, 2016b; Mavko et al., 2020) can be used as shown in Landrø et al. (2003), Trani et al. (2011), Bhakta and Landrø (2014), and Dupuy et al. (2021b). This approach requires adding one degree of freedom for pressure variations in the inversion. In Appendix D, I describe my initial attempts to achieve simultaneous inversion of CO_2 saturation and pore pressure.

The local smoothness is not always desirable, because it causes an attenuation of the high wavenumbers present in the model. In the CO_2 case, I found this constraint helpful in reducing undesired discontinuities and driving the convergence towards geologically meaningful models. However, one needs to weigh the smoothness carefully to keep the level of detail expected in a FWI result.

As a local inversion method, FWI bears the danger to end up in one of the numerous local minima. A good initial model is required to mitigate this problem. In practice, the initial porosity and clay content models can be obtained using some geostatistical interpolation of filtered logs following the seismically interpreted horizons, and using some correlated variable such as stacking velocities. The initial CO_2 model can be generated by simulating the fluid flow in the aquifer, according to the injection parameters and the rock properties estimated from the baseline survey (Grana et al., 2021).

Geophysical reservoir monitoring can be integrated into history matching and data assimilation workflows (Tavakoli et al., 2013; Ghorbanidehno et al., 2015) by combining the information from geophysical modeling with dynamic fluid flow simulation to increase the accuracy of the predicted model during injection and reduce the uncertainty in the model predictions (Chen et al., 2020; Liu and Grana, 2020; Tveit et al., 2020). This approach is particularly useful for CO_2 sequestration and enhanced oil recovery studies where production data such as oil production and borehole pressure can be used to validate and update the reservoir model (Babak and Deutsch, 2008; Jahangiri and Zhang, 2012; Gao et al., 2016; Kamali et al., 2017).

The inversion code is written in MATLAB. The computational cost for the proposed model including 101×201 grid cells with three unknown variables at each location for a total of 60903 unknowns is approximately 1.5 hours, with a coarse parallelization over frequencies on a computer with an Intel Core i5-8600 3.10GHz processor. I note that the computational cost of this problem is about the same per iteration as for a conventional EFWI because the additional cost for parameterization is negligible. For large-scale field data applications, I recommend implementing this algorithm in a precompiled language and using massive parallelization on high-performance computers.

5.6 Conclusion

I present a quantitative CO_2 monitoring approach which is based on seismic FWI. Unlike conventional FWI approaches which aim at determination of elastic properties, the proposed scheme allows direct prediction of rock physics properties from seismic data. I propose to estimate rock frame properties, such as porosity and clay content, from baseline data (before CO_2 injection), and then use the results as input to estimate CO_2 saturation from monitor data. The method was tested on a synthetic model developed from the Johansen dataset. With a suitable initial model, the method exhibits higher prediction accuracy than conventional two-step approaches. However, the difference between the direct and two-step inversions remains methodological and depends on the availability of sufficient constraints to the inversion. The results with noisy data and erroneous rock physics model further verify the robustness of the direct approach. The proposed methodology was applied to a saline aquifer but could be extended to depleted hydrocarbon reservoirs as well as enhanced oil recovery and carbon capture, utilization, and storage (CCUS) applications.

Chapter 6

Quantitative FWI characterization of reservoir properties at the CMC Newell County Facility

6.1 Summary

Combining elastic full waveform inversion (FWI) with rock physics can extend the role of FWI from seismic imaging to quantitative prediction and monitoring of reservoir parameters. Distributed Acoustic Sensing (DAS), a rapidly developing seismic acquisition technology, has the potential to be an enabler for such applications of FWI. In this study, I apply a sequential inversion scheme combining elastic FWI and Bayesian rock physics inversion to a vertical seismic profile (VSP) dataset acquired with accelerometers and collocated distributed acoustic sensing (DAS) fiber at the Carbon Management Canada's Newell County Facility. The goal is to build a baseline model of porosity and lithology parameters to support later monitoring of CO_2 storage. The key strategies include an effective source approach to cope with near-surface complications, a modeling strategy to simulate DAS data directly comparable

to the field data, and a Gaussian mixture approach to capture the bimodality of rock properties. I performed FWI tests on the accelerometer, DAS, and combined accelerometer-DAS data. While the inversion results can accurately reproduce either type of data, the elastic models inverted from the accelerometer data outperform the other two in matching well logs and identifying the target reservoir. I attribute this result to the insignificant advantage of DAS data, in this case, over accelerometer data, which also suffers from single-component measurements and lower signal-to-noise ratios. The porosity and lithology models predicted from the accelerometer elastic models are reasonably accurate at the well location and are geologically meaningful in spatial distribution.

6.2 Introduction

The Carbon Management Canada's (CMC) Newell County Facility is a platform for development and performance validation of technologies intended for measurement, monitoring and verification of CO_2 storage (Lawton et al., 2019; Macquet et al., 2022). In 2018, a vertical seismic profile (VSP) survey was acquired using accelerometers and collocated distributed acoustic sensing (DAS) fiber in an observation well at the field site (Hall et al., 2019). One of the goals of this survey was to obtain a baseline data set to compare against later monitoring data, gathered during the course of CO_2 storage. In this study, I propose a workflow combining full waveform inversion (FWI) and rock physics to predict reservoir properties from the measured data, to develop the pre-injection baseline model.

A combination of seismic inversion for elastic properties (e.g., velocity, density, and modulus) and rock physics for predicting reservoir properties (e.g., porosity, lithology, and fluid saturation) is a classical procedure in reservoir characterization (Doyen, 2007; Dvorkin et al., 2014; Grana et al., 2021). The seismic inversion is generally performed using the convolutional model based on a linearized approximation of the Zoeppritz equations (Aki and Richards, 2002; Buland and Omre, 2003). This approach is simple to implement and computationally fast. FWI methods, although computationally challenging, have the capacity to

produce a more accurate elastic model by involving a more complete subset of the information content of seismic data (Tarantola, 1986; Brossier et al., 2009; Virieux and Operto, 2009; Mallick and Adhikari, 2015; Pan et al., 2018a; Hu et al., 2021). Therefore, FWI appears to be a potentially powerful tool for reservoir characterization. The prediction of reservoir properties from elastic attributes requires a rock physics model (Mavko et al., 2020). The model adopted in the inversion depends on the geological environment and must be calibrated using well logs or laboratory measurements of core samples. The rock physics inversion is often formulated in a Bayesian framework, allowing uncertainty in the model predictions to be assessed through a probability density function (Bosch et al., 2010). Under some restrictive assumptions (Grana et al., 2021), I can derive a closed-form solution to this problem, thus significantly reducing the computational cost. In CO_2 storage applications, progress has been reported in combining FWI and rock physics for predicting the time evolution of CO_2 saturation (Queißer and Singh, 2013a; Dupuy et al., 2016b, 2021a; Hu et al., 2023). In these studies, the recovered baseline model of reservoir properties, such as porosity and lithology, help to reduce the uncertainty in fluid predictions of the monitor stage.

Since the estimates of elastic parameters directly affect the result of rock physics interpretation, obtaining an accurate FWI model is the key to using FWI for reservoir characterization. At the land-based Newell County Facility, one of the challenges FWI faces is the near-surface heterogeneity. The unconsolidated nature of the sediment in proximity to Earth's surface leads to complex seismic wave propagation that is heavily influenced by surface waves, attenuation and dispersion, and spatially varying source signatures (Eaid, 2022). Additionally, there is limited prior information about the near-surface that can be used to constrain the inversion. As a result, FWI may fail to converge because of the difficulties that exist in accurately characterizing the near-surface and the significant impact it has on seismic data. Efforts have been made to use surface wave based approaches for near-surface velocity estimation (Dokter et al., 2017; Köhn et al., 2019; Borisov et al., 2020; Colombo et al., 2021; Pan et al., 2023). In the absence of robust near-surface information, Keating et al. (2021)

proposed an effective source approach for VSP FWI. The idea is to remove the near surface from inversion by introducing an unknown variable characterizing the wavefield at a depth that best explains the data. This approach does not require a complete understanding of surface source signatures.

Another challenge for FWI is the incomplete nature of the data we record. Due to limitations on the acquisition geometry and seismic bandwidth, multiparameter FWI of land data is a difficult proposition (Brossier et al., 2009; Plessix et al., 2013; Stopin et al., 2014). The advent of DAS, an acquisition technology that employs optical fibers to sense seismically induced strain (Posey Jr et al., 2000), supplies an additional subset of the data that could contain the information required to propel FWI forward (Egorov et al., 2018; Eaid et al., 2020; Pan et al., 2023). In fact, the conventional point sensors (e.g., 3C geophone) directly measure multiple elastic wavefield components, and do so with a relatively high signal-to-noise ratio (SNR), but are limited in the low-frequencies they can sense and where they can be cost-effectively deployed; DAS senses low-frequencies effectively (Becker et al., 2017; Jin and Roy, 2017), and can occupy boreholes without disturbing production processes (Mateeva et al., 2014; Harris et al., 2016; Byerley et al., 2018), but have a generally lower SNR and are fundamentally single-component (Kuvshinov, 2016). The two sensor types can be viewed as supplying complementary datasets, which may lead to improved inversion results.

This study is a continuation of the FWI analysis from Eaid (2022) in the target area, and the main purpose is to explore the potential of FWI in quantitative seismic reservoir characterization. The chapter is organized as follows. First, I present the FWI framework used throughout this study. I show how to convert a conventional FWI scheme into a simultaneous inversion for source wavefields and elastic models. I also describe the modeling strategies that can simulate DAS data that are directly comparable to the field data. Then, I describe the Bayesian approach I use to predict reservoir properties from FWI results. In the section of field data application, I first give a brief introduction to the VSP experiment

at the CMC Newell County Facility. I then describe the preparations before inversion, including seismic data processing and rock physics analysis of well-log data. Finally, I apply a sequential inversion scheme combing FWI and rock physics to the processed data, including both accelerometer and DAS measurements.

6.3 Theory

6.3.1 FWI as a constrained optimization problem

The FWI problem can be framed as an attempt to minimize the mismatch between data and model predictions, subject to a wave propagation model linking the wavefield and subsurface together (Métivier et al., 2017). The inverse problem can be stated as

$$\min_{\mathbf{m}} E = \frac{1}{2} \sum_{i=1}^{ns} \sum_{j=1}^{n\omega} \|\mathbf{R}\mathbf{u}_{i,j} - \mathbf{d}_{i,j}\|_2^2 \quad \text{subject to} \quad \mathbf{A}(\omega, \mathbf{m})\mathbf{u} = \mathbf{f}(\omega), \tag{6.1}$$

where E is the objective function, $\mathbf{d}$ is the observed data, $\mathbf{R}$ is a sampling matrix representing receiver measurement, and ns and $n\omega$ are the number of sources and the number of frequencies, respectively. Here I consider the 2D frequency-domain isotropic-elastic wave equation (Pratt, 1990): $\mathbf{A}$ is the finite-difference forward operator dependent on the modeled frequency ω and the medium properties $\mathbf{m}$, $\mathbf{u}$ is the displacement wavefield, and $\mathbf{f}$ is the source term. In the following discussion, I will not explicitly state the sums over sources and frequencies for simplicity.

According to the adjoint state method (Plessix, 2006), the Lagrangian of the minimization problem in equation (6.1) is

$$L(\mathbf{m}, \mathbf{u}, \upsilon) = \frac{1}{2} \|\mathbf{R}\mathbf{u} - \mathbf{d}\|_2^2 + \Re\langle \mathbf{A}\mathbf{u} - \mathbf{f}, \upsilon \rangle, \tag{6.2}$$

where υ is the Lagrange multiplier, $\Re$ indicates the real part, and $\langle ., . \rangle$ is the scalar product, e.g., for two complex matrices, $\mathbf{a}$ and $\mathbf{b}$, of the size N, $\langle \mathbf{a}, \mathbf{b} \rangle = \sum_{i=1}^{N} \mathbf{a}_i^* \mathbf{b}_i$, where the

superscript * represents the complex conjugate. Let $\overline{\mathbf{u}}$ denotes the solution of the wave equation, such that $\mathbf{A}\overline{\mathbf{u}} = \mathbf{f}$, we have

$$L(\mathbf{m}, \overline{\mathbf{u}}, v) = E, \tag{6.3}$$

and the gradient of E yields

$$\nabla_{\mathbf{m}} E = \frac{dL(\mathbf{m}, \overline{\mathbf{u}}, v)}{d\mathbf{m}} = \frac{\partial L(\mathbf{m}, \overline{\mathbf{u}}, v)}{\partial \mathbf{m}} + \frac{\partial L(\mathbf{m}, \overline{\mathbf{u}}, v)}{\partial \mathbf{u}} \frac{\partial \overline{\mathbf{u}}}{\partial \mathbf{m}}. \tag{6.4}$$

The adjoint state $\overline{v}$ is defined by $\frac{\partial L(\mathbf{m}, \overline{\mathbf{u}}, \overline{v})}{\partial \mathbf{u}} = 0$, which is equivalent to

$$\mathbf{A}^\dagger \overline{v} = \mathbf{R}^\dagger (\mathbf{d} - \mathbf{R}\overline{\mathbf{u}}), \tag{6.5}$$

where the superscript † represents the conjugate transpose. Therefore, the gradient from equation (6.4) is reduced to

$$\nabla_{\mathbf{m}} E = \frac{\partial L(\mathbf{m}, \overline{\mathbf{u}}, \overline{v})}{\partial \mathbf{m}}. \tag{6.6}$$

It then follows from equation (6.2) that the individual components of the gradient vector can be expressed as

$$\nabla_{m_i} E = \Re \langle \frac{\partial \mathbf{A}}{\partial m_i} \overline{\mathbf{u}} \ , \overline{v} \ \rangle. \tag{6.7}$$

Within a Newton optimization approach, the search direction $\delta\mathbf{m}$ for model update is the solution of

$$\mathbf{H} \ \delta\mathbf{m} = -\nabla_{\mathbf{m}} E, \tag{6.8}$$

where $\mathbf{H}$ is the Hessian of the objective function. I solve equation (6.8) using the l-BFGS method, which uses the information of gradient and model stored from a limited number of previous iterations to approximate the inverse $\mathbf{H}$ (Nocedal and Wright, 2006).

6.3.2 Effective source approach

I consider here an effective source approach for VSP FWI, which attempts to remove the near-surface from the inversion problem (Keating et al., 2021). In this approach, I imagine a line source $\mathbf{f}^*$ at depth z^* such that, when activated, it reproduces the wavefield that would be obtained by propagation through the near surface. The optimization problem is given by

$$\min_{\mathbf{m}^*,\mathbf{f}^*} E = \frac{1}{2}\left\|\mathbf{R}^*\mathbf{u}^* - \mathbf{d}^*\right\|_2^2 \quad \text{subject to} \quad \mathbf{A}^*(\mathbf{m}^*)\mathbf{u}^* = \mathbf{f}^*, \tag{6.9}$$

where each of the * variables is only allowed to take values at depths below z^*. equation (6.9) is effectively the same optimization problem as the conventional one, equation (6.1), with the exception that I define the problem on a smaller model domain, and I invert for both an unknown model, $\mathbf{m}^*$, and an unknown source term $\mathbf{f}^*$. In effect, this formulation replaces the problem of characterizing a complex, heterogeneous near surface given a known source term with the problem of characterizing the wavefield produced by the interaction of the two at a chosen depth. This type of problem is illustrated schematically in Figure 6.1.

We can obtain the gradient with respect to the source term $\mathbf{f}^*$ in a way similar to that of the model gradient (equations 6.2-6.7). The result is

$$\nabla_{f_i} E = -\overline{v}_i, \tag{6.10}$$

where v_i is the adjoint wavefield at an effective source location indexed by i. In practice, I initialize $\mathbf{f}^*$ using the modeled wavefield at depth z^* from the initial model, and then simultaneously update $\mathbf{f}^*$ and $\mathbf{m}^*$ using the data recorded at depths below z^*. The choice of z^* requires testing, with the goal being to select the depth that allows the downgoing wavefield complexity to be explained by the effective source.

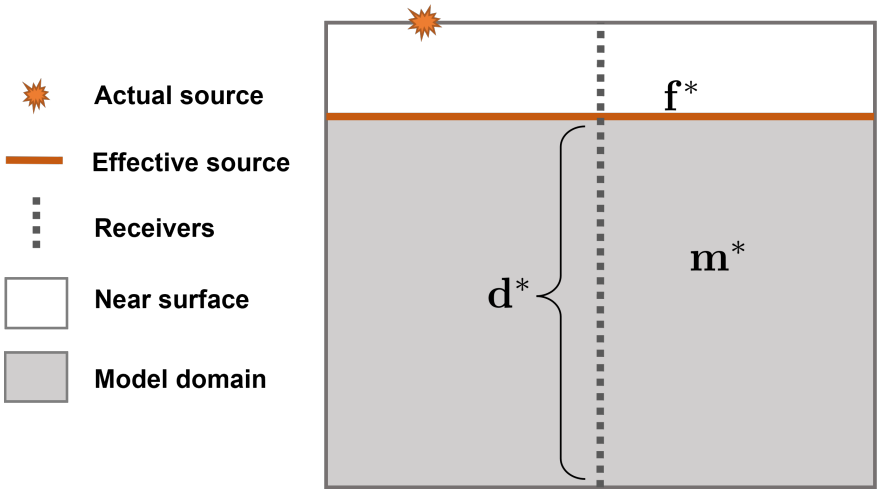

Figure 6.1: Schematic depiction of the effective source approach for VSP FWI.

6.3.3 FWI incorporating DAS data

DAS fiber response is proportional to the strain induced in the fiber by a propagating seismic wavefield. Following the approach of Eaid et al. (2020), we can generate strain data directly in forward modeling to compare with the field DAS data. Here I give a brief description of this approach.

The strain tensor can be defined in Cartesian coordinates as

$$e_{ij} = \frac{1}{2}\left(\frac{\partial u_i}{\partial x_j} + \frac{\partial u_j}{\partial x_i}\right), \quad i,j = 1,2,3. \tag{6.11}$$

where u_i is the particle displacement in the ith direction. To simulate fiber response, the Cartesian strain tensor must be transformed into the local system describing the fiber, from which the tangential component is extracted. Let the unit vectors $\{\hat{\mathbf{x}}, \hat{\mathbf{y}}, \hat{\mathbf{z}}\}$ denote the inline-crossline-depth Cartesian system and $\{\hat{\mathbf{t}}, \hat{\mathbf{n}}, \hat{\mathbf{b}}\}$ denote the local fiber coordinate defined by the tangent, normal, and binormal directions, we have

$$\mathbf{e}' = \mathbf{P}\mathbf{e}\mathbf{P}^T, \tag{6.12}$$

where

$$\mathbf{e} = \begin{bmatrix} e_{xx} & e_{xy} & e_{xz} \\ e_{yx} & e_{yy} & e_{yz} \\ e_{zx} & e_{zy} & e_{zz} \end{bmatrix}, \ \mathbf{e}' = \begin{bmatrix} e_{tt} & e_{tn} & e_{tb} \\ e_{nt} & e_{nn} & e_{nb} \\ e_{bt} & e_{bn} & e_{bb} \end{bmatrix}, \tag{6.13}$$

and $\mathbf{P}$ is the rotation matrix:

$$\mathbf{P} = \begin{bmatrix} \hat{\mathbf{t}} \cdot \hat{\mathbf{x}} & \hat{\mathbf{t}} \cdot \hat{\mathbf{y}} & \hat{\mathbf{t}} \cdot \hat{\mathbf{z}} \\ \hat{\mathbf{n}} \cdot \hat{\mathbf{x}} & \hat{\mathbf{n}} \cdot \hat{\mathbf{y}} & \hat{\mathbf{n}} \cdot \hat{\mathbf{z}} \\ \hat{\mathbf{b}} \cdot \hat{\mathbf{x}} & \hat{\mathbf{b}} \cdot \hat{\mathbf{y}} & \hat{\mathbf{b}} \cdot \hat{\mathbf{z}} \end{bmatrix}. \tag{6.14}$$

The tangential strain is then

$$\begin{aligned} e_{tt} =& (\hat{\mathbf{t}} \cdot \hat{\mathbf{x}})^2 e_{xx} + (\hat{\mathbf{t}} \cdot \hat{\mathbf{y}})^2 e_{yy} + (\hat{\mathbf{t}} \cdot \hat{\mathbf{z}})^2 e_{zz} \\ &+ 2(\hat{\mathbf{t}} \cdot \hat{\mathbf{x}})(\hat{\mathbf{t}} \cdot \hat{\mathbf{y}}) e_{xy} + 2(\hat{\mathbf{t}} \cdot \hat{\mathbf{x}})(\hat{\mathbf{t}} \cdot \hat{\mathbf{z}}) e_{xz} + 2(\hat{\mathbf{t}} \cdot \hat{\mathbf{y}})(\hat{\mathbf{t}} \cdot \hat{\mathbf{z}}) e_{yz}. \end{aligned} \tag{6.15}$$

For straight fibers deployed in vertical wells, the fibers have a single, vertical tangent direction, namely $\hat{\mathbf{t}} = \hat{\mathbf{z}}$, resulting in a DAS system sensitive only to the normal strain e_{zz}. In practice, I compute e_{zz} on a grid staggered to that of the displacements, so the strain at each grid cell is approximated as a weighted sum of the neighboring vertical displacements u_z.

FWI incorporating DAS data requires an objective function that compares the observed and modeled fiber strains. The receiver matrix $\mathbf{R}$ in equation (6.1) can be understood more generally as an operator that transforms the simulated wavefield into quantities directly comparable to the observed data. Therefore, we can include DAS data in FWI by simply reformulating R. Specifically, I design some rows of R to map the displacement wavefield to the accelerometer positions and the others to compute the tangential strain at channel positions along the fiber. This process of modeling the combined accelerometer and DAS

data, $\mathbf{d} = \mathbf{R}\mathbf{u}$, can be expressed as

$$\begin{bmatrix} d_x^1 \\ \vdots \\ d_x^{N_a} \\ d_z^1 \\ \vdots \\ d_z^{N_a} \\ e_{tt}^1 \\ \vdots \\ e_{tt}^{N_d} \end{bmatrix} = \begin{bmatrix} & 1 & & & & & & & \\ \vdots & & & & & & & & \\ & & & & & 1 & & & \\ & & & 1 & & & & & \\ \vdots & & & & & & & & \\ & & & & & & & 1 & \\ & w_1 & w_2 & \dots & w_3 & w_4 & & & \\ \vdots & & & & & & & & \\ & & & w_1 & w_2 & \dots & w_3 & w_4 \end{bmatrix} \begin{bmatrix} u_x^1 \\ u_z^1 \\ u_x^2 \\ u_z^2 \\ \vdots \\ u_x^N \\ u_z^N \end{bmatrix}, \tag{6.16}$$

where N is the total number of discrete spatial positions, N_a and N_d are the numbers of accelerometer and DAS sensors, respectively, and w_1, w_2, w_3, w_4 are finite-difference coefficients. This formulation also allows us to include a data weighting matrix in the objective function to control the relative importance of accelerometer data and DAS data in recovering the subsurface model.

6.3.4 Bayesian rock physics inversion

Once I have obtained a model of elastic properties $\mathbf{m}$ from seismic data, I then aim to estimate the rock properties $\mathbf{r}$, from $\mathbf{m}$ as the solution of another inverse problem

$$\mathbf{m} = f_{\text{RPM}}(\mathbf{r}) + \epsilon, \tag{6.17}$$

where f_{RPM} is the rock physics model and ϵ is the data error. In this study, the vector $\mathbf{m}$ includes P- and S-wave velocities plus density, and the model variable $\mathbf{r}$ includes porosity and mineral volume fractions. I operate in a Bayesian setting to assess the conditional probability

$P(\mathbf{r}|\mathbf{m})$:

$$P(\mathbf{r}|\mathbf{m}) = \frac{P(\mathbf{r},\mathbf{m})}{P(\mathbf{m})} = \frac{P(\mathbf{m}|\mathbf{r})P(\mathbf{r})}{P(\mathbf{m})}, \tag{6.18}$$

where $P(\mathbf{r},\mathbf{m})$ is the joint distribution of rock and elastic properties, $P(\mathbf{r})$ is the prior distribution, $P(\mathbf{m}|\mathbf{r})$ is the likelihood function, and $P(\mathbf{m})$ is a normalizing constant. For the prior distribution, I assume a multivariate Gaussian mixture distribution of N_f components:

$$P(\mathbf{r}) = \sum_{k=1}^{N_f} \lambda_k \mathcal{N}(\mathbf{r}; \boldsymbol{\mu}_r^k, \boldsymbol{\Sigma}_r^k), \tag{6.19}$$

where the distributions $\mathcal{N}(\mathbf{r}; \boldsymbol{\mu}_r^k, \boldsymbol{\Sigma}_r^k)$ represent the k^{th} Gaussian component and the coefficients λ_k are the weights of the linear combination. This assumption allows us to model each litho-fluid class detectable by rock physics analysis as a single component of the Gaussian mixture.

I use the semi-analytical approach of Grana and Rossa (2010) to estimate the conditional probability $P(\mathbf{r}|\mathbf{m})$. First, I generate a set of Monte Carlo samples from the prior distribution $P(\mathbf{r})$ and apply rock physics modeling to obtain the corresponding set of elastic properties $\mathbf{m}$; I then use these samples as a training dataset to estimate the joint distribution of rock and elastic properties assuming a Gaussian mixture distribution:

$$P(\mathbf{r},\mathbf{m}) = \sum_{k=1}^{N_f} \lambda_k \mathcal{N}(\mathbf{y}; \boldsymbol{\mu}_y^k, \boldsymbol{\Sigma}_y^k), \tag{6.20}$$

where $\mathbf{y} = (\mathbf{r},\mathbf{m})$, and the joint mean and covariance of each component are given by

$$\boldsymbol{\mu}_y^k = \begin{bmatrix} \boldsymbol{\mu}_r^k \\ \\ \boldsymbol{\mu}_m^k \end{bmatrix}, \quad \boldsymbol{\Sigma}_y^k = \begin{bmatrix} \boldsymbol{\Sigma}_{r,r}^k & \boldsymbol{\Sigma}_{r,m}^k \\ \\ \boldsymbol{\Sigma}_{m,r}^k & \boldsymbol{\Sigma}_{m,m}^k \end{bmatrix}. \tag{6.21}$$

The quantities in equation (6.21) can be determined using maximum likelihood estimation (Myung, 2003). As a consequence, the conditional distribution $P(\mathbf{m}|\mathbf{d})$ is a Gaussian mix-

ture:

$$P(\mathbf{r}|\mathbf{m}) = \sum_{k=1}^{N_f} \lambda_k^{'} \mathcal{N}(\mathbf{r}; \boldsymbol{\mu}_{r|m}^k, \boldsymbol{\Sigma}_{r|m}^k), \tag{6.22}$$

where the conditional weights are given by

$$\lambda_k^{'} = \frac{\lambda_k \mathcal{N}(\mathbf{r}; \boldsymbol{\mu}_{r|m}^k, \boldsymbol{\Sigma}_{r|m}^k)}{\sum_{h=1}^{N_f} \lambda_h \mathcal{N}(\mathbf{r}; \boldsymbol{\mu}_{r|m}^h, \boldsymbol{\Sigma}_{r|m}^h)}, \tag{6.23}$$

and the conditional mean and covariance can be analytically derived as

$$\begin{aligned} \boldsymbol{\mu}_{r|m}^k &= \boldsymbol{\mu}_r^k + \boldsymbol{\Sigma}_{r,m}^k (\boldsymbol{\Sigma}_{m,m}^k)^{-1} (\mathbf{m} - \boldsymbol{\mu}_m^k) \\ \boldsymbol{\Sigma}_{r|m}^k &= \boldsymbol{\Sigma}_{r,r}^k - \boldsymbol{\Sigma}_{r,m}^k (\boldsymbol{\Sigma}_{m,m}^k)^{-1} \boldsymbol{\Sigma}_{m,r}^k. \end{aligned} \tag{6.24}$$

6.4 Applications

6.4.1 VSP experiment at CMC Newell County Facility

The Carbon Management Canada's (CMC) Newell County Facility is located 200 km southeast of Calgary, Alberta, Canada. A key goal of this project is the development of technologies for monitoring CO_2 storage (Lawton et al., 2019). The field site houses three wells, including the well being used for CO_2 injection, and two observation wells, colloquially referred to as the geophysics and geochemistry wells. The injection of CO_2 at this site, at a shallow depth of approximately 300 m and at a low flow rate of several tens of tonnes per year (Macquet et al., 2022), is designed to simulate leakage of CO_2 from a deep sequestration site into formations at shallow to intermediate depths. Among the baseline surveys collected in the field, I focus on the multi-azimuth walk-away vertical seismic profile (VSP) dataset acquired in September 2018, which is primarily intended for use in full-waveform inversion (FWI) and modeling studies (Hall et al., 2019).

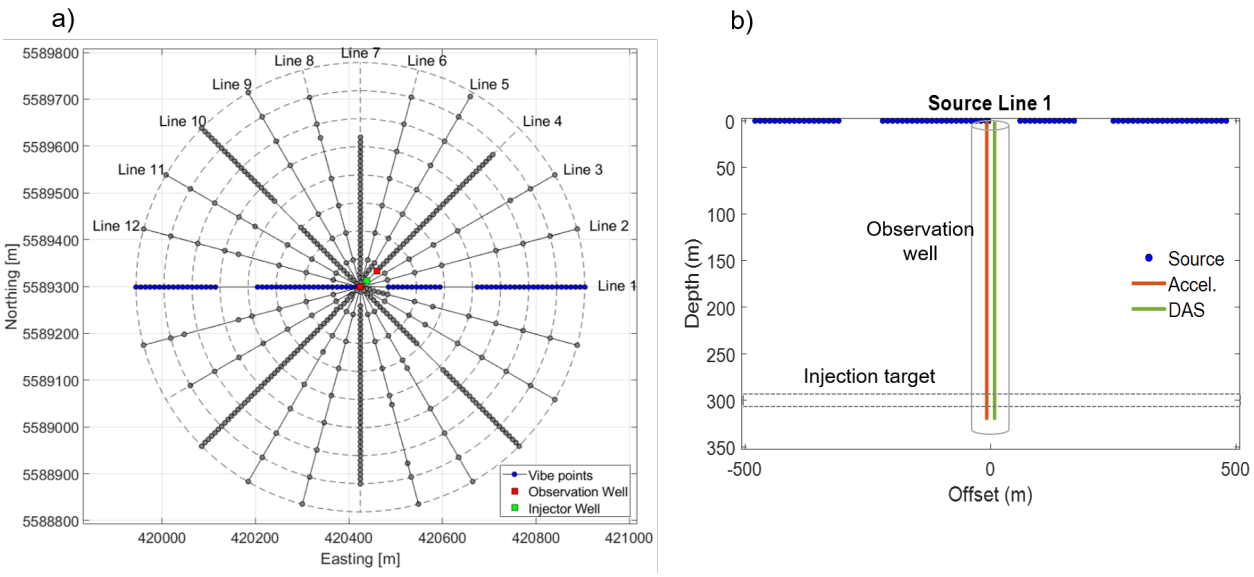

Figure 6.2: (a) Shot geometry of the multi-azimuth walk-away VSP experiment at the Newell County Facility. The gray circles represent the locations of vibe points, the green square marks the location of the injection well, and the two red squares mark the locations of the geophysics and geochemistry wells, offset from the injection well by 20 m to south-west and 30 m to north-east, respectively. (b) Section view of the VSP acquisition with respect to source line 1. The horizontal dashed lines delineate the top and bottom of the Basal Belly River Sandstone target reservoir.

.

The 2018 VSP has 12 source lines separated by counter-clockwise fifteen-degree rotations, centered on the geophysics well (Figure 6.2a). Source lines 1, 4, 7, and 10 were acquired at a 10 m vibe point spacing and the others were acquired at 60 m spacing. The source was an Inova Univib running a linear sweep from 1-150 Hz over 16 seconds, using 0.2 second half cosine tapers and a 3 second listening time. For this survey, a string of Inova 3C VectorSeis accelerometers were deployed at 1 m spacing from the surface to the bottom hole at about 324 m depth. In addition, the geophysics well has a straight DAS fiber and a helical fiber cemented over the entire length of the well, which are part of a 5 km DAS fiber loop permanently buried in the field. Due to computational limitations, I consider 2D FWI, and

restrict my analysis to the data generated by source line 1, including both accelerometer and straight DAS fiber measurements (Figure 6.2b). This line has 77 shot points. The minimum shot offset from the well was 6 m, and the maximum was 480 m.

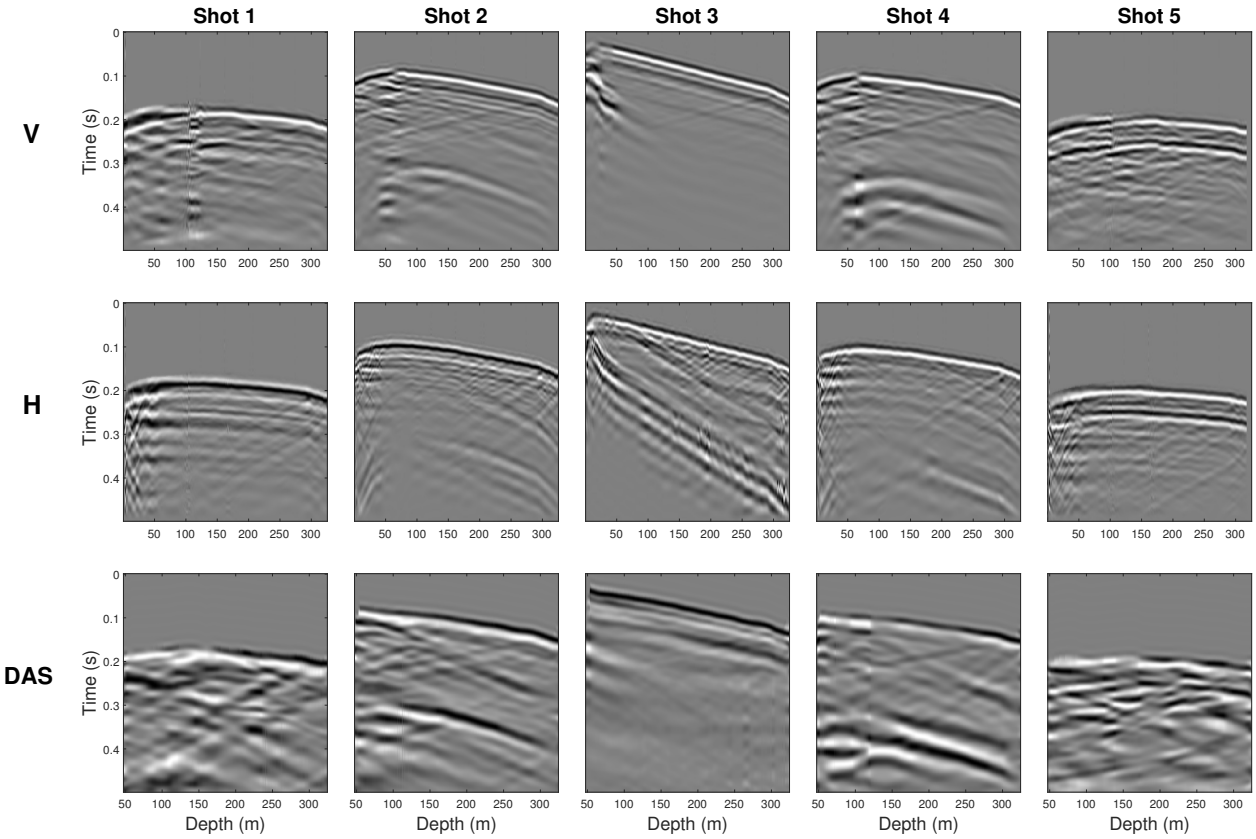

Figure 6.3: Processed accelerometer and DAS data for 5 shots on source line 1. Top row: vertical component of acceleration. Middle row: horizontal component of acceleration. Bottom row: DAS-recorded strain. Each column represents the data of a single shot. Shots 1 to 5 correspond to offsets 370 m, 170 m, -20 m, -200 m, and -430 m, respectively.

6.4.2 Seismic data processing

The seismic data have been carefully processed to be more comparable to simulated data generated by modeling procedures (Eaid, 2022). The accelerometer data were processed using a standard workflow for multi-component VSP data, including first break picking, coordinate rotations, trace interpolation, and denoising. The DAS data underwent a similar processing

workflow but was simplified due to the single-component nature of DAS sensing. However, due to uncertainties in the trace spacing and locations, special attention was directed to the depth registration of the DAS data. Figure 6.3 plots the processed accelerometer and DAS data for five shot points on source line 1, which represent a portion of the input data for FWI. The result is a high-fidelity two-component accelerometer dataset, whereas the DAS dataset has a relatively low signal-to-noise ratio, especially at far-offset.

6.4.3 Rock physics analysis of well-log data

A comprehensive log suite was acquired at the injection well (before CO_2 injection), which was drilled to a depth of 550 m to characterize the overburden and the underburden within the field research station. The wireline logs were further interpreted that provide depth profiles of porosity and mineral composition (Figure 6.4). The Basal Belly River Sandstone (BBRS) injection zone is at a depth of 296 m below the ground surface, and it is a 7-m-thick, fine to medium-grained sandstone at the base of the Foremost Fm. The overlying sealing succession is composed of interbedded mudstone, fine-grained sandstone, and uncleated coals that directly overlie BBRS. Additional seals are provided by a stratigraphically higher coal zone at about 170 m depth. Together, the potential top seal has a combined average thickness of 225 m in the study area (Lawton et al., 2019). Based on the well-log data of the range 223-520 m, I have constructed a rock physics model combining the soft-sand model and Gassmann's equations (Mavko et al., 2020) to predict P-wave velocity (V_{P}), S-wave velocity (V_{S}), and density (ρ) as a function of porosity (ϕ) and mineral volume fractions (equation 3.37):

$$(V_{\mathrm{P}}, V_{\mathrm{S}}, \rho) = f_{\mathrm{RPM}}(\phi, V_{\mathrm{qu}}, V_{\mathrm{cl}}, V_{\mathrm{co}}), \tag{6.25}$$

where V_{qu}, V_{cl}, and V_{co} represent the volume fractions of quartz, clay, and coal, respectively, and $V_{\mathrm{qu}} + V_{\mathrm{cl}} + V_{\mathrm{co}} = 1$. Because the in-situ hydrocarbon saturation is sufficiently small (Macquet et al., 2019), the brine saturation was assumed to be 100%. Given its visible fit to the data (Figures 6.4a-c), the rock physics model was then used to reconstruct the velocity

and density logs missed at shallow depths 0-223 m, using the corresponding rock property logs as input. The predictions have a good match with the local geology as well as the first-arrival traveltimes picked on zero-offset seismic data (Kolkman-Quinn, 2022). These increase my confidence in the rock physics model. In the following analysis, the velocity and density logs I refer to contain the model predictions at shallow depths 0-223 m and the original measured data at depths below 223 m.

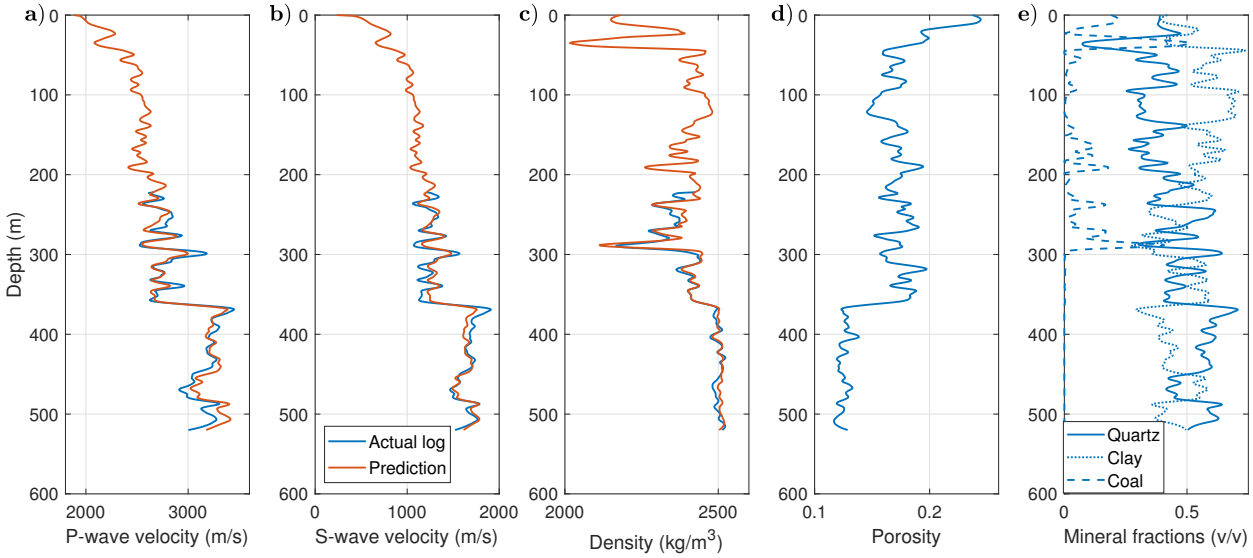

Figure 6.4: Well logs (upscaled) of the injection well: (a) P-wave velocity, (b) S-wave velocity, (c) density, (d) total porosity, and (e) the volume fractions of quartz, clay, and coal. Well-log data are in blue and rock physics model predictions in orange.

To validate my choice of Gaussian mixture models for describing parameter distributions, I draw crossplots of the well-log data in Figure 6.5. These data correspond to a depth range of 50 to 350 m, in order to be consistent with the target depth range of subsequent inversions. I assume a joint Gaussian mixture distribution with two components for the elastic and rock properties. For illustration purposes, I only display the bivariate projections in the petro-elastic domain of P-wave velocity and quartz volume, and in the petrophysical domain of porosity and clay volume. The Gaussian mixture model captures the bimodal behavior of the data, with the two components that can be associated with sandy ($V_{\text{clay}} < 0.45$) and

shaley ($V_{\text{clay}} > 0.45$) facies.

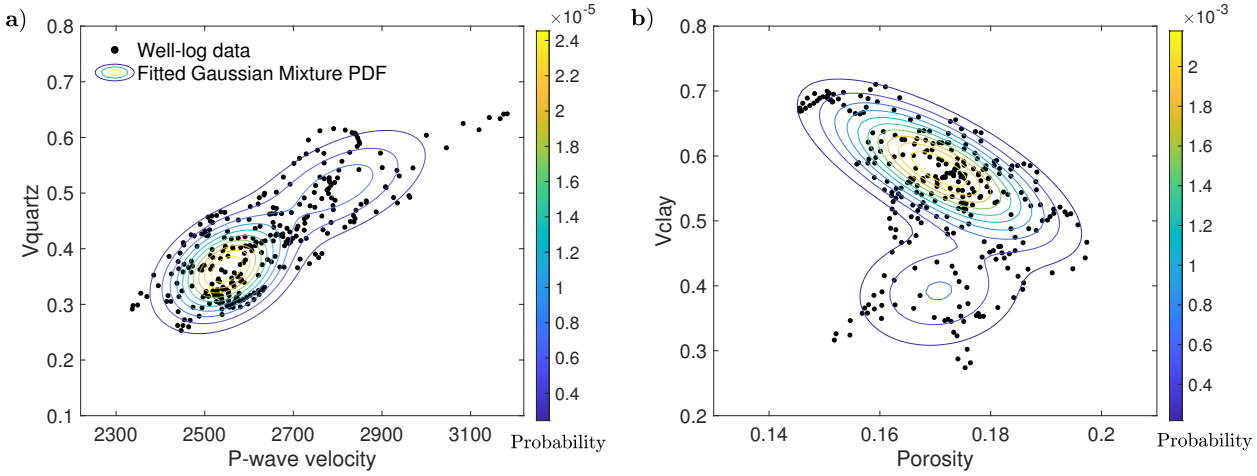

Figure 6.5: Bivariate Gaussian mixture probability density function (PDF) estimated from well-log data, in the domain of (a) P-wave velocity and quartz volume, and (b) porosity and clay volume.

6.4.4 Elastic FWI results

I consider here a 2D, frequency-domain, three-parameter elastic FWI algorithm. The model I consider is 1000 m wide by 350 m deep (as shown in Figure 6.2b), with 2.5 m grid spacing. I use 63 shots from source line 1 that lead to both accelerometer and DAS measurements. Each shot gather is converted from the time domain to the frequency domain through a temporal Fourier transform. The inversion is computed over 7 frequency bands, each containing 6 frequencies that are slightly overlapped, following the multiscale strategy promoted by Keating and Innanen (2019a). The minimum frequency I use is 10 Hz, which is found to be the lowest frequency at which the signal-to-noise ratio is acceptable, and the maximum frequency is 25 Hz, which is limited by the computational cost of moving to the smaller finite-difference grid spacing necessary for higher frequencies. I perform 10 iterations of L-BFGS optimization at each frequency band, simultaneously updating the model area below 50 m depth and the effective source at 40 m depth.

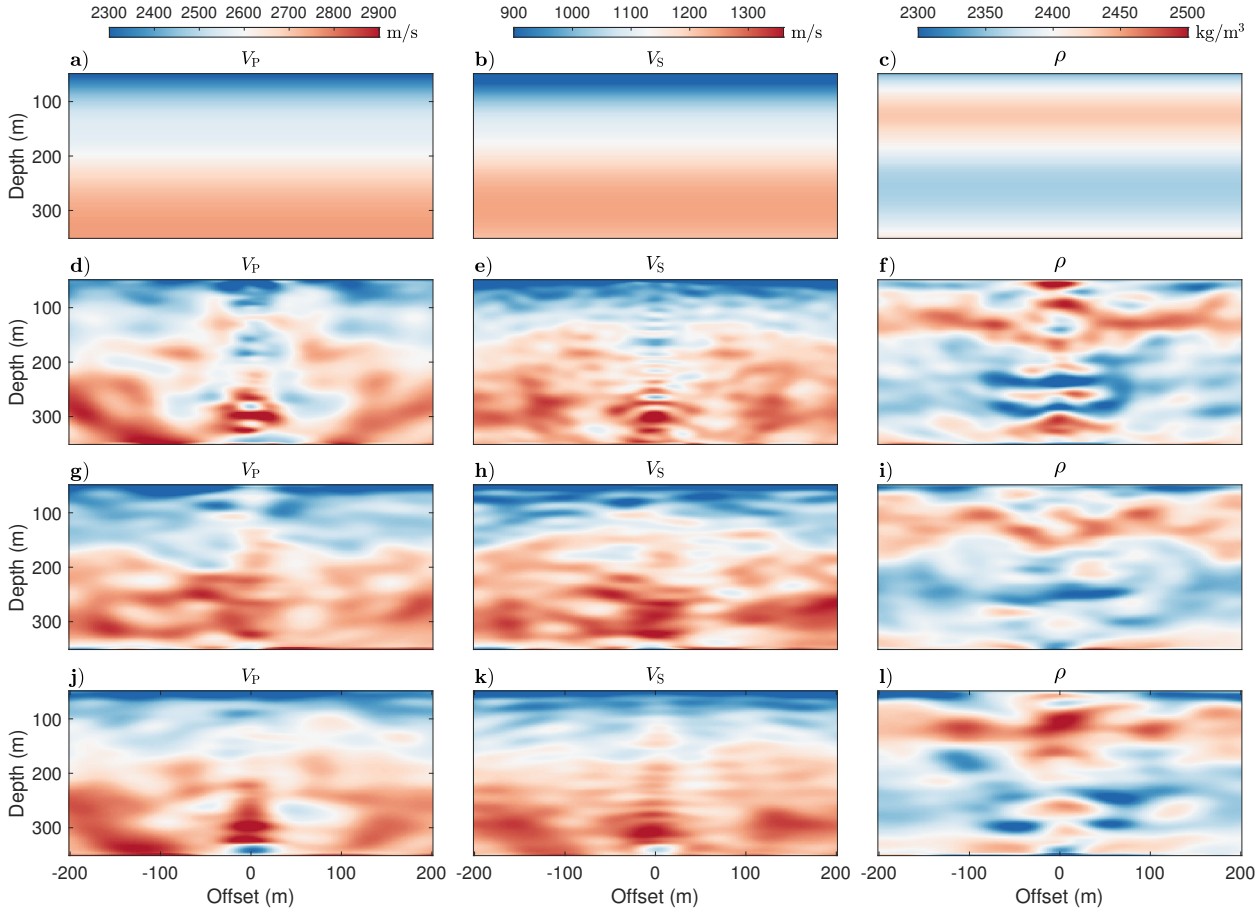

Figure 6.6: (a)-(c) Initial models of P-wave velocity, S-wave velocity, and density. (d-f) Inverted models from accelerometer data. (g-i) Inverted models from DAS data. (j-l) Inverted models from the combined accelerometer and DAS data.

The initial models are created by applying Gaussian smoothing to the well logs of V_{P}, V_{S}, and ρ. I run inversions using the accelerometer, DAS, and combined accelerometer-DAS datasets respectively. Due to limited observation aperture, I only demonstrate the recovered models within 200 m offset. In Figure 6.6, the results are summarized. The inverted models from either dataset exhibit sufficient updates from the initial one, but have different features. The accelerometer inverted models reveal a reasonable amount of detail in the vicinity of the observation well, but lack lateral continuity, especially for P-wave velocity. The DAS model updates are largely layer-like, possibly more geologically meaningful, but have a relatively poor resolution in the near-offset region. The inverted models using both datasets neutralize

the model characteristics for each individual data, indicating that my inversion approach is stable. Observation of the model profiles in Figure 6.7 suggest that the accelerometer inverted models correlate strongly to the well logs, and capture the large elastic contrast between the caprock and reservoir formations, at approximately 300 m depth. The DAS models correlate relatively poorly with well logs and fail to identify the reservoir of interest. This also brings a great obstacle for us to use the DAS data alone to predict reservoir parameters. I attribute this deficiency to the limited sensitivity of DAS to the wavefield creating strain that is perpendicular to the fiber and the lower signal-to-noise ratio of the DAS data compared to the accelerometer data.

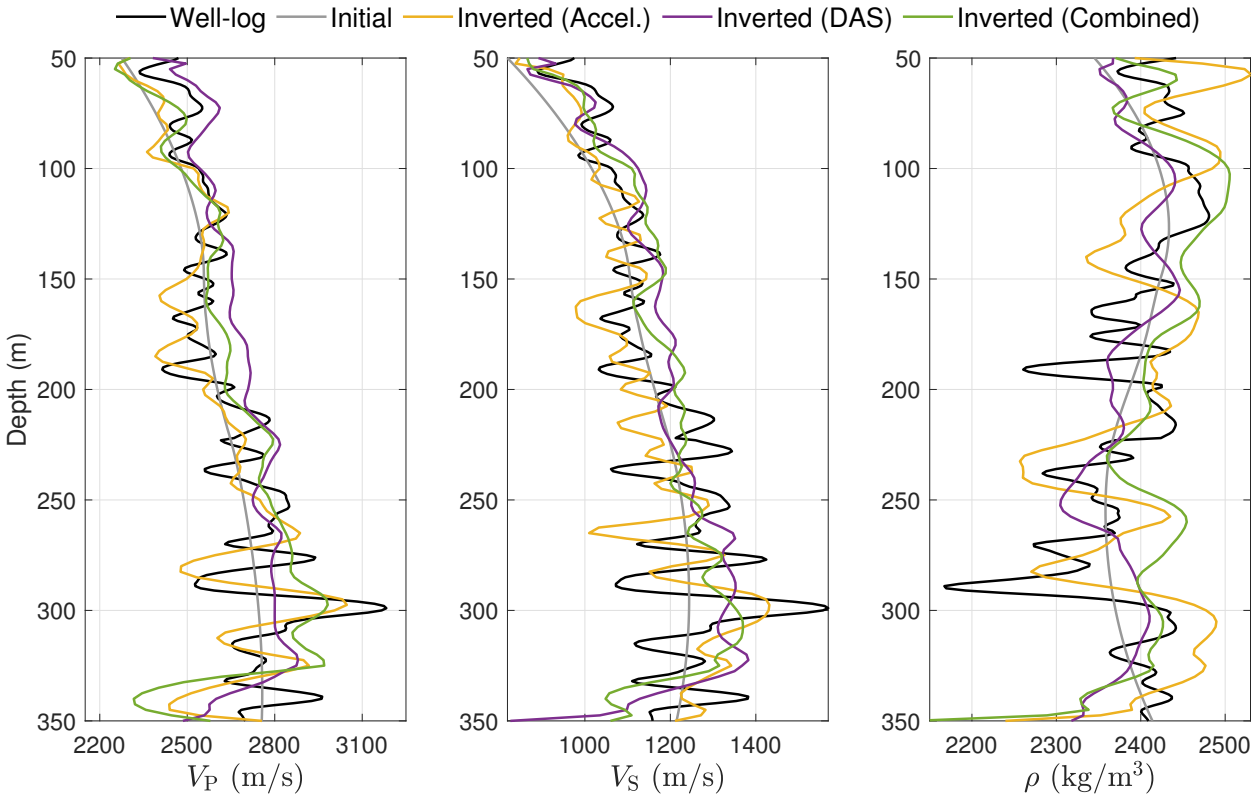

Figure 6.7: Comparison of the well logs and the vertical profiles extracted from the initial and inverted models (Figure 6.6) at offset 20 m.

In my FWI procedure, the field data are normalized for each source-receiver pair, to prevent under-emphasizing measurements from deeper areas. In order to compare these re-

scaled data to my simulated data in the inversion, the modeled data are also scaled similarly. In Figure 6.8, the normalized frequency-domain measured data for the shot at 70 m offset and the corresponding modeled data, simulated from the initial and inverted models, are plotted. As this comparison demonstrates, the data misfit is significantly reduced after inversion. In fact, across all shots, data misfit was reduced by 95% for the accelerometer data and 70% for the DAS data, after each type of data was inverted alone. However, for a joint inversion of the accelerometer and DAS data, the degree of data fitting will be reduced because each data set will be less emphasized than their individual inversions.

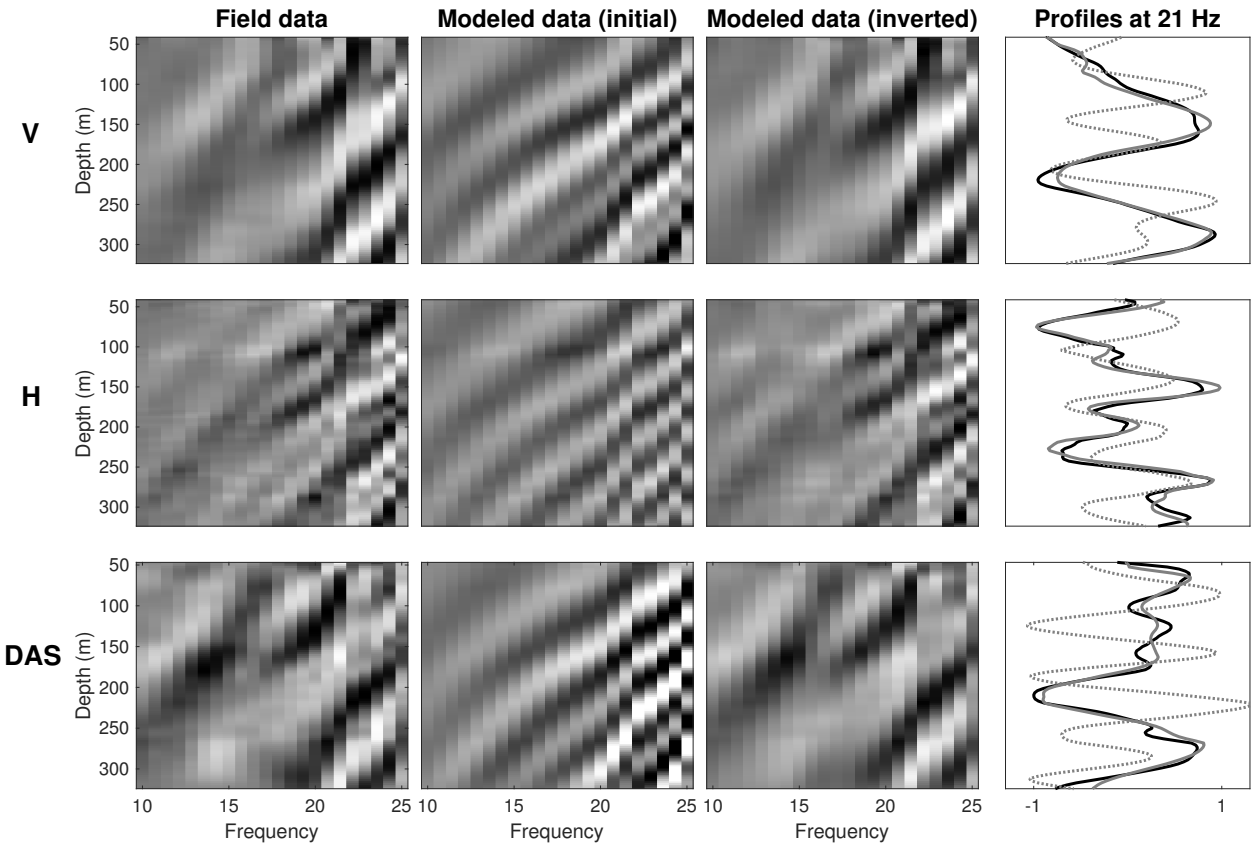

Figure 6.8: Real part of frequency domain data for shot at 70 m offset. Top row: vertical component of acceleration. Middle row: horizontal component of acceleration. Bottom row: DAS-recorded strain. Columns from left to right: Field data, modeled data simulated from the initial model, modeled data simulated from the inverted model, and comparison of the 21 Hz field data (solid black line), initial modeled data (dotted gray line), and inverted data (solid gray line).

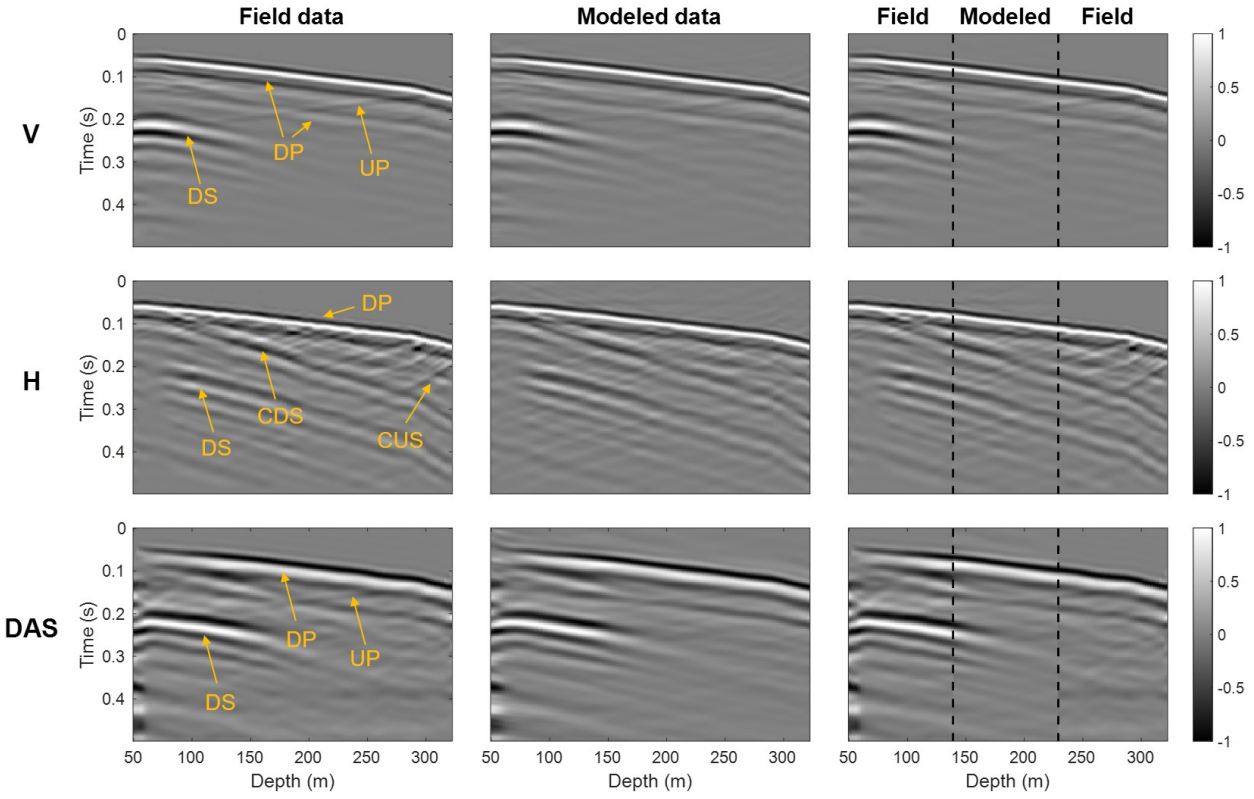

Figure 6.9: Time domain data for shot at 70 m offset. Top row: vertical component of acceleration. Middle row: horizontal component of acceleration. Bottom row: DAS-recorded strain. Columns from left to right: Field data, modeled data simulated from the inverted model, and a mixture of field and modeled data. In the panels of field data I marked the different types of waves. DP: downgoing P-waves. DS: downgoing S-waves. UP: upgoing P-waves. CDS: converted downgoing S-waves. CUS: converted upgoing S-waves.

Next, I examine the modeled data in the time domain. To achieve this, I introduce more frequencies to the modeled data, based on the inverted models, and then use inverse Fourier transform to obtain synthetic shot gathers. Figure 6.9 illustrates that the modeled data match closely the field data in terms of both amplitude and phase. While the prediction of downgoing wavefield relies on accurate source information and a reasonable initial model, the prediction of upgoing wavefield relies heavily on model updating. The accurate reproduction of both downgoing and upgoing wavefields illustrates that the effective source method is fairly robust.

6.4.5 Rock physics inversion results

In this section, I adopt the FWI models from the accelerometer data to predict the spatial distribution of reservoir properties, given that they outperform the results of either DAS or combined accelerometer-DAS data in identifying the target reservoir. Based on the analysis of well-log data, I define three model unknowns: porosity, quartz volume, and clay volume. The goal is to obtain the posterior probability distribution of these variables conditioned on the FWI models.

I first build a training dataset of 1000 Monte Carlo samples, by sampling from a prior Gaussian mixture distribution, $P(\phi, V_{\mathrm{qu}}, V_{\mathrm{cl}})$, estimated from the porosity and lithology logs, and applying rock physics model to obtain the corresponding elastic parameters. I then estimate the parameters of the joint distribution, $P(\phi, V_{\mathrm{qu}}, V_{\mathrm{cl}}, V_{\mathrm{P}}, V_{\mathrm{S}}, \rho)$, from the training dataset. Finally, I compute the posterior distribution of rock properties conditioned on each set of the elastic parameters from FWI, $P(\phi, V_{\mathrm{qu}}, V_{\mathrm{cl}} \mid V_{\mathrm{P}}, V_{\mathrm{S}}, \rho)$, using equations (6.22)-(6.24).

The inversion is first applied at the well location to compare the results with the actual curves of porosity and mineral volumes. In Figure 6.10, we observe that the posterior distributions capture the trend of the well logs, with a high fraction of true samples falling inside the 0.95 confidence interval. The maximum a posteriori (MAP) estimate of porosity, although correlates relatively poorly with the actual log, reveals the limited variations of this property across the depth profile, and has a root mean squared error of 0.017. The MAP estimates of mineral volumes are more accurate in deep regions than in shallow ones. For the interval from 280 to 320 m, the correlation between model predictions and well logs is 0.80 for quartz volume and 0.83 for clay volume. I point out that the misclassifications in the posterior probability distributions are due to the lack of accuracy of the FWI results as well as the rock physics model.

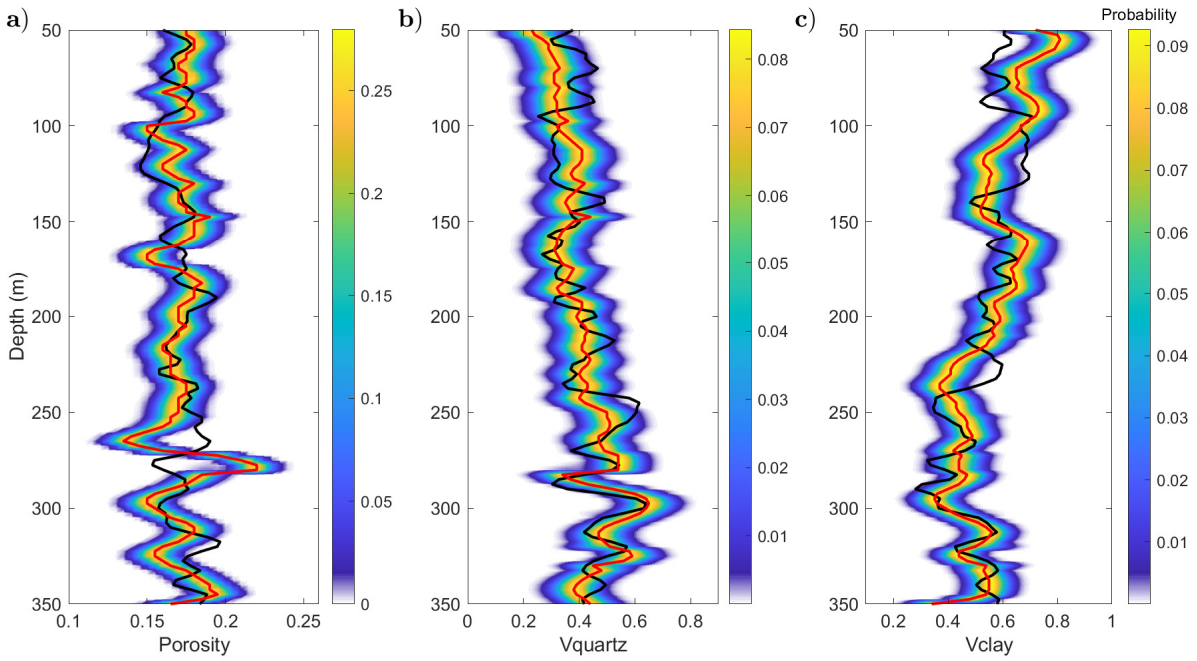

Figure 6.10: Posterior distributions of (a) porosity, (b) quartz volume, and (c) clay volume, truncated within the 0.95 confidence interval. The black lines represent the actual well logs and the red lines represent the maximum a posteriori.

Next, I apply the Bayesian approach to the entire FWI model. In Figure 6.11, the MAP models of porosity and mineral volumes are plotted. The coal volume is derived from the predicted quartz and clay volumes, as the sum of their volume fractions equals 1 in my formulation. Due to the lack of ground-truth data to compare against, it is difficult for us to verify the distribution of these parameters away from the well. However, we can find several positive features from this result, the most important of which is the successful identification of the laterally continuous coal zones in the depth range of 200 m to 300 m. These coal zones are estimated to be the main sealing units above the injection area (BBRS). Also, the inverted clay volume is relatively high throughout the model space, which is consistent with the geology in this area, namely, the lithology of the shallow strata is dominated by mudstone and shale-rich sandstone. The inverted porosity values are relatively stable, mainly between 0.15 and 0.2. However, its spatial distribution exhibits a strong degree of blockiness and may contain some artifacts.

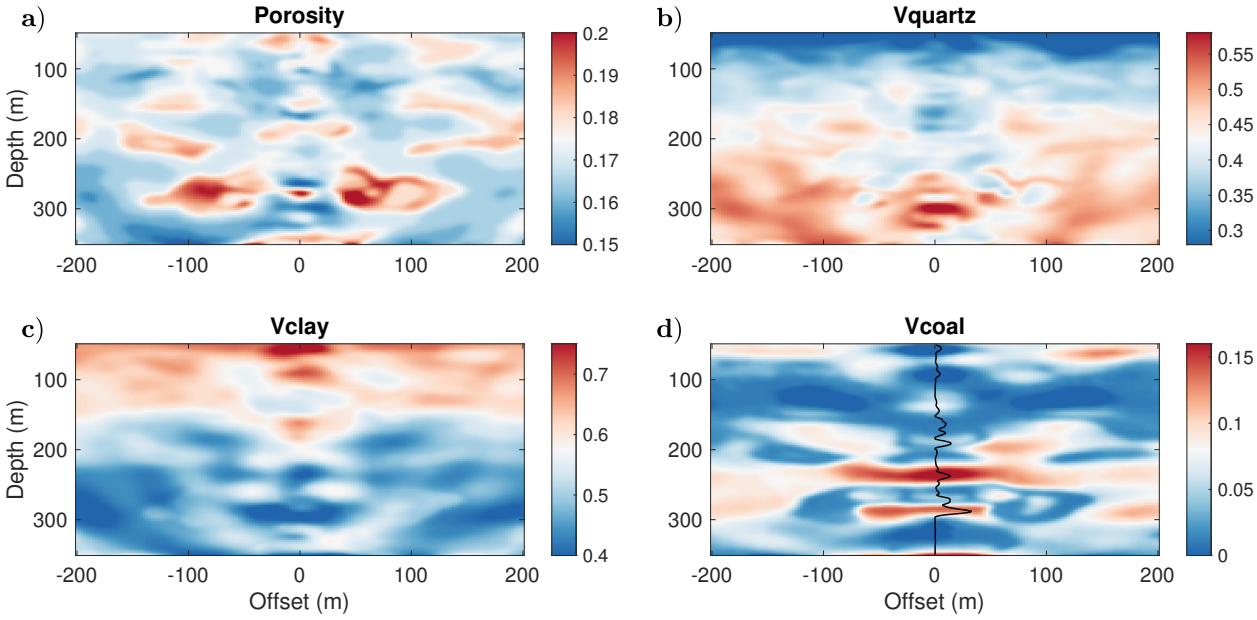

Figure 6.11: Inverted models of (a) porosity, (b) quartz volume, (c) clay volume, and (d) coal volume (superimposed the actual log curve).

6.5 Discussion

Although I expect that the combination of DAS and accelerometer data can improve the results of FWI, the premise that this expectation can be realized is that the two types of data are complementary. For example, combining permanently buried DAS fibers in wells with sparsely distributed conventional geophones on the surface can provide the latter with larger observation apertures, more types of seismic waves, denser sampling data, and even lower frequencies. However, when the supplementary effect of DAS is limited, but there are obvious shortcomings, it is worth thinking about whether incorporating DAS data can improve the inversion result. Take the application of this article as an example. The acquisition geometry corresponding to the DAS and accelerometers is the same, the sampling density is the same (1 m), and the lowest acceptable frequency is similar (about 10 Hz), but the DAS can only collect the vertical component of the wavefield, and has a remarkably lower signal-to-noise ratio. Then the help of DAS data is limited, and may even have an adverse impact on

the inversion due to data quality. Therefore, I believe it is reasonable to conclude that the accelerometer inversion model is optimal in this case. However, the proposed inversion strategy may play a greater role when DAS data has a clear advantage over conventional geophones, or DAS is the only seismic acquisition mode.

The proposed effective source method can be regarded as a redatuming method for the VSP system, which takes advantage of the one-way propagation of the wavefield. The reason for us to adopt this approach is that the near-surface complexities bring great difficulties to wavelet estimation and inversions in my study. Although the effective source approach can reduce the near-surface impact, it also brings new challenges, because introducing the wavefield at depth as a variable will increase the non-linearity and non-uniqueness of the inverse problem. So the key is, which one is easier to address, the challenge brought by directly characterizing the near surface with an erroneous wavelet or the challenge brought by the effective source approach. The answer to this question is not unique, depends on the near-surface conditions of the work area, and also depends on the development of inversion strategies for these two types of problems. As far as the field example in this chapter is concerned, I found that the effective source method is feasible, and can be viewed as a candidate for solving the near-surface inversion problem.

For clastic rocks, porosity, clay volume, and water or gas saturation are the three most common parameters of interest, and are usually treated as unknowns in the inversion. Although some studies have simplified this problem by assuming that the porosity or lithology of the target reservoir interval is known and constant, this treatment is dangerous. There are laboratory studies showing that porosity and clay content are the first and second most important parameters affecting the elastic properties of sand-shale samples. This is why I treat porosity as a model variable, even though its well log exhibits limited variation. In the same way, because the shallow coal seams in the study area greatly reduce the velocity and density of rock, I regard the coal volume as an implicit unknown quantity. One of my simplifications for the baseline study is that the water saturation is 100%. This treatment is

fair because previous studies have shown that the in-situ oil and gas saturation is sufficiently low, and also because this parameter is subject to low sensitivity and large uncertainty when it is inverted simultaneously with porosity and lithology parameters. The sensitivity issues of fluid saturation also exist in the monitor survey. To reduce the uncertainty in the prediction of dynamic reservoir parameters, especially CO_2 saturation and pore pressure, one strategy is to derive porosity and lithology models from baseline data, and then use the results as input for the monitor stage. This makes the baseline prediction of porosity and lithology parameters very important in CO_2 applications, which is also the significance of my research.

6.6 Conclusion

Carbon capture and storage is an important technology for greenhouse gas mitigation. Due to the limited knowledge of rock properties before injection, model predictions are often uncertain and must be updated when new measurements are available. The 2018 CMC VSP survey provided a dataset (accelerometers + DAS) suitable for creating a baseline model for later time-lapse analysis. In this study, I focus on integrating FWI and rock physics to recover porosity and lithology models from the measured data. To cope with near-surface complications, I used an effective source approach that allows simultaneous updating of wavefield at depth and elastic models. To include DAS data in FWI, I used a modeling strategy that can simulate DAS data that is directly comparable to the field data. To capture the bimodality of rock properties, I used a Gaussian mixture approach to predict the posterior distribution of rock physics variables conditioned on FWI results. The inverted elastic models from the accelerometer, DAS, and combined accelerometer-DAS data exhibited different features. In the absence of other verification methods, I judged that the result with acceleration data alone is more accurate according to the degree of matching with well-log data. I therefore used this result for predicting reservoir parameters and obtained meaningful results. This study represents an attempt to bring FWI technology into practical use for reservoir characterization.

Chapter 7

Conclusions

7.1 Summary

Full waveform inversion (FWI) techniques are powerful and promise to provide high-resolution estimates of subsurface properties. However, FWI is still viewed more as an imaging tool than a reservoir characterization tool. Although an increasing number of studies demonstrate the use of multiparameter elastic FWI for reservoir characterization, such characterization remains in the elastic domain and does not involve quantitative interpretation of reservoir or rock physics properties. This thesis fully explores the combination of FWI and rock physics, intending to realize the potential of FWI in quantitative prediction and monitoring of reservoir properties. In Chapter 2 and Chapter 3, I introduced the forward and inverse problems of FWI and rock physics respectively. Most of the rock physics models mentioned here were tested in subsequent chapters. At the same time, the inversion methods discussed in these two chapters allow me to implement a classic reservoir characterization workflow, where seismic inversion is geared towards the determination of elastic properties, followed by rock physics inversion that transforms these elastic properties into reservoir properties.

Estimating rock properties directly from seismic data is gaining popularity in AVO studies, but this mode of inversion is not yet examined in FWI studies. In Chapter 4, I proposed

a novel FWI approach that allows directly extracting rock and fluid properties from seismic data. I achieved this by re-parameterizing the inversion using a rock physics model. Several advantages of this approach were illustrated: 1) it allows examination of any rock physics property that has a well-defined relationship with elastic parameters; 2) it shares the same numerical structure as the conventional EFWI, allowing various existing inversion strategies to be integrated; 3) it leads to more stable solutions in comparison to those produced through sequential inversion. I also pointed out several challenges associated with this approach: 1) parameter crosstalk is generally an issue for recovering rock physics properties; 2) fluid saturation suffers from very low sensitivity when it is updated simultaneously with porosity and lithology parameters; 3) subject to the framework of local optimization, this approach cannot take full advantage of the prior information on parameter distributions like Bayesian rock physics inversion (Chapter 3). Therefore, the difference between the direct and indirect approaches remains methodological, whereas a crucial issue is to develop the direct inversion by combining prior information. In Appendix C, I considered a favorable case where two of the rock physics variables are highly correlated, I then demonstrated that by constraining their relationship in inversion via a regularization term, the inversion convergence can be improved. However, it is worth exploring the regularization strategies for describing more general parameter distribution characteristics.

Based on the novel approach described in Chapter 4, I formulated a time-lapse FWI framework to predict the time evolution of CO_2 saturation from seismic data (Chapter 5). Practical issues associated with field data applications, such as acquisition limitations, construction of the initial model, noise, and uncertainty in the rock physics model, are taken into account in the simulation. The results demonstrate the robustness of the proposed method for reconstructing both static rock properties (e.g., porosity and mineral volumes) and dynamic reservoir properties such as CO_2 saturation. To deal with the cases where pressure variations during CO_2 sequestration are relatively large, in Appendix D I proposed a joint rock physics model combing Gassmann's equation with the modified Macbeth relation

to account for both the fluid effect and the pressure effect. I then modified the time-lapse FWI strategy discussed in Chapter 5 to allow simultaneous prediction of CO_2 saturation and pore pressure. The effectiveness of this approach is validated on a synthetic dataset. Potentially the proposed methodology could be extended to depleted hydrocarbon reservoirs as well as enhanced oil recovery and carbon capture, utilization, and storage (CCUS) applications.

In Chapter 6, I applied a sequential inversion scheme combining elastic FWI (Chapter 2) and Bayesian rock physics inversion (Chapter 3) to a VSP dataset acquired with accelerometers and DAS fiber at the CMC Newell County Facility. The goal is to build a baseline model of porosity and lithology parameters to support later monitoring of CO_2 storage. To cope with near-surface complications, I used an effective source approach that allows simultaneous updating of wavefield at depth and elastic models. To include DAS data in FWI, I used a modeling strategy that can simulate DAS data that is directly comparable to the field data. To capture the bimodality of rock properties, I used a Gaussian mixture approach to predict the posterior probability distribution of rock physics variables conditioned on FWI results. While the inversion results can accurately reproduce either type of data, the elastic models inverted from the accelerator data outperform the other two in matching well logs and identifying the target reservoir. I attribute this result to the insignificant advantage of DAS data, in this case, over accelerometer data, which also suffers from single-component measurements and lower signal-to-noise ratios. The porosity and lithology models predicted from the accelerometer elastic models are reasonably accurate at the well location and are geologically meaningful in spatial distribution.

7.2 Future work

For future work, I think it is especially meaningful to explore the following four areas:

(1) Field data application

In August 2022, a VSP survey was shot at the CMC Newell County Facility as a follow-up to the 2018 survey, after years of CO_2 injection at the site (Innanen et al., 2022). Based on the work presented in Chapter 6, the FWI and rock physics methods discussed in this thesis can be applied to the 2022 monitor survey, to predict the spatial distribution of CO_2 saturation and pore pressure. Another potential application target is the 2022 rapid-repeat time-lapse VSP experiment, conducted also at the Newell County Facility (Cai et al., 2022). We have already verified that the transient changes in CO_2 can be detected by FWI, and the next step is to carry out rock physics analysis.

(2) Scale issues in rock physics transform

Scale issues have always been at the heart of rock physics research. To interpret seismic data for rock physics properties, an important question is whether the rock physics models established in the laboratory or well can be used at the seismic scale. Logs and cores give a resolution of less than 0.3 m, while seismic resolution is often no better than 15 m (Dewar and Pickford, 2001). This can also be expressed in terms of the frequency ranges used: laboratory frequencies are around 10^6 Hz, logging frequencies are around 10^4 Hz, whereas the frequencies of *in-situ* seismic data are less than 100 Hz (Mavko et al., 2020). The rock physics transforms are generally considered to be scale-dependent. However, Dvorkin and Wollner (2017) illustrate that these transforms can be approximately scale-independent, and that a rock-physics model established at the borehole approximately holds at the seismic scale. They further point out that the real question in the subject of scale is: What are the averaged (smeared) rock physics properties and conditions that the seismically derived elastic properties point to? To the best of my knowledge, the scale issue has not been resolved until now and it raises a lot of debate. In Chapter 6, I constructed a rock physics model based on

arithmetically upscaled well logs and used it to interpret the elastic parameters derived from FWI. However, whether this averaging method is optimal, for example, compared to the Backus average, and what kind of "effective property" each average method leads to. I plan to conduct further research and understanding on the scale issue, to guide the integration of different data.

(3) Integrated time-lapse feasibility study

A feasibility study is of crucial importance for time-lapse seismic monitoring because the extraction of useful information is possible only if the signals are detectable and the noise is insignificant (Lumley, 2001). An integrated feasibility study generally includes three important elements: reservoir simulation, rock physics, and seismic modeling. Reservoir simulation is used to understand how fluids flow within a reservoir given a geologic model, and the simulation provides time-dependent pressure and fluid saturation of the reservoir. Rock physics is used to produce the elastic model corresponding to the reservoir model; then seismic modeling is used to simulate the seismic response. Macquet et al. (2019) reports an integrated feasibility study for the CMC Newell County facility. However, due to limited knowledge of rock properties before injection, reservoir simulation results are subject to uncertainty and must be updated as new measurements become available. The porosity and lithology parameter models I developed in Chapter 6 can be used to update the baseline model and thus improve the feasibility analysis for this project.

(4) Uncertainty quantification

Reservoir characterization usually requires integrating different types of data. The uncertainty associated with this process comes from several sources: measurement errors in seismic and well-log data, data processing, approximate wave propagation model, and the rock physics transformation from elastic properties to reservoir properties. One fundamental reason for quantifying uncertainty is to report error bars along with interpretation results. A more practical reason is for risk analysis and optimal decision-making (Bosch et al., 2010).

For an inverse problem, when quantifying uncertainty a user seeks to determine the posterior probability distribution of model variables conditioned on the measured data. The Bayesian rock physics inversions discussed in Chapter 3 and Chapter 6 do not account for the uncertainty in the estimation of elastic properties (i.e., uncertainty in FWI). Due to the high dimensionality of the model space paired with the computational costs of the forward problem, stochastic methods such as Monte Carlo are generally infeasible for FWI, causing the development of uncertainty quantification in FWI lagged considerably behind. Most proposed approaches in this area are based on low-rank estimates of the posterior covariance matrix, for example, the inverse Hessian. New approaches are also emerging (Gebraad et al., 2020; Keating and Innanen, 2021). Comparing the pros and cons of current methods and exploring the scheme of quantifying more general uncertainty in FWI are what I would like to work on in the future.

Bibliography

Aki, K., and P. G. Richards, 2002, Quantitative seismology.

Alemie, W. M., 2017, Time-lapse full waveform inversion methods: PhD thesis, Alberta University.

Alkhalifah, T., and R. É. Plessix, 2014, A recipe for practical full-waveform inversion in anisotropic media: An analytical parameter resolution study: Geophysics, **79**, R91–R101.

Anagaw, A. Y., and M. D. Sacchi, 2018, Model parametrization strategies for Newton-based acoustic full waveform inversion: Journal of Applied Geophysics, **157**, 23–36.

Aragao, O., and P. Sava, 2020, Elastic full-waveform inversion with probabilistic petrophysical model constraints: Geophysics, **85**, R101–R111.

Arts, R., A. Chadwick, O. Eiken, S. Thibeau, and S. Nooner, 2008, Ten years' experience of monitoring CO_2 injection in the Utsira Sand at Sleipner, offshore Norway: First break, **26**.

Arts, R., O. Eiken, A. Chadwick, P. Zweigel, L. Van der Meer, and B. Zinszner, 2003, Monitoring of CO_2 injected at Sleipner using time lapse seismic data: Greenhouse Gas Control Technologies-6th International Conference, Elsevier, 347–352.

Asnaashari, A., R. Brossier, S. Garambois, F. Audebert, P. Thore, and J. Virieux, 2013, Regularized seismic full waveform inversion with prior model information: Geophysics, **78**, R25–R36.

———, 2015, Time-lapse seismic imaging using regularized full-waveform inversion with a prior model: which strategy?: Geophysical prospecting, **63**, 78–98.

Avseth, P., T. Mukerji, and G. Mavko, 2010, Quantitative seismic interpretation: Applying rock physics tools to reduce interpretation risk: Cambridge university press.

Babak, O., and C. Deutsch, 2008, Simulating oil recovery during CO_2 sequestration into a mature oil reservoir: Journal of Canadian Petroleum Technology, **47**, 34–40.

Bachrach, R., 2006, Joint estimation of porosity and saturation using stochastic rock-physics modeling: Geophysics, **71**, O53–O63.

Bachrach, R., and P. Avseth, 2008, Rock physics modeling of unconsolidated sands: Accounting for nonuniform contacts and heterogeneous stress fields in the effective media approximation with applications to hydrocarbon exploration: Geophysics, **73**, E197–E209.

Barnes, C., and M. Charara, 2009, The domain of applicability of acoustic full-waveform inversion for marine seismic data: Geophysics, **74**, WCC91–WCC103.

Batzle, M., and Z. Wang, 1992, Seismic properties of pore fluids: Geophysics, **57**, 1396–1408.

Becker, M. W., C. Ciervo, M. Cole, T. Coleman, and M. Mondanos, 2017, Fracture hydromechanical response measured by fiber optic distributed acoustic sensing at millihertz frequencies: Geophysical Research Letters, **44**, 7295–7302.

Berenger, J. P., 1994, A perfectly matched layer for the absorption of electromagnetic waves: Journal of computational physics, **114**, 185–200.

Bergmo, P. E. S., A.-A. Grimstad, and E. Lindeberg, 2011, Simultaneous CO_2 injection and water production to optimise aquifer storage capacity: International Journal of Greenhouse Gas Control, **5**, 555–564.

Berryman, J. G., 1995, Mixture theories for rock properties: Rock physics and phase relations: A handbook of physical constants, **3**, 205–228.

Bhakta, T., and M. Landrø, 2014, Estimation of pressure-saturation changes for unconsolidated reservoir rocks with high Vp/Vs ratio: Geophysics, **79**, M35–M54.

Biot, M. A., 1956, Theory of propagation of elastic waves in a fluid-saturated porous solid. II. Higher frequency range: The Journal of the acoustical Society of america, **28**, 179–191.

Borisov, D., F. Gao, P. Williamson, and J. Tromp, 2020, Application of 2D full-waveform

inversion on exploration land data: Geophysics, **85**, R75–R86.

Bosch, M., L. Cara, J. Rodrigues, A. Navarro, and M. Díaz, 2007, A Monte Carlo approach to the joint estimation of reservoir and elastic parameters from seismic amplitudes: Geophysics, **72**, O29–O39.

Bosch, M., T. Mukerji, and E. F. Gonzalez, 2010, Seismic inversion for reservoir properties combining statistical rock physics and geostatistics: A review: Geophysics, **75**, 75A165–75A176.

Bozdağ, E., J. Trampert, and J. Tromp, 2011, Misfit functions for full waveform inversion based on instantaneous phase and envelope measurements: Geophysical Journal International, **185**, 845–870.

Brie, A., F. Pampuri, A. Marsala, and O. Meazza, 1995, Shear sonic interpretation in gas-bearing sands: Presented at the SPE Annual Technical Conference and Exhibition, OnePetro.

Brittan, J., and I. Jones, 2019, FWI evolution—From a monolith to a toolkit: The Leading Edge, **38**, 179–184.

Brossier, R., S. Operto, and J. Virieux, 2009, Seismic imaging of complex onshore structures by 2D elastic frequency-domain full-waveform inversion: Geophysics, **74**, WCC105–WCC118.

Buland, A., O. Kolbjørnsen, R. Hauge, Ø. Skjæveland, and K. Duffaut, 2008, Bayesian lithology and fluid prediction from seismic prestack data: Geophysics, **73**, C13–C21.

Buland, A., and H. Omre, 2003, Bayesian linearized AVO inversion: Geophysics, **68**, 185–198.

Bunks, G., F. M. Saleck, S. Zaleski, and G. Chavent, 1995, Multiscale seismic waveform inversion: Geophysics, **60**, 1457–1473.

Byerley, G., D. Monk, P. Aaron, and M. Yates, 2018, Time-lapse seismic monitoring of individual hydraulic frac stages using a downhole DAS array: The Leading Edge, **37**, 802–810.

Cai, X., K. Innanen, Q. Hu, K. W. Hall, and D. C. Lawton, 2022, VSP imaging of CO_2 injection with rapid-repeat time lapse full waveform inversion: CREWES Research Reports, **34**.

Carcione, J. M., and P. Avseth, 2015, Rock-physics templates for clay-rich source rocks: Geophysics, **80**, D481–D500.

Castagna, J., M. Batzle, T. Kan, and M. Backus, 1993, Rock physics—the link between rock properties and AVO response: Offset-dependent reflectivity—Theory and practice of AVO analysis: SEG, **8**, 135–171.

Chadwick, R., R. Arts, and O. Eiken, 2005, 4D seismic quantification of a growing CO_2 plume at Sleipner, North Sea: Geological Society, London, Petroleum Geology Conference series, Geological Society of London, 1385–1399.

Chen, B., D. R. Harp, Z. Lu, and R. J. Pawar, 2020, Reducing uncertainty in geologic CO_2 sequestration risk assessment by assimilating monitoring data: International Journal of Greenhouse Gas Control, **94**, 102926.

Chen, K., 2018, Elastic least-squares reverse time migration and elastic Gauss-Newton full-waveform inversion: PhD thesis, University of Alberta.

Colombo, D., E. Sandoval-Curiel, D. Rovetta, and A. Kontakis, 2021, Near-surface full-waveform inversion in a transmission surface-consistent schemefwi in a surface-consistent scheme: Geophysics, **86**, U15–U29.

Connolly, P., 2017, Inversion of seismic data for reservoir properties: recent advances and the road ahead: 87th Annual International Meeting, SEG, Expanded Abstracts, 5267–5272.

Davis, T. L., M. Landrø, and M. Wilson, 2019, Geophysics and geosequestration: Cambridge University Press.

De Barros, L., and M. Dietrich, 2008, Perturbations of the seismic reflectivity of a fluid-saturated depth-dependent poroelastic medium: The Journal of the Acoustical Society of America, **123**, 1409–1420.

De Barros, L., M. Dietrich, and B. Valette, 2010, Full waveform inversion of seismic waves

reflected in a stratified porous medium: Geophysical Journal International, **182**, 1543–1556.

Dewar, J., and S. Pickford, 2001, Rock physics for the rest of us-an informal discussion: CSEG Recorder, **26**, 42–49.

Dokter, E., D. Köhn, D. Wilken, D. De Nil, and W. Rabbel, 2017, Full waveform inversion of SH-and Love-wave data in near-surface prospecting: Geophysical Prospecting, **65**, 216–236.

Doyen, P., 2007, Seismic reservoir characterization: An earth modelling perspective: EAGE publications.

Dubrule, O., M. Thibaut, P. Lamy, and A. Haas, 1998, Geostatistical reservoir characterization constrained by 3D seismic data: Petroleum Geoscience, **4**, 121–128.

Duong, C., C. Bower, K. Hume, L. Rock, and S. Tessarolo, 2019, Quest carbon capture and storage offset project: Findings and learnings from 1st reporting period: International Journal of Greenhouse Gas Control, **89**, 65–75.

Dupuy, B., A. Asnaashari, R. Brossier, S. Garambois, L. Métivier, A. Ribodetti, and J. Virieux, 2016a, A downscaling strategy from FWI to microscale reservoir properties from high-resolution images: The Leading Edge, **35**, 146–150.

Dupuy, B., S. Garambois, A. Asnaashari, H. M. Balhareth, M. Landrø, A. Stovas, and J. Virieux, 2016b, Estimation of rock physics properties from seismic attributes — Part 2: Applications: Geophysics, **81**, M55–M69.

Dupuy, B., S. Garambois, and J. Virieux, 2016c, Estimation of rock physics properties from seismic attributes — Part 1: Strategy and sensitivity analysis: Geophysics, **81**, M35–M53.

Dupuy, B., A. Romdhane, P. Eliasson, E. Querendez, H. Yan, V. A. Torres, and A. Ghaderi, 2017, Quantitative seismic characterization of CO_2 at the Sleipner storage site, North Sea: Interpretation, **5**, SS23–SS42.

Dupuy, B., A. Romdhane, P. Eliasson, and H. Yan, 2021a, Combined geophysical and rock physics workflow for quantitative CO_2 monitoring: International Journal of Greenhouse

Gas Control, **106**, 103217.

Dupuy, B., A. Romdhane, P.-L. Nordmann, P. Eliasson, and J. Park, 2021b, Bayesian rock-physics inversion: Application to CO_2 storage monitoring: Geophysics, **86**, M101–M122.

Dvorkin, J., 2004, Seismic reflections of rock properties: Hart's E & P, **77**, 59–61.

Dvorkin, J., M. A. Gutierrez, and D. Grana, 2014, Seismic reflections of rock properties: Cambridge University Press.

Dvorkin, J., and A. Nur, 1996, Elasticity of high-porosity sandstones: Theory for two North Sea data sets: Geophysics, **61**, 1363–1370.

Dvorkin, J., M. Prasad, A. Sakai, and D. Lavoie, 1999, Elasticity of marine sediments: Rock physics modeling: Geophysical research letters, **26**, 1781–1784.

Dvorkin, J., and U. Wollner, 2017, Rock-physics transforms and scale of investigation: Geophysics, **82**, MR75–MR88.

Eaid, M., 2022, Distributed acoustic sensing: modelling, full waveform inversion, and its use in seismic monitoring: PhD thesis.

Eaid, M., S. Keating, and K. Innanen, 2022, Combined elastic fwi of accelerometer and DAS VSP data from a CO_2 sequestration test site in newell county, alberta: SEG International Exposition and Annual Meeting, SEG, D011S045R003.

Eaid, M. V., S. D. Keating, and K. A. Innanen, 2020, Multiparameter seismic elastic full-waveform inversion with combined geophone and shaped fiber-optic cable data: Geophysics, **85**, R537–R552.

Eberhart-Phillips, D., D.-H. Han, and M. Zoback, 1989, Empirical relationships among seismic velocity, effective pressure, porosity, and clay content in sandstone: Geophysics, **54**, 82–89.

Egorov, A., J. Correa, A. Bóna, R. Pevzner, K. Tertyshnikov, S. Glubokovskikh, V. Puzyrev, and B. Gurevich, 2018, Elastic full-waveform inversion of vertical seismic profile data acquired with distributed acoustic sensors: Geophysics, **83**, R273–R281.

Eigestad, G. T., H. K. Dahle, B. Hellevang, F. Riis, W. T. Johansen, and E. Øian, 2009,

Geological modeling and simulation of CO_2 injection in the Johansen formation: Computational Geosciences, **13**, 435.

Fu, X., S. Romahn, and K. Innanen, 2020, Double-wavelet double-difference time-lapse waveform inversion, *in* SEG Technical Program Expanded Abstracts 2020: Society of Exploration Geophysicists, 3764–3767.

Furre, A.-K., A. Kiær, and O. Eiken, 2015, CO_2-induced seismic time shifts at Sleipner: Interpretation, **3**, SS23–SS35.

Gao, R. S., A. Y. Sun, and J.-P. Nicot, 2016, Identification of a representative dataset for long-term monitoring at the Weyburn CO_2-injection enhanced oil recovery site, Saskatchewan, Canada: International Journal of Greenhouse Gas Control, **54**, 454–465.

Gardner, G., L. Gardner, and A. Gregory, 1974, Formation velocity and density—the diagnostic basics for stratigraphic traps: Geophysics, **39**, 770–780.

Gassmann, F., 1951, Elastic waves through a packing of spheres: Geophysics, **16**, 673–685.

Gebraad, L., C. Boehm, and A. Fichtner, 2020, Bayesian elastic full-waveform inversion using Hamiltonian Monte Carlo: Journal of Geophysical Research: Solid Earth, **125**, e2019JB018428.

Ghorbanidehno, H., A. Kokkinaki, J. Y. Li, E. Darve, and P. K. Kitanidis, 2015, Real-time data assimilation for large-scale systems: The spectral Kalman filter: Advances in water resources, **86**, 260–272.

Ghosh, R., M. K. Sen, and N. Vedanti, 2015, Quantitative interpretation of CO_2 plume from Sleipner (North Sea), using post-stack inversion and rock physics modeling: International journal of greenhouse gas control, **32**, 147–158.

Grana, D., 2014, Probabilistic approach to rock physics modeling: Geophysics, **79**, D123–D143.

———, 2016a, Bayesian linearized rock-physics inversion: Geophysics, **81**, D625–D641.

———, 2016b, Pressure–velocity relations in reservoir rocks: Modified MacBeth's equation: Journal of Applied Geophysics, **132**, 234–241.

Grana, D., M. Liu, and M. Ayani, 2020, Prediction of CO_2 saturation spatial distribution using geostatistical inversion of time-lapse geophysical data: IEEE Transactions on Geoscience and Remote Sensing, **59**, 3846–3856.

Grana, D., T. Mukerji, and P. Doyen, 2021, Seismic reservoir modeling: Theory, examples, and algorithms: John Wiley & Sons.

Grana, D., and E. D. Rossa, 2010, Probabilistic petrophysical-properties estimation integrating statistical rock physics with seismic inversion: Geophysics, **75**, O21–O37.

Grude, S., M. Landrø, and B. Osdal, 2013, Time-lapse pressure–saturation discrimination for CO_2 storage at the Snøhvit field: International Journal of Greenhouse Gas Control, **19**, 369–378.

Guitton, A., 2012, Blocky regularization schemes for full-waveform inversion: Geophysical Prospecting, **60**, 870–884.

Guitton, A., G. Ayeni, and G. Gonzales, 2010, A preconditioning scheme for full waveform inversion: SEG International Exposition and Annual Meeting, SEG, SEG–2010.

Hall, K. W., K. L. Bertram, M. Bertram, K. Innanen, and D. C. Lawton, 2019, Simultaneous accelerometer and optical fibre multi-azimuth walk-away VSP experiment: Newell County, Alberta, Canada: Presented at the SEG International Exposition and Annual Meeting, OnePetro.

Han, D.-h., 1987, Effects of porosity and clay content on acoustic properties of sandstones and unconsolidated sediments: Stanford University.

Harris, K., D. White, D. Melanson, C. Samson, and T. M. Daley, 2016, Feasibility of time-lapse VSP monitoring at the aquistore CO_2 storage site using a distributed acoustic sensing system: International Journal of Greenhouse Gas Control, **50**, 248–260.

Hill, R., 1952, The elastic behaviour of a crystalline aggregate: Proceedings of the Physical Society. Section A, **65**, 349.

Hu, Q., D. Grana, and K. A. Innanen, 2023, Feasibility of seismic time-lapse monitoring of CO_2 with rock physics parametrized full waveform inversion: Geophysical Journal Inter-

national, **233**, 402–419.

Hu, Q., and K. Innanen, 2021, Elastic full-waveform inversion with rock-physics constraints: First International Meeting for Applied Geoscience & Energy, Society of Exploration Geophysicists, 662–666.

Hu, Q., S. Keating, K. A. Innanen, and H. Chen, 2021, Direct updating of rock-physics properties using elastic full-waveform inversion: Geophysics, **86**, MR117–MR132.

Innanen, K., K. Hall, and D. Lawton, 2022, A time-lapse multi-offset, multi-azimuth VSP acquired as a candidate for low-cost monitoring of CO_2 injection and storage: CREWES Research Reports, **34**.

Innanen, K. A., 2014, Seismic AVO and the inverse Hessian in precritical reflection full waveform inversion: Geophysical Journal International, **199**, 717–734.

Isaac, J. H., and D. C. Lawton, 2016, A case study showing the value of multioffset synthetic seismograms in seismic data interpretation: Interpretation, **4**, T455–T459.

Ivandic, M., C. Juhlin, S. Lueth, P. Bergmann, A. Kashubin, D. Sopher, A. Ivanova, G. Baumann, and J. Henninges, 2015, Geophysical monitoring at the Ketzin pilot site for CO_2 storage: New insights into the plume evolution: International Journal of Greenhouse Gas Control, **32**, 90–105.

Jahangiri, H. R., and D. Zhang, 2012, Ensemble based co-optimization of carbon dioxide sequestration and enhanced oil recovery: International Journal of Greenhouse Gas Control, **8**, 22–33.

Jin, G., and B. Roy, 2017, Hydraulic-fracture geometry characterization using low-frequency DAS signal: The Leading Edge, **36**, 975–980.

Johansen, T. A., E. H. Jensen, G. Mavko, and J. Dvorkin, 2013, Inverse rock physics modeling for reservoir quality prediction: Geophysics, **78**, M1–M18.

Johnson, D. L., D. L. Hemmick, and H. Kojima, 1994, Probing porous media with first and second sound. I. dynamic permeability: Journal of Applied Physics, **76**, 104–114.

Johnston, D. H., 2013, Practical applications of time-lapse seismic data: Society of Explo-

ration Geophysicists.

Jones, S. M., 1995, Velocities and quality factors of sedimentary rocks at low and high effective pressures: Geophysical Journal International, **123**, 774–780.

Kamali, F., F. Hussain, and Y. Cinar, 2017, An experimental and numerical analysis of water-alternating-gas and simultaneous-water-and-gas displacements for carbon dioxide enhanced oil recovery and storage: SPE Journal, **22**, 521–538.

Kamath, N., I. Tsvankin, and E. Z. Naeini, 2017, Facies-constrained FWI: Toward application to reservoir characterization: The Leading Edge, **36**, 924–930.

Kamei, R., and D. Lumley, 2017, Full waveform inversion of repeating seismic events to estimate time-lapse velocity changes: Geophysical Journal International, **209**, 1239–1264.

Keating, S., M. Eaid, and K. Innanen, 2021, Effective sources: removing the near surface from the VSP FWI problem: CREWES Research Reports, **33**.

Keating, S., and K. A. Innanen, 2019a, Parameter cross-talk and leakage between spatially-separated unknowns in viscoelastic FWI: 89th Annual International Meeting, SEG, Expanded Abstracts, 1415–1419.

———, 2019b, Parameter crosstalk and modeling errors in viscoacoustic seismic full-waveform inversion: Geophysics, **84**, R641–R653.

Keating, S. D., and K. A. Innanen, 2021, Null-space shuttles for targeted uncertainty analysis in full-waveform inversion: Geophysics, **86**, R63–R76.

Kemper, M., and J. Gunning, 2014, Joint impedance and facies inversion–seismic inversion redefined: First Break, **32**, 89–95.

Köhn, D., D. Wilken, D. De Nil, T. Wunderlich, W. Rabbel, L. Werther, J. Schmidt, C. Zielhofer, and S. Linzen, 2019, Comparison of time-domain SH waveform inversion strategies based on sequential low and bandpass filtered data for improved resolution in near-surface prospecting: Journal of Applied Geophysics, **160**, 69–83.

Kolkman-Quinn, B. J., 2022, Time-lapse VSP monitoring of CO_2 sequestration at the CaMI Field Research Station: Master's thesis, Science.

Kuster, G. T., and M. N. Toksöz, 1974, Velocity and attenuation of seismic waves in two-phase media: Geophysics, **39**, 587–618.

Kuvshinov, B., 2016, Interaction of helically wound fibre-optic cables with plane seismic waves: Geophysical Prospecting, **64**, 671–688.

Lailly, P., 1983, The seismic inverse problem as a sequence of before stack migrations: Presented at the Conference on inverse scattering: Theory and application.

Landrø, M., 2001, Discrimination between pressure and fluid saturation changes from time-lapse seismic data: Geophysics, **66**, 836–844.

Landrø, M., H. H. Veire, K. Duffaut, and N. Najjar, 2003, Discrimination between pressure and fluid saturation changes from marine multicomponent time-lapse seismic data: Geophysics, **68**, 1592–1599.

Lawton, D. C., J. Dongas, K. Osadetz, A. Saeedfar, and M. Macquet, 2019, Development and analysis of a geostatic model for shallow CO_2 injection at the field research station, southern alberta, canada: Geophysics and Geosequestration. Cambridge University Press, Cambridge, **280**, 296.

Lie, K.-A., 2019, An introduction to reservoir simulation using MATLAB/GNU Octave: User guide for the MATLAB Reservoir Simulation Toolbox (MRST): Cambridge University Press.

Lions, J. L., 1971, Optimal control of systems governed by partial differential equations: Springer, **170**.

Liu, M., and D. Grana, 2018, Stochastic nonlinear inversion of seismic data for the estimation of petroelastic properties using the ensemble smoother and data reparameterization: Geophysics, **83**, M25–M39.

———, 2020, Petrophysical characterization of deep saline aquifers for CO_2 storage using ensemble smoother and deep convolutional autoencoder: Advances in Water Resources, **142**, 103634.

Lumley, D. E., 2001, Time-lapse seismic reservoir monitoring: Geophysics, **66**, 50–53.

MacBeth, C., 2004, A classification for the pressure-sensitivity properties of a sandstone rock frame: Geophysics, **69**, 497–510.

Macquet, M., D. Lawton, K. Osadetz, G. Maidment, M. Bertram, K. Hall, B. Kolkman-Quinn, J. M. Parra, F. Race, G. Savard, et al., 2022, Overview of Carbon Management Canada's pilot-scale CO_2 injection site for developing and testing monitoring technologies for carbon capture and storage, and methane detection: CSEG Recorder, **47**, 1–27.

Macquet, M., D. C. Lawton, A. Saeedfar, and K. G. Osadetz, 2019, A feasibility study for detection thresholds of CO_2 at shallow depths at the CaMI Field Research Station, Newell County, Alberta, Canada: Petroleum Geoscience, **25**, 509–518.

Maharramov, M., B. Biondi, and M. Meadows, 2016, Time-lapse inverse theory with applications: Geophysics, 81: R485–R501.

Mallick, S., 1999, Some practical aspects of prestack waveform inversion using a genetic algorithm: An example from the east Texas Woodbine gas sand: Geophysics, **64**, 326–336.

———, 2007, Amplitude-variation-with-offset, elastic-impedence, and wave-equation synthetics—a modeling study: Geophysics, **72**, C1–C7.

Mallick, S., and S. Adhikari, 2015, Amplitude-variation-with-offset and prestack-waveform inversion: A direct comparison using a real data example from the Rock Springs Uplift, Wyoming, USA: Geophysics, **80**, B45–B59.

Marfurt, K. J., 1984, Accuracy of finite-difference and finite-element modeling of the scalar and elastic wave equations: Geophysics, **49**, 533–549.

Martin, G. S., R. Wiley, and K. J. Marfurt, 2006, Marmousi2: An elastic upgrade for marmousi: The leading edge, **25**, 156–166.

Mateeva, A., J. Lopez, H. Potters, J. Mestayer, B. Cox, D. Kiyashchenko, P. Wills, S. Grandi, K. Hornman, B. Kuvshinov, et al., 2014, Distributed acoustic sensing for reservoir monitoring with vertical seismic profiling: Geophysical Prospecting, **62**, 679–692.

Mavko, G., T. Mukerji, and J. Dvorkin, 2020, The rock physics handbook: Cambridge

university press.

Menke, W., 2018, Geophysical data analysis: Discrete inverse theory: Academic press.

Métivier, L., A. Allain, R. Brossier, Q. Mérigot, E. Oudet, and J. Virieux, 2018, Optimal transport for mitigating cycle skipping in full-waveform inversion: A graph-space transform approach: Geophysics, **83**, R515–R540.

Métivier, L., R. Brossier, S. Operto, and J. Virieux, 2017, Full waveform inversion and the truncated Newton method: SIAM Review, **59**, 153–195.

Mindlin, R. D., 1949, Compliance of elastic bodies in contact.

Morency, C., Y. Luo, and J. Tromp, 2009, Finite-frequency kernels for wave propagation in porous media based upon adjoint methods: Geophysical Journal International, **179**, 1148–1168.

Mukerji, T., A. Jørstad, P. Avseth, G. Mavko, and J. Granli, 2001, Mapping lithofacies and pore-fluid probabilities in a North Sea reservoir: Seismic inversions and statistical rock physics: Geophysics, **66**, 988–1001.

Mulder, W., and R.-E. Plessix, 2008, Exploring some issues in acoustic full waveform inversion: Geophysical Prospecting, **56**, 827–841.

Myung, I. J., 2003, Tutorial on maximum likelihood estimation: Journal of mathematical Psychology, **47**, 90–100.

Naeini, E. Z., T. Alkhalifah, I. Tsvankin, N. Kamath, and J. B. Cheng, 2016, Main components of full-waveform inversion for reservoir characterization: First Break, **34**, 37–48.

Nocedal, J., and S. J. Wright, 2006, Numerical optimization.

Operto, S., Y. Gholami, V. Prieux, A. Ribodetti, R. Brossier, L. Metivier, and J. Virieux, 2013, A guided tour of multiparameter full-waveform inversion with multicomponent data: From theory to practice: The Leading Edge, **32**, 1040–1054.

Pan, W., K. A. Innanen, and Y. Geng, 2018a, Elastic full-waveform inversion and parametrization analysis applied to walk-away vertical seismic profile data for unconventional (heavy oil) reservoir characterization: Geophysical Journal International, **213**,

1934–1968.

Pan, W., L. Qu, K. A. Innanen, J. Dettmer, M. Macquet, D. Lawton, and Y. Wang, 2023, Imaging near-surface s-wave velocity and attenuation models by full-waveform inversion with distributed acoustic sensing-recorded surface waves: Geophysics, **88**, R65–R78.

Pan, W. Y., Y. Geng, and K. A. Innanen, 2018b, Interparameter trade-off quantification and reduction in isotropic-elastic full-waveform inversion: synthetic experiments and Hussar land data set application: Geophysical Journal International, **213**, 1305–1333.

Pan, W. Y., K. A. Innanen, Y. Geng, and J. X. Li, 2019, Interparameter trade-off quantification for isotropic-elastic full-waveform inversion with various model parameterizations: Geophysics, **84**, R185–R206.

Pan, W. Y., K. A. Innanen, and W. Y. Liao, 2017, Accelerating Hessian-free Gauss-Newton full-waveform inversion via l-BFGS preconditioned conjugate-gradient algorithm: Geophysics, **82**, R49–R64.

Pendrel, J., 2001, Seismic inversion—the best tool for reservoir characterization: CSEG Recorder, **26**, 18–24.

Picotti, S., J. M. Carcione, and J. Ba, 2018, Rock-physics templates based on seismic Q: Geophysics, **84**, MR13–MR23.

Plessix, R., P. Milcik, H. Rynja, A. Stopin, K. Matson, and S. Abri, 2013, Multiparameter full-waveform inversion: Marine and land examples: The Leading Edge, **32**, 1030–1038.

Plessix, R. E., 2006, A review of the adjoint-state method for computing the gradient of a functional with geophysical applications: Geophysical Journal International, **167**, 495–503.

Plessix, R.-E., S. Michelet, H. Rynja, H. Kuehl, C. Perkins, J. de Maag, and P. Hatchell, 2010, Some 3D applications of full waveform inversion: 72nd EAGE Conference and Exhibition-Workshops and Fieldtrips, European Association of Geoscientists & Engineers, cp–162.

Pörtner, H. O., D. C. Roberts, H. Adams, C. Adler, P. Aldunce, E. Ali, R. A. Begum, R. Betts, R. B. Kerr, R. Biesbroek, et al., 2022, Climate change 2022: impacts, adaptation

and vulnerability.

Posey Jr, R., G. Johnson, and S. Vohra, 2000, Strain sensing based on coherent Rayleigh scattering in an optical fibre: Electronics Letters, **36**, 1.

Pratt, R. G., 1990, Frequency-domain elastic wave modeling by finite differences: A tool for crosshole seismic imaging: Geophysics, **55**, 626–632.

Pratt, R. G., C. Shin, and G. J. Hick, 1998, Gauss–Newton and full Newton methods in frequency–space seismic waveform inversion: Geophysical Journal International, **133**, 341–362.

Prieux, V., R. Brossier, S. Operto, and J. Virieux, 2013a, Multiparameter full waveform inversion of multicomponent ocean-bottom-cable data from the Valhall field. Part 1: Imaging compressional wave speed, density and attenuation: Geophysical Journal International, **194**, 1640–1664.

———, 2013b, Multiparameter full waveform inversion of multicomponent ocean-bottom-cable data from the Valhall field. Part 2: Imaging compressive-wave and shear-wave velocities: Geophysical Journal International, **194**, 1665–1681.

Queißer, M., and S. C. Singh, 2013a, Full waveform inversion in the time lapse mode applied to CO_2 storage at Sleipner: Geophysical prospecting, **61**, 537–555.

———, 2013b, Localizing CO_2 at Sleipner-seismic images versus P-wave velocities from waveform inversion: Geophysics, **78**, B131–B146.

Ravaut, C., S. Operto, L. Improta, J. Virieux, A. Herrero, and P. Dell'Aversana, 2004, Multiscale imaging of complex structures from multifold wide-aperture seismic data by frequency-domain full-waveform tomography: Application to a thrust belt: Geophysical Journal International, **159**, 1032–1056.

Raymer, L. L., E. R. Hunt, and J. S. Gardner, 1980, An improved sonic transit time-to-porosity transform: SPWLA Annual Logging Symposium, SPWLA, SPWLA–1980.

Ringrose, P., 2020, How to store CO_2 underground: insights from early-mover CCS Projects: Springer.

Roach, L. A., D. J. White, and B. Roberts, 2015, Assessment of 4D seismic repeatability and CO_2 detection limits using a sparse permanent land array at the aquistore CO_2 storage site: Geophysics, **80**, WA1–WA13.

Rocha, D., and P. Sava, 2018, Elastic reflection waveform inversion with petrophysical model constraints: 88th Annual International Meeting, SEG, Expanded Abstracts, 1203–1207.

Romdhane, A., and E. Querendez, 2014, CO_2 characterization at the Sleipner field with full waveform inversion: Application to synthetic and real data: Energy procedia, **63**, 4358–4365.

Russell, B. H., 1988, Introduction to seismic inversion methods: SEG Books.

Russell, B. H., D. Gray, and D. P. Hampson, 2011, Linearized AVO and poroelasticity: Geophysics, **76**, C19–C29.

Rütters, H., I. Möller, F. May, K. Flornes, V. Hladik, A. Arvanitis, N. Gülec, C. Bakiler, A. Dudu, L. Kucharic, et al., 2013, State-of-the-art of monitoring methods to evaluate storage site performance: CGS Europe Key Report, **1**, 109.

Saltzer, R., C. Finn, and O. Burtz, 2005, Predicting Vshale and porosity using cascaded seismic and rock physics inversion: The Leading Edge, **24**, 732–736.

Sambridge, M., 1999, Geophysical inversion with a neighbourhood algorithm—i. searching a parameter space: Geophysical journal international, **138**, 479–494.

Sayers, C. M., 2006, Sensitivity of time-lapse seismic to reservoir stress path: Geophysical prospecting, **54**, 369–380.

Schuster, G. T., 2017, Seismic inversion: Society of Exploration Geophysicists.

Sen, M. K., 2006, Seismic inversion: Society of Petroleum Engineers Richardson, TX.

Sen, M. K., and I. G. Roy, 2003, Computation of differential seismograms and iteration adaptive regularization in prestack waveform inversion: Geophysics, **68**, 2026–2039.

Sen, M. K., and P. L. Stoffa, 2013, Global optimization methods in geophysical inversion: Cambridge University Press.

Sheriff, R. E., and L. P. Geldart, 1995, Exploration seismology: Cambridge university press.

Shi, Y. M., W. Z. Zhao, and H. Cao, 2006, Nonlinear process control of wave-equation inversion and its application in the detection of gas: Geophysics, **72**, R9–R18.

Shin, C., and Y. Ho Cha, 2009, Waveform inversion in the Laplace-Fourier domain: Geophysical Journal International, **177**, 1067–1079.

Shuey, R., 1985, A simplification of the zoeppritz equations: Geophysics, **50**, 609–614.

Shulakova, V., R. Pevzner, J. C. Dupuis, M. Urosevic, K. Tertyshnikov, D. E. Lumley, and B. Gurevich, 2015, Burying receivers for improved time-lapse seismic repeatability: CO_2CRC otway field experiment: Geophysical Prospecting, **63**, 55–69.

Singh, S., I. Tsvankin, and E. Z. Naeini, 2018, Bayesian framework for elastic full-waveform inversion with facies information: The Leading Edge, **37**, 924–931.

Singh, S., I. Tsvankin, and E. Zabihi Naeini, 2020, Full-waveform inversion with borehole constraints for elastic VTI media: Geophysics, **85**, R553–R563.

Spikes, K., T. Mukerji, J. Dvorkin, and G. Mavko, 2007, Probabilistic seismic inversion based on rock-physics models: Geophysics, **72**, R87–R97.

Stolt, R. H., and A. B. Weglein, 2012, Seismic imaging and inversion: Volume 1: Application of linear inverse theory: Cambridge University Press, **1**.

Stopin, A., R.-É. Plessix, and S. Al Abri, 2014, Multiparameter waveform inversion of a large wide-azimuth low-frequency land data set in oman: Geophysics, **79**, WA69–WA77.

Tarantola, A., 1984, Inversion of seismic reflection data in the acoustic approximation: Geophysics, **49**, 1259–1266.

———, 1986, A strategy for nonlinear elastic inversion of seismic reflection data: Geophysics, **51**, 1893–1903.

———, 2005, Inverse problem theory and methods for model parameter estimation: SIAM.

Tavakoli, R., H. Yoon, M. Delshad, A. H. ElSheikh, M. F. Wheeler, and B. W. Arnold, 2013, Comparison of ensemble filtering algorithms and null-space Monte Carlo for parameter estimation and uncertainty quantification using CO_2 sequestration data: Water Resources Research, **49**, 8108–8127.

Terazaghi's, K., 1965, Theoretical soil mechanics: John Wiley and Sons.

Tetyukhina, D., S. M. Luthi, and D. Gisolf, 2014, Acoustic nonlinear full-waveform inversion on an outcrop-based detailed geological and petrophysical model (Book Cliffs, Utah) acoustic nonlinear full-waveform inversion: AAPG Bulletin, **98**, 119–134.

Tikhonov, A. N., and V. Y. Arsenin, 1977, Solutions of ill-posed problems: Winston and Sons.

Trani, M., R. Arts, O. Leeuwenburgh, and J. Brouwer, 2011, Estimation of changes in saturation and pressure from 4D seismic AVO and time-shift analysis: Geophysics, **76**, C1–C17.

Tveit, S., T. Mannseth, J. Park, G. Sauvin, and R. Agersborg, 2020, Combining CSEM or gravity inversion with seismic AVO inversion, with application to monitoring of large-scale CO_2 injection: Computational Geosciences, **24**, 1201–1220.

Van Riel, P., 2000, The past, present, and future of quantitative reservoir characterization: The leading edge, **19**, 878–881.

Vanorio, T., 2015, Recent advances in time-lapse, laboratory rock physics for the characterization and monitoring of fluid-rock interactions: Geophysics, **80**, WA49–WA59.

Vialle, S., and T. Vanorio, 2011, Laboratory measurements of elastic properties of carbonate rocks during injection of reactive CO_2-saturated water: Geophysical Research Letters, **38**.

Virieux, J., and S. Operto, 2009, An overview of full-waveform inversion in exploration geophysics: Geophysics, **74**, WCC1–WCC26.

Wang, Z., 2001, Y2k tutorial: Fundamentals of seismic rock physics: Geophysics, **66**, 398–412.

Warner, M., A. Ratcliffe, T. Nangoo, J. Morgan, A. Umpleby, N. Shah, V. Vinje, I. Štekl, L. Guasch, C. Win, et al., 2013, Anisotropic 3D full-waveform inversion: Geophysics, **78**, R59–R80.

Wu, R.-S., and K. Aki, 1985, Scattering characteristics of elastic waves by an elastic heterogeneity: Geophysics, **50**, 582–595.

Wyllie, M., G. Gardner, and A. Gregory, 1962, Studies of elastic wave attenuation in porous media: Geophysics, **27**, 569–589.

Yang, Q., and A. Malcolm, 2019, Single parameter full waveform inversion in fluid-saturated porous media: 89th Annual International Meeting, SEG, Expanded Abstracts, 1450–1454.

Yang, Q., A. Malcolm, H. Rusmanugroho, and W. Mao, 2019, Analysis of radiation patterns for optimized full waveform inversion in fluid-saturated porous media: Geophysical Journal International, **216**, 1919–1937.

Yilmaz, Ö., 2001, Seismic data analysis: Processing, inversion, and interpretation of seismic data: Society of exploration geophysicists.

Zhang, F., C. Juhlin, M. Ivandic, and S. Lüth, 2013, Application of seismic full waveform inversion to monitor CO_2 injection: Modelling and a real data example from the Ketzin site, Germany: Geophysical Prospecting, **61**, 284–299.

Zhang, Z. D., and T. Alkhalifah, 2019, Regularized elastic full-waveform inversion using deep learning: Geophysics, **84**, R741–R751.

Zhang, Z. D., T. Alkhalifah, E. Z. Naeini, and B. B. Sun, 2018, Multiparameter elastic full waveform inversion with facies-based constraints: Geophysical Journal International, **213**, 2112–2127.

Zimmerman, R. W., 1990, Compressibility of sandstones: Elsevier.

Appendix A

The VRH model partial derivatives

Let X denote any of the three rock physics properties, ϕ, C, and S_w, and let the prime $'$ denote the partial derivative with respect to X. Substituting equations 4.10 and 4.11 into equation 4.12, I calculate the partial derivatives of P- and S-wave velocities with respect to X:

$$\frac{\partial V_{\mathrm{P}}}{\partial X} = \frac{1}{4\rho^2 V_{\mathrm{P}}}\left[\left(K'_{\mathrm{V}} + K'_{\mathrm{R}} + \frac{4}{3}\mu'_{\mathrm{V}}\right)\rho - \left(K_{\mathrm{V}} + K_{\mathrm{R}} + \frac{4}{3}\mu_{\mathrm{V}}\right)\rho'\right], \tag{A.1}$$

$$\frac{\partial V_{\mathrm{S}}}{\partial X} = \frac{1}{4\rho^2 V_{\mathrm{S}}}(\mu'_{\mathrm{V}}\rho - \mu_{\mathrm{V}}\rho'). \tag{A.2}$$

When X is porosity,

$$\begin{aligned}
K'_{\mathrm{V}} &= -K_c C - K_q(1-C) + K_w S_w + K_h(1-S_w),\\
K'_{\mathrm{R}} &= K_{\mathrm{R}}^2\left(\frac{C}{K_c} + \frac{1-C}{K_q} - \frac{S_w}{K_w} - \frac{1-S_w}{K_h}\right),\\
\mu'_{\mathrm{V}} &= -\mu_c C - \mu_q(1-C),\\
\rho' &= \rho_f - \rho_m.
\end{aligned} \tag{A.3}$$

When X is clay content,

$$\begin{aligned} K'_{\mathrm{V}} &= (1-\phi)(K_c - K_q), \\ K'_{\mathrm{R}} &= (1-\phi)K_{\mathrm{R}}^2\left(\frac{1}{K_q} - \frac{1}{K_c}\right), \\ \mu'_{\mathrm{V}} &= (1-\phi)(\mu_c - \mu_q), \\ \rho' &= (1-\phi)(\rho_c - \rho_q). \end{aligned} \tag{A.4}$$

When X is water saturation,

$$\begin{aligned} K'_{\mathrm{V}} &= \phi(K_w - K_h), \\ K'_{\mathrm{R}} &= \phi K_{\mathrm{R}}^2\left(\frac{1}{K_h} - \frac{1}{K_w}\right), \\ \mu'_{\mathrm{V}} &= 0, \\ \rho' &= \phi(\rho_w - \rho_h). \end{aligned} \tag{A.5}$$

The partial derivatives of density with respect to ϕ, C, and S_w are the same as in equation 4.7.

Appendix B

The KT model partial derivatives

The partial derivatives of P- and S-wave velocities with respect to any rock physics property X can be written as

$$\frac{\partial V_{\mathrm{P}}}{\partial X} = \frac{1}{2\rho^2 V_{\mathrm{P}}} \left[\left(K'_{\mathrm{sat}} + \frac{4}{3}\mu'_{\mathrm{sat}} \right) \rho - \left(K_{\mathrm{sat}} + \frac{4}{3}\mu_{\mathrm{sat}} \right) \rho' \right], \tag{B.1}$$

$$\frac{\partial V_{\mathrm{S}}}{\partial X} = \frac{1}{2\rho^2 V_{\mathrm{S}}} (\mu'_{\mathrm{sat}}\rho - \mu_{\mathrm{sat}}\rho'), \tag{B.2}$$

where as in Appendix A the prime $'$ denotes the relevant partial derivative operation. From equation 4.13,

$$K_{\mathrm{sat}} = \frac{P}{Q}, \quad \mu_{\mathrm{sat}} = \frac{S}{T}, \tag{B.3}$$

so

$$K'_{\mathrm{sat}} = \frac{P'Q - PQ'}{Q^2}, \quad \mu'_{\mathrm{sat}} = \frac{S'T - ST'}{T^2}, \tag{B.4}$$

where

$$
\begin{aligned}
P &= 4K_m\mu_m + 3K_mK_f + 4\mu_mK_f\phi - 4K_m\mu_m\phi,\\
Q &= 4\mu_m + 3K_f - 3K_f\phi + 3K_m\phi,\\
S &= \mu_m(9K_m + 8\mu_m)(1-\phi),\\
T &= 9K_m + 8\mu_m + 6(K_m + 2\mu_m)\phi.
\end{aligned}
\tag{B.5}
$$

When X is porosity,

$$
\begin{aligned}
P' &= 4\mu_mK_f - 4K_m\mu_m,\\
Q' &= -3K_f + 3K_m,\\
S' &= -\mu_m(9K_m + 8\mu_m),\\
T' &= 6(K_m + 2\mu_m),\\
\rho' &= \rho_f - \rho_m.
\end{aligned}
\tag{B.6}
$$

When X is clay content,

$$
\begin{aligned}
P' &= 4(1-\phi)(K'_m\mu_m + K_m\mu'_m) + 3K_fK'_m + 4K_f\phi\mu'_m,\\
Q' &= 4\mu'_m + 3\phi K'_m,\\
S' &= (1-\phi)[\mu'_m(9K_m + 8\mu_m) + \mu_m(9K'_m + 8\mu'_m)],\\
T' &= 9K'_m + 8\mu'_m + 6\phi(K'_m + 2\mu'_m),\\
\rho' &= (1-\phi)(\rho_c - \rho_q),
\end{aligned}
\tag{B.7}
$$

where

$$
\begin{aligned}
K'_m &= \frac{1}{2}\left[K_c - K_q - \left(\frac{1}{K_c} - \frac{1}{K_q}\right) \Big/ \left(\frac{C}{K_c} + \frac{1-C}{K_q}\right)^2\right],\\
\mu'_m &= \frac{1}{2}\left[\mu_c - \mu_q - \left(\frac{1}{\mu_c} - \frac{1}{\mu_q}\right) \Big/ \left(\frac{C}{\mu_c} + \frac{1-C}{\mu_q}\right)^2\right].
\end{aligned}
\tag{B.8}
$$

When X is water saturation,

$$\begin{aligned} P' &= (3K_m + 4\mu_m\phi)(K_w - K_h), \\ Q' &= 3(1-\phi)(K_w - K_h), \\ S' &= 0, \\ T' &= 0, \\ \rho' &= \phi(\rho_w - \rho_h). \end{aligned} \tag{B.9}$$

The partial derivatives of density with respect to ϕ, C, and S_w are the same as in equation 4.7.

Appendix C

Rock physics parameterized FWI with regularization

Because the rock physics FWI approach shares the same numerical structure as the conventional EFWI, it allows various existing inversion strategies, such as regularization, to be integrated conveniently. Here I consider the regularization scheme, discussed in Chapter 2, that encourages explicit relationships between different physical parameters. I assume that porosity ϕ and clay content C in the target area are highly correlated, and their relationship, $C = f(\phi)$, can be obtained by regression of well-log data. I then include this prior information via a model term E_m in the objective function E:

$$\begin{aligned} E(\mathbf{m}) &= E_d(\mathbf{m}) + \gamma E_m(\mathbf{m}), \\ &= E_d(\mathbf{m}) + \gamma \sum_{\mathbf{x}} (C - f(\phi))^2. \end{aligned} \tag{C.1}$$

I test this approach on a selected part of the elastic Marmousi2 model, in which rock physics properties are assigned to each cell. In Figure C.1a and C.1e, the "true" porosity and clay content models are plotted. A gas sand trap, at a depth of 0.25 km and positioned at 0.8 km laterally, is distinguished by a higher porosity of 0.26 and a lower clay content of

0.1. The initial models in Figure C.1b and C.1f are smoothed versions of the true models. Without model constraint, we observe an insufficient update for both ϕ and C (Figure C.1c and C.1g), especially in the deeper part of the C model. By constraining the relationship between updated ϕ and C, the two properties are better resolved, with a similar resolution, capturing the relevant reservoir structures (Figure C.1d and C.1h). In Figure C.2, projections of these models in the $\phi - C$ domain are demonstrated.

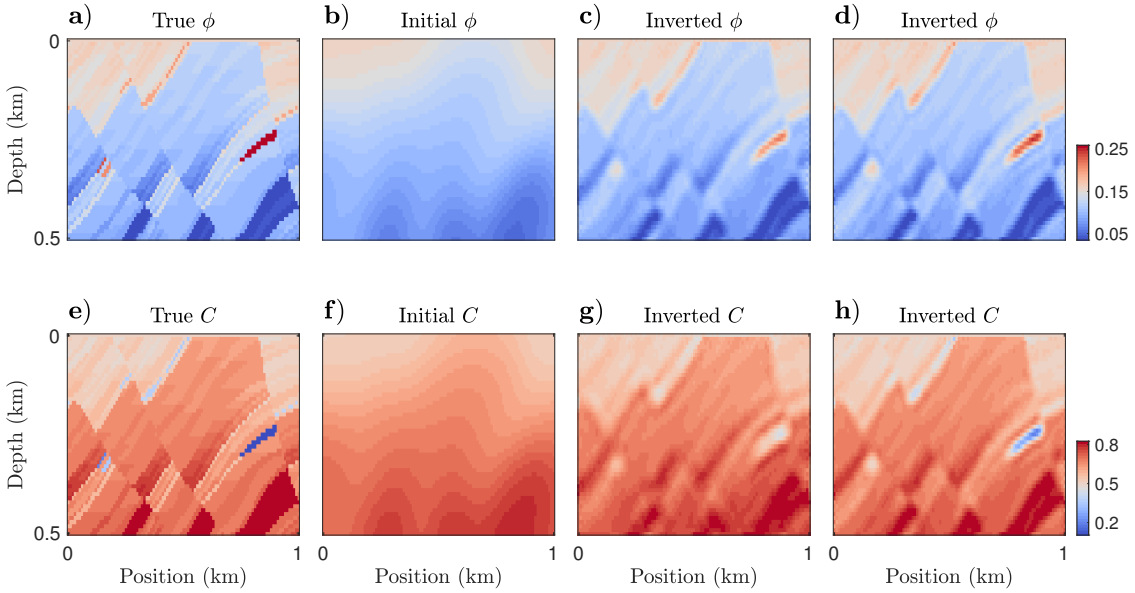

Figure C.1: (a,e) True models and (b,f) initial models of porosity and clay content. (c,g) Inverted models without constraint. (d,h) Inverted models with constraint.

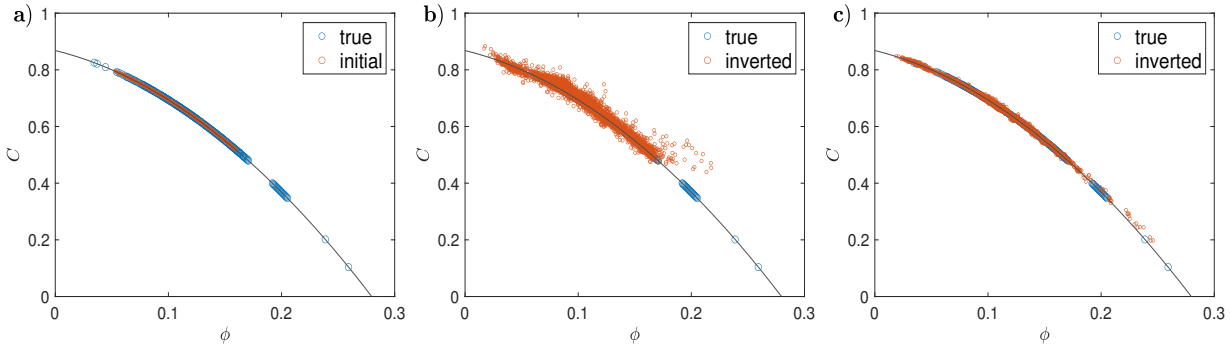

Figure C.2: ϕ-C crossplots of the (a) initial model, (b) inverted model without constraint, and (c) inverted model with constraint. The gray line denotes the ϕ-C relationship used as model constraint.

Appendix D

Towards simultaneous prediction of CO_2 saturation and pore pressure

In the previous simulation, the pressure difference between the baseline survey and the monitor survey is relatively small, therefore I assume that the pressure's effect on seismic changes is negligible. For some fields or segments within a field, both fluid and pressure changes have approximately the same degree of impact on the seismic data (Landrø et al., 2003). To deal with this situation, the rock physics model and time-lapse FWI strategy I proposed must be adjusted to account for the pressure effect. With the fluid effect at seismic frequency being well described by Gassmann's equation, the main challenge lies in the description of pressure within the rock physics model.

I should first clarify the different types of geopressure. Pore pressure (P_p) is the pressure of fluids in the pore space of the rock. When pore pressure is hydrostatic, we have

$$P_p = \rho_w g z, \tag{D.1}$$

where z is the depth, g is the acceleration of gravity, and ρ_w is the density of water. When pore pressure exceeds the hydrostatic pressure, an overpressure situation occurs. The confin-

ing or overburden pressure P_c results from the weight of overlying sediments and is generally obtained by integrating the density log:

$$P_c = g \int_0^z \rho(z')dz', \tag{D.2}$$

where ρ is the bulk density of the rock. Based on Terazaghi's (1965) principle, the effective pressure P_e is defined as the difference between overburden pressure and pore pressure:

$$P_e = P_c - P_p. \tag{D.3}$$

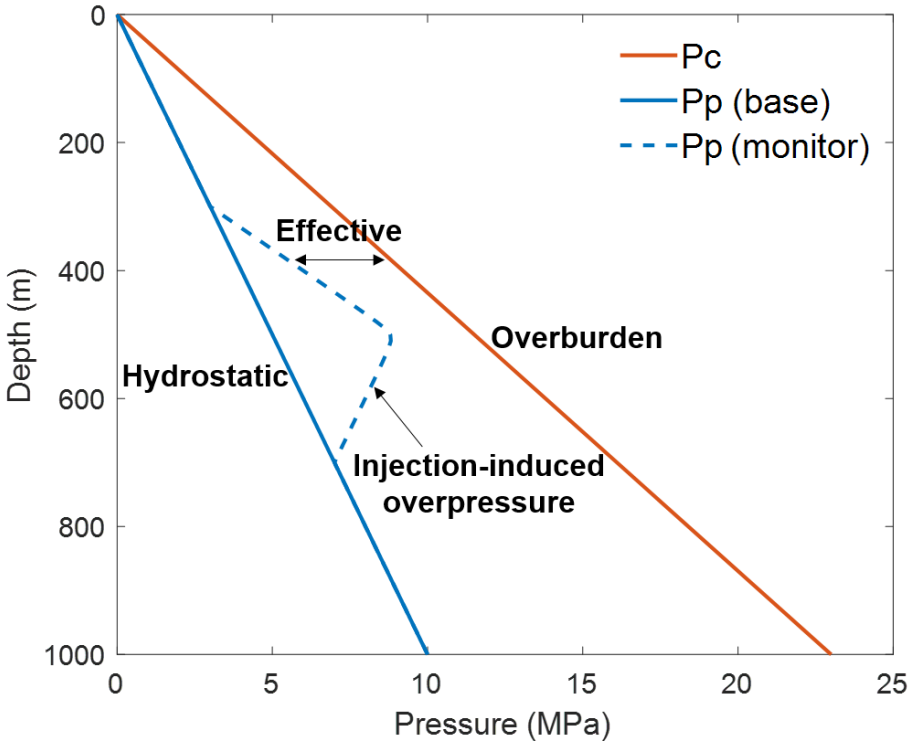

Figure D.1: Example of different pressures with depth.

In Figure D.1, I demonstrate the typical trends of these three pressures with depth, as well as possible overpressure anomalies due to CO_2 injection. Pore pressure and its development over time is a critical parameter for storage safety and it is also the main limiting factor for large-scale storage of CO_2 (Ringrose, 2020). However, since the effective pressure is more

relevant to affecting the elastic properties of the rock, seismic pore pressure prediction is generally achieved by an accurate characterization of effective pressure on the assumption that overburden pressure is known. Similarly, although my inversion target is pore pressure, the key to this research is the modeling of effective pressure.

D.1 Considerations for the rock physics model

An important criterion for me to choose a pressure model is whether it can be integrated into the entire modeling process based on Gassmann's equation, because only in this way can I also consider the influence of other important parameters (such as porosity, lithology, and fluid) on rock elastic properties. Therefore, while there are many empirical formulas describing the relationship between velocity and effective pressure in the literature (Han, 1987; Eberhart-Phillips et al., 1989; Landrø, 2001; Jones, 1995; Sayers, 2006), these are outside the scope of my study.

In equations D.4-D.6, Gassmann's equation and density equation are given with underlined dependencies to the pressures and CO_2 saturation:

$$K_{\text{sat}}(S_{\text{co}_2}, P_p, P_e) = K_{\text{dry}}(P_e) + \frac{[1 - K_{\text{dry}}(P_e)/K_m]^2}{\phi/K_f(S_{\text{co}_2}, P_p) + (1-\phi)/K_m - K_{\text{dry}}(P_e)/K_m^2}, \tag{D.4}$$

$$\mu_{\text{sat}}(P_e) = \mu_{\text{dry}}(P_e), \tag{D.5}$$

$$\rho_{\text{sat}}(S_{\text{co}_2}, P_p) = (1-\phi)\rho_m + \phi\rho_f(S_{\text{co}_2}, P_p), \tag{D.6}$$

where the subscripts $m, f, \text{dry}, \text{sat}$ indicate solid matrix, fluid phase, dry rock, and saturated rock, respectively. Based on the principle that effective pressure and pore pressure are interchangeable at a given overburden pressure, the effect of pressure on the elastic properties of fluid-saturated rock is due to its influence on the bulk modulus and density of fluid (K_f and ρ_f) and the elastic moduli of dry rock (K_{dry} and μ_{dry}). The former can be well described by the empirical formula proposed by Batzle and Wang (1992), while the latter

requires more thought. An intuitive choice is a dry-rock theoretical model which includes pressure in its expression, such as the granular media models that are based on the Hertz-Mindlin contact theory (Chapter 3). However, in a Hertz-Mindlin model, the dry-rock elastic modulus is proportional to the cube root of effective pressure, $K_{\text{dry}} \propto \sqrt[3]{P_e}$, which violates the exponential relationship illustrated by many laboratory studies. Given this, I focus on the modified MacBeth's relation proposed by Grana (2016b).

MacBeth (2004) proposed an analogous equation to link dry-rock bulk modulus to effective pressure using an exponential relation:

$$K_{\text{dry}}(P_e) = \frac{K^{\infty}}{1 + A_K e^{-\frac{P_e}{P_K}}}, \tag{D.7}$$

where K^{∞}, A_K, and P_K are empirical parameters: K^{∞} represents the asymptotic value as effective pressure increases, whereas A_K and P_K are related to the curvature. Grana (2016b) illustrates that K^{∞} and A_K are not independent if the dry-rock modulus K_0 at a given effective pressure P_0 is known, and modified equation D.7 to include dependence on porosity ϕ and clay content V_{clay}:

$$K_{\text{dry}}(P_e) = \frac{K^{\infty}}{1 + \frac{K^{\infty} - K_0}{K_0} e^{-\frac{P_{\text{eff}} - P_0}{P_K}}}; \tag{D.8}$$

$$K^{\infty} = \lambda_1(\phi + aV_{\text{clay}}) + \lambda_2, \tag{D.9}$$

where a, λ_1, and λ_2 are empirical parameters that must be fitted using lab measurements. Datasets from literature or nearby fields could be used to integrate the available core samples, as long as the observed pressure effect on elastic properties has the same behavior. Similar results have been obtained for the shear modulus:

$$\mu_{\text{dry}}(P_e) = \frac{\mu^{\infty}}{1 + \frac{\mu^{\infty} - \mu_0}{\mu_0} e^{-\frac{P_e - P_0}{P_\mu}}}; \tag{D.10}$$

$$\mu^{\infty} = \lambda_3(\phi + aV_{\text{clay}}) + \lambda_4, \tag{D.11}$$

where μ_0 is the dry-rock shear modulus at effective pressure P_0; λ_3 and λ_4 are empirical parameters.

The modified MacBeth's equation focus on the effect of pressure on elastic properties and lack mechanisms to account for the impact of rock properties, such as porosity and lithology. By contrast, the Hertz-Mindlin based models, although have a pressure term in their expressions, are classically used to predict static rock properties rather than pressure changes. To combine the advantages of both, we can use the modified MacBeth's equation as the dry-rock model for time-lapse study, but with the initial/baseline moduli, K_0 and μ_0, computed by a Hertz-Mindlin model.

I take three core samples from a published dataset of Han (1987) to illustrate how to calibrate the rock physics model in practical applications. My goal is to calibrate the model so that it can accurately predict velocity as a function of porosity, clay content, and effective pressure.

I assume that the initial or baseline pressure is 10 MPa and that the data at other pressures correspond to monitor surveys. I first examine the Hertz-Mindlin model. This means that once we calibrate the model at an initial pressure, the model automatically predicts the value at future pressures. Figure D.2 shows that the Hertz-Mindlin model does not correctly approximate the nonlinear behavior of velocity due to pressure changes. On the other hand, the modified Macbeth's relation predicts the data accurately (Figure D.3). Indeed, the main advantages of this model are the exponential trend and the inclusion of empirical parameters that can be calibrated to match the observations.

D.2 Time-lapse FWI strategy

Once the rock physics model is built and calibrated, I modify the previous time-lapse FWI framework to include one degree of freedom for pressure variations. Still, I use baseline data ($\mathbf{d}_{\text{obs\_b}}$) to estimate the static rock properties, such as porosity (ϕ) and clay content (C); I then use these baseline models as prior knowledge (fixed values) to estimate dynamic

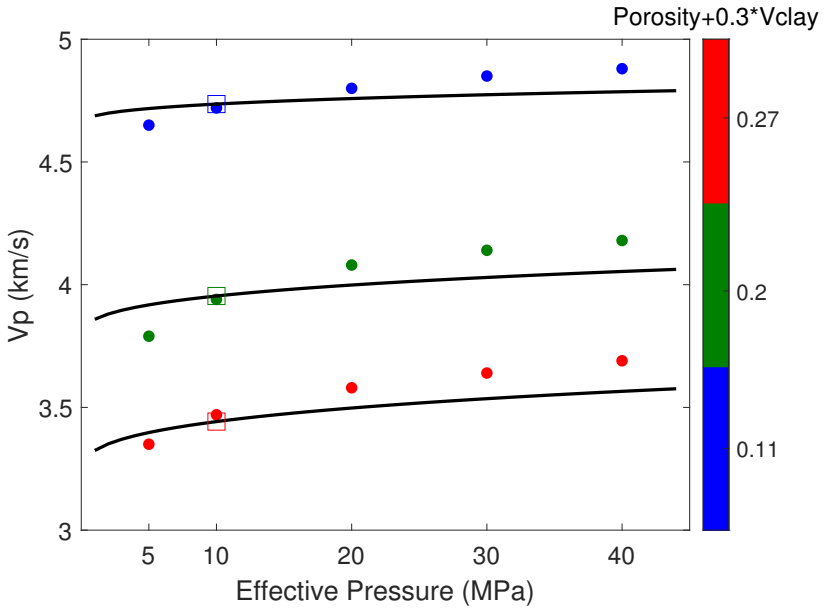

Figure D.2: Calibration of rock physics model using Han's dataset (subset of 3 samples). Hertz-Mindlin model is combined with Gassmann's equations to predict saturated-rock velocity as a function of effective pressure including porosity and mineralogy effects. The model is calibrated at pressure 10 MPa, then automatically predicts the data at 5,20,30,40 MPa.

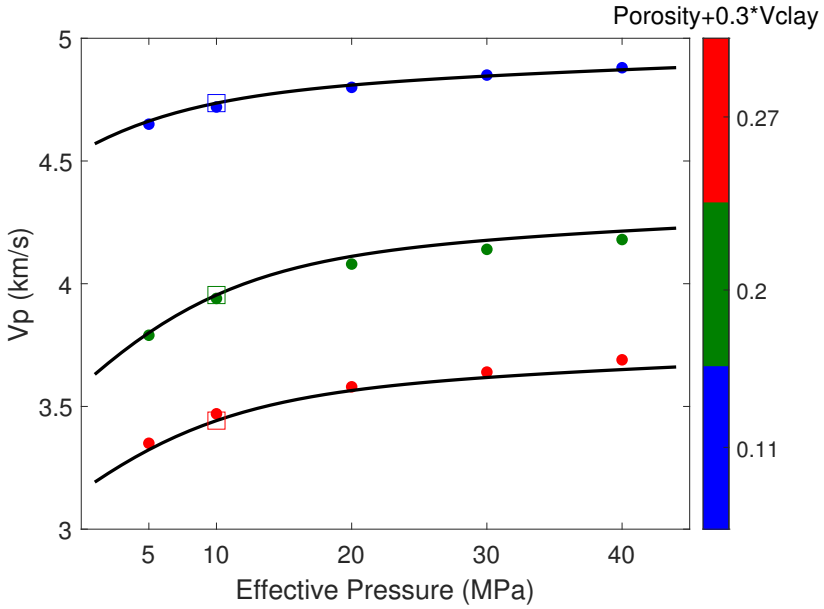

Figure D.3: Macbeth's relation combined with Gassmann's equations to predict saturated-rock velocity as a function of effective pressure including porosity and mineralogy effects. Hertz-Mindlin predictions at pressure 10 MPa are used as input in Macbeth's model.

reservoir properties, such as CO_2 saturation (Sc) and pore pressure (P_p), from monitor data ($\mathbf{d}_{\text{obs\_m}}$). The objective functions for this problem are expressed as

$$E_b = \left\|\mathbf{d}_{\text{obs\_b}}(\phi^t, C^t) - \mathbf{d}_{\text{syn\_b}}(\phi, C)\right\|^2, \tag{D.12}$$

and

$$E_m = \left\|\mathbf{d}_{\text{obs\_m}}(\phi^t, C^t, Sc^t, {P_p}^t) - \mathbf{d}_{\text{syn\_m}}(\phi^b, C^b, Sc, P_p)\right\|^2. \tag{D.13}$$

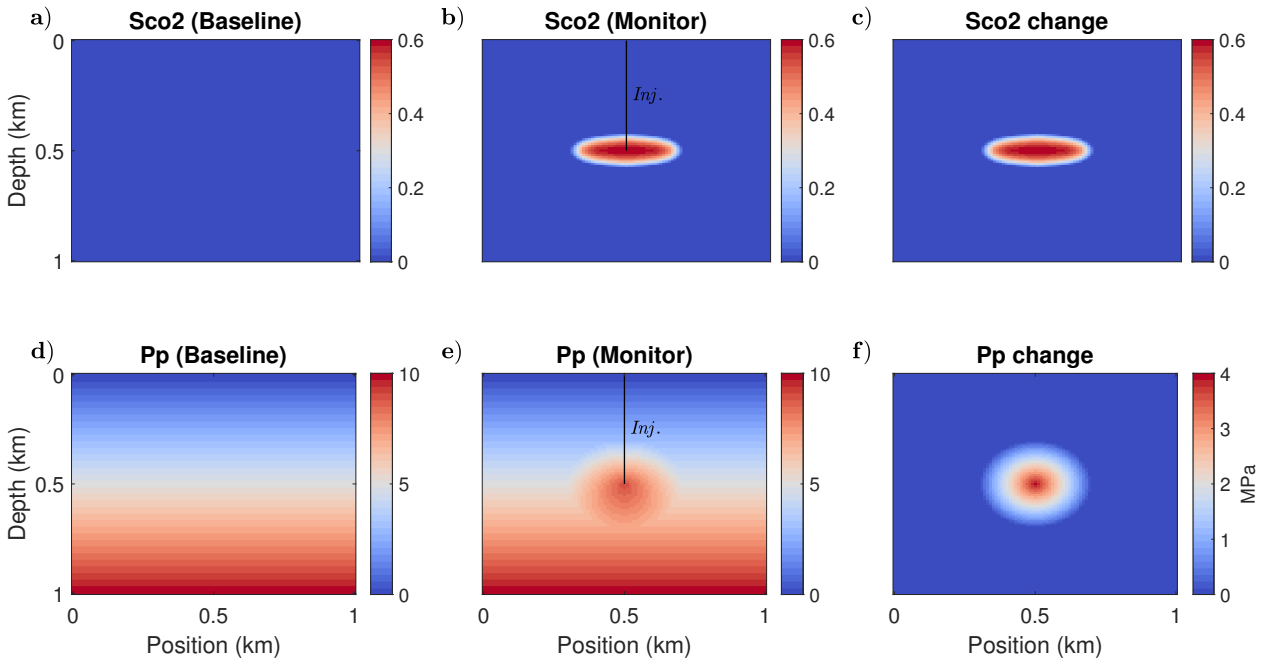

Figure D.4: True baseline, monitor, and time-lapse models of CO_2 saturation and pore pressure. The black line indicates the location of the injection well.

D.3 Numerical example

I apply the method to a synthetic model as shown in Figure D.4. The initial CO_2 saturation is 0 everywhere and the initial pore pressure is hydrostatic. The two models then change locally due to the injection of CO_2 at 500 m depth and 500 m position. In this simulation, I neglect the uncertainty associated with the baseline model reconstruction, namely, I assume

the porosity and clay models are accurately predicted. The details of the pressure model are illustrated in Figure D.1, where I consider a clear pressure build-up due to CO_2 injection.

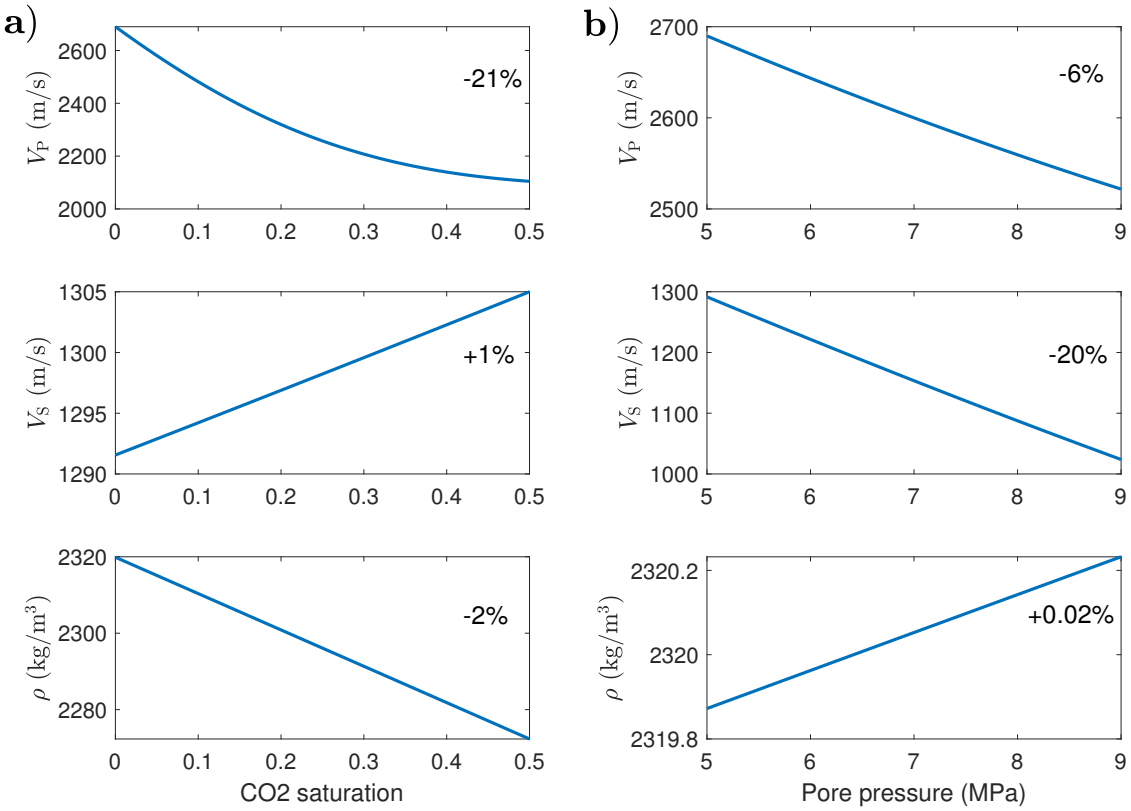

Figure D.5: Theoretical curves of the proposed rock physics model: P-wave velocity, S-wave velocity, and density versus (a) CO_2 saturation and (b) pore pressure.

In Figure D.5, I compute the theoretical curves of velocities and density as a function of CO_2 saturation and pore pressure based on the rock physics model. The results are consistent with existing studies: if CO_2 saturation increases, the P-wave velocity and density decrease, whereas the S-wave velocity slightly increases; both P- and S-wave velocities decrease as pore pressure increases, whereas the pressure effect on density is negligible. I point out that there are two reasons leading to the significant velocity changes in this test: 1) The rock physics model I choose corresponds to weakly consolidated rocks; 2) the depth range I set corresponds to low-pressure values, as compared to many studies where the reservoir is located at a deeper location.

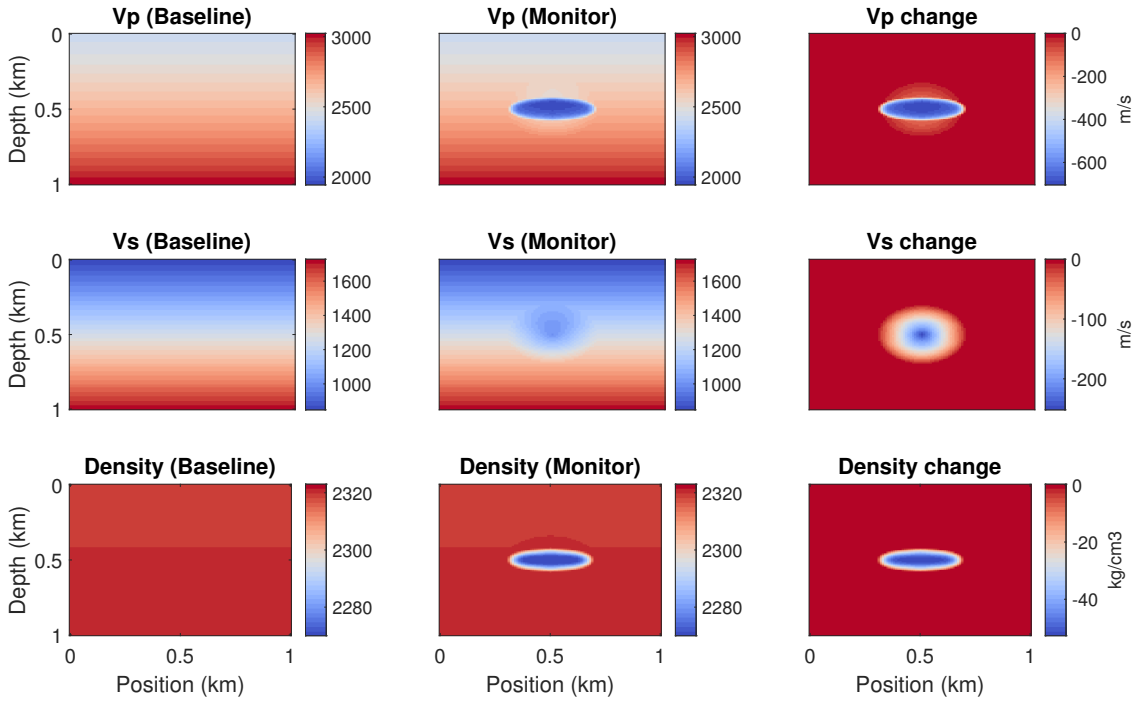

Figure D.6: Baseline, monitor, and time-lapse models of P- and S-wave velocity plus density.

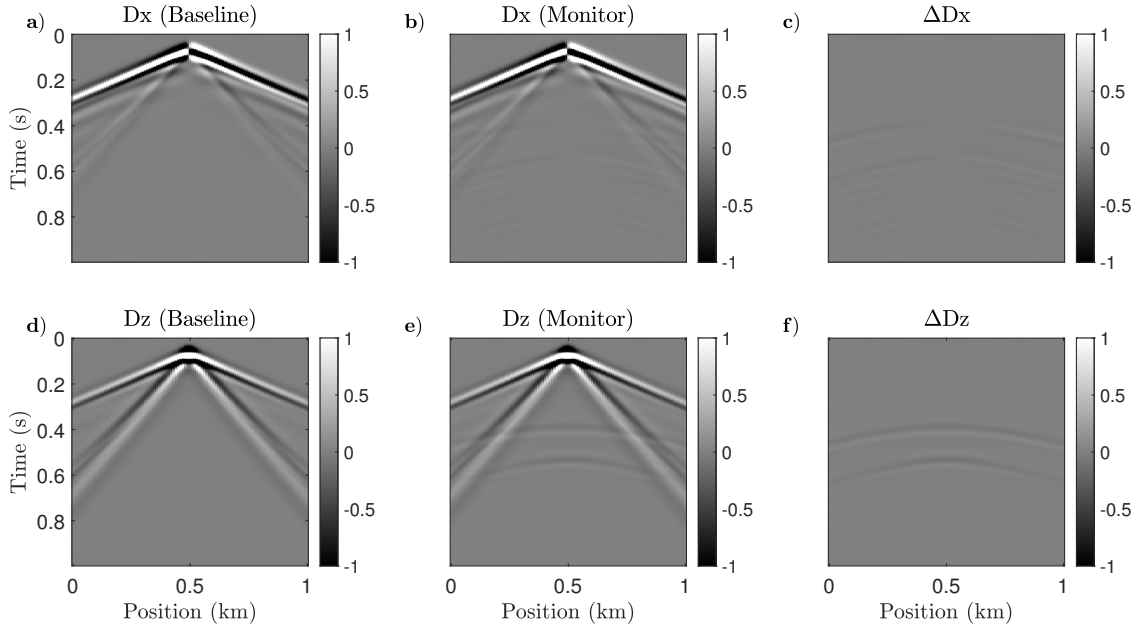

Figure D.7: Baseline, monitor, and differential seismograms (horizontal and vertical displacements) computed for the true model.

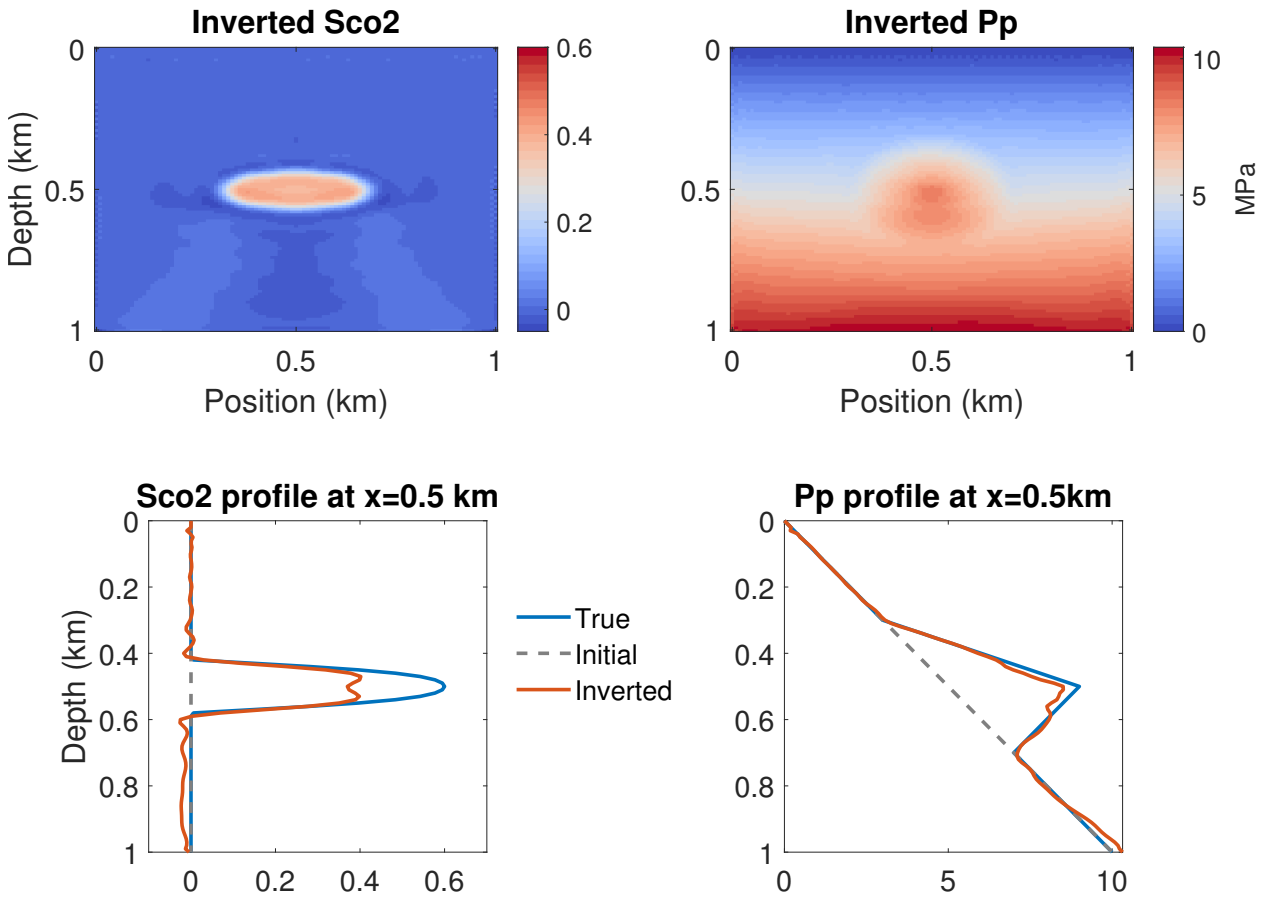

Figure D.8: Recovered monitor model of CO_2 saturation and pore pressure.

In Figure D.6, I plot the velocity and density models corresponding to the rock property model. The time-lapse elastic changes are consistent with the analysis in Figure D.5. Consequently, we observe clear time-lapse events in the noise-free synthetic data (Figure D.7). The recovered monitor model of CO_2 saturation and pore pressure are plotted in Figure D.8, which shows a good agreement with the true models. The parameter crosstalk is weak. I attribute this to the fact that the two properties have very different sensitivities with respect to the P- and S-wave velocities (Figure D.5). In Figure D.9, the convergence properties of the inversion are summarized. We observe the convergence characteristics of a reliable inversion.

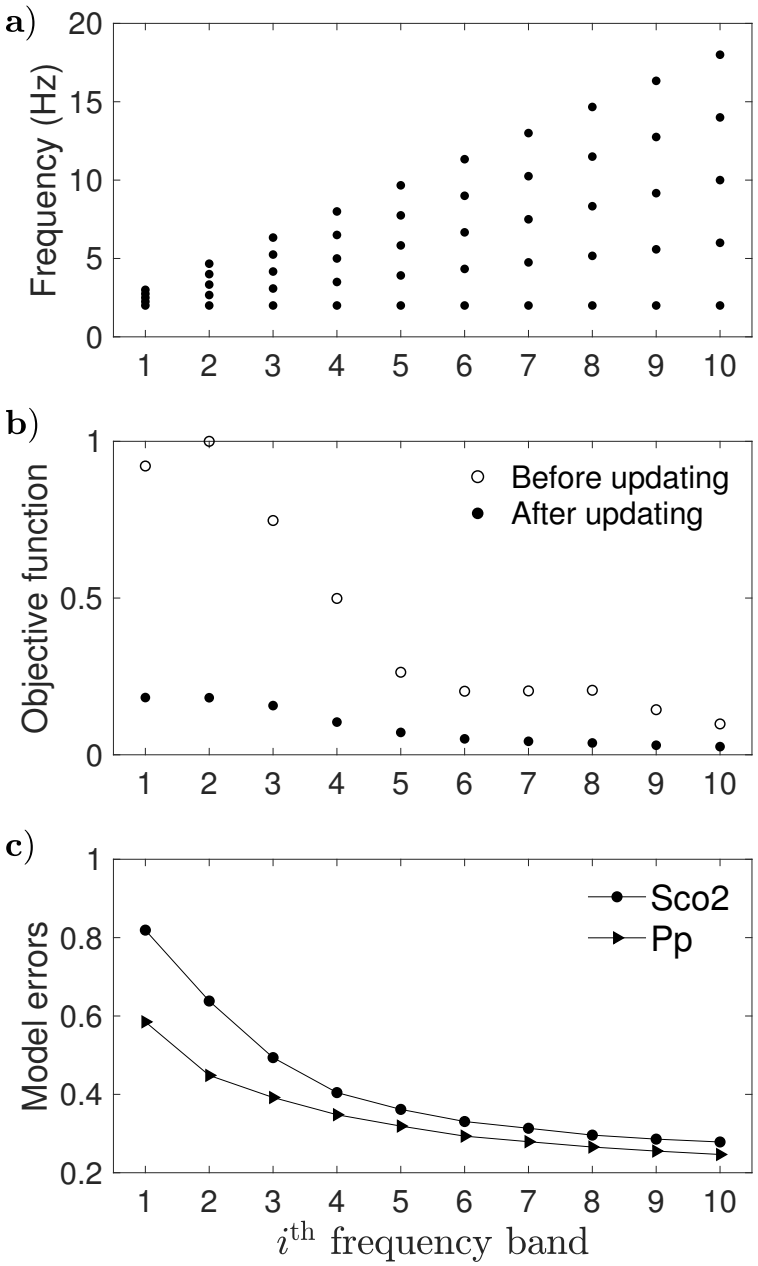

Figure D.9: Convergence properties. (a-c) Frequencies, objective functions, and model errors (after updating) within a frequency band, respectively.

D.4 Conclusions

The estimation of CO_2 saturation and pore pressure from time-lapse seismic data requires a physical model relating the variations in reservoir properties to the changes in seismic attributes. I proposed a rock physics workflow combing the modified Macbeth's relation

and Gassmann's equation to predict elastic properties as a function of porosity, mineralogy, saturation, and pressure. I validated this workflow using a published dataset. In particular, I demonstrated the advantages of the modified Macbeth's model in predicting pressure changes. Furthermore, I proposed a full waveform inversion (FWI) algorithm for quantitative prediction of CO_2 saturation and pore pressure from time-lapse seismic data. I illustrated the potential of the approach using a synthetic time-lapse dataset. Examination of complex geological models and uncertainties associated with the rock physics model, the observed data, and the baseline inversion result are important steps in moving this research forward.